Structural and electrical characterization of novel layered intergrowth compounds: $[(MSe)_{1+\delta}]_m[NbSe_2]_n$ ferecrystals with M = Pb and Sn

D I S S E R T A T I O N

zur Erlangung des akademischen Grades

doctor rerum naturalium
(Dr. rer. nat.)
im Fach Physik

eingereicht an der
Mathematisch-Naturwissenschaftlichen Fakultät
der Humboldt-Universität zu Berlin

von
M.Sc. Corinna Grosse

Präsident der der Humboldt-Universität zu Berlin
Prof. Dr. Jan-Hendrik Olbertz

Dekan der Mathematisch-Naturwissenschaftlichen Fakultät
Prof. Dr. Elmar Kulke

Gutachter/innen:
1. Prof. Dr. Saskia F. Fischer
2. Prof. Dr. Wolfgang Neumann
3. Prof. Dr. Christoph Strunk

Tag der mündlichen Prüfung: 27.01.2016

Abstract

The ferecrystals $[(M\mathrm{Se})_{1+\delta}]_m[\mathrm{NbSe_2}]_n$ with M = Pb and Sn are novel layered intergrowth compounds of m $\mathrm{NbSe_2}$ monolayers (consisting of three atomic monolayers: Se-Nb-Se), stacked repeatedly with n PbSe or SnSe atomic bilayers. Bulk $\mathrm{NbSe_2}$ is a layered compound showing charge density waves and superconductivity. Due to their artificially atomic-scale layered structure, ferecrystals could serve as model systems for layered superconductors. In this study, their structural and electrical properties are investigated. Using transmission electron microscopy a turbostratically disordered, nanocrystalline structure of the ferecrystals is revealed. The atomic structure within the individual layers is similar as for bulk $\mathrm{NbSe_2}$, PbSe and SnSe, with the crystallographic c-axes of $\mathrm{NbSe_2}$, PbSe and SnSe parallel to the stacking direction in the ferecrystals. The in-plane electrical resistivity values are within the range of values reported for bulk $\mathrm{NbSe_2}$ and PbSe or SnSe. The dependence of the in-plane resistivity and Hall coefficient on m and n reveals deviations from a simple parallel resistors model, showing a contribution of the PbSe and SnSe layers to the electrical transport in the ferecrystals. A quantitative analysis using a two-layer model fit to the magnetic field dependence of the resistance yields a carrier type and density in the $\mathrm{NbSe_2}$ layers, which are similar as reported for isolated $\mathrm{NbSe_2}$ monolayers and differ from those of bulk $\mathrm{NbSe_2}$. A normal-to-superconducting transition has been detected for the first time in ferecrystals. The transition temperatures are $T_\mathrm{c} \approx 0.82(5)$ K to 2.66(4) K. For the ferecrystals $[(\mathrm{PbSe})_{1+\delta}]_1[\mathrm{NbSe_2}]_n$ with $n = 1, 2, 3$, T_c is only 44 % to 64 % of T_c of analogous non-turbostratically disordered misfit layer compounds. This reduction in T_c can be ascribed to the turbostratic disorder in ferecrystals if non-stoichiometry and octahedral coordination of the Nb atoms by Se can be excluded. The ratio between the cross-plane Ginzburg-Landau coherence length and the cross-plane distance between the $\mathrm{NbSe_2}$ layers for the ferecrystals $[(\mathrm{SnSe})_{1+\delta}]_m[\mathrm{NbSe_2}]_1$ is lower than for bulk $\mathrm{NbSe_2}$ and non-disordered misfit layer compounds, making ferecrystals promising candidates for (quasi-)two-dimensional superconductors.

Keywords: ferecrystals, transition metal dichalcogenides, transmission electron microscopy, electrical properties, layered superconductors

Zusammenfassung

Die Ferekristalle $[(M\mathrm{Se})_{1+\delta}]_m[\mathrm{NbSe_2}]_n$ mit M = Pb und Sn sind neuartige Verwachsungs-Schichtverbindungen aus m $\mathrm{NbSe_2}$ Monolagen (bestehend aus drei Atomlagen: Se-Nb-Se), die wiederholt mit n atomaren Bilagen PbSe oder SnSe geschichtet sind. $\mathrm{NbSe_2}$ ist eine Verbindung mit Schichtstruktur, die Ladungsdichtewellen und Supraleitung zeigt. Aufgrund ihrer synthetischen, atomar geschichteten Struktur könnten Ferekristalle als Modellsysteme für geschichtete Supraleiter dienen. In dieser Arbeit werden ihre strukturellen und elektrischen Eigenschaften untersucht. Mittels Transmissionselektronenmikroskopie wird die turbostratisch ungeordnete, nanokristalline Struktur der Ferekristalle nachgewiesen. Die atomare Struktur innerhalb der einzelnen Schichten ist ähnlich wie in den Volumenmaterialien $\mathrm{NbSe_2}$, PbSe und SnSe, wobei die kristallographischen c-Achsen von $\mathrm{NbSe_2}$, PbSe und SnSe parallel zur Stapelrichtung in den Ferekristallen zeigen. Die elektrischen Widerstände der Ferekristalle sind innerhalb des Bereichs von Werten, die für die Volumenmaterialien $\mathrm{NbSe_2}$, PbSe bzw. SnSe berichtet wurden. Die Abhängigkeit des Widerstandes und des Hallkoeffizienten von m und n ergibt Abweichungen von einem einfachen Parallelwiderstandsmodell, was zeigt, dass die PbSe und SnSe-Schichten zum elektrischen Transport beitragen. Eine quantitative Analyse unter Verwendung eines Zwei-Schicht-Modells und der Magnetfeldabhängigkeit des Widerstands liefert eine ähnliche Ladungsträgerdichte und Ladungsträgertyp in den $\mathrm{NbSe_2}$ Schichten wie für isolierte Einzellagen von $\mathrm{NbSe_2}$ berichtet wurden und unterscheiden sich von denen des Volumenmaterials $\mathrm{NbSe_2}$. Ein Übergang vom normalleitenden in den supraleitenden Zustand wurde zum ersten Mal in Ferekristallen nachgewiesen. Die Übergangstemperaturen sind $T_\mathrm{c} \approx 0.82(5)\,\mathrm{K}$ bis $2.66(4)\,\mathrm{K}$. Für die Ferekristalle $[(\mathrm{PbSe})_{1+\delta}]_1[\mathrm{NbSe_2}]_n$ mit $n = 1, 2, 3$ ist T_c nur 44 % bis 64 % von T_c der nicht turbostratisch ungeordneten Misfitschichtverbindungen. Diese Reduzierung von T_c kann der turbostratischen Unordnung der Ferekristalle zugeordnet werden, wenn Nichtstöchiometrie und oktaedrische Koordination der Nb-Atome durch die Se-Atome in den $\mathrm{NbSe_2}$ Schichten ausgeschlossen werden können. Das Verhältnis zwischen der schichtsenkrechten Ginzburg-Landau-Kohärenzlänge und dem Abstand zwischen den supraleitenden Schichten ist bei den Ferekristallen kleiner als bei $\mathrm{NbSe_2}$ Volumenmaterial und einkristallinen Misfit-Schichtverbindungen, was Ferekristalle zu vielversprechenden Kandidaten für (quasi-)zwei-dimensionale Supraleiter macht.

Schlagwörter: Ferekristalle, Übergangsmetalldichalcogenide, Transmissionselektronenmikroskopie, elektrische Eigenschaften, geschichtete Supraleiter

Contents

1 Introduction to ferecrystals

Materials design on the atomic scale can open up new pathways for the understanding of the properties of novel solid state materials. Recently, transition metal dichalcogenides (TMDCs) have drawn much attention due to the possibility to exfoliate them to single or few atomic layer thin, two-dimensional (2D) sheets [1–10]. Transition metal dichalcogenides are layered materials with versatile electronic properties ranging from insulating, semiconducting, semimetallic to metallic. Some of them, for example $NbSe_2$, show low-temperature phenomena such as superconductivity and charge density waves (CDWs) [1–11]. This makes TMDCs promising candidates for the targeted design of novel 2D materials and the exploration of 2D effects [1–10, 12–15].

Ferecrystals are novel layered intergrowth compounds consisting of atomically thin layers of a TMDC stacked alternately with few-atomic-layer thin metal monochalcogenide layers, as shown schematically in Fig. 1.1a. Ferecrystals are particularly interesting because their layer stacking sequences can be controlled on the atomic scale, they are non-epitaxial and they can be prepared with a wide range of possible material combinations [16–22]. With their artificially layered structure, ferecrystals could serve as model systems for layered superconductors. Ferecrystals are synthesized using physical vapor deposition and subsequent annealing [16–20, 22–27]. This method could serve as a new approach for the preparation of materials with properties similar to those of TMDC monolayers for large-scale applications. In contrast to isolated exfoliated TMDC flakes, which are usually limited in size and susceptible for oxidation and interfacial contamination [1–3, 9, 10, 13], the TMDC layers in the ferecrystals investigated in this work are embedded in a semiconducting material, hindering oxidation and increasing their chemical stability. Furthermore, the ferecrystals can be fabricated on a macroscopic scale and they are not restricted to a certain substrate material.

The general formula of ferecrystals is $[(MX)_{1+\delta}]_m[TX_2]_n$, where M is a metal, T is a transition metal and X is Se or Te [16]. In ferecrystals a repeat unit consisting of m atomic bilayers of MX and n monolayers of TX_2 (each monolayer consisting of three atomic layers: X-T-X) is stacked repeatedly up to a total film thickness of about 50 nm. The index δ represents the crystallographic misfit between the MX and the TX_2 layers and is typically $0.08 \leq \delta \leq 0.23$ [16, 17, 20, 21, 28]. Ferecrystals have a turbostratically disordered, nanocrystalline structure [16, 19, 29, 30]. Turbostratic disorder means that the MX and TX_2 layers show an apparently random rotation around their crystallographic c-axes, while their c-axes are paral-

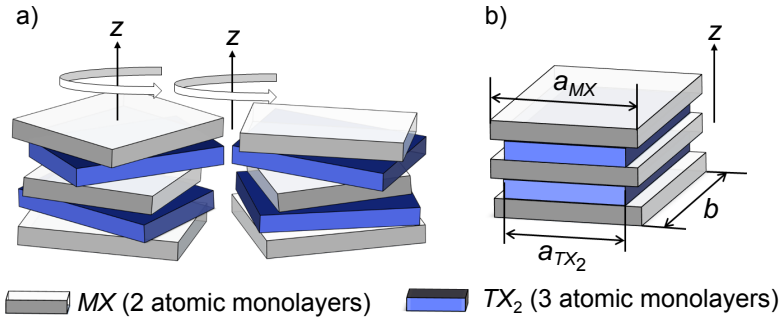

Figure 1.1: Schematic of the structure of a) ferecrystals and b) conventional misfit layer compounds [24].

lel to the stacking direction. Ferecrystals exhibit a turbostratic disorder between subsequent MX and TX_2 layers along the stacking direction and between grains within the layer plane, as depicted in Fig. 1.1a [16, 17, 22–24, 30, 31]. Despite the turbostratic disorder between adjacent grains within the layer plane, continuous layers of composition TX_2 and MX are usually maintained across the grain boundaries throughout the ferecrystal sample. Due to the turbostratic disorder the name 'ferecrystals', from the latin word '*fere*' meaning 'almost', has been introduced for these compounds. The origin of the chemical stability of the ferecrystals, the mechanisms of a possible charge transfer and the charge-distribution in the ferecrystals are not fully understood yet [16]. It has been shown that different stacking sequences can be used to systematically change their electrical properties [16–23, 31–33]. One of the most intriguing questions regarding the ferecrystals is, whether their properties can be related to those of the single-layer 2D TMDCs [1, 2, 8, 15]. Several key points for answering this question using the ferecrystals $[(PbSe)_{1+\delta}]_1[NbSe_2]_n$ and $[(SnSe)_{1+\delta}]_m[NbSe_2]_1$ will be described in the following.

A first open question is whether the atomic structures of the TX_2 and MX layers in the ferecrystals are similar to those in the binary compounds. It has been shown that the crystal lattice of SnSe in ferecrystals containing $MoSe_2$- and VSe_2 changes from (quasi-)tetragonal to the orthorhombic lattice of bulk SnSe at room temperature, when increasing the thickness of the SnSe layers [19, 25, 34]. Furthermore, defects in the local structure, such as stacking defects and grain boundaries, can have a high impact on the electrical properties of a material and are difficult to detect by X-ray diffraction methods due to the turbostratically disordered, nanocrystalline microstructure of the ferecrystals. It is therefore advantageous to use transmission electron microscopy (TEM) to investigate their local structure.

Secondly, the influence of a structural peculiarity of the ferecrystals, namely

their turbostratic disorder, on the electrical transport properties is still unknown. In order to investigate the effects of the turbostratic disorder on the electrical properties, the electrical properties of the ferecrystals can be compared to those of compounds with similar layer stacking sequences of TX_2 and MX, but which do not show turbostratic disorder. Such compounds are the so called misfit layer compounds (MLCs), which have been known for several decades [35–41]. Misfit layer compounds are described by the same chemical formula as ferecrystals but do not show turbostratic disorder and are typically grown as single crystalline platelets [35–41]. In contrast to ferecrystals, MLCs can only be synthesized with layer stacking sequences where $m \leq 3$ and $n \leq 3$ [16, 18–21, 35–38]. The electrical properties of single-crystalline MLCs $[(PbSe)_{1+\delta}]_1[NbSe_2]_n$ have been investigated thoroughly [39–43] and they can therefore serve as single-crystalline analogues for ferecrystals to study the influence of turbostratic disorder. Turbostratic disorder can result in new properties. For example, indications for a CDW transition have been found in electrical resistivity and Hall coefficient in ferecrystals containing VSe_2 layers. A similar effect has not been reported for MLCs [19, 25, 35]. A CDW is a periodic modulation of the conduction electron density and is a phenomenon observed in low-dimensional solids [1, 12, 44–49]. The origin of CDWs and their effects on structural and electrical properties are still not fully understood and are an active area of research [1, 12, 15, 44, 48, 50, 51]. It has been suggested that lattice distortions to achieve lattice matching along one direction in MLCs leads to the suppression of a CDW in MLCs [19, 36]. A CDW transition in single- and few-layer $NbSe_2$ has been reported by Xi *et al.* [1].

Furthermore, it would be interesting to know how and to which extend the MX layers in the ferecrystals change the electrical properties in comparison to isolated TX_2. Bulk single crystalline $NbSe_2$ is a well-investigated metal-like TMDC with interesting properties such as a CDW state below a temperature of $T_{\mathrm{CDW}} \approx 34\,\mathrm{K}$ [1, 12, 44, 50–57] and superconductivity below $T_{\mathrm{c}} \approx 7\,\mathrm{K}$ [58–63]. There are several reports on electrical properties of isolated $NbSe_2$ mono- or few-layers [1, 2, 8–10]. $NbSe_2$ monolayers (consisting of three atomic monolayers: X-T-X) were found to be semimetallic [8, 15] in contrast to metal-like bulk compounds. The $[(PbSe)_{1+\delta}]_m[NbSe_2]_n$ and $[(SnSe)_{1+\delta}]_m[NbSe_2]_n$ ferecrystals contain n monolayers of $NbSe_2$, which are separated by m atomic bilayers of a semiconductor. One open question is, whether these ferecrystals show indications for a CDW transition, similar to those observed for $[(SnSe)_{1+x}]_m[VSe_2]_n$ ferecrystals [19, 25, 64].

Using the compounds PbSe and SnSe in the ferecrystals in this study allows for the comparison of the effects of a narrow-gap semiconductor, PbSe ($E_g \approx 0.28\,\mathrm{eV}$ [65, 66]), in contrast to SnSe, a semiconductor with a wider band gap ($E_g \approx 0.9\,\mathrm{eV}$ [67–69]). For the compound $[(PbSe)_{1.14}]_1[NbSe_2]_1$ a density functional theory calculation has suggested a charge transfer from the PbSe to the $NbSe_2$ layers and that the valence band edge of the PbSe layers is shifted to energies above the

Fermi level in the ferecrystals [23]. Experimental band structures of ferecrystals and a quantitative influence of the *MX* layers on the low-temperature electrical transport properties have not been reported before.

In this study, the influence of the *MX* layers on the transport properties of the ferecrystals is investigated by analyzing the resistivity, carrier density and mobility with respect to single-band and two-band models and by comparing their values and their temperature dependencies to those of bulk and few-layer $NbSe_2$.

One of the most interesting questions related to the ferecrystals is whether they show 2D superconductivity, similar as reported for isolated $NbSe_2$ bilayers [2]. Superconductivity for ferecrystals containing only 1, 2 or 3 $NbSe_2$ layers (or layers of other superconducting materials) in the repeat unit has not been reported before. Bulk $NbSe_2$ is a well-investigated superconductor [58–63, 70] and there are several reports on superconductivity in single-, bi- and few-layer $NbSe_2$ [1, 2, 9, 10]. An open question is whether the ferecrystals containing single or few layers of $NbSe_2$ show similar transition temperatures T_c and similar trends in T_c with increasing $NbSe_2$ thickness as reported for single- or few-layer $NbSe_2$ and MLCs. Furthermore, the effect of turbostratic disorder on the superconducting properties of the ferecrystals has also been unknown so far. The ferecrystal system $[(PbSe)_{1+\delta}]_1[NbSe_2]_n$ allows to study the effect of turbostratic disorder, because superconducting transition temperatures have been reported for the analogous $[(PbSe)_{1+\delta}]_1[NbSe_2]_n$ MLCs [39–43]. The in-plane polycrystalline microstructure of the ferecrystals is not expected to influence T_c as it does not influence T_c of bulk $NbSe_2$ substantially [71, 72].

Finally, it is not clear whether the individual $NbSe_2$ layers in the ferecrystals would act as independent superconducting $NbSe_2$ layers or whether they are coupled across the SnSe layers. The turbostratic disorder in the ferecrystals results in an incoherent atomic structure perpendicular to the layers, which could result in a small cross-plane Ginzburg-Landau coherence length. A cross-plane coherence length smaller than the distance between superconducting layers is a signature of 2D superconductivity [73–75]. 2D superconductivity has, for example, been reported for $NbSe_2$ bilayers [2], LaSe-based misfit layer compounds [74], Nb layers [76], layered Nb/Ge composites [77], $SrTiO_3$ heterostructures [73] and for Pb/Ge double bilayers [78]. The superconducting properties of single $NbSe_2$ layers separated by a semiconductor of systematically varying thickness have not been reported so far. In this study, a possible 2D superconductivity is investigated for the $[(SnSe)_{1+\delta}]_m[NbSe_2]_1$ system by measuring the temperature dependent critical magnetic fields and by determining the cross-plane Ginzburg-Landau coherence lengths. Due to their layered structure and their versatility in material combinations and stacking sequences, ferecrystals might serve as model systems for layered superconductors, such as high-T_c superconductors.

2 Structural and electrical properties of ferecrystals

2.1 The atomic structure of ferecrystals and misfit layer compounds

Ferecrystals and conventional misfit layer compounds (MLCs) consist of m atomic bilayers of a monochalcogenide MX (M: metal, X: S, Se) stacked alternately with n monolayers of a transition metal dichalcogenide TX_2 (T: transition metal). The expression 'TX_2 monolayer' denotes a unit consisting of three atomic monolayers, i. e. X-T-X, as indicated in Fig. 2.2. The general formula for both, ferecrystals and MLCs, is $[(MX)_{1+\delta}]_m[TX_2]_n$, where M can be a divalent or trivalent metal (Sn, Pb, Sb, Bi, or a rare earth), T is a transition metal (Nb, V, Ta, Ti, Cr) and X = Se, Te or S. The crystal structures of MX and TX_2 are non-commensurate, with a misfit between the two subsystems MX and TX_2 in the ferecrystals. The volume ratio between MX and TX_2 units in a fixed volume is given by the misfit parameter $1 + \delta = 2V_{TX_2}/V_{MX}$, where V_{TX_2} and V_{MX} are the volumes of the unit cells of TX_2 and MX, respectively [36]. Misfit layer compounds have been known for several decades, occur in nature and are well-investigated [36, 38], whereas ferecrystals are newer compounds, the synthesis of which has been developed by David C. Johnson and co-workers [16, 17, 26, 27]. In the following, differences between the synthesis process and structural properties of ferecrystals and MLCs will be described.

Synthesis process: Ferecrystals are synthesized using the so-called modulated elemental reactants (MER) method [16–20, 24, 26, 27]. This method consists of physical vapor deposition (PVD) of a sequence of individual monoatomic layers and subsequent annealing of these precursors. During annealing a self-assembly of the deposited amorphous precursors takes place during which the layers become crystalline within the layer plane [16]. Using this method, the sequence of atomic layers can be controlled on the atomic scale [16, 18–20]. The resulting ferecrystals are turbostratically disordered, nanocrystalline thin films with a typical total thickness of 40 nm to 50 nm.

Misfit layer compounds can be grown as plate-like crystals with a thickness of several tens of micrometers using high-temperature vapor transport methods,

often using halogen as transport agent [36–43, 79]. Usually, powder mixtures of the elements or binary compounds are heated for several hours, ground to a powder and then heated again in sealed evacuated quartz ampules in a temperature gradient with temperatures of up to 700 °C - 1300 °C with the powder positioned in the hot end, for several days [36, 80].

Thermodynamic stability: Ferecrystals are kinetically trapped, thermodynamically metastable compounds [16–18], whereas misfit layer compounds are thermodynamically stable compounds [36, 38].

Stacking sequences: The synthesis process of the MLCs provides little control over the stacking sequence and it is usually limited to values $m \leq 2, n \leq 3$ [16, 36]. In contrast, for the ferecrystals the stacking sequence of MX bilayers and TX_2 monolayers in the repeat unit is freely tunable [16–20]. Ferecrystals with m up to 30 have been prepared so far [31, 34]. This offers a wide range of possibilities for compounds and structural isomers that can be synthesized for many material combinations. Using a repetitive layer stacking sequence is advantageous for monitoring the quality of the samples using X-ray diffraction, necessary for the calibration process for the synthesis.

Atomic structure: In this work $[(PbSe)_{1+\delta}]_1[NbSe_2]_n$ and $[(SnSe)_{1+\delta}]_m[NbSe_2]_1$ ferecrystals will be investigated. Therefore, the atomic structure of $NbSe_2$, PbSe, SnSe and structure data previously reported for typical MLCs and ferecrystals will be described in this section.

$NbSe_2$ is a typical TMDC with a layered structure consisting of single $NbSe_2$ monolayer sheets separated by van der Waals gaps (Fig. 2.1a). Each $NbSe_2$ monolayer is built up of one atomic monolayer of Nb atoms, which is sandwiched between two Se monolayers, i. e. the stacking sequence in a $NbSe_2$ monolayer is Se-Nb-Se. Several polytypes exist for $NbSe_2$, e. g. $2H$-, $3R$- and $4H$-$NbSe_2$, depending on the stacking order of the individual TMDC layers and on the coordination of the Nb atoms by the Se atoms [29, 81–83]. The most common polytype at room temperature (rt) is $2H$-$NbSe_2$ with a hexagonal lattice showing a trigonal prismatic coordination of Nb atoms by Se.

Binary lead selenide (PbSe) has a rock-salt structure (Fig. 2.1a). The crystal structure of tin selenide (SnSe) is layered consisting of stacked bilayers of SnSe [67, 84]. At rt SnSe exists in the orthorhombic α-SnSe phase and undergoes a displacive type of phase transition to the pseudo-tetragonal β-SnSe phase upon increasing the temperature above 807 K [67, 84].

In MLCs and ferecrystals $NbSe_2$ and PbSe (or SnSe) are stacked alternately with their c-axes parallel to the stacking direction. For a certain orientation relation between $NbSe_2$ and PbSe (or SnSe) with parallel c-axes, the in-plane lattice peri-

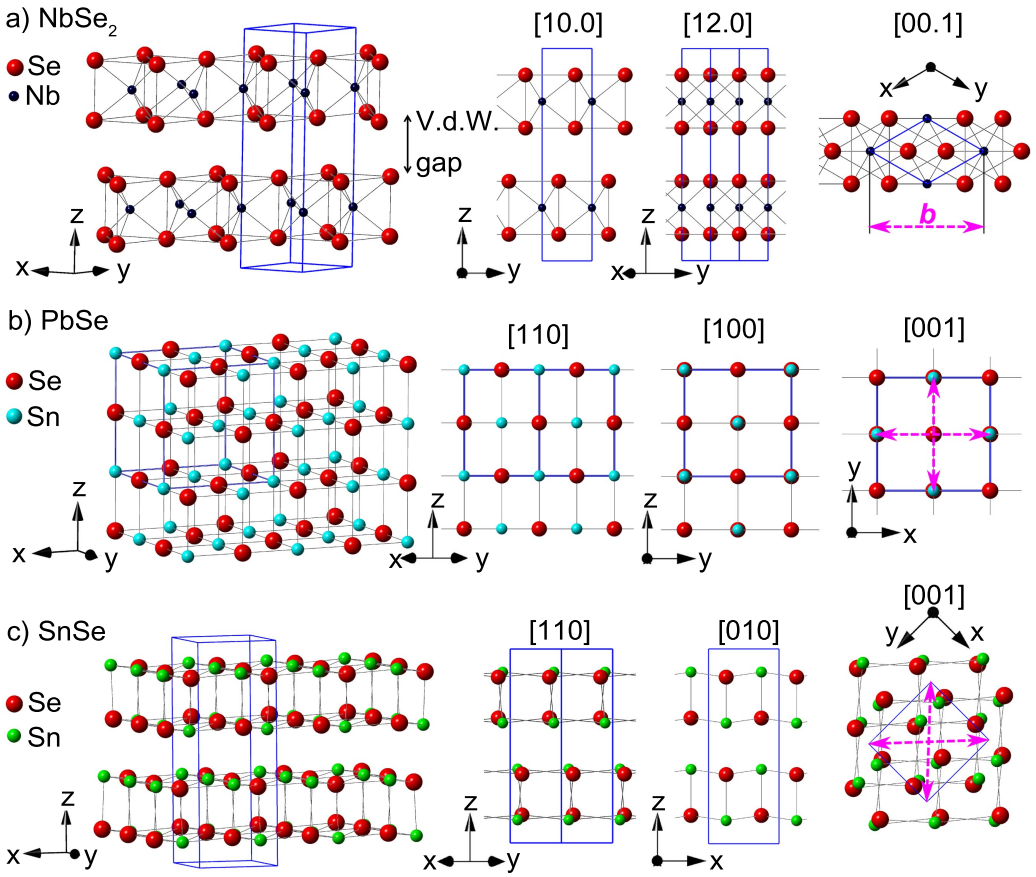

Figure 2.1: Schematic of the structure of a) $2H$-$NbSe_2$, space group $P6_3/mmc$ with projections along [1 0 . 0], [1 2 . 0] and [0 0 . 1] according to [82], b) PbSe, space group $Fm\bar{3}m$ [85] c) α-SnSe, space group $Pmcn$ [84]. Unit cells are indicated by blue solid lines. The dashed arrows in the [001] projections indicate possible commensurate orientations with respect to the parameter b marked in the $NbSe_2$ unit cell in a) relatively to the PbSe and SnSe unit cells.

odicities of $NbSe_2$ and PbSe (or SnSe) are nearly commensurate along one in-plane direction. They are incommensurate along all other in-plane directions. In Fig. 2.1 the possible commensurate directions of $NbSe_2$ and PbSe (or SnSe) are indicated by dashed arrows in the [0 0 1] projections of PbSe and SnSe. The length of the dashed arrow indicates the length of the longer diagonal of the rhombus-shaped in-plane unit cell of $NbSe_2$ with $b = \sqrt{3} \cdot a_{NbSe_2}$, where a_{NbSe_2} is the in-plane lattice parameter of $2H$-$NbSe_2$. In MLCs the layers are stacked in such a way that $NbSe_2$ and PbSe (or SnSe) are aligned along the commensurate direction. The atomic structure of a typical MLC, $[(SnSe)_{1+\delta}]_1[NbSe_2]_1$ [35] is shown in Fig. 2.2. Sim-

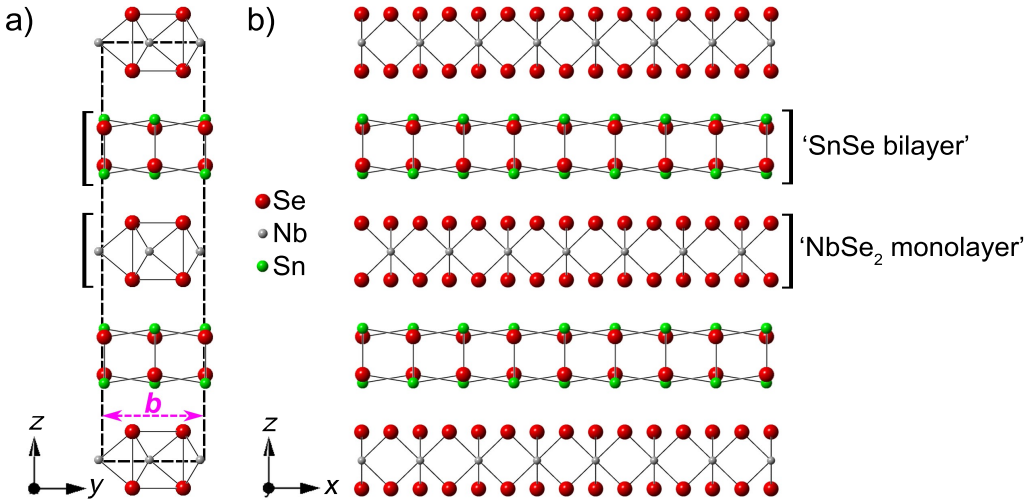

Figure 2.2: Crystal structure of the MLC $[(SnSe)_{1.16}]_1[NbSe_2]_1$ [30, 35]: a) projection of the crystal structure along the x-direction. The unit cell is indicated by a black dashed line, the lattice parameter b is indicated by a dashed arrow. b) Projection along the y-direction.

ilar to the ferecrystals, the c-axes of $NbSe_2$ and SnSe in the MLCs are oriented parallel to the stacking direction. The structure of this MLC is representative for many other MLCs, such as $[(PbSe)_{1+\alpha}]_1[NbSe_2]_1$ [36, 38, 40]. In the MLC $[(SnSe)_{1+\delta}]_1[NbSe_2]_1$ the atomic structure of SnSe is slightly distorted compared to the bulk structure in order to achieve lattice matching along the commensurate direction, i. e. along the y direction in Fig. 2.2. In the projection of the structure along x a unit cell with lattice parameters b and c can therefore be found and is indicated by black dashed lines in Fig. 2.2a. Along all other in-plane directions the two crystal structures are incommensurate.

In contrast to MLCs, ferecrystals possess a turbostratically disordered, nanocrystalline structure, as shown schematically in Fig. 1.1a. Turbostratic disorder means that the MX and TX_2 layers are rotated (apparently randomly) around the crystallographic c-axes, with the c-axes oriented parallel to the stacking direction [17, 19, 22, 23, 25, 30, 31]. This turbostratic disorder is present between successive layers along the stacking direction and between adjacent grains within the layer plane. Despite the nanocrystalline microstructure, the MX and TX_2 layers in the ferecrystals form mostly continuous layers throughout the sample [16, 17, 19, 22, 23, 25, 30, 31].

For ferecrystals trigonal prismatic and octahedral coordination of Nb atoms by Se atoms has been observed [29], whereas in MLCs containing $NbSe_2$ the coordination is reported to be trigonal prismatic [35, 41, 43, 43].

The origins of the stability of MLCs and ferecrystals and the mechanisms of the interlayer bonding are not fully understood yet [16, 86–89]. Two possible bonding mechanisms have been suggested for MLCs [86]: (1) non-stoichiometric composition, where either δ differs from the value resulting from the unit cell volumes, or extra T atoms are introduced between two TX_2 layers, or a substitution of M atoms by T atoms takes place, and (2) metal cross-substitution, where T atoms replace M in the MX layers and the same amount of M atoms replace T in the TX_2 layers. The influence of the turbostratic disorder on the bonding mechanisms and electrical properties of the ferecrystals in comparison to MLCs is unknown [16].

2.2 Electrical properties of ferecrystals and misfit layer compounds

2.2.1 Electrical properties of transition metal dichalcogenides

Transition metal dichalcogenides (TMDCs) possess a large variety of electrical properties, ranging from insulating, semiconducting, semimetallic, metallic to superconducting [3–5]. In addition, they show low-temperature phenomena, such as superconductivity and charge density waves (CDWs) [1, 3–5, 11, 83, 90, 91]. Transition metal dichalcogenides with a transition metal from the same periodic table group number show similarities in their electrical properties [4, 5, 92]. In addition, the electrical properties depend on the coordination of the transition metal atoms by the chalcogenide atoms, which can be either trigonal prismatic or octahedral [4, 29, 82, 83].

Group V TMDCs, especially $NbSe_2$, will be described in the following, because they will be relevant for this work. The compounds $NbSe_2$, $TaSe_2$ and VSe_2 are narrow band metals or semimetals [4, 52, 60, 92–95] and are reported to form charge density waves (CDWs) [4, 44, 50–57, 91, 94–96]. Bulk $NbSe_2$ has a complex band structure with several bands crossing the Fermi level [12, 15, 89, 97, 98]. The metallic character of bulk $NbSe_2$ is mainly attributed to a half-filled Nb-$4d_{z^2}$-band [15, 23, 52, 89, 97–102]. Room temperature (rt) *ab*-plane resistivity values for bulk $NbSe_2$ single crystals have been reported as $(0.7 - 1.6)\,\mu\Omega m$ [60, 63, 71, 83]. Polycrystalline $NbSe_2$ is reported to show a rt resistivity of $(1.96)\,\mu\Omega m$ [71]. For bulk $NbSe_2$ single-crystals a rt carrier density of about $1.3 \times 10^{22}\,cm^{-3}$ can be obtained using a single-band model from the in-plane Hall coefficients reported in [60] and [52]. The in-plane Hall mobility for bulk $NbSe_2$ single crystals calculated from reported Hall coefficients and resistivity values is $\mu \approx 3\,cm^2/Vs$ at rt [60] and $\mu \approx (48 - 100)\,cm^2/Vs$ at $T = 10\,K$ [52, 60]. The Seebeck coefficient of bulk $NbSe_2$ at rt has been reported as *n*-type and changes the sign below a temperature of about 50 K [83, 103]. Bulk $2H$-$NbSe_2$ single crystals with a high residual resistance

ratio RRR ($RRR > 27$) have shown a positive Hall coefficient for temperatures down to about (30-60)K and a negative Hall coefficient for lower temperatures [52, 54, 60]. This change in the sign of the Hall coefficient has been proposed to be related to a charge density wave (CDW) transition at this temperature [1, 54–57, 104]. A CDW is a periodic modulation of the conduction electron density and is a phenomenon restricted to low-dimensional solids [1, 44–49, 104], (Sect. 2.4.3). Their origin and effects on structural and electrical properties are still not fully understood yet and an active area of research [1, 15, 44, 48, 50, 51]. For $NbSe_2$ single crystals with a residual resistance ratio of $RRR > 27$ an anomaly in the slope of the resistance is also observed at the CDW transition temperature [1, 10, 50, 52, 53, 105]. For lower RRR the anomaly in resistivity and the change in the sign of the Hall coefficient are not observed, the samples remain p-type [1, 10, 52, 54]. However, although no signs in the resistivity and Hall coefficients are observed, a CDW can still be present: in isolated mono-, bi- and trilayers of $NbSe_2$ CDW transitions were detected by Raman spectroscopy although no indications for a CDW in the resistivity or Hall coefficients have been observed [1]. An isolated single crystalline $NbSe_2$ monolayer at rt has been reported to be semimetallic, to show n-type conductivity, a carrier density two orders of magnitude lower than the bulk carrier density and a similar carrier mobility as for bulk $NbSe_2$ single crystals [8, 15]. At $T_c = 7\,K$ bulk $2H$-$NbSe_2$ shows a normal to superconducting transition [58–63, 83, 105]). The polytype $4H$-$NbSe_2$ shows a transition temperature of (6.3-6.5) K [83, 106] and a higher CDW transition temperature. Isolated single crystalline mono-, bi- tri and few-layers of $NbSe_2$ have been reported to become superconducting below 7 K with the transition temperature systematically decreasing with decreasing layer thickness [1, 9, 10, 63]. Other polytypes of $NbSe_2$ and non-stoichiometric bulk $NbSe_2$ have shown different superconducting transition temperatures [61, 83], but the most common polytype of $NbSe_2$ at room temperature is $2H$-$NbSe_2$. $NbSe_2$ is a type II s-wave superconductor [13].

Bulk $2H$-$TaSe_2$ becomes superconducting at $T_c \approx 100\,mK - 200\,mK$ [107], whereas bulk VSe_2 does not become superconducting down to 12 mK [108]. However, the CDW transition temperatures of $2H$-$TaSe_2$ and VSe_2 single crystals are higher than for $NbSe_2$: for $2H$-$TaSe_2$ single crystals the CDW transition temperature is reported as $T_{CDW} \approx 85\,K - 110\,K$ [91, 109–111] and for VSe_2 single crystals it is $T_{CDW} \approx 100\,K - 140\,K$) [90, 95, 112, 113]. $NbSe_2$ is a prototype CDW material [12, 13, 114] and TMDC superconductor with one of the highest superconducting transition temperatures T_c among the TMDCs.

2.2.2 Electrical properties of PbSe and SnSe

PbSe is a narrow direct band gap semiconductor with an energy gap of 0.27 eV-0.29 eV [65, 66]. Band structure calculations and measurements of the density of

state are reported in [115–117]. For PbSe n-type and p-type Hall coefficients have been reported [65, 66]. Room temperature resistivity values of 19 µΩm - 200 µΩm have been reported for PbSe single crystal films and bulk single crystals [65, 66]. For polycrystalline PbSe films of thickness $(12 - 960)$ nm rt resistivity values of $(30 - 1000)$ µΩm have been reported [118, 119]. The resistivity of polycrystalline PbSe films is reported to increase with decreasing temperatures between $(110 - 400)$ K [118–120].

Room temperature hole density values of polycrystalline thin PbSe films of thickness $(100 - 550)$ nm have been reported as $(0.2 - 1) \times 10^{18}\,\mathrm{cm}^{-3}$ [119, 120]. The rt charge carrier density of single crystalline bulk and single crystalline thin film PbSe is reported as approximately $(0.4 - 3) \times 10^{18}\,\mathrm{cm}^{-3}$ [65, 66]. For bulk PbSe single crystals, carrier densities at $T = 4.2\,\mathrm{K}$ of $(2.4 - 4.3) \times 10^{18}\,\mathrm{cm}^{-3}$ have been reported [65] and for epitaxial PbSe thin films, carrier densities of $(0.4 - 2.0) \times 10^{18}\,\mathrm{cm}^{-3}$ at $T = 77\,\mathrm{K}$ have been reported [66].

For bulk PbSe single crystals Hall mobility values of $(4 - 14) \times 10^4\,\mathrm{cm}^2/\mathrm{Vs}$ at $T = 4.2\,\mathrm{K}$ and of approximately $1000\,\mathrm{cm}^2/\mathrm{Vs}$ at rt have been reported [65]. For PbSe single crystal thin films, mobility values of $(0.2 - 1) \times 10^4\ \mathrm{cm}^2/\mathrm{Vs}$ at $T = 77\,\mathrm{K}$ and $(0.3 - 1) \times 10^3\,\mathrm{cm}^2/\mathrm{Vs}$ at rt have been reported [66]. PbSe is reported to become superconducting only under high pressure of about 300 kbar [121].

SnSe is a semiconductor with an indirect band gap of 0.61 eV to 0.90 eV and a direct gap of 1.3 eV [67–69]. Band structure calculations for SnSe are shown in [67, 122]. For bulk SnSe single crystals rt resistivity values of $3 \times 10^{-4}\,\Omega\,\mathrm{m}$ to $4 \times 10^{-2}\,\Omega\,\mathrm{m}$ have been reported [67, 123, 124] and for polycrystalline thin films of thickness 80 nm to 410 nm rt resistivity values of $0.05\,\Omega\,\mathrm{m}$ to $5\,\Omega\,\mathrm{m}$ have been reported [125–127]. Polycrystalline SnSe films with a preferential orientation of the c-axis of SnSe normal to the resistivity measurement direction and with a thickness 250 nm showed a rt resistivity of $0.05\,\Omega\mathrm{m}$ [125]. In the ferecrystals the c-axis of SnSe is also normal to the measurement direction.

SnSe is reported to show p-type conductivity [124–126, 128, 129] for $T = 77\,\mathrm{K}$ to 300 K with a rt carrier density of $p = 0.3 \times 10^{16}\,\mathrm{cm}^{-3}$ to $2 \times 10^{18}\,\mathrm{cm}^{-3}$ [67, 124–126]. The measurements reported in [124] were carried out within the ab-plane as for SnSe in the ferecrystals and showed $p = 2 \times 10^{17}\,\mathrm{cm}^{-3}$ to $2 \times 10^{18}\,\mathrm{cm}^{-3}$ at rt. Polycrystalline SnSe films of thickness 250 nm with a preferential orientation of the c-axis of SnSe normal to the measurement direction showed a rt carrier density of $p = 10^{16}\,\mathrm{cm}^{-3}$ and a charge carrier mobility of about $50\,\mathrm{cm}^2/\mathrm{Vs}$ at rt [125].

For SnSe single crystals rt in-plane carrier mobility values of about $80\,\mathrm{cm}^2/\mathrm{Vs}$-$200\,\mathrm{cm}^2/\mathrm{Vs}$ averaged over both in-plane directions have been reported [67, 124]. At $T = 77\,\mathrm{K}$ in-plane carrier mobilities of $600\,\mathrm{cm}^2/\mathrm{Vs}$-$7000\,\mathrm{cm}^2/\mathrm{Vs}$ have been reported for bulk single crystals [124]. The carrier mobility of $7000\,\mathrm{cm}^2/\mathrm{Vs}$ at $T = 77\,\mathrm{K}$ is reported for bulk single crystals with carrier densities of only $3 \times 10^{16}\,\mathrm{cm}^{-3}$ at $T = 77\,\mathrm{K}$ [124]. The mobility in bulk SnSe single crystals is reported to de-

crease continuously with increasing carrier density, and mobility values of only $\mu \approx 500\,\mathrm{cm}^2/(\mathrm{Vs})$ have been reported for samples with $p = 2 \times 10^{18}\,\mathrm{cm}^{-3}$ at $T = 77\,\mathrm{K}$ [124]. Reports on the measurement of carrier density and mobility of SnSe for $T \leq 77\,\mathrm{K}$ have not been found. SnSe is reported to become superconducting only above a pressure of 600 kbar [130].

Recently, *ab-initio* calculations for SnSe with a rocksalt structure and measurements on expitaxially grown SnSe have shown that rocksalt SnSe is a topological crystalline insulator (TCI) [131, 132]. However, usually, bulk SnSe shows an orthorhombic unit cell at rt. In the MLCs, SnSe shows a square in-plane unit cell [35] (Fig. 2.2), which is more similar to the rocksalt structure.

2.2.3 Electrical properties of $NbSe_2$-, PbSe- and SnSe-based misfit-layer compounds

Band structure and electrical properties

The MLCs containing NbX_2 and TaX_2 show resistivity values of a few µΩm, similar as the host compounds NbX_2 and TaX_2 [38]. These MLCs show a metallic temperature dependence of the resistivity and a Debye temperature of approximately 200 K [38]. The anisotropy between the cross-plane resistivity ρ_c measured along the stacking direction and the in-plane resistivity ρ_{ab} of $[(SnS)_{1.17}][NbS_2]$ is reported as $\rho_c/\rho_{ab} = 200$ at rt [38]. For MLCs with M = Sn, Pb or Bi, positive Hall coefficients and negative Seebeck coefficients have been reported [38].

The misfit layer compounds are often considered as intercalates of the TMDCs, the intercalated material being the MX double layers. TMDCs intercalated with alkali metals have been thoroughly investigated and a rigid-band model has been successfully applied to explain their bonding mechanism and electrical properties [38, 133]. In this model it is assumed that the only change in the electronic structure of the host material TX_2 is a change in the band filling due to electron donation from the intercalated material. To explain the electrical properties of MLCs, the rigid band model has also been used as a first approximation. X-ray photoelectron spectroscopy (XPS) of the MLCs $[(SnS)_{1.20}][TS_2]$ with T = Nb, Ti and Ta, have shown that the band structure is approximately a superposition of those of the respective TX_2 and MX compounds [134–138]. Accurate band structure calculations of the MLCs or ferecrystals are difficult due to the incommensurability between the two layer types in the MLCs. The structure has to be approximated by a commensurate structure with a large unit cell and this might lead to deviations from the actual band structure. Band structure calculations of $[(SnSe)_{1+\delta}]_m[NbSe_2]_n$ or $[(PbSe)_{1+\alpha}]_m[NbSe_2]_n$ have not been reported so far.

As a well-known example of a band structure model for MLCs is $[(SnS)_{1.20}][NbS_2]$ will be explained in the following. Band structure calculations suggest that the electronic structure of this compound can be approximated by a superposition of

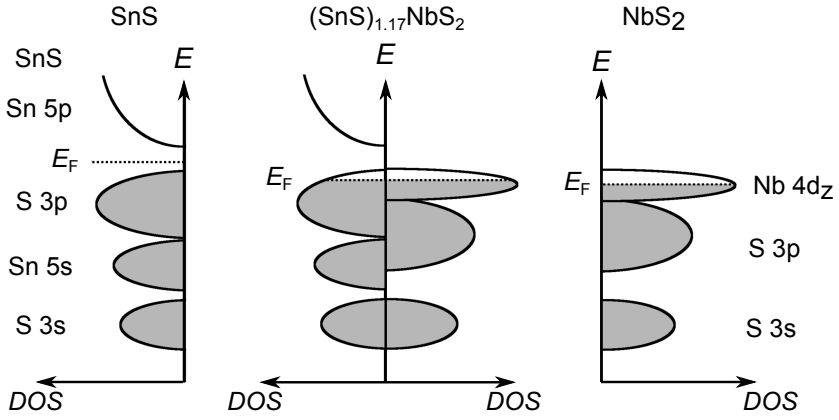

Figure 2.3: Schematic band alignment of SnS and NbS in $[(SnS)_{1.20}][NbS_2]$ from [38, 42, 135] (*DOS*: density of electronic states, E: electron energy). The states are occupied up to the Fermi level E_F, indicated by a dashed line.

the electronic structures of SnS and NbS_2 with a charge transfer of a bout $0.4e$ per Nb atom from SnS to NbS_2 [139]. A schematic diagram showing the density of states for SnS and NbS_2 as deduced from [139] and as shown in [16, 38] is given in Fig. 2.3. According to the band structure calculations for $[(SnS)_{1.20}][NbS_2]$, due to the charge transfer from SnS to NbS there are unoccupied holes in the valence band of SnS (as shown schematically in Fig. 2.3). The holes in the SnS layer contribute to the electrical transport in the MLC in addition to the holes in the Nb-d_z bands and have to be considered when calculating the carrier density or mobility from the Hall coefficients. A similar result is obtained for the density of states calculated for $[(PbSe)_{1.13}][NbSe_2]$ in [23]. However, a final conclusion on the band structure of this MLC has not been given yet. Effects of the incommensurability are neglected in this calculation. Some reports confirm a charge transfer from SnS to NbS, deduced from XPS spectra [138], whereas other reports of XPS measurements of this compound conclude little or no charge transfer [136]. From the band structure calculations for $[(SnS)_{1.20}][NbS_2]$ in [139] it is concluded that there is a covalent interlayer interaction between Sn 5s and S(NbS2) 3p bands[139] and that there is no simple relation between the Fermi surfaces of $[(SnS)_{1.20}][NbS_2]$, SnS and NbS_2 [139], showing that also at the Fermi surface there is considerable covalent mixing of the wave functions of the two systems [139]. This is similar to a report on $(PbS)_{1.14}(NbS_2)$ in [89], where angle resolved photoemission spectroscopy and band structure calculations suggest that the electronic dispersion of the MLC is drastically changed in comparison to NbS_2. There are no reports on the band structure of $[(SnSe)_{1+\delta}]_m[NbSe_2]_n$ MLCs.

Properties of the MLCs $[(PbSe)_{1+\delta}]_m[NbSe_2]_n$

In-plane electrical properties for $[(PbSe)_{1+\alpha}]_1[NbSe_2]_n$ MLCs have been reported by [39–43, 140]. The rt resistivity is reported to be 1 µΩ to 6 µΩm [40–43]. Hall measurements have only been been reported for a powder compact of $n = 1$, which showed a positive Hall coefficient with a carrier density of about $p = 6 \times 10^{21}\,\mathrm{cm}^{-3}$ obtained using a single-band model from the Hall coefficient [42]. The transition temperatures to superconductivity for MLC single crystals with $n = 1$ and $n = 2$ obtained by in-plane resistance measurements are between 3 and 5 K [40–43, 140]. MLC single crystals with $n = 1$ and $n = 2$ have been reported to show an increase in T_c with increasing n [39–43, 140]. Critical magnetic field measurements for $n = 2$ reported by Nader *et al.* [41] indicated in-plane and cross-plane Ginzburg-Landau coherence lengths of 16.8 nm and 3.4 nm, respectively.

Properties of the MLCs $[(SnSe)_{1+\delta}]_m[NbSe_2]_n$

In-plane electrical properties for MLCs of the type $[(SnSe)_{1+\delta}]_m[NbSe_2]_n$ have not been reported yet. However, there is a report on a $[(SnSe)_{1.16}][NbSe_2]$ powder compact [35], which shows a metal-like temperature dependence of the resistivity, a rt resistivity of about 6 µΩm and a hole density obtained by a single-band model from the Hall coefficient of about $p = 3 \times 10^{21}\,\mathrm{cm}^{-3}$.

Reviews of the structural and electrical properties of many other MLCs are given in [36, 38].

2.2.4 Electrical properties of ferecrystals

Electrical properties of several types of ferecrystals have been reported [16–19, 21–24, 31–33]. Most of these measurements have been performed above temperatures of $T = 20$ K. Depending on the composition of the constituent layers, semiconducting to metallic properties are observed, similar as for MLCs. Transport properties at lower temperature, especially superconducting properties of most ferecrystals, e.g. $[(PbSe)_{1+\delta}]_1[NbSe_2]_n$ and $[(SnSe)_{1+\delta}]_m[NbSe_2]_1$, are still unknown. The influence of the turbostratic disorder and polycrystallinity on the electrical properties is still an open question. Therefore, in this work the ferecrystals $[(PbSe)_{1+\delta}]_1[NbSe_2]_n$ are investigated with the goal to compare their structural and electrical properties to those of the analogous MLCs, for which data on structural and electrical properties (temperature-dependent resistivity, superconductivity) have been reported [39–43]. Furthermore, the ferecrystals $[(SnSe)_{1+\delta}]_m[NbSe_2]_1$ are investigated in this work in order to study the effects of increasing the distance between $NbSe_2$ layers by introducing a certain number m of SnSe bilayers between them. In contrast to MLCs, for ferecrystals it is possible to increase m and n to values larger than 3. In addition, the turbostratic disorder might lead to a decoupling of the transport in the individual

layers in the ferecrystals and to an increased two-dimensional behavior. This might lead to an enhancement of low-dimensional effects, such as charge density waves, which occur, e.g., in $NbSe_2$ [44, 51–55] or of 2D superconductivity. Therefore, the structural and electrical properties of the ferecrystals $[(SnSe)_{1+\delta}]_m[NbSe_2]_1$ were investigated in this work. The effect of an increasing separation between single atomic layers of $NbSe_2$ by introducing a semiconductor between the layers on the superconductivity has not been reported until this work. Furthermore, a comparison of the electrical properties to those of $[(PbSe)_{1+\alpha}]_m[NbSe_2]_1$ ferecrystals, also to those with $m = 1-6$ reported in [23], allows to observe the effect of exchanging the narrow-band-gap semiconductor (PbSe) with a larger band gap semiconductor (SnSe) in the ferecrystals.

2.3 Single- and two-layer models for electrical transport

2.3.1 Drude-Sommerfeld model

The Drude-Sommerfeld model of quasi-free charge carriers described below is a model for electrical transport in metals with a single parabolic band. It can be used to describe the influence of material parameters such as carrier density and mobility on the electrical resistivity, Hall coefficient and magnetoresistance. The Drude-Sommerfeld model uses the following equation of motion for charge carriers with the effective mass m^*, the relaxation time τ, the drift velocity v_D and the charge q in a homogeneous, isotropic metal in an electric field $\vec{\mathcal{E}}$ and a magnetic field $\vec{B}$:

$$\frac{m^*\vec{v}_\mathrm{D}}{\tau} = q(\vec{\mathcal{E}} + \vec{v}_\mathrm{D} \times \vec{B}). \tag{2.1}$$

The charge q is negative for electrons ($q = -e$) and positive for holes ($q = e$), where $e = 1.602 \times 10^{-19}\,\mathrm{C}$ is the elementary charge. The effective mass and the relaxation time are assumed to be independent of the energy of the charge carriers in this model. For the evaluation of this equation a simple exemplary measurement setup suitable for the measurement of resistivity, Hall coefficient and magnetoresistance is shown schematically in Fig. 2.4. A current with density $\vec{J}$ is applied along the direction x of a bar-shaped sample. The components of the current along y and z are zero. The voltage V_x is measured parallel to the current. The Hall voltage V_H is measured along the direction y and for the magnetoresistance and Hall measurements a magnetic field $\vec{B} = (0, 0, B)$ is applied. Using Eq. (2.1) the relation between the electric field and the current density $\vec{J}$ is given by [141,

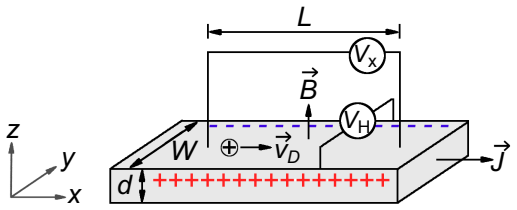

Figure 2.4: Schematic measurement setup for Hall and magnetoresistance measurements with a bar-shaped sample in a magnetic field $\vec{B}$ and with a current density $\vec{J}$.

Ch. 3.4], [142, Ch. 7.3]

$$\vec{J} = qn\vec{v}_{\mathrm{D}} = \frac{n\mu}{1+\mu^2B^2}\begin{pmatrix} |q| & q\mu B & 0 \\ -q\mu B & |q| & 0 \\ 0 & 0 & |q|(1+\mu^2B^2) \end{pmatrix}\vec{\mathcal{E}} = \bar{\bar{\sigma}}\vec{\mathcal{E}} = \bar{\bar{\rho}}^{-1}\vec{\mathcal{E}}, \quad (2.2)$$

where $\mu = |v_D|/|E| = |q|\tau/m^*$ is the charge carrier mobility [143, Ch. 8] [144, Ch. 9.5] and n is the charge carrier density. The tensor $\bar{\bar{\sigma}}$ is the conductivity tensor and the resistivity tensor $\bar{\bar{\rho}}$ is given by the inverse of $\bar{\bar{\sigma}}$. Using the resistivity tensor, equations for the resistivity and the Hall coefficient in terms of charge carrier density and mobility can be derived (Sects. 2.3.2 and 2.3.3).

The equations derived using the Drude-Sommerfeld model can also be derived using the linearized Boltzmann equation [143, 144]. In the Boltzmann equation the dependence of the scattering time τ on the energy E is considered, which can be important for semiconductors, where τ can vary strongly with E [141, 145]. In this case the interpretation of the Hall coefficient and magnetoresistance then requires the knowledge of the scattering time τ averaged over the energy (e. g. the Hall scattering factor for the Hall coefficient), which is often unknown. However, for simple metals and semimetals the variation of τ with E can be regarded as small and τ mainly depends on the Fermi Energy, $\tau \approx \tau(\mathrm{E_F})$ and the results derived with the Drude-Sommerfeld model agree with the results obtained from the Boltzmann equation for metals [145]. Furthermore, the derived equations only hold for sufficiently small fields E and B which do not change the carrier density. Otherwise, quantum effects in high magnetic fields and at low temperatures need to be considered.

2.3.2 Resistivity, Hall coefficient and magnetoresistance in a single-band model

In this section the Drude-Sommerfeld model will be applied to the measurement setup in Fig. 2.4 with the assumption of homogeneous, isotropic metals with a

single parabolic band. The resistivity ρ for ($B = 0$) is measured by applying a current I along x and measuring the voltage V_x

$$\rho = \frac{V_x \cdot W \cdot d}{I \cdot L} = \frac{|\vec{\mathcal{E}}|}{|\vec{J}|}, \tag{2.3}$$

where W is the width, d the thickness of the sample and L is the distance between the voltage contacts (Fig. 2.4). With $B = 0$ in Eq. (2.2),

$$\vec{J} = qn\vec{v}_{\mathrm{D}} = |q|n\mu\vec{\mathcal{E}} = \sigma\vec{\mathcal{E}} = \rho^{-1}\vec{\mathcal{E}}. \tag{2.4}$$

The directions of the current density and the electric field are parallel. The resistivity is given by

$$\rho = (|q|n\mu)^{-1}. \tag{2.5}$$

The temperature dependence of ρ of metals can be derived using Matthiessen's rule, which implies that the different scattering processes of the charge carriers in the material are independent. If only scattering at neutral-impurities and electron-phonon scattering are present, the resistivity is a sum of a temperature-independent term ρ_0, resulting from scattering at neutral impurities and a second, temperature-dependent term resulting from electron-phonon scattering. For simple metals the latter term is given by the Bloch-Grüneisen equation [146, 147].

$$\rho(T) = \rho_0 + \alpha \cdot \left(\frac{T}{\theta_{\mathrm{D}}}\right)^5 \int_0^{\Theta_D/T} \frac{x^5 dx}{(e^x - 1)(1 - e^{-x})}, \tag{2.6}$$

where θ_{D} is the Debye temperature and α is a constant which depends on material parameters, such as the Fermi energy, which are assumed to be temperature-independent. For $T \gtrsim \theta_{\mathrm{D}}$, $\rho \propto T$ and for $T << \theta_{\mathrm{D}}$, $\rho \propto T^5$. Hall measurements are performed by applying a magnetic field B along z, a current I along x and measuring the Hall voltage V_{H} along y (Fig. 2.4). The Hall voltage is given by

$$V_{\mathrm{H}} = \mathcal{E}_{\mathrm{y}} \cdot W = \rho_{\mathrm{yx}} \cdot J \cdot W = \rho_{\mathrm{yx}} \cdot I/d, \tag{2.7}$$

where $\mathcal{E}_{\mathrm{y}}$ is the y-component of the electric field and $J_y = J_z = 0$. Using Eq. (2.2) gives $\rho_{\mathrm{yx}} = B/(qn)$. The Hall coefficient R_{H} is defined as

$$R_{\mathrm{H}} \equiv \rho_{\mathrm{yx}}/B = \frac{d \cdot V_{\mathrm{H}}}{I \cdot B} = \frac{1}{qn}. \tag{2.8}$$

Therefore, in a single-band model, the carrier density n and the sign of the charge carriers (electrons or holes) can be directly obtained by measuring the Hall coef-

ficient. Using Eq. (2.5) the charge carrier mobility is

$$\mu = \frac{|R_{\mathrm{H}}|}{\rho}. \tag{2.9}$$

With the carrier density n and the mobility μ, the mean free path of the charge carriers can be calculated:

$$l = \tau \cdot v_F = \frac{\hbar\mu}{e}\left(3\pi^2 n\right)^{1/3}, \tag{2.10}$$

with $\tau = m^*\mu/e$ and the Fermi velocity $v_F = \hbar(3\pi^2 n)^{1/3}/m^*$.

Transversal magnetoresistance measurements are performed by applying a magnetic field B along z, a current I along x and measuring the voltage V_x (Fig. 2.4). The transversal magnetoresistance MR is given by

$$MR \equiv \frac{R(B) - R(B=0)}{R(B=0)} = 0, \tag{2.11}$$

where $R(B) = V_x(B)/I$ and $V_x = E_x \cdot L = \rho_{\mathrm{xx}} \cdot J \cdot L$. Since $\rho_{\mathrm{xx}} = 1/(|q|n\mu)$ (Eq. (2.2)), R is independent of B and the magnetoresistance is zero in the single band model.

2.3.3 Resistivity, Hall coefficient and magnetoresistance in a two-band model

Two-band model

In many semiconductors or semimetals two or more types of charge carriers contribute to the electrical transport, e. g. electrons and holes, light and heavy holes or s-and d-type electrons or different parallel layers with different carrier densities and mobilities. In this section the Drude-Sommerfeld model of quasi-free charge carriers will be applied again with the assumption of homogeneous, isotropic samples with parabolic bands. If charge carriers from several bands in the sample contribute to the electrical transport, their two current densities add up to the total current density $\vec{J} = \sum_{i=1}^{2} \bar{\bar{\sigma}}_i \vec{\mathcal{E}} = \bar{\bar{\rho}}^{-1}\vec{\mathcal{E}}$, with

$$\bar{\bar{\sigma}}_i = \frac{n_i\mu_i}{1+\mu_i^2 B^2}\begin{pmatrix} |q_i| & q_i\mu_i B & 0 \\ -q_i\mu_i B & |q_i| & 0 \\ 0 & 0 & |q_i|(1+\mu_i^2 B^2) \end{pmatrix}, \tag{2.12}$$

where q_i n_i and μ_i are the charge, density and mobility of the charge carriers from the ith band [141, Ch. 3.4], [142, Ch. 7.3]. The resistivity tensor is calculated from the inverse of the total conductivity tensor $\bar{\bar{\rho}} = (\bar{\bar{\sigma}}_1 + \bar{\bar{\sigma}}_2)^{-1}$. The resistivity for

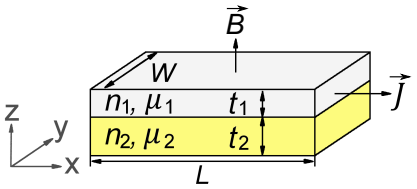

Figure 2.5: Schematic of the two-layer model for resistivity, Hall coefficient and magnetoresistance measurements with a bar-shaped sample in a magnetic field B along z and with a current density J along x.

$B = 0$ is then given by

$$\rho = (|q_1|n_1\mu_1 + |q_2|n_2\mu_2)^{-1}, \tag{2.13}$$

where $|q_1| = |q_2| = e$, the elementary charge. For $\vec{B} = (0, 0, B)$ the Hall coefficient is given by [141, Ch. 3.4] [142, Ch. 9.6]

$$R_{\mathrm{H}} = \rho_{\mathrm{yx}}/B = \frac{1}{|q_1|^2}\left(\frac{(q_1 n_1\mu_1^2 + q_2 n_2\mu_2^2) + B^2\mu_1^2\mu_2^2(q_1 n_1 + q_2 n_2)}{(n_1\mu_1 + n_2\mu_2)^2 + B^2\mu_1^2\mu_2^2(n_1 + n_2 q_1/q_2)^2}\right). \tag{2.14}$$

For $B \to 0$ and $B \to \infty$ the Hall coefficient is independent of B. The transversal magnetoresistance is given by [148], [142, Ch. 9.6], [149, Ch. 7.1.2]

$$MR = \frac{\rho_{\mathrm{xx}}(B) - \rho_{\mathrm{xx}}(0)}{\rho_{\mathrm{xx}}(0)} = \frac{B^2 n_1 n_2 \mu_1\mu_2(\mu_1 - \mu_2 q_1/q_2)^2}{(n_1\mu_1 + n_2\mu_2)^2 + B^2\mu_1^2\mu_2^2(n_1 + n_2 q_1/q_2)^2}. \tag{2.15}$$

The magnetoresistance is always positive in this model. For $B \to 0$, $MR \propto B^2$ and for $B \to \infty$, MR saturates.

Two-layer model

If the two types of charge carriers in the sample are located in two different independent parallel layers with thicknesses t_1 and t_2 as shown schematically in Fig. 2.5, the current density is given by

$$\vec{J} = \frac{t_1\bar{\bar{\sigma}}_1 + t_2\bar{\bar{\sigma}}_2}{(t_1 + t_2)}\vec{\mathcal{E}} = \bar{\bar{\rho}}^{-1}\vec{\mathcal{E}}. \tag{2.16}$$

with $\bar{\bar{\sigma}}_i$ defined as in Eq. (2.12). The resistivity for $B = 0$ is then given by

$$\rho = \frac{(t_1 + t_2)}{|q_1|n_1 t_1\mu_1 + |q_2|n_2 t_2\mu_2}. \tag{2.17}$$

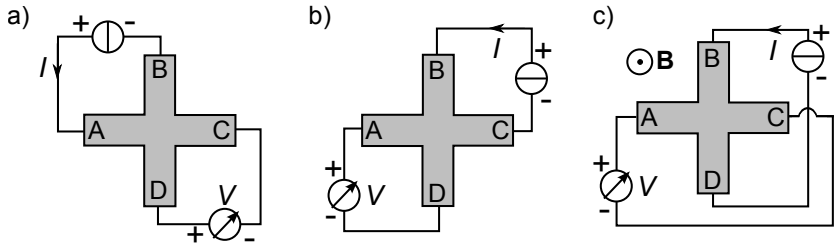

Figure 2.6: Schematic measurement setup for a) and b) van der Pauw resistivity measurements and c) Hall measurements.

The Hall coefficient is then given by [141, 142]

$$R_{\mathrm{H}} = \frac{(t_1+t_2)}{|q_1|^2}\left(\frac{(q_1 n_1 t_1 \mu_1^2 + q_2 n_2 t_2 \mu_2^2) + B^2\mu_1^2\mu_2^2(q_1 n_1 t_1 + q_2 n_2 t_2)}{(n_1 t_1 \mu_1 + n_2 t_2 \mu_2)^2 + B^2\mu_1^2\mu_2^2(n_1 t_1 + n_2 t_2 q_1/q_2)^2}\right). \tag{2.18}$$

The magnetoresistance is given by [142, 148]

$$MR = \frac{B^2 n_1 t_1 n_2 t_2 \mu_1 \mu_2 (\mu_1 - \mu_2 q_1/q_2)^2}{(n_1 t_1 \mu_1 + n_2 t_2 \mu_2)^2 + B^2\mu_1^2\mu_2^2(n_1 t_1 + n_2 t_2 q_1/q_2)^2}. \tag{2.19}$$

Equations 2.18 and 2.19 are similar as Eqs. 2.15 and 2.15, except the carrier densities n_i are replaced by the respective products $n_i t_i$. A program written to calculate the Hall coefficient and magnetoresistance in the two-layer model in this work is shown in Sect. B.18.

2.3.4 Van der Pauw method

The van der Pauw method is a special four-terminal sensing measurement technique useful for measuring the resistivity and Hall coefficients of thin films of arbitrary shape. Four contacts have to be applied to the sample, as shown schematically in Fig. 2.6. Four conditions which have to be fulfilled:

1. The contacts are at the circumference of the sample.
2. The contacts are sufficiently small.
3. The sample is homogeneous in thickness.
4. The surface of the sample is singly connected, i. e. the sample does not have isolated holes.

Van der Pauw resistivity measurement

Under the above conditions, the resistivity ρ of a thin film of arbitrary shape is given by [150, 151]

$$\rho = \frac{\pi d}{\ln 2} \frac{(R_{\mathrm{AB,DC}} + R_{\mathrm{BC,AD}})}{2} f\left(\frac{R_{\mathrm{AB,DC}}}{R_{\mathrm{BC,AD}}}\right), \tag{2.20}$$

where d is the total sample thickness and the resistance $R_{\mathrm{AB,DC}} = V_{\mathrm{DC}}/I_{\mathrm{AB}}$ is measured by applying a current from contact A to B and measuring the potential difference $V_{\mathrm{D}} - V_{\mathrm{C}}$ between contacts D and C, as illustrated in Fig. 2.6a. Similarly, the resistance $R_{\mathrm{BC,AD}} = V_{\mathrm{AD}}/I_{\mathrm{BC}}$ is determined by applying a current from contact B to C and measuring the potential difference $V_{\mathrm{A}} - V_{\mathrm{D}}$ between contacts A and D (Fig. 2.6a). The factor f is a function of the ratio $R_{\mathrm{AB,DC}}/R_{\mathrm{BC,AD}}$ and is determined by the transcendental equation [150, 151]

$$\cosh\left(\frac{R_{\mathrm{AB,DC}}/R_{\mathrm{BC,AD}} - 1}{R_{\mathrm{AB,DC}}/R_{\mathrm{BC,AD}} + 1} \frac{\ln 2}{f}\right) = \frac{1}{2} \exp\left(\frac{\ln 2}{f}\right). \tag{2.21}$$

In this work, Eq. (2.21) is solved numerically using a MATLAB program shown in Sect. B.15).

Van der Pauw Hall coefficient

For the Hall measurements a magnetic field B is applied perpendicularly to the layer surface (Fig. 2.6a). The Hall coefficient R_{H} is given by [150, 151]

$$R_H = -\frac{d \cdot [R_{\mathrm{CA,BD}}(B) - R_{\mathrm{CA,BD}}(B = 0)]}{B} = -\frac{d \cdot V_{\mathrm{H}}(B)}{I \cdot B}, \tag{2.22}$$

where d is the total sample thickness and the resistance $R_{\mathrm{AC,BD}}$ is measured by applying a current I from contact C to A and by measuring the voltage between contacts B and D.

Estimations of the errors in resistivity and Hall coefficient caused by deviations from the ideal contact sizes and positions are given in [150, 151] and are described in Sect. 4.3.

2.4 Dimensionality effects on electrical transport

2.4.1 Normal state properties

For many transition metal dichalcogenides it is still an open question how their thickness influences their electrical properties [1–4]. A prominent example for a TMDC showing a drastic effect when reducing the thickness along the cross-plane direction is MoS_2 [4, 7]. Bulk MoS_2 is a semiconductor with an indirect band gap, whereas an isolated MoS_2 monolayer is a direct band gap semiconductor with an increased luminescence quantum efficiency by more than a factor of 10^4 [7]. This transition from direct to indirect is attributed to a quantum confinement effect [7].

For VSe_2 intercalated with Cs atoms a 3D- to 2D-transition when increasing the separation between the VSe_2 monolayers, has been observed in the band structure using angle-resolved photoemission spectroscopy [152].

For isolated 2D monolayers of $NbSe_2$ the electric field and temperature dependence of their conductivity has been reported [1, 8]. From the electric field dependence it is concluded that a $NbSe_2$ monolayer is a semimetal with electron conduction [8], in contrast to bulk $NbSe_2$ which is metal-like with hole-conduction. Furthermore, the carrier density in a monolayer of $NbSe_2$ is two orders of magnitude lower than the carrier density in bulk $NbSe_2$ [8]. The mobility of the charge carriers in the monolayer was found to be similar to the mobility of the 3D-$NbSe_2$ compound [8]. A density functional theory calculation has shown that a charge density wave state, which is typical for $NbSe_2$, causes the $NbSe_2$ monolayer to become semimetallic, whereas it in the bulk system it remains a 'good metal' in the CDW state [15]. Other groups calculated metallic properties for a monolayer of $NbSe_2$ [98, 153, 154]. Resistance measurements of single, bi- and trilayers of $NbSe_2$ have shown a metal-like temperature dependence of the resistance [1]. SnSe, is reported to remain semiconducting when the thickness is reduced to four-atomic layer thick nanosheets [155]. A density functional calculation suggests that SnSe and PbSe remain semiconductors as 2D compounds, but their band gap increases in comparison to the bulk band gap [156].

2.4.2 Superconductivity

Thin $NbSe_2$ flakes have shown a decrease in T_c with decreasing sample thickness along the cross-plane direction of $NbSe_2$ [1, 9, 10, 63]. For bulk $2H$-$NbSe_2$ the transition temperature is $T_c = 7.2\,\mathrm{K}$, whereas for monolayers T_c of approximately $3.1\,\mathrm{K}$, for bilayers $T_c = 5.5\,\mathrm{K}$ and for trilayers $T_c = 6.2\,\mathrm{K}$ have been reported [1]. For $NbSe_2$ flakes with a thickness of $10\,\mathrm{nm}$ T_c is reported as $5.7\,\mathrm{K}$ to $6.7\,\mathrm{K}$ [9, 10]. Flakes which were 2-3-$NbSe_2$ monolayers thick reported in [9, 10] were nonconductive and after a high-current cleaning the flakes reported in [10] became superconducting with $T_c = 2\,\mathrm{K}$ to $2.5\,\mathrm{K}$. The 2-3 monolayer thick $NbSe_2$ flakes reported in [9] did not become superconducting down to $2.0\,\mathrm{K}$. A possible explanation for the fact that no superconductivity has been observed in the reports [9, 10] could be a degradation of the flakes due to air or UV exposure [3, 13]. A final explanation for the amount of decrease in T_c with decreasing thickness of $NbSe_2$ has not been found yet [9, 10, 13].

An experiment in which the distance between six superconducting $NbSe_2$ layers separated by non-superconducting $TiSe_2$ is increased is reported in [157]. In this experiment the increase in $TiSe_2$ layer thickness has lead to a decrease in transition temperature from $T_c = 4.4\,\mathrm{K}$ to $T_c = 2.6\,\mathrm{K}$ [157].

2D superconductivity in layered materials has been described using the Lawrence-Doniach and Ginzburg-Landau theories [2, 73, 75, 114] (Sect. 2.5). A superconduc-

tor is called a 2D superconductor if the cross-plane Ginzburg-Landau coherence length ξ_c is smaller than $s/\sqrt{2}$, where s is the distance between the superconducting planes [74, 114]. The effects of a 3D-to-2D cross-over will be described in more detail in Sect. 2.5.2. 2D superconductivity has, for example, been reported for $NbSe_2$ bilayers [2], thin Nb films [76], $SrTiO_3$ heterostructures [73], layered Nb/Ge composites [77], Pb/Ge double bilayers [78]. A list of experiments on 2D superconductivity is given in [114]. Investigations of the dimensionality of the superconductivity in ferecrystals have not been reported yet. Furthermore, the effect of increasing the thickness of one of the layer types in the ferecrystals on the superconducting properties has still been an open question.

2.4.3 Charge density waves

A charge density wave (CDW) is a spatial periodic modulation of the conduction charge carrier density and is accompanied by commensurate or incommensurate periodic lattice distortions [1, 12, 46, 47, 91, 109–111]. Charge density waves appear in low-dimensional, (quasi-)2D or 1D, materials [46, 47]. Their origin and effects of CDWs on structural and electrical properties are not yet fully understood and are still an active area of research [1, 10, 15, 44, 48, 50, 51, 54, 158]. The mechanism leading to CDWs in a one-dimensional metal has first been described by Peierls [46, 159]. The transition to a CDW state sets in below a CDW transition temperature, T_{CDW}, and is accompanied with the opening of an energy gap at the Fermi energy [47]. The connection between charge density waves and superconductivity in $NbSe_2$ has not yet been fully understood, also for bulk $NbSe_2$ [1, 10, 54, 158]. A charge density wave state has been observed for several TMDCs, e. g. for VSe_2 by electron diffraction [96], scanning tunneling microscopy [44] or other methods [54, 55, 57]. A change in the slopes of the temperature-dependence of the resistivity (hump feature) and Hall coefficient are indications for a CDW transition in $NbSe_2$ [1, 10, 50, 50, 52–57, 60, 60, 95, 105, 112, 113]. For $NbSe_2$ such anomalies in the resistivity are only observed for samples with a high RRR [1, 52, 105, 160]. However, although in isolated $NbSe_2$ mono-, bi- or trilayers no indications for a CDW transition have been observed in the resistivity, CDW transitions in these flakes have been detected by optical methods [1]. In bulk $NbSe_2$ single crystals T_{CDW} is approximately 33 K, whereas for a few-layer $NbSe_2$ T_{CDW} has been reported to increase up to $T_{\mathrm{CDW}} = 145$ K for a monolayer [1]. No indications for CDW transitions in resistivity or Hall coefficient have been found in MLCs. However, in the ferecrystals $[(SnSe)_{1+x}]_m[VSe_2]_n$ indications for a CDW transition in resistivity and Hall coefficient have been observed [19, 25].

2.5 Fundamentals of superconductivity

2.5.1 Basic phenomena

The research on superconductors started in 1911, when H. Kamerlingh Onnes observed that the electrical resistance of various metals vanished abruptly below a critical temperature temperature T_c [161]. A basic characteristic of superconductors is perfect conductivity. Another hallmark of superconductors is the expulsion of a magnetic field from the inside of the superconductor as it is cooled below T_c (Meissner effect). The existence of the Meissner effect also implies that superconductivity is suppressed as the magnetic field exceeds a critical value H_c. Equations describing the Meissner effect were derived by the London brothers in 1935 (London-equations) [162]. In 1950 Ginzburg and Landau [163] developed a macroscopic theory of superconductivity (Ginzburg-Landau theory). The advantage of the Ginzburg-Landau (GL) theory in contrast to the London theory is the possibility to treat a spatial variation of the density of the superconducting electrons n_s and non-linear effects of strong fields which can influence n_s [75]. The first microscopic theory for superconductivity was proposed in 1957 by Bardeen, Cooper and Schrieffer (BCS theory) [164]. In 1986 high-temperature superconductors were discovered by the measurement of $T_c \approx 30\,\mathrm{K}$ for the quaternary compound La-Ba-Cu-O by Bednorz and Müller [165]. In 1987 the first superconductor with T_c above the boiling point of liquid N_2 was found with $YBa_2Cu_3O_{7-\delta}$. These superconducting copper oxide compounds are layered materials containing atomically thin copper oxide planes. The highest ambient pressure transition temperature reported so far is $T_c = 133\,\mathrm{K}$ for $Hg_2Ba_2Ca_2Cu_3O_{10+\delta}$, which also shows a layered crystal structure [114, 166]. The microscopic mechanisms of high-temperature superconductivity are still unknown so far.

$NbSe_2$ has one of the highest critical temperatures among the transition metal dichalcogenides, with $T_c \approx 7\,\mathrm{K}$ [58–63, 83, 105]. $NbSe_2$ shows a layered structure with van der Waals gaps between atomically thin Se-Nb-Se layers. In the ferecrystals single $NbSe_2$ layers are stacked alternately with thin PbSe or SnSe layers. Bulk PbSe or SnSe do not become superconducting at normal pressure [121, 130]. Due to their layered structure, the variety of possible material combinations and the possibility to systematically vary the stacking sequences on the atomic scale, the ferecrystals could serve as model systems for layered high-temperature superconductors. In the following the expression $\mu_0 H$ will be used for the magnetic field instead of B in order to facilitate the comparison to literature on theory of superconductivity, where H is frequently used. SI units are used in this work.

BCS theory

The BCS theory is a microscopic theory of superconductivity. It explains superconductivity by pairing of electrons into Cooper pairs, caused by electron-phonon

coupling. The Cooper pairs are bound pairs of electrons with equal and opposite wave vectors and spins and form a correlated coherent superconducting state. The BSC theory predicts the existence of an energy gap $E_g = 2\Delta$ between the superconducting ground state and excited states. The BCS theory yields the following relation between Δ and the transition temperature T_c

$$\Delta(T = 0) = 1.764 k_B T_c, \tag{2.23}$$

where $\Delta(T = 0)$ is the energy gap of superconductivity at zero temperature and k_B is the Boltzmann constant.

Ginzburg-Landau theory

The Ginzburg-Landau (GL) theory is a phenomenological theory of superconductivity, which describes the macroscopic properties of superconductors [75, 163]. In the GL theory a complex pseudowavefunction ψ is introduced as order parameter, which describes the superconducting electrons. The local density of superconducting electrons n_s is given by [75]

$$n_s = |\psi(x)|^2 . \tag{2.24}$$

The GL theory is usually only valid near T_c, where the order parameter ψ is sufficiently small. In the GL theory a characteristic length, the GL coherence length ξ, is introduced. The GL coherence length is the distance over which $\psi(\mathbf{r})$ can vary without undue energy increase [75].

For pure materials with a large mean free path l of the normal-state charge carriers ($l \to \infty$), the GL coherence length is given by [75]

$$\xi(T) = 0.74 \frac{\xi_0}{(1 - T/T_c)^{1/2}} \qquad \text{(pure limit)}, \tag{2.25}$$

where ξ_0 is the temperature-independent BCS coherence length. For materials, in which the charge carriers have a small mean free path l, ($l \ll \xi_0$), the relation between the GL-coherence length ξ and the BCS coherence length ξ_0 is given by [75]

$$\xi(T) = 0.855 \frac{(\xi_0 l)^{1/2}}{(1 - T/T_c)^{1/2}} \qquad \text{(dirty limit)}, \tag{2.26}$$

where l is the mean free path of normal metals.

The temperature-independent BCS coherence length for materials in the dirty limit can therefore be estimated from extrapolating the Ginzburg-Landau coherence length to $T = 0$ by [75, 76]

$$\xi_0 = \frac{\xi^2(0)}{l \cdot (0.855)^2} \qquad \text{(dirty limit)}. \tag{2.27}$$

In the following, type-I and type-II superconductors will be described. Type-I and type-II superconductors can be distinguished by the so-called GL parameter κ. For samples in the pure limit, the GL parameter is given by [75]:

$$\kappa = 0.96 \frac{\lambda_L(0)}{\xi_0} \qquad \text{(pure limit)}, \tag{2.28}$$

where $\lambda_L(0)$ is the London penetration depth extrapolated to $T = 0$ and ξ_0 is the BCS coherence length. For samples with a small mean free path ($l \ll \xi_0$), the GL parameter is given by

$$\kappa = 0.715 \frac{\lambda_L(0)}{l} \qquad \text{(dirty limit)}. \tag{2.29}$$

For $\kappa < 1/\sqrt{2}$ the material is a type-I superconductor and for $\kappa > 1/\sqrt{2}$ it is a type-II superconductor.

Type-I superconductors

Type-I superconductors can be in two different states, i. e. the Meissner state and the normal state. For magnetic fields higher than the thermodynamic critical magnetic field $H_c(T)$, the material is in the normal conducting state and for $H < H_c$ it is in the superconducting state below T_c. The empirical temperature dependence of the critical magnetic field for type-I superconductors is

$$H_c(T) \approx H_c(0)[1 - (T/T_c)^2]. \tag{2.30}$$

Type-II superconductors

Type-II superconductors are characterized by two critical magnetic fields, the lower critical magnetic field H_{c1} and the upper critical magnetic field H_{c2}. For magnetic fields H below the lower critical magnetic field H_{c1}, type-II superconductors are in the Meissner state. For magnetic fields higher than the upper critical magnetic field H_{c2}, superconductivity completely vanishes. For $H_{c1} < H < H_{c2}$ the type-II superconductor is in the mixed state (Shubnikov phase). In the mixed state there is a partial magnetic flux penetration in the sample increasing continuously upon increasing H up to H_{c2}. In the mixed state the flux penetrates the type-II superconductor in a regular array of flux tubes, each carrying a flux quantum, which is given by

$$\Phi_0 = \frac{h}{2e} = 2.07 \cdot 10^{-15}\,\mathrm{T\,m^2}, \tag{2.31}$$

where h is Planck's constant and e the elementary charge [75]. In each unit cell of the array there is a vortex (also called Abrikosov vortex) of supercurrent concentrating the flux towards the vortex center.

The temperature dependence of the critical magnetic field for type-II superconductors has been approximated by the empirical formula [167, 168]

$$H_c(T) \approx H_c(0)[1 - a(T/T_c)^2], \tag{2.32}$$

which is valid for temperatures near $T = 0$ and a value of $a \approx 2$ has been reported for type-II superconductors [167, 168].

The ferecrystals discussed here are assumed to be type-II superconductors, because they contain $NbSe_2$, which is a type-II superconductor [9, 59, 167, 169–172]. Other intercalated transition metal dichalcogenides have also shown type-II superconductivity [173].

2.5.2 Superconductivity in layered materials

The Lawrence-Doniach model

Lawrence and Doniach [174] introduced a model in which layered superconductors are described as a stack of infinitely thin (2D), planar superconducting layers separated by a vacuum or insulating material. The stacked array of two-dimensional superconductors is coupled by Josephson tunneling between the superconducting layers [75]. Josephson tunneling is the phenomenon of Cooper pairs tunneling between two superconductors which are separated by a non-superconducting material (weak link), even at zero voltage difference between the two superconductors [75, 175]. The Lawrence-Doniach (LD) model has been extensively applied to transition metal dichalcogenides intercalated with organic molecules [173, 176] and can also be useful to describe effects in high-temperature superconductors [75, 177]. In this work the LD theory is applied to ferecrystals, assuming that the $NbSe_2$ layers are infinitely thin superconducting layers and SnSe is a non-superconducting material between the $NbSe_2$ layers.

The LD theory is based on the introduction of an anisotropic effective mass tensor where m_c is the effective mass component of the paired quasi-particles along the stacking direction and m_{ab} is the component along the in-plane direction [114, 178]. An anisotropy of the effective mass within the layer plane is neglected. The LD model reduces to the anisotropic 3D GL theory near T_c and it can yield new results at lower temperatures when crossing over to 2D behavior [75]. In the anisotropic GL theory, the in-plane GL coherence length ξ_{ab} and the cross-plane GL coherence length ξ_c have to be distinguished. According to the LD theory, the following equations hold for an anisotropic superconductor [75]:

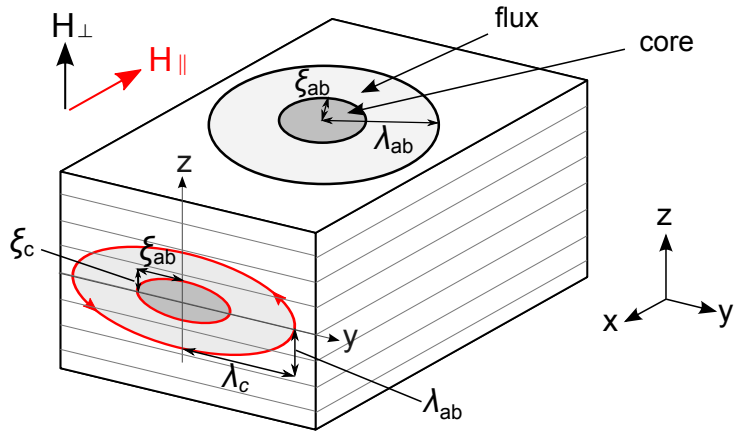

Figure 2.7: Schematic drawing an anisotropic layered type-II superconductor with schematics of vortices [62, 75]. The elliptical vortex (framed in red) forms for magnetic fields applied parallel to the layer planes, $H_{\parallel}$. The circular vortex (framed in black) forms for magnetic fields perpendicular to the layers, $H_{\perp}$. The dimensions ξ_{ab}, ξ_c, λ_{ab} and λ_c are related by Eq. (2.33).

$$\gamma \equiv \left(\frac{m_c}{m_{ab}}\right)^{1/2} = \frac{\lambda_c}{\lambda_{ab}} = \frac{\xi_{ab}}{\xi_c} = \frac{H_{c2\parallel}}{H_{c2\perp}}, \tag{2.33}$$

where m_{ab} and m_c are the in-plane and cross-plane components of the effective mass components of the quasi-particles, ξ_{ab} and ξ_c are the in-plane and cross-plane GL coherence lengths, and $H_{2c\parallel}$ and $H_{2c\perp}$ are in-plane and cross-plane upper critical magnetic fields. The parameter γ is the anisotropy parameter commonly used to describe the anisotropy of layered superconductors [114].

A schematic drawing of an anisotropic, layered superconductor with the cross sections of vortices for parallel and perpendicular magnetic fields are shown in Fig. 2.7. The superconductor is assumed to be isotropic in the a-b crystal plane. Therefore, the vortex cross-section perpendicular to the layer stacking direction is circular [75] for magnetic fields applied perpendicularly to the layer plane. The in-plane coherence length ξ_{ab} determines the vortex core radius for perpendicular fields. For magnetic fields parallel to the sample surface, the vortices have an elliptical cross section in the $x-z$ or $y-z$ plane. The in-plane and cross-plane coherence lengths ξ_{ab} and ξ_c determine the shape of the vortex core for magnetic fields parallel to the layer surface [75]. The penetration depths λ_{ab} and λ_c describe the distance of the decay of the supercurrents flowing along the $x-y$ plane and along the z-direction, respectively. They are related inversely to the coherence lengths according to Eq. (2.33). A material of layered superconducting planes is called a 3D superconductor if the cross-plane coherence length ξ_c is larger than

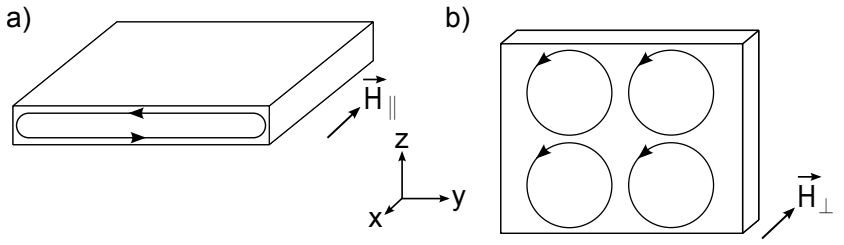

Figure 2.8: Schematic drawing of current configuration in a superconducting thin film of thickness $d_{sc} \leq \lambda\sqrt{5}$ in a magnetic field a) parallel to the film surface, $H_{\parallel}$ and b) perpendicular to the film surface, $H_{\perp}$ [178].

$s/\sqrt{2}$, where s is the distance between the superconducting planes [74]. In superconductors with a strong anisotropy, the cross-plane coherence length ξ_c can become very small. The dimensional cross-over from 3D to 2D for a layered material below T_c according to the LD model takes place when ξ_c becomes smaller than $s/\sqrt{2}$. For a (quasi-) 2D superconductor ($\xi_c \leq s/\sqrt{2}$) the vortices are confined between the superconducting layers for a magnetic field applied parallel to the layer surface [74, 75].

To determine the in-plane and cross-plane coherence lengths ξ_{ab} and ξ_c of layered materials and to determine whether a material shows 2D or 3D superconductivity, measurements of the temperature-dependent perpendicular and parallel critical magnetic fields have been commonly used [73, 75, 77, 78, 114]. For 3D superconductors the temperature dependence follows the anisotropic 3D GL equations and for 2D superconductors the critical fields are similar to the critical fields of a single isolated thin film of thickness $d_{sc} \leq \sqrt{5}\lambda$, where lambda is the penetration depth, as defined in the GL theory [73–75, 77].

The configuration of the supercurrents in an isolated superconducting thin film in a parallel and a perpendicular magnetic field is shown schematically in Fig. 2.8. In the parallel magnetic field the width of a current loop is limited by the film thickness. In the perpendicular field the vortex size can adjust according to the magnetic field strength [178].

The perpendicular critical magnetic field

2D and 3D superconductors: The in-plane coherence length ξ_{ab} can be determined by the measurement of the temperature dependence of the perpendicular critical magnetic field. For a magnetic field applied perpendicularly to the layer plane of a layered superconductor, the following equation from the GL theory can be applied for temperatures near T_c [2, 73, 75, 179, 180]:

$$\mu_0 H_{c2\perp}(T) = \frac{\Phi_0}{2\pi {\xi_{ab}}^2(T)} = \frac{\Phi_0}{2\pi {\xi_{ab}}^2(0)} \left(1 - \frac{T}{T_c}\right), \tag{2.34}$$

where μ_0 is the vacuum permeability, Φ_0 is the flux quantum and ξ_{ab} is the in-plane Ginzburg-Landau coherence length. Eq. (2.34) is valid for 2D as well as 3D type-II superconductors in a perpendicular magnetic field. It also holds for thin films of type-I superconductors in magnetic fields perpendicular to the film, but with $H_{c2\perp}$ replaced by the thermodynamic critical field $H_{c\perp}$ [75, 179].

The parallel critical magnetic field

The temperature dependence of the parallel critical magnetic field of thin layered materials differs for 2D and 3D superconductors.

3D superconductors: The temperature dependence of the parallel critical magnetic field of an anisotropic 3D superconductor can be described using the anisotropic GL equations and is given by [75, 179, 180]

$$\mu_0 H_{c2\parallel}(T) = \frac{\Phi_0}{2\pi\xi_c(T)\xi_{ab}(T)} = \frac{\Phi_0}{2\pi\xi_c(0)\xi_{ab}(0)}\left(1-\frac{T}{T_\mathrm{c}}\right), \tag{2.35}$$

where ξ_{ab} is the in-plane GL coherence length and ξ_c is the coherence length perpendicular to the layer plane. This equation is valid for temperatures near T_c.

2D superconductors: The temperature dependence of the parallel critical magnetic field of a 2D superconductor can be approximated by the temperature dependence of an isolated thin film with the thickness $d_{sc} \leq \sqrt{5}\lambda$ [2, 73–75, 176]. The following equation was derived by the GL theory [75] for a thin film with thickness $d_{sc} \leq \sqrt{5}\lambda$

$$\mu_0 H_{c2\parallel}(T) = \frac{\sqrt{3}\Phi_0}{\pi d_{sc}\xi_{ab}(T)} = \frac{\sqrt{3}\Phi_0}{\pi d_{sc}\xi_{ab}(0)}\left(1-\frac{T}{T_\mathrm{c}}\right)^{1/2}, \tag{2.36}$$

where d_{sc} is the (temperature-independent) thickness of the superconducting thin film or a length scale for the spatial distribution of the order parameter perpendicular to the layer planes [73, 75]. The temperature T^* with $\xi_c(T^*) = s/\sqrt{2}$ is the cross-over temperature below which the layered superconductor shows 2D behavior in the temperature dependence of the parallel critical magnetic field [73–77, 176].

Angle dependence of the critical magnetic field

3D superconductors: The angle dependence of the critical magnetic field depends on the dimensionality of the superconductor [74, 75, 177]. For a 3D layered type-II superconductor, the angle dependence of the critical magnetic field in the anisotropic GL limit of the LD theory is given by [74, 75, 177]

$$\left(\frac{H_{c2}(\theta)\sin\theta}{H_{c2\perp}}\right)^2 + \left(\frac{H_{c2}(\theta)\cos\theta}{H_{c2\parallel}}\right)^2 = 1 \tag{2.37}$$

where θ is the angle between the magnetic field and the layer-plane [75]. Eq. (2.37) can also be written as

$$\mu_0 H_{c2}(\theta) = \frac{\gamma\mu_0 H_{c2\perp}}{\left(\cos^2\theta + \gamma^2\sin^2\theta\right)^{1/2}}, \tag{2.38}$$

where γ is the anisotropy parameter given by Eq. (2.33).

2D superconductors: For the angle dependence of the critical magnetic field $H_c(\theta)$ of a 2D superconductor the equation

$$\left|\frac{H_c(\theta)\sin\theta}{H_{c\perp}}\right| + \left(\frac{H_c(\theta)\cos\theta}{H_{c\parallel}}\right)^2 = 1, \tag{2.39}$$

is obtained for isolated thin films with a thickness $d_{sc} \leq \lambda\sqrt{5}$ from the GL theory [73–75, 177–179].

3 Experimental details for transmission electron microscopy

3.1 Specimen preparation for transmission electron microscopy

For structural analyses using transmission electron microscopy (TEM) the samples under investigation have to be electron transparent. In order to resolve atomic columns using high-angle annular dark-field scanning transmission electron microscopy HAADF-STEM, which is applied in this work, the samples should be ideally only a few atomic layers thick.

In this work, the samples have been prepared for TEM using a conventional cross-sectional preparation technique. The preparation steps are summarized in Fig. 3.1. The first step in TEM specimen preparation was the formatting of the samples. The samples, which were synthesized on Si(100) substrates have been cleaved along the easily cleavable Si(110) planes using a scalpel. The samples on quartz substrates were sawed with a diamond wire saw without water and lubricant to prevent the ferecrystals to peel off the substrate. Subsequently, the samples were glued face-to-face using the glue M-Bond 610, with subsequent curing of the glue in a drying chamber at 150 °C for 2 h. After curing, the samples were glued into a thin-walled ceramics tube using MBond AE 15 glue. This glue was cured at 80 °C for 1.5 h. Subsequently, the samples were sawed into disks with a thickness of about 300 µm using a diamond-wire saw. The slices were then ground using abrasive diamond polishing paper and water containing a lubricant. The smallest grain sizes of the polishing paper used were 9 µm for the first side and 1 µm for the second side of the disk-shaped sample. The final thickness of the slice after grinding both sides was about 80 µm. A wax was used to affix the sample to the sample holder. In order to apply and remove the wax, it had to be heated to 80 °C. The height of the disk before and after each polishing step was measured with a caliper. On the side of the disk which had been ground with a grain size down to 9 µm, an about 30 µm deep dimple was ground using the Gatan Dimple Grinder Model 656 with a grinding wheel and diamond suspension. This dimple was then polished with diamond suspensions with a grain size of 1 µm and 0.25 µm using a wheel covered with felt for about 20 min for each grain size. The second side of the disk was polished with diamond suspensions with a grain size of 1 µm and a 0.25 µm for about 20 min for each grain size until the color of the silicon

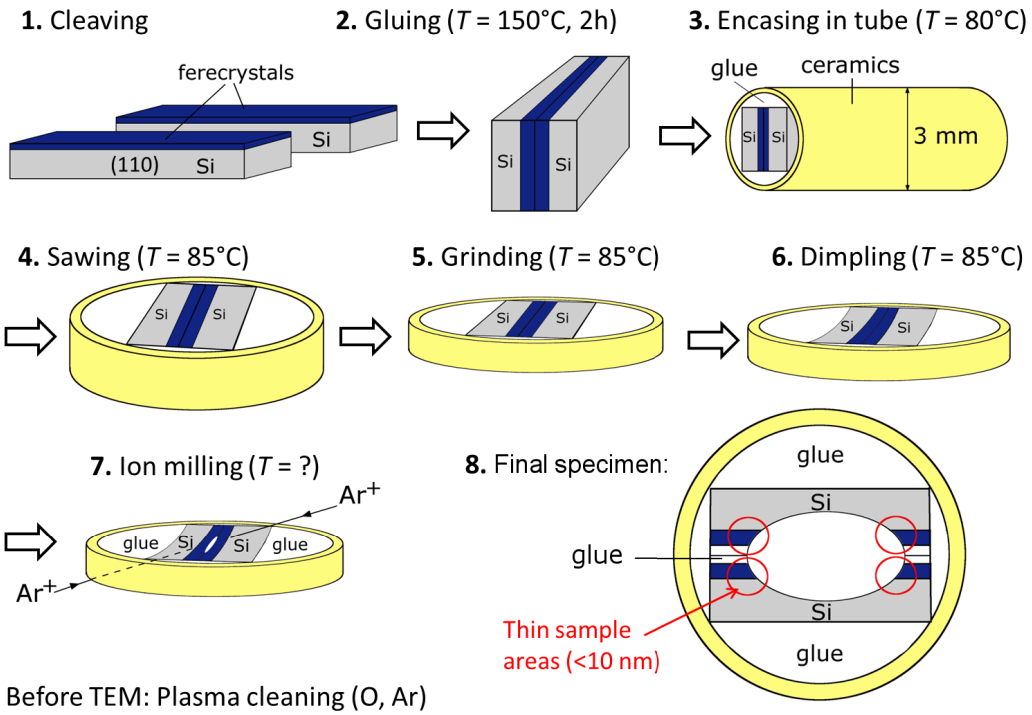

Figure 3.1: TEM specimen preparation steps.

substrate turned red. The thin samples (called specimens in the following) were removed from the sample holders by dissolving the wax in trichloroethylene (for several hours), acetone (for 10 min) and in methanol for (10 min). The specimens were then ion milled using Ar ions in a Rapid Etching System RES010 (Baltec) at the Humboldt-Universität zu Berlin and one specimen was ion milled in a Precision Ion Polishing System (PIPS) at the Institut für Kristallzüchtung (IKZ). The angle between the disk surface and the ion beam was 10°. During ion milling it was possible to cool the specimens using liquid nitrogen. Finally, the specimens were plasma cleaned for 3 min using an Ar/O gas to prevent contamination of the specimens. Detailed TEM specimen preparation parameters for each specimen are listed in Table A.1.

3.2 High-angle annular dark-field scanning transmission electron microscopy

High-angle annular dark-field scanning transmission electron microscopy (HAADF-STEM) is a method used for the investigation of the local structure of materials on the atomic scale. A focused electron probe is scanned across the specimen and

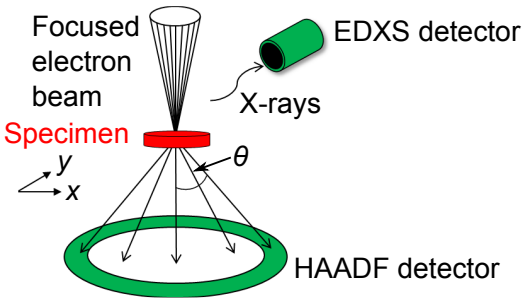

Figure 3.2: Schematic representation of the HAADF-STEM and the EDXS technique.

for each probe position the number of electrons impinging at the annular dark field detector behind the specimen is displayed as pixel intensity in the image. Typically, an electron energy between 100 keV and 300 keV is used. A schematic measurement setup for HAADF-STEM is shown in Fig. 3.2. The specimen preparation process of the TEM sample is described in Sect. 3.1. The size of the electron probe on the specimen determines the maximum resolution of the STEM images (which is about 0.2 nm for the TEM/STEM JEOL JEM2200FS). The annular detector is centered on the optical axis of the TEM. Only electrons that are scattered into high angles are detected. Hence, diffraction contrast is smoothed out at such high angles and is negligible for the image contrast [181]. As a first approximation the intensity of electrons at the annular detector can be explained by Rutherford scattering of the electrons at the nuclei of the sample atoms. The Rutherford cross section corrected for screening by inner shell electrons and relativity effects for electrons that are elastically scattered by the nucleus into angles larger than θ is [181]

$$\sigma = 1.62 \cdot 10^{-24} \left(\frac{Z}{E_0} \right)^2 \cot^2 \frac{\theta}{2}, \tag{3.1}$$

where E_0 is the electron energy and Z is the atomic number. Therefore, HAADF-STEM images reveal an atomic number-thickness contrast. The image is brighter for those sample positions which show a higher mean atomic number and a higher thickness. The Rutherford cross section model can only be applied accurately for incident electron energies E_0 of less than about 300 keV and atomic numbers Z less than about 30 [181]. The electron energy used in this study is 200 keV, but the atomic numbers of Sn ($Z = 50$), Se ($Z = 34$), Nb ($Z = 41$) and Pb ($Z = 41$) are higher than 30 and therefore Eq. (3.1) is only a first approximation. For more quantitative calculations of the scattering cross sections other models can be found e. g. in [182] or [183]. In this study of ferecrystals, only a qualitative interpretation of the images is made and the approximation Eq. (3.1) is usually sufficient. Electron channeling effects, which are not described by Eq. (3.1), can

lead to further intensity enhancement effects in the HAADF-STEM images, as described in [184, 185]. HAADF-STEM of cross-sectional ferecrystal samples has turned out to be a powerful tool for the investigation of the local atomic structure of ferecrystals [19, 22, 29, 30, 32, 186, 187]. In this study, a TEM/STEM JEOL JEM2200FS with an electron energy of 200 keV and a high-angle annular dark-field (HAADF) detector has been used to obtain the HAADF-STEM images. The microscope is equipped with a field emission gun. A double-tilt specimen holder has been used. For the HAADF-STEM images in this work a probe spot size of 0.2 nm was used, defining the maximum spatial resolution.

3.3 Energy-dispersive X-ray spectroscopy

Energy-dispersive X-ray spectroscopy (EDXS) is an analytical technique used in TEM, which provides information about the chemical elements and their spatial distribution in the sample. The incident electron beam causes the excitation of inner shell electrons in the sample. Outer shell electrons fill the hole in the inner shell created by the excitation. The energy difference is released by the emission of characteristic X-rays from the sample. The emitted X-rays are detected by an EDXS detector above the sample, as shown schematically in Fig. 3.2. The electronics attached to the detector then converts the charge pulse created by the incoming X-ray into a voltage pulse, which is stored in the respective energy channel [181]. EDX data can be acquired as point spectra, line scans and maps. In this work, for EDXS, a focused electron beam is incident on the sample. In order to choose the sample area for the acquisition of the EDX spectrum, HAADF-STEM has been used beforehand to create an image of the sample. The spot size of the electron probe for the EDX-spectra was 1 nm. A liquid nitrogen-free energy dispersive X-ray SD detector (Bruker) has been used to obtain the EDXS spectra. This detector is Peltier cooled and has an energy resolution of 129 eV (MnK). For a quantification of sample composition the thin-foil approximation was used, for which absorption and fluorescence of X-rays are ignored. In this approximation the ratio between the concentrations of two elements in the sample is given by [181]

$$\frac{C_i}{C_j} = k_{ij}\frac{I_i}{I_j} \quad \text{with} \quad \sum_i C_i = 100\,\%, \tag{3.2}$$

where C_i is the concentration of element i, I_i is the intensity measured for the respective characteristic X-ray peak and k_{ij} is the Cliff-Lorimer factor. The Cliff-Lorimer factors should be calibrated for the certain composition and known specimen thickness. This was not available in the present experiment, thus theoretical Cliff-Lorimer factors from the software Bruker Esprit 1.9 were used for the quantification.

3.4 Selected-area electron diffraction

For selected-area electron diffraction (SAED) the specimen is illuminated by a parallel electron beam, which is parallel to the layer planes of the ferecrystals, as shown in Fig. 3.3. The sample area which contributes to the diffraction pattern is chosen in the transmission electron microscopy (TEM) image mode using the selected-area aperture. The diffraction pattern is then displayed on the viewing screen by adjusting the intermediate lens to display the back-focal plane of the objective lens. For a qualitative explanation of the intensity distribution, i. e. the location of intensity maxima in the diffraction pattern, the kinematical approximation for electron diffraction can be used. In the kinematical approximation, the scattering processes of the electrons in the sample are assumed to be elastic and only single scattering events are considered [181, 188]. This approach holds for specimens, which are sufficiently thin along the direction of the electron beam and which contain elements with low atomic numbers. Thin TEM specimens with thicknesses below 10 nm along the direction of the incident electron beam can be prepared. It is therefore possible to fulfill the latter condition. The kinematical approximation, however, does not allow for a precise prediction of the relative intensity distribution in the diffraction patterns. For a more detailed analysis of the intensity distribution in diffraction patterns a dynamical theory would have to be applied, which, for example, also takes into account multiple scattering events [181, 188, 189]. The MX and TX_2 layers in the ferecrystals are not only thin along the electron beam direction, but they are also only a few atomic layers thick along the layer stacking direction, i. e. perpendicular to the incident electron beam, Fig. 3.3. The kinematical approximation can be used to describe how the size of a crystal affects its diffraction pattern. For a qualitative description, a crystal is assumed with a rectangular unit cell and N_x, N_y and N_z unit cells along the directions of the unit vectors $\vec{e}_x$, $\vec{e}_y$ and $\vec{e}_z$. The position vectors $\vec{r}_n$ of the unit cells are given by $\vec{r}_n = n_x a_x \vec{e}_x + n_y a_y \vec{e}_y + n_z a_z \vec{e}_z$, where a_i are the unit cell parameters along the directions of the unit vectors $\vec{e}_i$ with $(i = x, y, z)$ and $n_i = 0, 1, ..N_i - 1$. Then, the intensity of the diffracted electron wave $I(\Delta\vec{k})$ is [181, 188]

$$I \propto \left|F(\Delta\vec{k})\right|^2 \frac{\sin^2(N_x \Delta k_x a_x/2)}{\sin^2(\Delta k_x a_x/2)} \frac{\sin^2(N_y \Delta k_y a_y/2)}{\sin^2(\Delta k_y a_y/2)} \frac{\sin^2(N_z \Delta k_z a_z/2)}{\sin^2(\Delta k_z a_z/2)}, \qquad (3.3)$$

where $\Delta\vec{k} = \vec{k}' - \vec{k}_0$, and $\vec{k}'$ and $\vec{k}_0$ are the wave vectors of the diffracted and the incident electron waves, respectively. The factor F is the structure factor, which is given by $F = \sum_j f_j \exp(-i\Delta\vec{k} \cdot \vec{r}_j)$, where f_j are the atomic form factors and $\vec{r}_j$ the position vectors of the atoms inside the unit cell. Equation (3.3) shows that if the crystal is very thin along at least one direction, the diffracted intensity I can be non-zero although the Laue- (or Bragg)-condition is not fulfilled, i. e. for $\Delta\vec{k} \neq \vec{G}_{hkl}$. If the crystal is very thin along a direction, the reciprocal lattice

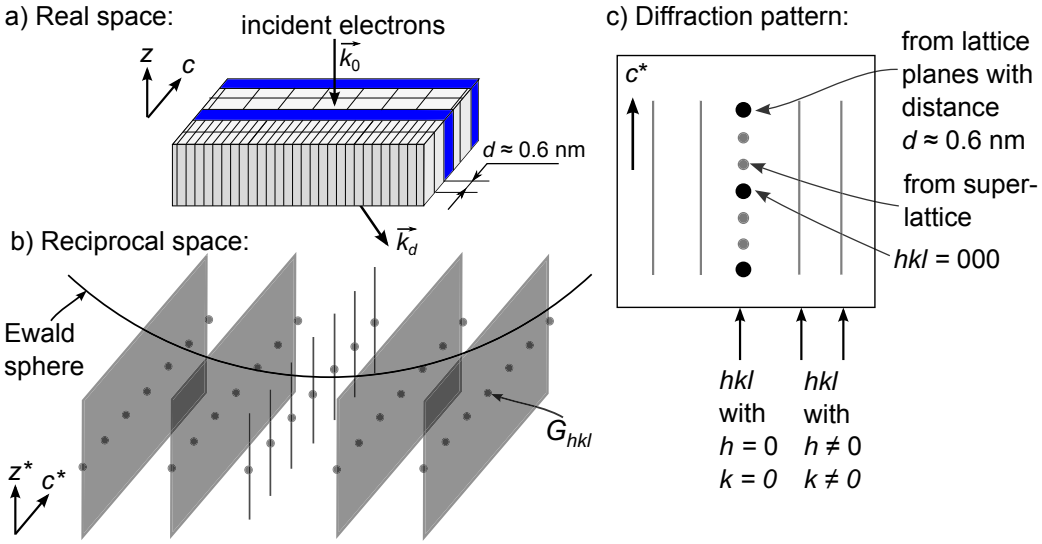

Figure 3.3: Schematic formation of an SAED pattern $[(M\mathrm{Se})_{1+\delta}]_{\boldsymbol{m}}(T\mathrm{Se}_2)_1$ with $m = 2$. a) Blue layers indicate $T\mathrm{Se}_2$, white layers $M\mathrm{Se}$. b) Reciprocal lattice points G_{hkl} with $h = k = 0$ are extended along z^* and those with $h \neq 0$ or $k \neq 0$ are extended along z^* and c^*. d) The SAED pattern shows intensity streaking for $h \neq 0$ or $k \neq 0$ and discrete spots for $h = 0$ and $k = 0$.

points are extended to so-called Laue lattice spikes (Lauesche Gitterstachel), also denoted as reciprocal lattice rods (*relrods*), along this direction [181].

The location of the diffraction spots in the SAED pattern can be determined using the Ewald sphere construction [181]. The Ewald sphere is constructed by drawing the wave vector $\vec{k}_0$ of the incident electron wave such that it points to a reciprocal lattice point, which is chosen as the origin of the reciprocal lattice. The length of $\vec{k}_0$ is given by $k_0 = 2\pi/\lambda$, where λ is the wavelength of the electrons. The origin of $\vec{k}_0$ is in the center of the Ewald sphere. The Ewald sphere has the radius $2\pi/\lambda$. The Laue conditions are fulfilled for those reciprocal-lattice points and relrods, which are cut by the Ewald sphere. The wave vectors $\vec{k}'$ of the diffracted waves are determined by their starting point in the center of the Ewald sphere and their ending point at the intersection of the Ewald sphere with the reciprocal lattice point or relrod. Since the TEM sample is very thin along the incident electron beam direction, i. e. along z, there are relrods in reciprocal space along $\vec{k}_0$, i. e. z^*. Furthermore, due to the small wavelength λ of the TEM electrons with an energy of about 200 keV, the Ewald sphere is almost flat and can cut many relrods for one incident beam direction. Hence, diffracted intensity from several different sets of lattice planes is visible on the screen, although the Laue conditions are not exactly fulfilled.

In addition, the turbostratic disorder of the very thin MSe and $T\mathrm{Se}_2$ layers results in further extension of the relrods parallel to the stacking direction in the ferecrystals. Figure 3.3 shows schematically that the reciprocal lattice points G_{hkl} with $h \neq 0$ and $k \neq 0$ are extended along z^* and c^* due to the small widths of the crystallites perpendicular to z (incitend electron beam direction) and c (stacking direction) and due to the lack of registry between subsequent layers. Therefore, in SAED patterns of ferecrystals an intensity streaking appears for hkl with $h \neq 0$ and $k \neq 0$ [16, 17, 19, 22, 23, 25, 30, 31]. The spots $hkl = 00l$ do not show intensity streaking, because the MSe and $T\mathrm{Se}_2$ crystallites in the ferecrystals are all aligned with their crystallographic c-axes parallel to the stacking direction. Therefore, there is no disorder along the common direction c. In ideal misfit layer compounds, all layers of a subsystem (MSe and $T\mathrm{Se}_2$) have a common orientation relationship throughout the sample, leading to diffraction spots instead of streaks in the diffraction patterns [190–193]. Intensity streaks in SAED patterns of MLCs, which have been observed are attributed to a stacking disorder in one or both subsystems [191–193].

In this study, a TEM/STEM JEOL JEM2200FS with an electron energy of 200 keV was used to obtain the selected-area electron diffraction SAED patterns. The smallest available selected-area aperture was used, which has a size of about 110 nm. Therefore, the SAED patterns contain information from the ferecrystals (50 nm thick) and from a part of the substrate. From the distance $r^*_{(h\,k\,l)}$ between the diffraction spots and the center of the diffraction pattern, the lattice parameters $d_{(h\,k\,l)}$ of the sample are determined by

$$d_{(h\,k\,l)} = \lambda L / r^*_{(h\,k\,l)}, \tag{3.4}$$

where L is the camera length and the product λL is called camera constant. The camera constant was calibrated using the silicon substrate as a reference.

4 Transport measurement details

4.1 Contacting the samples for transport measurements

In order to carry out electrical transport measurements, thin gold wires of diameter 25 µm and purity 99.99 % (Heraeus) were affixed to the samples using indium with a purity of 99.998 % (Alfa Aesar). An example of contacted samples is shown in Fig. 5.1b. The samples were glued into a chip carrier using a drop of silver paint (high purity silver paint, SPT-supplies) between the chip carrier and the back of the substrate to allow for good thermal contact. The chip carrier consists of ceramics covered by a gold alloy. The gold wires are affixed to the chip carrier using silver paste (G3303B Leitsilber, Plano GmbH). The chip carrier is clamped into a socket, which is integrated in a sample holder for the particular cryostat. In the cryostat sample holder thin wires lead from the chip carrier to BNC connectors. Low-noise BNC-cables were used for all measurements to connect the sample from the cryostat sample holder to the measurement instruments.

4.2 Cryostats

4.2.1 Flow-cryostat

A continuous-flow cryostat (Cryovac KONTI-IT) was used for measurements at temperatures between 1.4 K and 310 K. The sample is located in a helium atmosphere. In order to obtain temperatures between 1.4 K and 4.2 K a rotary pump was used to decrease the helium pressure and therefore the temperature. A Cernox CX-1050 thermometer located close to the chip carrier socket was used to measure the temperature. This thermometer is suitable for use in magnetic fields with only a very low magnetic field dependence (see Cernox CX-1050 data sheet). The temperature was controlled using the TIC 304-MA temperature controller and a custom LABVIEW program. An electromagnet (Bruker Magnet B-E10V) was used for magnetoresistance and Hall measurements in this cryostat. The magnet is suitable for static magnetic fields of up to 670 mT. The cryostat is equipped with a rotating system with which the thin film sample surface can be rotated within an angle range of 0°-360° relative to the direction of the magnetic field.

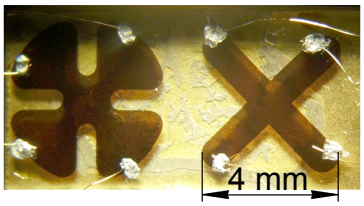

Figure 4.1: Photograph of the ferecrystals contacted for electrical measurements. left: clover leaf ('sample A'), right: cross ('sample B').

4.2.2 He-3-cryostat

For measurements down to temperatures of 250 mK a helium-3-system (Heliox VL insert, Oxford instruments) has been used. In this system the sample is located in vacuum. For measurements in magnetic fields of up to 2 T the Helium-3-system was used in a Helium dewar. The 2 T-magnet is a superconducting magnet which can be mounted directly to the helium-3-system. For measurements in magnetic fields of up to 10 T the helium-3-system was used in a cryostat (Oxford instruments) equipped with a 10 T-superconducting magnet. Temperatures between rt and $T = 1.3$ K were measured using the calibrated Lakeshore Cernox CX-1050-AA-1.4L thermometer, which is located at the Helium-3-pot. A ruthenium oxide thermometer (LakeShore RX-202A-AA-0.05B) calibrated between 0.04 K and 45 K was used for measurements at lower temperatures. The ruthenium oxide thermometer is located directly below the chip carrier with the sample. The temperature of the helium-3-system was controlled using the Mercury iTC temperature controller (Oxford instruments) and a custom LABVIEW program. The magnetic field was set using the Mercury iPS controller (Oxford instruments) for both superconducting magnets and a custom LABVIEW program. The helium-3-system is equipped with a static holder (no rotating system) suitable for measurements with the film surface perpendicular and parallel to the magnetic field. The error in the angle between film surface and magnetic field is estimated as 2°.

4.3 Van der Pauw resistivity and Hall measurements

4.3.1 Van der Pauw resistivity measurements

The measurement setup for the van der Pauw resistivity and Hall measurements is shown schematically in Fig. 2.6. Figures 2.6 a) and b) show two measurement configurations used for the van der Pauw resistivity measurements. There are six further equivalent measurement configurations, in which the resistances have also been measured in order to reduce the error. The resistivity has been calculated by [150, 151]

$$\rho = \frac{\pi d}{\ln 2} \frac{(\hat{R}_{\mathrm{AB,DC}} + \hat{R}_{\mathrm{BC,AD}})}{2} f\left(\frac{\hat{R}_{\mathrm{AB,DC}}}{\hat{R}_{\mathrm{BC,AD}}}\right) \tag{4.1}$$

where d is the total sample thickness and f is given by Eq. (2.21). Applying the notation introduced in Sect. 2.3.4, the resistances $\hat{R}_{\mathrm{AB,DC}}$ and $\hat{R}_{\mathrm{BC,AD}}$ are

$$\hat{R}_{\mathrm{AB,DC}} = \frac{R_{\mathrm{AB,DC}} + R_{\mathrm{BA,CD}} + R_{\mathrm{CD,BA}} + R_{\mathrm{DC,AB}}}{4} \tag{4.2}$$

and

$$\hat{R}_{\mathrm{BC,AD}} = \frac{R_{\mathrm{BC,AD}} + R_{\mathrm{CB,DA}} + R_{\mathrm{AD,BC}} + R_{\mathrm{DA,CB}}}{4}. \tag{4.3}$$

The resistance measurements were performed using a Keithley 6221 Current Source, a Keithley 2182 Nanovoltmeter and a Keithley 2401 Low Voltage SourceMeter instrument. The resistances were determined from linear, least square fits of the current-voltage (I-V)-curves measured with direct currents of up to 20 µA consisting of 30 measurement points, starting at 0 A. The measured resistance values range between 5 Ω and 320 Ω. The switch system (Keithley 7001 Switch/Control Mainframe with two 7012-C Matrix cards) and a custom LabView program were used to switch between the different van der Pauw measurement configurations for the two samples and the Hall measurement configuration.

For the calculation of the error in ρ the sheet resistance R_{s} is introduced, which is defined by

$$\rho = d \cdot R_{\mathrm{s}}, \tag{4.4}$$

where d is the total sample thickness, given in Tables 5.1 and 6.1. Using Gauss error propagation, the absolute error u_ρ in resistivity is calculated by

$$u_\rho = \pm\sqrt{(d \cdot u_{R\mathrm{s}})^2 + (u_d \cdot R_{\mathrm{s}})^2}, \tag{4.5}$$

where u_d is the absolute error in thickness, given in Tables 5.1 and 6.1. The term $u_{R\mathrm{s}}$ is the absolute error in sheet resistance which was calculated by

$$u_{R\mathrm{s}} = \pm\sqrt{(u_{R\mathrm{s,fit}})^2 + (u_{R\mathrm{s,contact}})^2}, \tag{4.6}$$

where $u_{R\mathrm{s,fit}}$ is the error in R_{s} calculated from the error of the linear fit of the I-V-curves. The term $u_{R\mathrm{s,contact}}$ is the systematic error in R_{s} due to the size of the contacts and has been calculated using an error approximation given in [150, 151] for samples with a circular shape:

$$u_{R\mathrm{s,contact}} = \pm R_{\mathrm{s}} \cdot 4 \cdot \left(l^2/(16D^2 \ln 2) + l^2/(4D^2 \ln 2)\right), \tag{4.7}$$

where $D \approx 3.5$ mm is the diameter of the sample and $l \approx 0.56$ mm is the diameter of each contact. The error $u_{R\mathrm{s,contact}}$ amounts to about $u_{R\mathrm{s,contact}} = 0.047 \cdot R_{\mathrm{s}}$ and

determines the main part of the error in ρ. The sheet resistances and errors were calculated using a MATLAB program written specifically for the measurements in this work (B.15). Bloch-Grüneisen fits were also performed using a MATLAB program (B.16).

4.3.2 Van der Pauw Hall measurements

Figure 2.6c shows the schematic setup of the van der Pauw Hall measurement. For the PbSe-based system, batch 3, the Hall measurements were performed in the Helium-3-System using a lock-in amplifier with a current of 2 µA and magnetic fields of up to 10 T. For the SnSe-based sample system the Hall measurements were performed in the flow-cryostat and using the Delta Mode of the Keithley 6221/2182 CurrentSource/Nanovoltmeter with currents of 150 µA. For the Hall measurements in the flow cryostat the orientation of the magnetic field was calibrated for each sample by rotating the sample in the magnetic field. The Hall voltages were plotted against the angle and a sine fit was used to find the angle in which the sample surface is perpendicular to the magnetic field. The magnetic field strength was measured with a Hall effect sensor located next to the sample outside of the flow-cryostat. The magnetic field strength was varied in 9 steps from $B = 0\,\mathrm{mT}$ to $670\,\mathrm{mT}$ with constant magnetic fields during each measurement. In between the measurements at different $B \neq 0$ the magnetic field was set to $B = 0$. The Hall voltage V_H was obtained from the difference between the average voltages measured at $B \neq 0$ and $B = 0$. The curves $V_\mathrm{H}(B)$ were checked for linearity. The Hall coefficient R_H was obtained from a linear, least square fit of the type $V_\mathrm{H} = a \cdot B$, where a is the fit parameter which contains R_H, according to Eq. (2.22). The sign of the Hall coefficient was determined from the sign of the slope of $V_\mathrm{H}(B)$. For the measurement setup shown in Fig. 2.6 a negative slope of $V_\mathrm{H}(B)$ would imply a positive Hall coefficient. For the calculation of the error in R_H the abbreviation $b = a/I$ is introduced, where a is the fit parameter mentioned above and I is the current. The Hall coefficient is then

$$R_\mathrm{H} = d \cdot b, \tag{4.8}$$

where d is the total sample thickness of the ferecrystal thin film, given in Tables 5.1 and 6.1. The absolute error u_{R_H} of R_H is calculated by

$$u_{R_\mathrm{H}} = \pm\sqrt{(d \cdot u_\mathrm{b})^2 + (u_\mathrm{d} \cdot b)^2}, \tag{4.9}$$

where u_d is the absolute error in sample thickness, given in Tables 5.1 and 6.1. The term u_b is calculated by

$$u_\mathrm{b} = \pm\sqrt{(u_\mathrm{b,fit})^2 + (u_\mathrm{b,contact})^2}, \tag{4.10}$$

where $u_{\mathrm{b,fit}}$ is the error in b calculated from the error of the linear fit of the V_{Hall} vs. B curves by error propagation. The term $u_{\mathrm{b,contact}}$ is the systematic error in b due to the size of the contacts and is calculated using an approximation given in [150, 151]:

$$u_{\mathrm{b,contact}} = \pm b \cdot 4 \cdot \left(2l/(\pi^2 D) + 4l/(\pi^2 D)\right), \tag{4.11}$$

where D is the diameter of the sample and l is the diameter of each contact, where the contacts and the sample are assumed to be circular with $D \approx 3.5\,\mathrm{mm}$ and $l \approx 0.56\,\mathrm{mm}$. This error term amounts to about $u_{\mathrm{b,contact}} = 0.39b$ and determines the main part of the error in R_{H}. The Hall coefficient and carrier density and their errors were calculated using a MATLAB program (Sect. B.17). To determine the sign of the Hall coefficient, p- and n-type silicon samples, for which the sign of the Hall coefficient was known, were measured in advance in the same measurement setup to confirm the correct sign of the Hall coefficient. For a few SnSe-based samples, the Hall voltage was not linear in B at low temperatures. (Due to the magnetoresistance effect resulting from a misalignment of the voltage contacts at the sample). Therefore, some of these measurements were repeated in the Helium-3-cryostat using a lock-in amplifier (DSP Model 7265) and a current of 2 µA and magnetic fields of up to 2 T. Those measurements will be described in Sect. 4.4.

4.4 Magnetoresistance measurements

The magnetoresistance measurements were carried out in the Helium-3-cryostat (Heliox VL) in magnetic fields of up to 10 T with AC resistance measurements. The measurement setup is sketched in Fig. 4.2. The resistance of the sample was measured in one of the van der Pauw measurement configurations using a lock-in amplifier (DSP Model 7265). The sample was located in a static sample holder and the magnetic field was applied with an angle of about 90° to the sample surface, within an error of a few degrees. The internal oscillator of the lock-in amplifier was used for the lock-in measurements. A resistor $R = 1\,\mathrm{M\Omega}$ was used in series to the sample in order to obtain a low current I_{rms} (root mean square value). The current through the 1 MΩ-resistor was adjusted before the magnetoresistance measurements by setting the voltage output of the lock-in amplifier such that a current of $I_{\mathrm{rms}} = 500\,\mathrm{nA}$ is obtained.

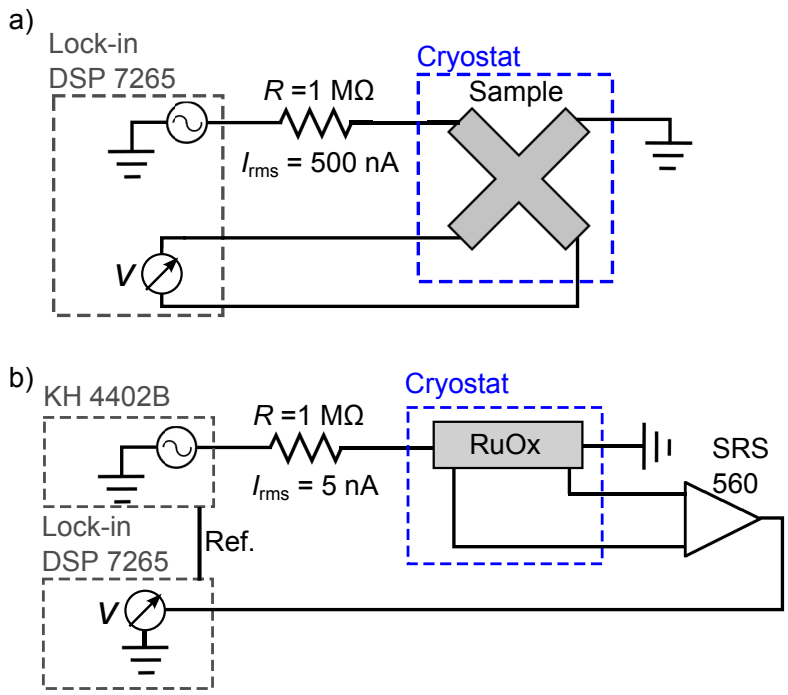

Figure 4.2: a) Schematic measurement setup for magnetoresistance measurements. b) Schematic setup for temperature measurements using the ruthenium oxide ("RuOx") thermometer.

4.5 Critical temperature and critical magnetic field measurements

The measurements of the temperature-dependent critical magnetic field and the critical temperature measurements were carried out in the Helium-3-cryostat using the same lock-in technique, as described in Sect. 4.4 for the magnetoresistance measurements and as shown in Fig. 4.2, the only difference being that a current of $I_{\mathrm{rms}} = 50\,\mathrm{nA}$ and a frequency of $f = 313\,\mathrm{Hz}$ were used for the critical magnetic field measurements. For the measurement of the critical temperature and for the temperature measurement during the critical magnetic field measurements, the temperature was measured using a ruthenium oxide thermometer (LakeShore RX-202A-AA-0.05B) calibrated between 0.04 K and 45 K. This thermometer was located directly below the chip carrier which contains the sample. The measurement setup for measuring the temperature is sketched in Fig. 4.2. For the temperature measurement an external current source (KH 4402B) was used to drive a current of 5 nA through the thermometer and the voltage at the thermometer was amplified using an SRS 560 Low Noise Voltage Preamplifier with a gain of

100 before the voltage measurement with the lock-in amplifier DSP7265. The temperatures and the error in temperature were determined using the polynomial fit coefficients which are given in the calibration report of the thermometer. Angle-dependent critical magnetic fields were measured in the flow-cryostat (Cryovac KONTI-Kryostat-IT) using the sample rotating system and a SR830 lock-in amplifier.

5 Structural and electrical properties of the ferecrystals $[(PbSe)_{1+\delta}]_1[NbSe_2]_n$

5.1 Synthesis of the ferecrystals $[(PbSe)_{1+\delta}]_m[NbSe_2]_n$

The $[(PbSe)_{1+\delta}]_m[NbSe_2]_n$ ferecrystal samples have been synthesized by Matti B. Alemayehu and Zachary Jones in the group of Prof. David C. Johnson at the Department of Chemistry, University of Oregon [18, 23]. The method used for the synthesis of the samples is called the modulated elemental reactants (MER) method [16–20, 22–27]. The first step in this method is the vacuum deposition of atomically thin alternating layers of Pb, Se and Nb onto substrates from elemental sources Pb (99.999 % purity), Nb (99.999 % purity) and Se (99.999 % purity). Lead and niobium are evaporated using electron beam guns and an effusion cell was used to evaporate Se. The deposition takes place in a high-vacuum chamber with a pressure of $p \approx 10 \times 10^{-7}$ mbar. The thickness of the deposited layers is controlled using pneumatic shutters. The first two layers deposited on the substrate are Pb and Se layers, followed by alternating layers of Nb, Se and Pb. The as-deposited (called 'precursors') layers are mainly amorphous and the sequence of the deposited layers closely resembles the sequence of layers in the desired final samples [18, 23, 194]. The deposition process ends with the deposition of Se-Nb-Se as the topmost layers. Subsequently, the samples are annealed in a nitrogen atmosphere for 1 hour at 450 °C. The calibration process for the amount of each element required during deposition and the optimal annealing temperature is described elsewhere [18, 23, 194]. The samples for the TEM investigations as well as for electrical transport measurements are from the same synthesis batches and were annealed in the same load.

Three batches of $[(PbSe)_{1+\delta}]_1[NbSe_2]_n$ samples have been synthesized. All samples for the TEM investigations were synthesized on silicon (100) substrates with a native oxide and a size of about 15 mm x 15 mm. The substrates are completely covered by ferecrystals. The samples for the electrical transport measurements were synthesized on electrically insulating fused quartz (batch 1 and 2) and on 300 nm thick silicon oxide on silicon substrates (batch 3). The substrates have the size of 10 mm x 5 mm. For batch 1 two samples with the shape of a Greek cross were deposited on each substrate. The shapes of the samples were obtained using metal shadow masks during deposition. The arms of the cross shaped samples have a width of 0.9 mm and each arm has a length of 2.2 mm. A second and

Table 5.1: Total sample thicknesses d of the ferecrystals $[(PbSe)_{1+\delta}]_m[NbSe_2]_n$ determined from X-ray reflectivity measurements by M. Alemayehu at the University of Oregon. The errors are given in parentheses.

(m,n)	Batch 1	Batch 2	Batch 3
	d (nm)	d (nm)	d (nm)
(1,1)	49(2)	49.7(2)	43.0(2)
(1,2)	51(2)	54.3(3)	37.3(2)
(1,3)	48(2)	52.1(4)	36.8(2)
(1,4)	Not synthesized.	46.5(4)	Not synthesized.
Substrate	Fused quartz	Fused quartz	300 nm SiO_2/Si

a third batch of samples have been synthesized using metal shadow masks with holes shaped as a clover leaf and a Greek cross. Such a sample is displayed as an example in Fig. 4.1. The clover leaf has a size of 0.46 mm x 0.46 mm. The Greek cross has the same dimensions as the cross described above. In the following the clover leaf shaped samples of batch 2 and 3 and the first cross of batch 1 will be referred to as 'sample A' and the Greek cross shaped sample for batch 2 and 3 and the second cross shaped sample for batch 1 will be referred to as 'sample B'. The substrate materials for the of the samples of all three batches and the total film thicknesses d are given in Table 5.1. The thicknesses were determined from X-ray reflectivity (XRR) measurements at the University of Oregon on samples of the same batch as those used for the electrical measurements. From these XRR measurements the repeat unit thicknesses c were obtained and a fit of c vs. n yielded a thickness of each $NbSe_2$ layer of $t_{NbSe_2} = 0.6336(3)$ nm and a thickness

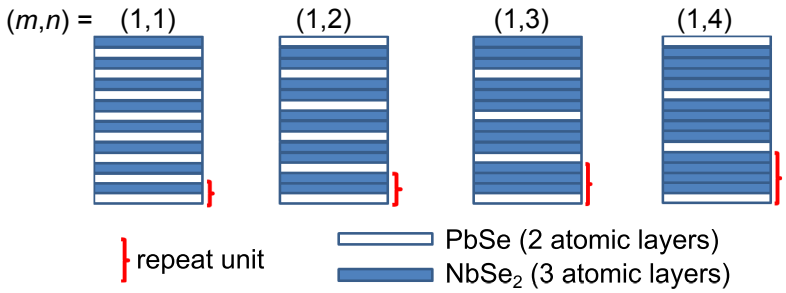

Figure 5.1: Schematic stacking sequences of the ferecrystals $[(PbSe)_{1+\delta}]_m[NbSe_2]_n$. The repeat units are stacked repeatedly up to a total sample thickness of about $d \approx 50$ nm, as given in Table 5.1.

of each PbSe layer of $t_{\mathrm{PbSe}} = 0.6097(8)$ nm. The stacking sequences of the samples prepared for the $[(\mathrm{PbSe})_{1+\delta}]_m[\mathrm{NbSe_2}]_n$ sample system are shown schematically in Fig. 5.1.

5.2 Intermediate layer formation in $[(\mathrm{PbSe})_{1+\delta}]_1[\mathrm{NbSe_2}]_n$ thin films

The crystal structure and compositional homogeneity of thin films predetermine their physical properties. Thus, to reveal the structural properties of the ferecrystals $[(\mathrm{PbSe})_{1+\delta}]_1[\mathrm{NbSe_2}]_n$, they were prepared for TEM analysis using the cross-sectional preparation technique described in Sect. 3.1. The HAADF-STEM images of the first two batches of samples $[(\mathrm{PbSe})_{1+\delta}]_1[\mathrm{NbSe_2}]_n$ revealed the presence of intermediate interfacial layers and surface layers, which do not contain the expected ferecrystal structure. The middle part of these thin film samples, however, has shown the expected 1:n stacking sequence of PbSe bilayers and $\mathrm{NbSe_2}$ single layers. In the following, different TEM specimen preparation parameters of the cross-sectional preparation technique will be discussed in order to clarify, if the intermediate layers form during the TEM specimen preparation process. Subsequently, the atomic structure and layer stacking periodicity within the undisturbed ferecrystal region will be described in dependence on the $\mathrm{NbSe_2}$ layer thickness. Finally, the chemical composition of the sample determined by energy-dispersive X-ray spectroscopy (EDXS) will be described and subsequently discussed with respect to the atomic structure of the samples.

In order to confirm the reproducibility of the synthesis and the TEM specimen preparation process, two batches of $[(\mathrm{PbSe})_{1+\delta}]_1[\mathrm{NbSe_2}]_1$ samples were synthesized using the same growth conditions (Sect. 5.1). Batches 1 and 2 were synthesized at two different dates. Fig. 5.2 shows representative HAADF-STEM images of the specimens of batch 1 and 2. Both images contain the Si substrate in the lower part of the image. The silicon oxide on top of the silicon is a few nanometers thick and appears dark in the image due to the low mean atomic number (Si: $Z = 14$, O: $Z = 8$). The ferecrystals are visible as bright film consisting of about 0.6 nm thin, alternately stacked layers of PbSe and $\mathrm{NbSe_2}$, as also visible in the high-resolution image in Fig. 5.8. The ferecrystals appear brighter than the silicon substrate due to the higher atomic numbers of the chemical elements constituting the ferecrystals (Si: $Z = 14$, Pb: $Z = 82$; Nb: $Z = 41$; Se: $Z = 34$). However, between the silicon oxide and the ferecrystals with their layered structure there is an about 12 nm thick intermediate layer with an inhomogeneous structure. This layer does not have a ferecrystalline structure and appears brighter than the ferecrystals in the images of Fig. 5.2. On top of the ferecrystals there is a similar inhomogeneous, non-ferecrystalline layer with a thickness of approximately 10 nm (surface layer). Such intermediate and surface layers would be disadvantageous for the investigation

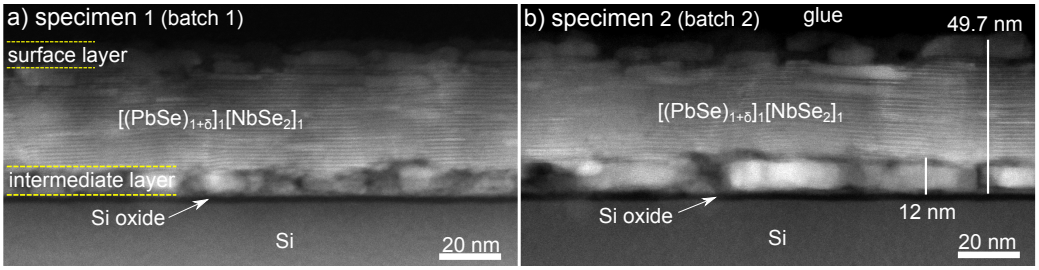

Figure 5.2: HAADF-STEM image of $[(PbSe)_{1+\delta}]_1[NbSe_2]_1$ a) specimen 1 (batch 1) and b) specimen 2 (batch 2). The film thickness of 49.7 nm has been determined by XRR.

of the electrical properties of the ferecrystals as a function of the $NbSe_2$ layer thickness, because they might act as parallel conductors in the in-plane resistivity measurements. The presence of glue above the surface layer in Fig. 5.2b shows that the ion milling has not removed the surface layers of the sample yet. The thickness of the ferecrystals of 49.7 nm was determined by XRR and is indicated in Fig. 5.2b. The XRR measurement was performed at samples of the same batch, soon after the synthesis. In the HAADF-STEM image, this thickness does not only include the ferecrystals, but it also contains the intermediate and surface layers. Both samples from both batches show similar intermediate layers. This indicates that the intermediate and surface layers observed in these specimens are not only an exception. The intermediate and surface layer extend over all specimen regions which were investigated by HAADF-STEM. An example is shown in the appendix in Fig. A.1, in which the intermediate and surface layers are visible over a range of more than 2.56 µm. These results give rise to the question whether the intermediate layers have already formed during synthesis or during the TEM specimen preparation process. Therefore, the influence of several TEM preparation parameters on the structure of the thin films has been investigated as discussed in the following.

5.3 The influence of specimen preparation parameters on the formation of intermediate layers

The influence of several TEM specimen preparation parameters of the conventional cross-section technique on the structure of the $[(PbSe)_{1+\delta}]_1[NbSe_2]_1$ samples has been investigated. In total, six specimens with different TEM specimen preparation parameters were investigated. The preparation parameters used for these specimens are summarized in Table 5.2. A more detailed overview of the preparation parameters is given in Table A.1. The HAADF-STEM images of specimens 1 and 2 of two different batches have been described in Sect. 5.2.

5.3.1 The influence of the ion milling process

Figures 5.3a, b, and c show HAADF-STEM images of $[(PbSe)_{1+\delta}]_1[NbSe_2]_1$ specimens 2, 3 and 4, respectively. These specimens have been prepared for TEM using different ion milling parameters (Table 5.2). These three specimens are from the same synthesis batch and the TEM preparation parameters used for mechanical thinning were similar. Specimen 2 was not cooled during ion milling and it shows intermediate layers brighter than the ferecrystals. Specimens 3 and 4 were cooled with liquid nitrogen (LN_2) during ion milling and they show intermediate layers which are not as bright as the ferecrystals. For specimens 2 and 3 the argon ion milling process was started with an ion energy $E_{ion} = 5\,keV$ and finished with $E_{ion} = 1.4\,keV$. In contrast, for specimen 4, the ion milling process was started

Table 5.2: TEM preparation parameters for sample $[(PbSe)_{1+\delta}]_1[NbSe_2]_1$: face-to-face gluing temperature, cooling during ion milling and ion energy used for final ion milling step.

Specimen name	**Synthesis batch**	**Gluing temperature** T_{glue} (°C)	**Cooling during ion milling**	**Ion milling energy** E_{ion} (keV)
specimen 1	1	150	not cooled	1.4
specimen 2	2	150	not cooled	1.4
specimen 3	2	150	LN_2-cooled	1.4
specimen 4	2	150	LN_2-cooled	0.2
specimen 5	2	80	LN_2-cooled	1.4
specimen 6	2	80	LN_2-cooled	1.4

with 3 keV and the final ion milling energy was $E_{\text{ion}} = 0.2$ keV. The resulting thickness of the intermediate layers is similar for all three specimens. These results suggest that the intermediate layer is not formed during ion milling, since the thickness of the intermediate layer is similar for all three sets of ion milling parameters. Consequently, the intermediate layer has been formed before the ion milling process. However, the specimen temperature during ion milling seems to influence the structure or the thickness of the intermediate layer along the electron beam direction, because the cooled specimens show darker, more continuous intermediate layers than the non-cooled specimens. In the non-cooled specimens the intermediate and surface layers show separated, brighter crystallites, suggesting that the intermediate layer might have crystallized due to the increased temperature

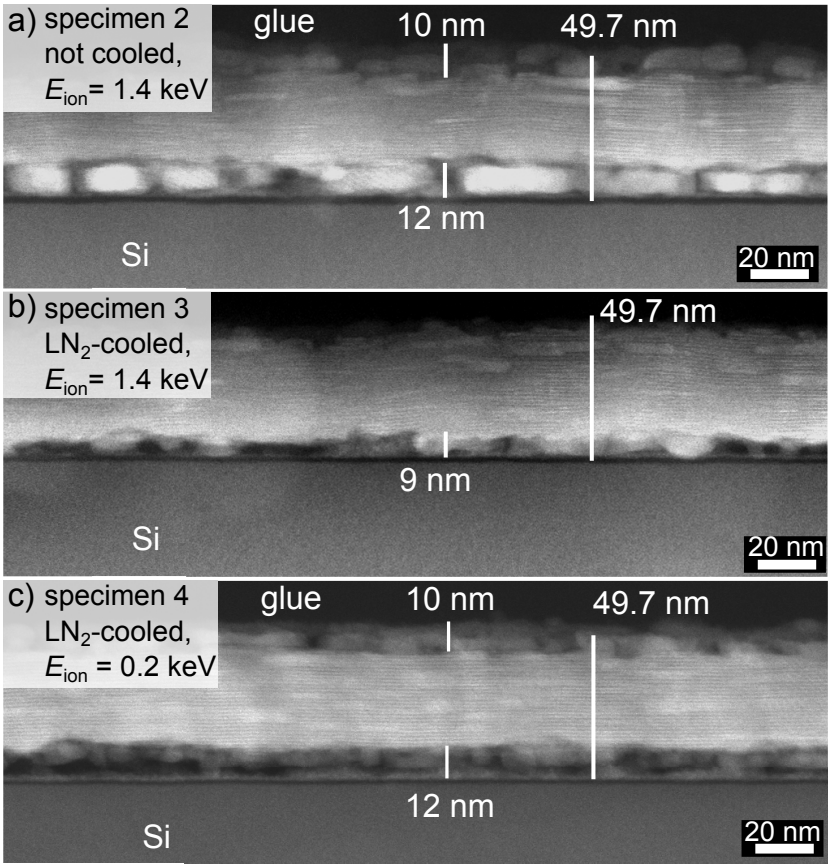

Figure 5.3: HAADF-STEM image of $[(PbSe)_{1+\delta}]_1[NbSe_2]_1$ a) specimen 2 prepared with final ion energy of 1.4 keV without cooling during ion milling, b) specimen 3 prepared with final ion energy of 1.4 keV with cooling during ion milling, c) specimen 4 prepared with final ion energy of 0.2 keV with cooling during ion milling. The film thickness of 49.7 nm has been determined by XRR.

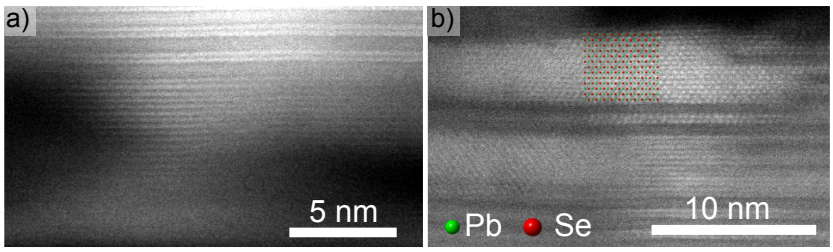

Figure 5.4: High-resolution HAADF-STEM images of a) the intermediate layer in specimen 4 (cooled during ion milling) showing lattice planes and b) the top part of specimen 2 of $[(PbSe)_{1+\delta}]_1[NbSe_2]_1$. The structure model shows PbSe according to [85], projected along the [110] direction.

during ion milling. However, the high-resolution images of the cooled specimens also exhibit lattice planes within parts of the intermediate layers. An example is shown in Fig. 5.4a. These lattice planes have a similar lattice plane distance as the distance between the PbSe bilayers, but they do not show a similar brightness as the PbSe bilayers in the adjacent ferecrystals. This might be attributed to a different channeling condition due to a different local PbSe orientation. A sample region near the surface layer of specimen 2 is displayed in Fig. 5.4b. A block of seven consecutive bilayers of PbSe oriented along PbSe[1 1 0] was identified from the HAADF-STEM image. This shows that the surface layer contains more PbSe than necessary for the intended composition. Results of an EDX analysis of the intermediate and surface layers will be shown in Sect. 5.5.

5.3.2 The influence of the gluing temperature

Another specimen preparation parameter tested for an influence on the specimen structure is the temperature used for the face-to-face gluing process. For specimen 3 this temperature was $T_{\mathrm{glue}} = 150\,^{\circ}\mathrm{C}$ while specimens 5 and 6 were prepared using $T_{\mathrm{glue}} = 80\,^{\circ}\mathrm{C}$. The resulting HAADF-STEM images are shown in Fig. 5.5. For specimen 5 the HAADF-STEM image shows less thick intermediate layers with a thickness of about 6 nm, whereas for specimen 6, which was prepared using the same method it shows a thickness of 9 nm, similar to specimen 3 which was glued at 150 °C. Obviously, there is no strong influence of the glue temperature, because intermediate layers are observed for both temperatures. The different thicknesses of the intermediate layer can be attributed to spacial variations initially present in the samples.

In conclusion, the optimum TEM specimen preparation parameters for the ferecrystals are those using a low ion energy and cooling (0.2 keV) during ion milling, however, for all tested parameters intermediate and surface layers are present.

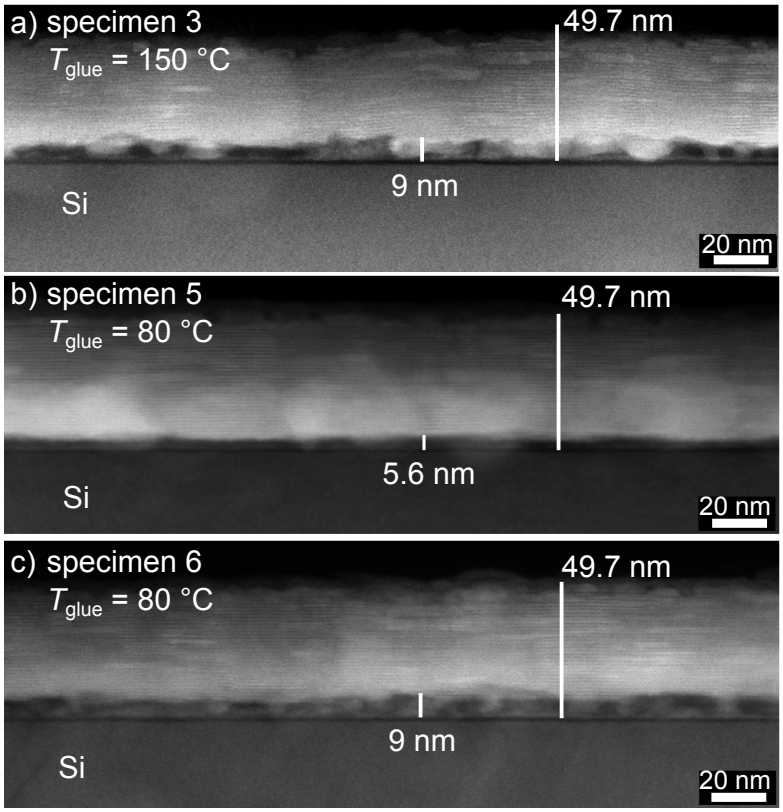

Figure 5.5: HAADF-STEM image of $[(PbSe)_{1+\delta}]_1[NbSe_2]_1$ a) specimen 3 prepared with a face-to-face-gluing temperature of $T_{glue} = 150\,°C$ b) and c) specimens 5 and 6 prepared with a face-to-face-gluing temperature of $T_{glue} = 80\,°C$. All specimens were cooled during ion milling and the final ion milling energy was $E_{ion} = 1.4\,keV$. The film thickness 49.7 nm has been determined by XRR.

5.3.3 The influence of the substrate material

For the samples of the type $[(PbSe)_{1+\delta}]_1[NbSe_2]_2$ three specimens were investigated by HAADF-STEM (Fig. 5.6). Specimens 1 and 2 are from two different synthesis batches and were both synthesized on silicon substrates using the same synthesis parameters. These two specimens were prepared to confirm the reproducibility of the synthesis and TEM preparation processes for this material. The HAADF-STEM images in Fig. 5.6 show that the specimens of the type $[(PbSe)_{1+\delta}]_1[NbSe_2]_2$ exhibit very thin intermediate layers with a thickness of about 3 nm to 4 nm. To exclude a possible influence of the substrate material on the layer structure, an additional specimen on quartz substrate was prepared for TEM analysis (specimen 3). A fused quartz substrate is also used for the samples for the electrical measurements. The HAADF-STEM images shown in Fig. 5.6

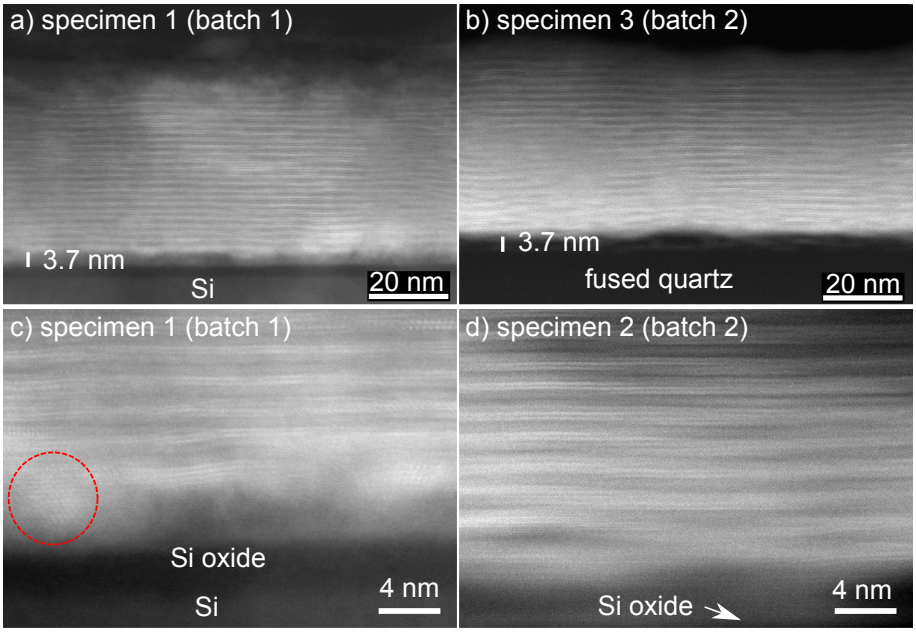

Figure 5.6: HAADF-STEM images of $[(PbSe)_{1+\delta}]_1[NbSe_2]_2$ a) specimen 1 from batch 1 on Si (100) with native oxide b) specimen 3 from batch 2 on fused quartz. c) Specimen 1, batch 1, d) specimen 2, batch 2. A red circle indicates a sample area with lattice planes in the intermediate layers.

yield similar results for the three specimens, which suggests that the synthesis of these samples is reproducible and that ferecrystals with a similar structure can be formed on quartz as well as on silicon substrates. The HAADF-STEM images of the interface between substrate and ferecrystals for specimens 1 and 2 in Fig. 5.6c and d, show that at some sample areas lattice planes are found in the intermediate layer, which do not agree with the intended ferecrystal structure.

5.4 Structural peculiarities of $[(PbSe)_{1+\delta}]_1[NbSe_2]_n$ ferecrystals

5.4.1 $[(PbSe)_{1+\delta}]_1[NbSe_2]_1$ ferecrystals

Figure 5.7 shows a HAADF-STEM image of $[(PbSe)_{1+\delta}]_1[NbSe_2]_1$, specimen 4. This specimen has been prepared with the lowest ion milling energy of $E_{\text{ion}} = 0.2\,\text{keV}$. In the center of the thin film, ferecrystals are visible. Between the silicon oxide and the ferecrystals there is an intermediate layer. In the following, the structure and homogeneity of the ferecrystalline part of the sample will be discussed. In the ferecrystals there are column-like areas, which are brighter than the neighboring sample areas to the left and right (also see Fig. A.2). These intensity changes in the HAADF-STEM images can be due to a slight change in the crystallographic orientation of the layers in one sample area with respect to another. The columns mostly expand throughout the whole ferecrystal thickness and have an in-plane width ranging from about 5 nm to 50 nm. Figure 5.8 contains two high-resolution images of $[(PbSe)_{1+\delta}]_1[NbSe_2]_1$. In Fig. 5.8a the layer stacking sequence corresponds to the initially intended stacking sequence: one bilayer of PbSe (bright in the HAADF-STEM image) is alternately stacked with one monolayer of $NbSe_2$ (darker in the HAADF-STEM image). Each $NbSe_2$ monolayer consists of three atomic monolayers: In the center there is a Nb monolayer, visible as a bright line and it is sandwiched between two Se layers, which appear dark in the HAADF-STEM image. A comparison to the structure models of PbSe and $NbSe_2$, displayed in Fig. 2.1, shows that the c-axes of PbSe and $NbSe_2$ are both parallel to the stacking direction of the layers in this sample. Single atomic columns are not visible in Fig. 5.8a, which results either from the fact that by chance none of the PbSe layers is oriented along a low-indexed zone axis, or, the sample region is thicker than the in-plane grain size and therefore several PbSe orientations overlap. In Fig. 5.8b two PbSe layers are projected along PbSe[1 1 0].

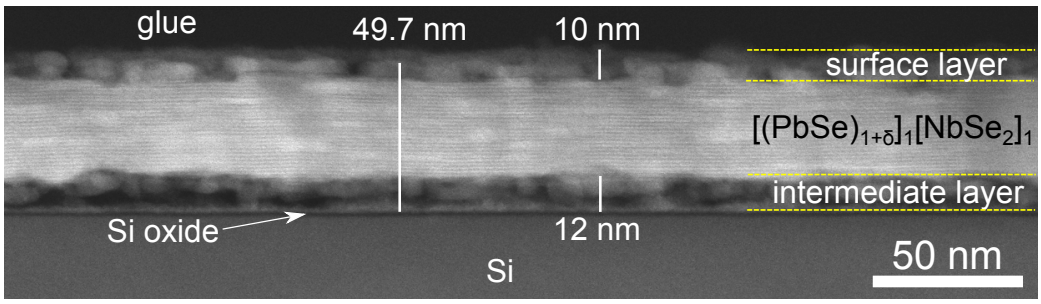

Figure 5.7: HAADF-STEM image of $[(PbSe)_{1+\delta}]_1[NbSe_2]_1$, specimen 4 (batch 2). The thickness 49.7 nm has been determined by X-ray diffraction.

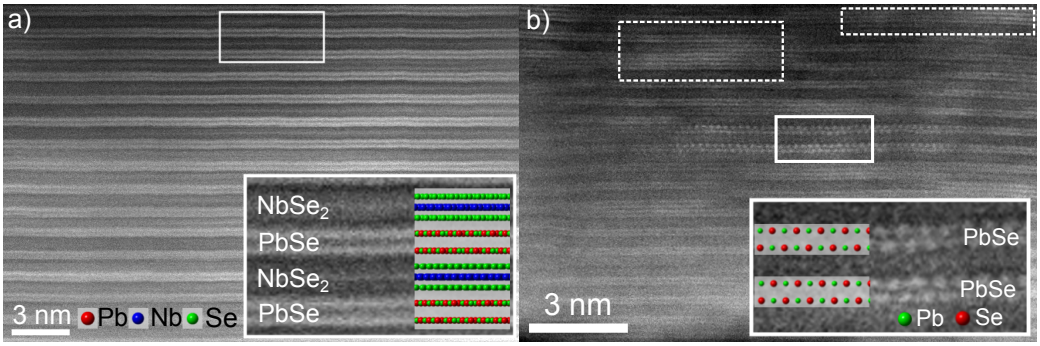

Figure 5.8: a) HAADF-STEM image of sample $[(PbSe)_{1+\delta}]_1[NbSe_2]_1$, specimen 4. Structure models of PbSe and $NbSe_2$ in the inset indicate arbitrary in-plane orientations of PbSe and $NbSe_2$, with the *c*-axes parallel to the stacking direction. b) High-resolution HAADF-STEM image of sample $[(PbSe)_{1+\delta}]_1[NbSe_2]_1$, specimen 3. Two layers in the framed area show a projection along PbSe[1 1 0]. The areas indicated by dashed boxes show stacking defects.

The adjacent PbSe layers do not show a similar in-plane atomic resolution, which suggests that they are rotated differently around the *c*-axis, proving the presence of turbostratic disorder of the ferecrystals. Figure 5.8 b) also shows that the sample contains areas in which the stacking sequence is not preserved (dashed boxes). These areas contain PbSe bilayers in place of $NbSe_2$ layers. The thickness of a PbSe bilayer is similar to the thickness of a $NbSe_2$ layer ($\approx 0.6\,\mathrm{nm}$). Therefore, the layers around these stacking defects are not much bent and the intended stacking sequence continues in the layers adjacent to these defects. This is also visible in Fig. 5.9a, which contains a HAADF-STEM image of specimen 4, which has been prepared with the lowest ion milling energies. It shows that a large part of the ferecrystal contains these defects. The fraction of this defect type in the projected ferecrystal area has been estimated as 13 % by summing the stacking defect area in the total projected ferecrystal area of about $4000\,\mathrm{nm}^2$ shown in Fig. A.4. A third batch of $[(PbSe)_{1+\delta}]_1[NbSe_2]_n$ ferecrystals with $n = 1$ has been synthesized showing no intermediate layers and no stacking errors and will be discussed in Sect. 5.4.5.

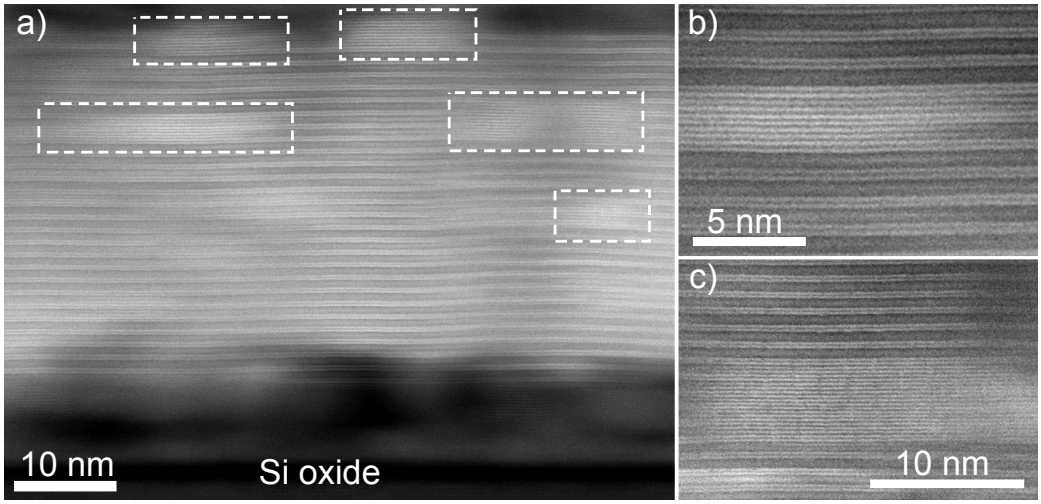

Figure 5.9: HAADF-STEM of sample $[(PbSe)_{1+\delta}]_1[NbSe_2]_1$ a) specimen 4 - defects in stacking sequence are indicated by dashed boxes, b) and c) show magnified parts of the image, which contain stacking defects.

5.4.2 $[(PbSe)_{1+\delta}]_1[NbSe_2]_2$ ferecrystals

Fig. 5.10 shows two high-resolution HAADF-STEM images of two specimens of $[(PbSe)_{1+\delta}]_1[NbSe_2]_2$ ferecrystals. The ideal stacking sequence for the sample system $[(PbSe)_{1+\delta}]_1[NbSe_2]_2$ is one PbSe bilayer alternating with two $NbSe_2$ layers. In between the two $NbSe_2$ layers there is a van der Waals gap visible as dark line in the HAADF-STEM images. The stacking sequence is mostly as expected. However several defects are also present, which are indicated by dashed boxes. Figure 5.11 shows magnified images of the areas marked by the red rectangles in Fig. 5.10a. The intended stacking sequence is not preserved here: there is only one layer of $NbSe_2$ instead of two $NbSe_2$ layers alternating with a PbSe layer. The orientation relation between several of the layers in Fig. 5.11b is similar to the orientation relations found in MLCs (Fig. 2.2). However, turbostratic disorder is also visible, as some of the adjacent PbSe layers show a different orientation around the *c*-axis.

5.4.3 $[(PbSe)_{1+\delta}]_1[NbSe_2]_3$ ferecrystals

For the ferecrystals of type $[(PbSe)_{1+\delta}]_1[NbSe_2]_3$ two specimens of two synthesis batches were investigated by HAADF-STEM. The results are shown in Fig. 5.12. The specimen of batch 1 shows many volume defects throughout the area observed by HAADF-STEM, which comprises a length of at least 2 µm along the sample surface. The specimen of batch 2 does not show these volume defects. The film

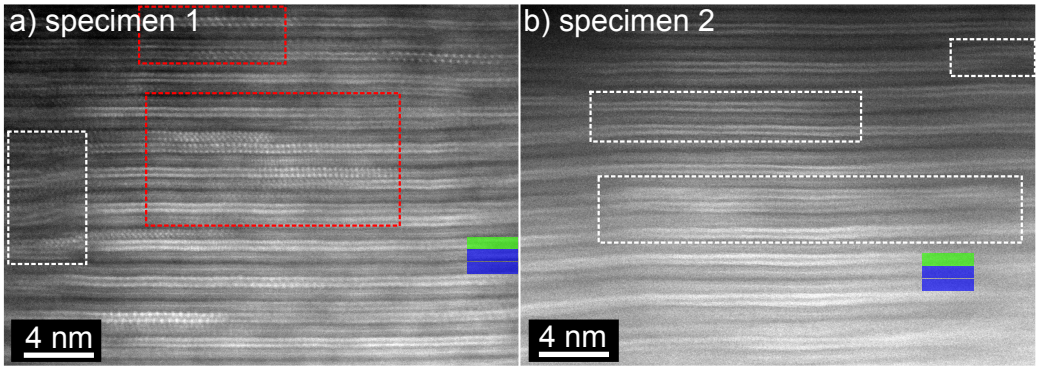

Figure 5.10: High-resolution HAADF-STEM images of sample $[(PbSe)_{1+\delta}]_1[NbSe_2]_2$ a) specimen 1, batch 1 and b) specimen 2, batch 2. Areas with stacking defects are indicated by dashed boxes. The green and the blue rectangles indicated PbSe bilayers and $NbSe_2$ layers, respectively. The areas in the red boxes are shown magnified in Fig. 5.11.

thickness of 52.1 nm was determined by XRR. A possible explanation for the appearance of the defects could be an aging of the sample, because for specimen 1 there were 16 month between the synthesis and the face-to-face-gluing, whereas for specimen 2 there were only 9 month between synthesis and the beginning of TEM preparation. However, the HAADF-STEM image in Fig. 5.12c shows that the ferecrystal layers are crystalline and bent around the dark defect features in the images. This suggests that the individual layers were deposited on the already existing non-planar surface. Since in the HAADF-STEM image the volume defects are dark in the center, they could be voids. A chemical analysis by EDXS shown in Sect. 5.5 confirms this. Figure 5.13 shows a high-resolution HAADF-STEM image of specimen 2 (batch 2). This specimen does not exhibit the volume defects. The intended stacking sequence of one PbSe bilayer alternating with three $NbSe_2$ monolayers can be seen in the HAADF-STEM image, except for some stacking defects, which are indicated by dashed boxes. A third batch of $[(PbSe)_{1+\delta}]_1[NbSe_2]_n$ ferecrystals with $n = 3$ has been synthesized showing no intermediate layers and no stacking defects and will be discussed in Sect. 5.4.5.

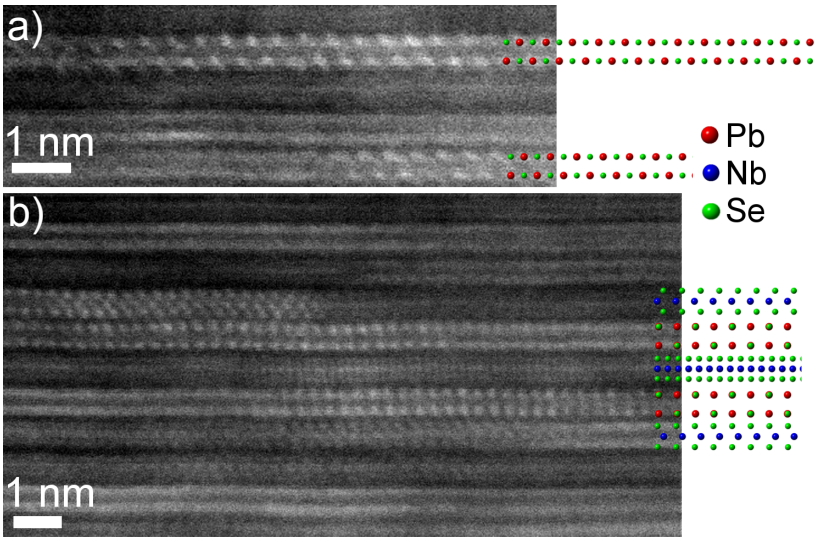

Figure 5.11: a) and b) High-resolution HAADF-STEM images of sample $[(PbSe)_{1+\delta}]_1[NbSe_2]_2$ with structure models for bulk binary PbSe [85] and $NbSe_2$ [82]. Both figures contain stacking defects in which one layer of PbSe alternates with only one layer of $NbSe_2$ instead of two layers of $NbSe_2$ nominally set during the synthesis.

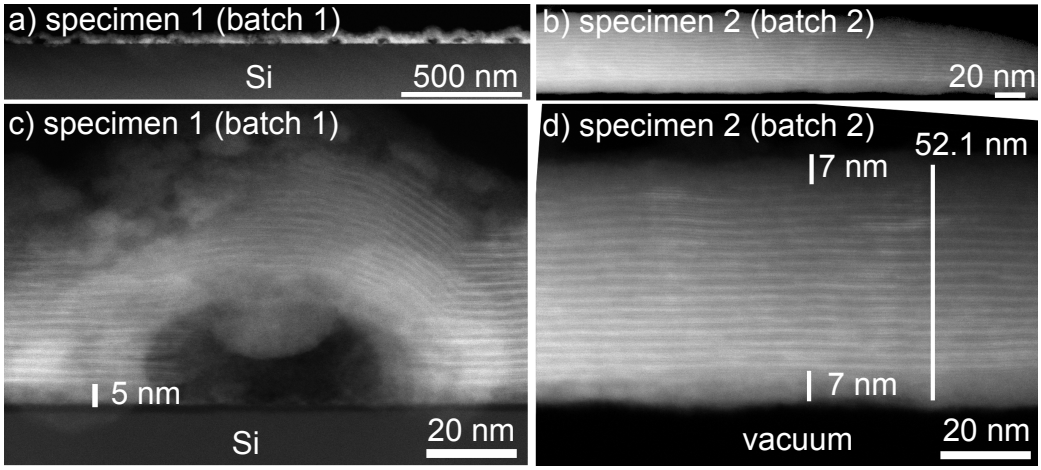

Figure 5.12: HAADF-STEM images of sample $[(PbSe)_{1+\delta}]_1[NbSe_2]_3$ a) specimen 1 (batch 1) showing volume defects. b) specimen 2 (batch 2) showing no volume defects and c) and d) magnified parts of the images in a) and b).

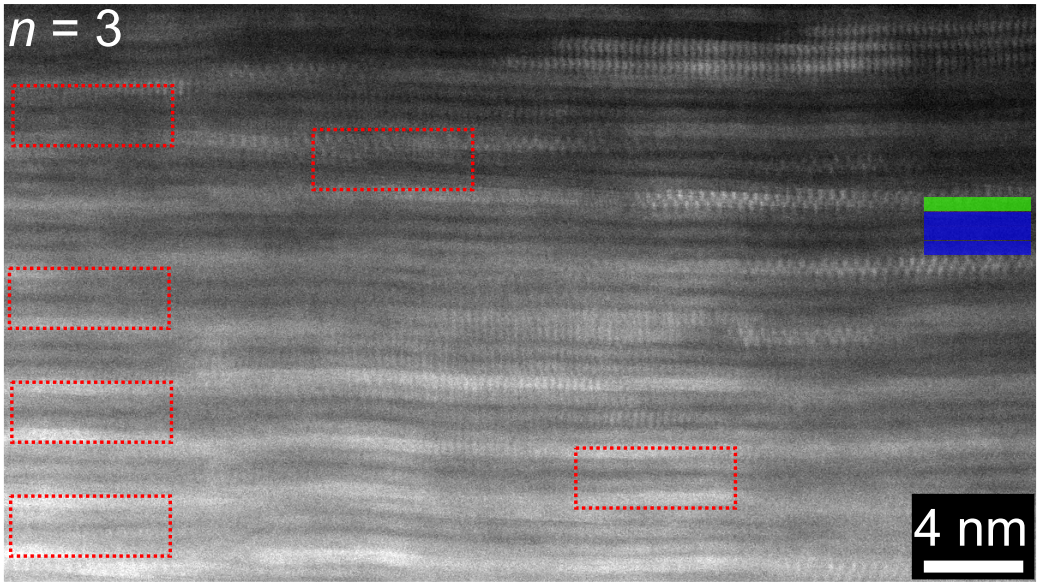

Figure 5.13: HAADF-STEM image of sample $[(PbSe)_{1+\delta}]_1[NbSe_2]_3$ specimen 2, batch 2. The green and the blue rectangles indicate PbSe bilayers and $NbSe_2$ monolayers, respectively. Red boxed areas indicate stacking defects. The film thickness of 52.1 nm has been determined by X-ray diffraction.

5.4.4 $[(PbSe)_{1+\delta}]_1[NbSe_2]_4$ ferecrystals

HAADF-STEM images of $[(PbSe)_{1+\delta}]_1[NbSe_2]_4$ are shown in Fig. 5.14. The ferecrystal sample does not show layers with clear interfaces. A HAADF-STEM image of the sample taken at a higher magnification in Fig. 5.14 b shows that the lattice planes of the silicon substrate are resolved, whereas ferecrystal lattice planes are not found. Since the viewing direction is along the Si[1 1 0] direction, the ferecrystals in this image should be projected perpendicularly to the stacking direction, i.e. along the layer planes. The fact that the individual layers are not resolved at these imaging conditions indicates that the PbSe and $NbSe_2$ layers are not fully crystallized. It has been noticed that the silicon substrate surface normal does not exactly agree with the Si [0 0 1] direction, but it is inclined by a few degrees, indicating a substrate offcut. However, for the applied synthesis process the substrate should not influence the layer sequence and crystallinity significantly, as has been shown for the $[(PbSe)_{1+\delta}]_1[NbSe_2]_2$ layers grown on Si and fused quartz (Fig. 5.6). This sample also shows intermediate layers. Since this sample is not fully crystallized, this suggests that the intermediate layers were already present before the crystallization of the ferercystals during annealing.

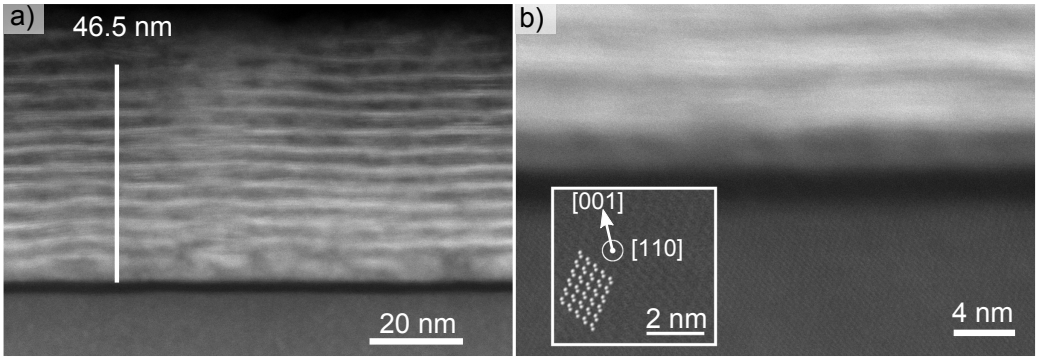

Figure 5.14: HAADF-STEM image of sample $[(PbSe)_{1+\delta}]_1[NbSe_2]_4$. a) Overview image. The film thickness of 46.5 nm was determined by XRR. b) Magnified image of the interface between substrate and sample. The inset shows a magnification of the substrate.

5.4.5 Focused ion beam prepared samples of a third batch

A third batch of $[(PbSe)_{1+\delta}]_1[NbSe_2]_n$ ferecrystal samples with $n = 1$ and 3 has been synthesized (batch 3) using the same nominal synthesis process as for batches 1 and 2. TEM specimens of this batch were prepared and investigated using HAADF-STEM by M. Alemayehu at the University of Oregon. For the TEM specimen preparation a FIB technique was used. Overview HAADF-STEM images of the samples with $n = 1$ and 3 of batch 3 are shown in Fig. 5.15. These images show no intermediate layers. At the top of the samples a disturbed surface layer is visible. The top of the samples might be preferentially damaged by the ion beam. High-resolution HAADF-STEM images of these samples are displayed in Fig. 5.16. They show that the ferecrystal stacking sequences are as expected. It is not clear

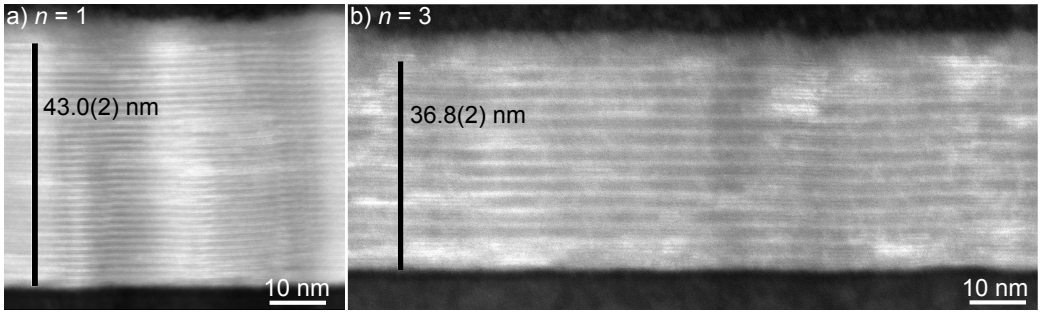

Figure 5.15: Overview HAADF-STEM images of $[(PbSe)_{1+\delta}]_1[NbSe_2]_n$ (batch 3) prepared by FIB (raw data by Matti B. Alemayehu, University of Oregon) for a) $n = 1$ and b) $n = 3$. The substrate is 300 nm silicon oxide on silicon.

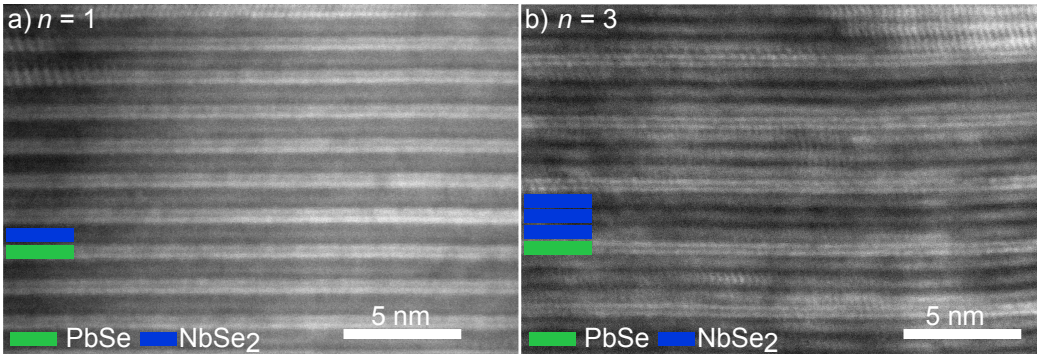

Figure 5.16: High-resolution HAADF-STEM images of $[(PbSe)_{1+\delta}]_1[NbSe_2]_n$ ferecrystals (batch 3) with a) $n = 1$ and b) $n = 3$ prepared by FIB (raw data by Matti B. Alemayehu, group of Prof. D. C. Johnson, University of Oregon).

whether the absence of intermediate layers in batch 3 is due to the FIB technique or some unintentional differences in the synthesis process. The nominal synthesis parameters for deposition of the elements and annealing were the same for batch 3 as for batches 1 and 2. Usually the FIB technique causes more damage of the sample than the conventional technique using grinding, polishing and ion milling at low energies.

5.5 Compositional analysis of $[(PbSe)_{1+\delta}]_1[NbSe_2]_n$ films

5.5.1 $[(PbSe)_{1+\delta}]_1[NbSe_2]_1$ ferecrystals

An EDXS hypermap was obtained from specimen 4 of $[(PbSe)_{1+\delta}]_1[NbSe_2]_1$, in which EDX spectra were measured simultaneously with the HAADF-STEM signal at each image point. The resulting HAADF-STEM image and the EDXS maps are shown in Fig. 5.17. Dashed lines indicate the interface between the silicon oxide and the intermediate layer and between the ferecrystals and the surface layer. As expected, the oxygen concentration is increased in the silicon oxide layer. Furthermore, the oxygen concentration is increased in the intermediate layer region and in the surface layer compared to the rest of the specimen. When comparing the elemental distributions of Nb, Se and Pb, one finds that Nb reaches down to the interface between the intermediate layer and the silicon oxide layer (dashed white line), whereas the Pb and especially the Se content drop before. The Nb content seems to be approximately constant throughout the film, including the surface layer, whereas the Se and Pb concentration are reduced in the surface layer. EDX spectra for different areas of the specimen are shown in Fig. 5.18a and b. The areas from which the spectra are obtained are marked by colored rectangles in the HAADF-STEM images shown in the insets. Within the intermediate layer,

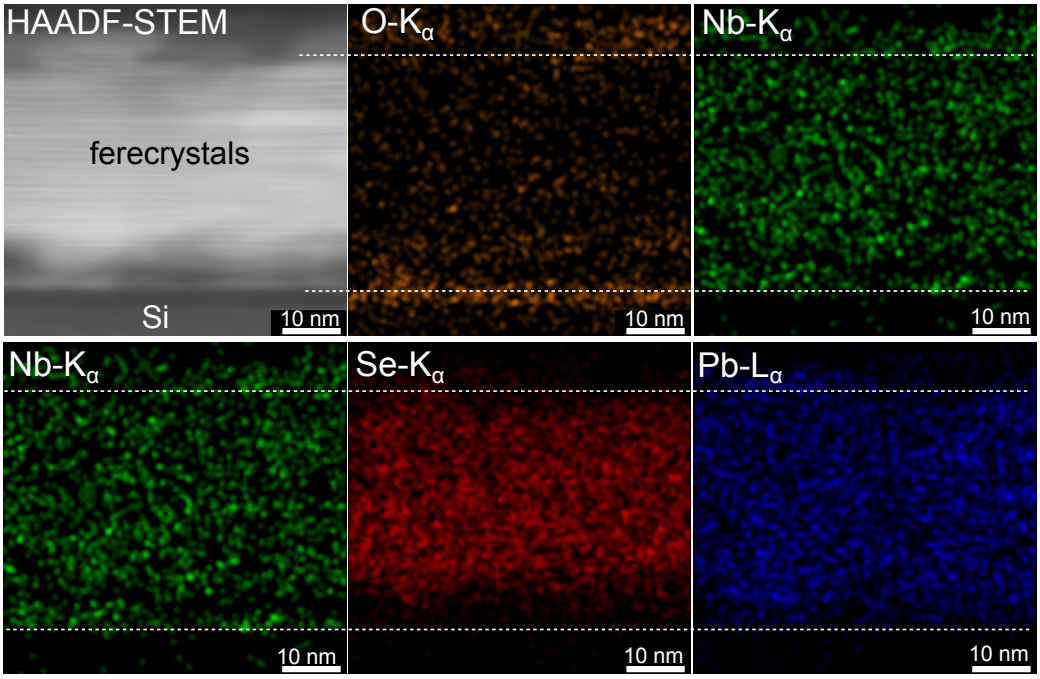

Figure 5.17: EDX maps of $[(PbSe)_{1+\delta}]_1[NbSe_2]_1$, specimen 4. The figures show the HAADF-STEM image and the simultaneously measured EDXS maps O, Nb, Se and Pb. The dashed lines indicate the interfaces between silicon oxide and intermediate layer as well as between the ferecrystals and surface layer.

ferecrystals and surface layer the EDXS spectra acquired for each image pixel were summed up and the background (Bremsstrahlung) was subtracted. The final spectra are shown in Figs. 5.18a and b. The spectra displayed in black originate from the ferecrystals in the center of the specimen, where the stacking sequence of PbSe and $NbSe_2$ is mostly as expected. In order to compare the spectra of the ferecrystals in the center of the thin film to the spectra of the intermediate layer, the spectrum of the intermediate layers shown in Fig. 5.18a has been multiplied by a factor of 4.5, so that the heights of the niobium peaks are approximately similar for both spectra. Similarly, this was done for the spectrum of the surface layer in Fig. 5.18b. The peaks visible in the EDX spectra can all be assigned to Pb, Nb, Se, O, C and Cu. Cu and C- contaminations are typically present in TEM specimens due to the TEM specimen preparation process. Consequently, these signals will be considered as spurious X-rays and will not be taken into account for compositional analysis of the specimens. The spectra in Fig. 5.18a show that in the intermediate layer the ratios Se:Nb and Pb:Nb are both lower than in the ferecrystal layers. Furthermore, the O:Nb ratio is increased in the intermediate layer compared to the ferecrystals. The increased oxygen peak intensity in the

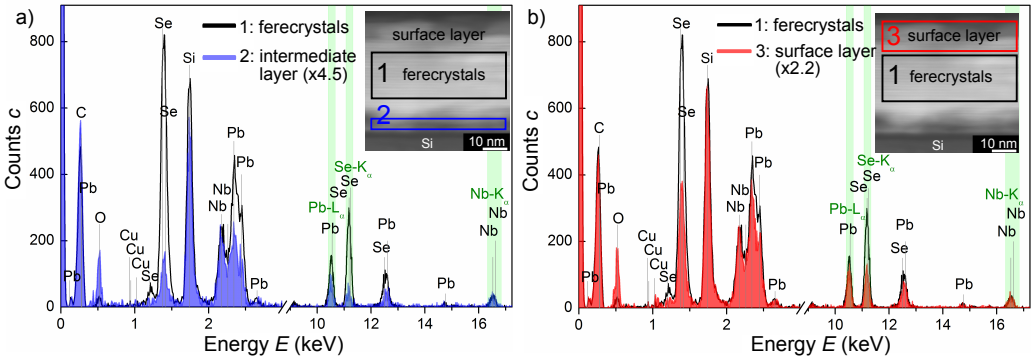

Figure 5.18: EDX spectra of $[(PbSe)_{1+\delta}]_1[NbSe_2]_1$, specimen 4. The specimen areas from which the spectra originate are marked by colored rectangles in the HAADF-STEM images in the insets. The spectra of the ferecrystal layers are displayed in black. a) The spectrum of the intermediate layer is displayed in blue; b) the spectrum of the surface layer is displayed in red. The energy ranges used for quantitative analysis are highlighted in green.

intermediate layer, however, could also be an artifact due to beam broadening in the specimen and thus detecting signals from the adjacent silicon oxide layer. The spectra in Fig. 5.18b show that the O:Nb ratio is also increased in the surface layer, which could be due to oxidation of the sample surface during the time between synthesis and TEM specimen preparation, when the specimen was stored in air. This result suggests that oxidation of the intermediate layer at the interface between SiO_2/Si substrate and ferecrystal layers can also be possible. The Se:Nb ratio is also reduced in the surface layer compared to the ferecrystals. Selenium has a high vapor pressure compared to Sn and Nb [195] and could possibly evaporate from the sample surface. The Pb:Nb ratio in the surface layer is similar as in the ferecrystals. A quantitative analysis of the spectra in Fig. 5.18 was carried out using theoretical Cliff-Lorimer factors. For this analysis the K-series of Nb ($E \approx 16.5$ keV), the K-series of Se ($E \approx 11.2$ keV), the K-series of O ($E \approx 0.5$ keV) and the L-series of Pb ($E \approx 10.5$ keV) were used. These peak positions are indicated in green in the spectra in Fig. 5.18. Table 5.3 shows the resulting chemical compositions of the different specimen regions, i.e. the ferecrystals (center of the thin film), the intermediate layer and the surface layer. The composition obtained for the ferecrystals is comparable with the composition of an ideal MLC with the formula $[(PbSe)_{1.10}]_1[NbSe_2]_1$. Table 5.3 confirms the results of the visual inspection of the EDX spectra: in the intermediate and the surface layer the selenium content is significantly reduced, whereas the oxygen content is significantly increased in comparison to the selenium and oxygen content in the ferecrystals.

Table 5.3: Composition of the different specimen regions of $[(PbSe)_{1+\delta}]_1[NbSe_2]_1$, specimen 4, determined from the EDX spectra in Fig. 5.18. The errors given in parenthesis are the 3σ errors. The chemical composition of an ideal misfit layer compound (MLC) $[(PbSe)_{1.10}]_1[NbSe_2]_1$ as described in [40] is also given for comparison.

Element	Ferecrystals	Intermediate layer	Surface layer	Ideal MLCs ($\delta = 0.1$)[40]
	at.%	at.%	at.%	at.%
Nb	17(3)	23(7)	19(4)	19.2
Se	56(6)	13(4)	26(4)	59.6
Pb	21(7)	16(6)	18(6)	21.2
O	6(2)	47(12)	36(7)	0

5.5.2 $[(PbSe)_{1+\delta}]_1[NbSe_2]_n$ ferecrystals with $n = 2$ and 3

Similar as for sample $n = 1$, the chemical composition of the central specimen area of the samples $n = 2$ and 3 of batch 2 of the ferecrystals agrees well with the composition of the analogous ideal MLCs. Near the substrate and in the surface layer for $n = 2$ and 3 the oxygen content is increased and the selenium content is decreased (Figs. A.5-A.9 and Tables A.6 and A.7).

A sample of batch 1 of $[(PbSe)_{1+\delta}]_1[NbSe_2]_3$ has shown large volume defects in the HAADF-STEM images. A HAADF-STEM image and EDXS maps of a specimen region around such a volume defect feature are shown in Fig. 5.19. In

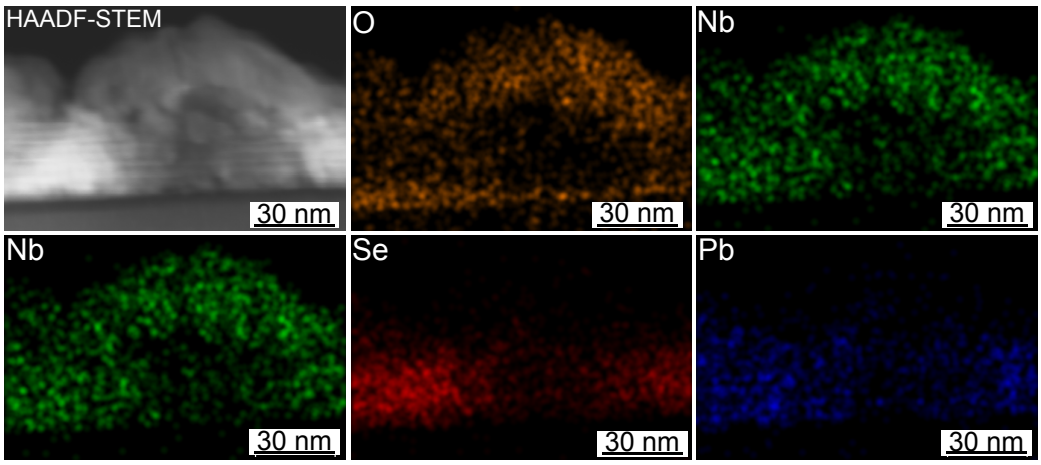

Figure 5.19: HAADF-STEM and EDXS maps of $[(PbSe)_{1+\delta}]_1[NbSe_2]_3$, specimen 1 (batch 1).

the defect region, which is dark in the HAADF-STEM image, the concentrations of O, Nb, Se and Pb are reduced compared to their concentrations in the rest of the specimen. Above the defect there is a non-layered grey area visible in this HAADF-STEM image. In this area the concentrations of Pb and Se are strongly reduced, only Nb and O are present. The total decrease in X-ray intensity inside this volume defect indicates that these volume defects are large voids. The formation of these voids is unclear. The possibility that they are due to aging can be excluded because around some of these voids, layered ferecrystals are observed (Fig. 5.12). The voids could potentially originate from possible droplets of some liquid material, which might have been initially present at the substrate surface and evaporated during the synthesis process. Based on these results, the samples $n = 3$ of batch 1 have been excluded from further discussion.

5.6 Discussion of the structural properties of the ferecrystals $[(PbSe)_{1+\delta}]_1[NbSe_2]_n$

For the first two batches of $[(PbSe)_{1+\delta}]_1[NbSe_2]_n$, the TEM analysis revealed the presence of non-layered intermediate layers between the ferecrystals and the substrate, as well as non-layered top layers at the surface of the thin film sample. A third batch of samples, prepared by FIB, did not show such defects. However, the origin of the absence of the intermediate layers in batch 3 is unclear. The intermediate and top layers differ in their structure and chemical composition from the ferecrystals in the center of the thin films. For the investigation of the electrical properties of the ferecrystals these intermediate and top layers are undesirable, because in the in-plane electrical transport measurements they might lead to unwanted currents parallel to the ferecrystal layers. The intermediate and top layers have different thicknesses and chemical compositions for the samples $n = 1, 2$ and 3. The intermediate and top layers are thickest for the samples with $n = 1$, where they are up to 12 nm and 10 nm thick, respectively, which is in total almost half of the film thickness. Therefore, the presence of the intermediate and top layers would make an unambiguous identification of the influence of the thickness of the $NbSe_2$ layers on the electrical properties impossible.

The intermediate and top layers can either form (1) during the synthesis process of the samples, (2) during the aging of the samples between synthesis and TEM analysis, or (3) during the TEM specimen preparation process.

1. **Synthesis:** For the synthesis process, the chemical composition and the annealing temperature have been optimized using electron probe microanalysis and X-ray diffraction [18, 23]. To confirm the reproducibility of the synthesis and the TEM specimen preparation process, two batches of $[(PbSe)_{1+\delta}]_1[NbSe_2]_n$ samples have been prepared and both batches have shown similar thicknesses of the intermediate layers and defect densities in

the center of the thin films. Therefore, the synthesis and TEM preparation processes of these samples have been shown to be reproducible. The HAADF-STEM images of sample $n = 4$ showed that this sample is not fully crystallized. However, this sample also shows intermediate layers. This suggests that, assuming the intermediate layer is not due to aging or specimen preparation (see below), it is formed during the deposition of the precursors or in the beginning of the annealing process, before the crystallization of the ferecrystals is completed. The third batch of samples which was prepared for TEM using a FIB technique did not show intermediate layers, despite the similar synthesis parameters. Usually, using a FIB preparation technique instead of the conventional cross-sectional preparation method used for the other samples, is more invasive because higher ion energies are used for the FIB technique. Therefore, the absence of intermediate layers in the FIB prepared samples is more likely due to differences in the sample synthesis process compared to the samples of the other batches. The samples of batch 3 have been synthesized on 300 nm silicon oxide on silicon in contrast to batch 1 and 2 which have been synthesized on native oxide on silicon. However, the influence of the substrate type (silicon or fused quartz) on the structure of the thin films was investigated for sample $n = 2$ and no significant influence of the substrate material on the crystal structure of the samples was found.

2. **Aging:** An influence of aging of the samples between synthesis and TEM specimen preparation cannot be excluded, because it was not possible to prepare all specimens at the same time. However, for the two batches of samples investigated for $n = 1$ and 2 there were different periods of time between synthesis and TEM preparation (for $n = 1$ 22 months for batch 1 and 10 month for batch 2 and for $n = 2$ 11 month for batch 1 and 14 months for batch 2) and both batches showed similar results. This suggests that aging does not have a significant influence on the structure of the thin films.

3. **TEM specimen preparation:** The influence of several TEM preparation parameters on the formation of the intermediate and top layers has been studied for sample $n = 1$. This sample type showed the thickest intermediate and top layers. It can be concluded that neither the specimen temperature during ion milling ($T \gtrsim 77\,\mathrm{K} - 300\,\mathrm{K}$), nor the ion energy $0.2\,\mathrm{keV} - 1.4\,\mathrm{keV}$), nor the face-to-face gluing temperature (80 °C-150 °C) have an influence on the thickness of the intermediate layers. However, with a reduced specimen temperature during ion milling and a reduced ion energy, the intermediate layers appear less bright in the HAADF-STEM images and do not show separated crystalline blocks as for higher temperatures and ion energies. This finding suggests that the intermediate layers were present before the TEM

preparation, and that high temperatures and increased ion energies during the specimen preparation for TEM cause a change in their crystal structure and composition. A third batch of $[(PbSe)_{1+\delta}]_1[NbSe_2]_n$ samples was synthesized and this batch showed no intermediate or surface layers, although the samples have been prepared using a more invasive TEM preparation method.

The observed results lead to the conclusion that the intermediate and top layers have probably been formed during synthesis, before the crystallization of the ferecrystals was completed. The reduced Se concentrations in the intermediate layers could be a result of a lack of Se during deposition of the first precursor layers. The decreased selenium content in the surface layers might be due to evaporation from the sample after deposition. Selenium has a relatively high vapor pressure, wile that of Sn and Nb are negligibly small [195]. Therefore, the selenium is susceptible for evaporation from the sample. In this case the excess Pb atoms might be incorporated in the upper layers disturbing the ideal stacking sequence of the ferecrystals. This might lead to the typical stacking defects in which PbSe layers replace a layer of $NbSe_2$, as shown e. g. in Fig. 5.9. Annealing of the samples in an atmosphere containing additional Se vapor might improve the sample quality.

The analysis of the distribution of the oxygen concentration showed increased oxygen values in the intermediate and top layers of the sample systems $n = 1, 2$ and 3. Since the samples were synthesized in high vacuum ($p \approx 7 \cdot 10^{-8}$ mbar), the oxidation at the surface must take place after deposition of the layers. The increased oxygen content near the substrate could either be an artifact of the EDXS method (e. g. the electron beam broadening leads to X-ray emission from the silicon oxide), or oxygen from the substrate surface diffused into the ferecrystals during or after synthesis. It cannot be excluded that the TEM specimens might have oxidized after preparation preferentially at the interface and surface layers.

In the intermediate and surface layers the Se and Pb concentrations are reduced, the oxygen content is increased and the niobium content is unchanged. According to these results NbO_x might have formed in the intermediate or surface layers. However, the intermediate layers appear brighter than the ferecrystals when the specimen was not cooled during ion milling or if high ion energies were used. This would be unlikely if the intermediate layers were niobium oxide layers, which would tend to appear darker than the ferecrystal layers due to the low atomic number of oxygen. But potentially, special channeling conditions or lower material removal rates during ion milling might lead to conditions at which NbO_x layers appear brighter.

5.7 Temperature-dependent resistivity and Hall coefficients of $[(PbSe)_{1+\delta}]_1[NbSe_2]_n$ ferecrystals

5.7.1 Results for temperature-dependent resistivity

In order to determine the resistivity of the samples, I-V curves have been measured. Exemplary I-V curves are shown in Fig. 5.20 for $[(PbSe)_{1+\delta}]_1[NbSe_2]_n$ with $n = 1$ of batch 3 and in Fig. B.1 for $n = 2$ of batch 3. The HAADF-STEM images of the samples of batch 3 have shown the best layer structure and contained no intermediate layers (Sect. 5.4.5). The I-V curves are linear for currents of up to at least $I = 2.4\,\mu A$ and they are similar for the two van der Pauw measurement configurations (a and b in Fig. 5.20). The thickness values for the evaluation of the resistivity using Eq. (4.1) were determined by XRR and are given in Table 5.1. The room temperature (rt) resistivity values ρ_{rt} obtained for the $[(PbSe)_{1+\delta}]_1[NbSe_2]_n$ ferecrystals of batch 3 are similar for $n = 1, 2$ and 3 with $\rho_{rt} = 3.3(3)\,\mu\Omega m$ for $n = 1$, $3.3(6)\,\mu\Omega m$ for $n = 2$ and $3.0(4)\,\mu\Omega m$ for $n = 3$ (Fig. B.2). The errors in resistivity include the errors of the fit of $I(V)$, the thickness measurement and the contact size, as described in Sect. 4.3.1.

The temperature dependence of the resistances of the $[(PbSe)_{1+\delta}]_1[NbSe_2]_n$ ferecrystals of batch 3 are displayed in Fig. 5.21. These measurements were performed during cooling in the Helium-3-cryostat in one of the van der Pauw configurations using a lock-in amplifier (DSP 7265) and currents of $I_{rms} = 2\,\mu A$. All ferecrystal samples show a metal-like temperature dependence of the resistance. The

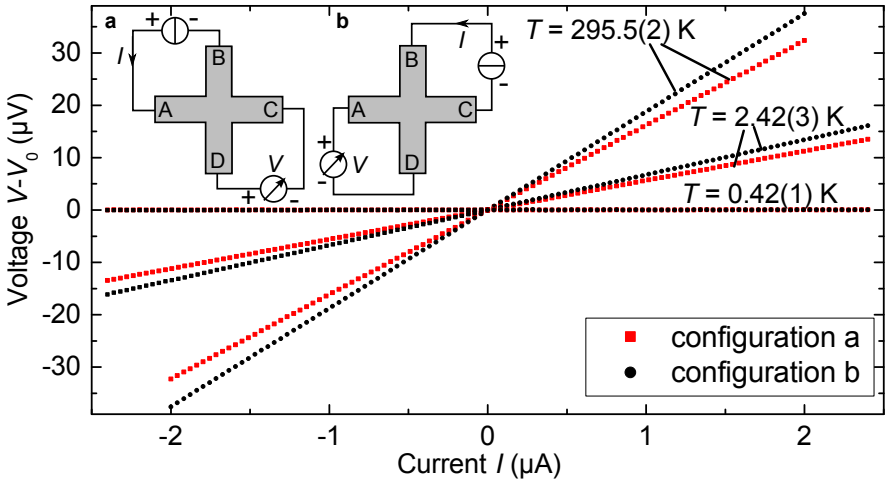

Figure 5.20: Exemplary I-V curves for different temperatures for sample $n = 1$ (A) of batch 3. Two van der Pauw measurement configurations (a and b) are shown schematically on the upper left-hand side.

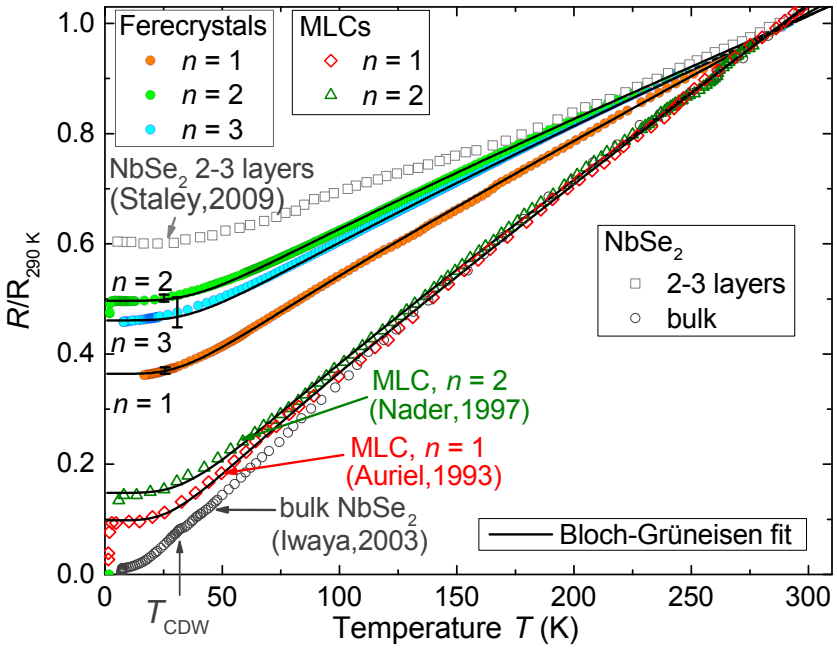

Figure 5.21: Temperature-dependent normalized resistances of $[(PbSe)_{1+\delta}]_1[NbSe_2]_n$ ferecrystals (batch 3) in comparison to in-plane resistivity reported for MLCs by Nader *et al.* [41] and Auriel *et al.* [40] and to data reported for single crystalline 2-3 layers thick $NbSe_2$ flakes (two-terminal measurements) by Staley *et al.* [10] and for bulk single crystals by Iwaya *et al.* [53]. Black solid lines indicate Bloch-Grüneisen fits.

temperature-dependent resistances between $T = 4\,\mathrm{K}$ and $290\,\mathrm{K}$ can be fitted by the Bloch-Grüneisen equation, Eq. (2.6). Indications for CDW transitions are not observed. Magnified parts of the resistances for temperatures of $20\,\mathrm{K} \leq T \leq 50\,\mathrm{K}$ are shown in Fig. B.3. The resistances for the temperature range $0.3\,\mathrm{K} \leq T \leq 6.0\,\mathrm{K}$ showing superconducting transitions are displayed in Fig. 5.26 and will be shown and discussed in Sects. 5.9 and 5.10.

The fits are shown as black solid lines in Fig. 5.21 and the data reported for MLCs has also been fitted. The Debye temperatures θ_D determined from these Bloch-Grüneisen fits for the ferecrystals increase from $\theta_\mathrm{D} = 209(1)\,\mathrm{kelvin}$ for $n = 1$ to $245(2)\,\mathrm{K}$ for $n = 2$ and to $245(7)\,\mathrm{K}$ for $n = 3$ and are displayed in Fig. 5.22.

The residual resistivity at $T = 4\,\mathrm{K}$ and the residual resistance ratio are displayed in Fig. 5.24. The residual resistivity increases from $\rho_{res} = 1.17(9)\,\mu\Omega\,\mathrm{m}$ for $n = 1$ to $\rho_{res} = 1.6(3)\,\mu\Omega\,\mathrm{m}$ for $n = 2$, whereas no further increase is observed for $n = 3$ with $\rho_{res} = 1.5(2)\,\mu\Omega\,\mathrm{m}$. Differences in the resistivity values between the samples A and B are ascribed to cases in which macroscopic defects, such as holes, occur which may influence the van der Pauw technique [150]. The residual resistance ratio

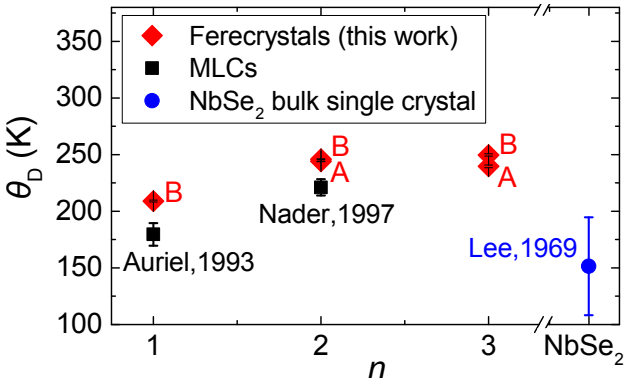

Figure 5.22: Debye temperatures determined for $[(PbSe)_{1+\delta}]_1[NbSe_2]_n$ ferecrystal samples. The labels A and B indicate the clover leaf and cross-shaped samples.

RRR, defined as $RRR = \rho_{rt}/\rho_{res}$ decreases with increasing n from $RRR = 2.80(3)$ for $n = 1$ to 2.03(3) for $n = 2$ and to 2.12(8) for $n = 3$.

The samples of batches 1 and 2 have shown non-layered intermediate and surface layers in the HAADF-STEM images. Their temperature-dependent resistivity values are shown in Figs. B.4 and B.5. The RRR values for the samples of batch 2 are about $RRR = 1.6$, which is only slightly lower than RRR of the samples of batch 3. The rt resistivity values are similar as for the ferecrystals of batch 3, indicating that the intermediate and surface layers do not influence the resistivity significantly.

5.7.2 Results for Hall coefficients

Figure 5.23a shows the magnetic field dependence of the Hall voltages V_{H} of the $[(PbSe)_{1+\delta}]_1[NbSe_2]_n$ ferecrystals at $T = 10\,\mathrm{K}$, multiplied by the total sample thickness d. The inset shows a schematic of the measurement setup. The measurements were performed using a lock-in amplifier (DSP 7265) with currents $I_{\mathrm{rms}} = 5\,\mu\mathrm{A}$. The current I was applied between two contacts at two opposite arms of the cross-shaped sample and the voltage V_m was measured between the contacts at the other two arms during slow ($0.2\,\mathrm{T\,min^{-1}}$) increasing or decreasing of the magnetic field. Due to slightly offset positions of the contacts at the samples, for $B = 0$ a non-zero voltage V_m is measured. The Hall voltages, as displayed in Fig. 5.23, have been determined by $V_{\mathrm{H}} = V_m(B) - V_m(B = 0)$. The Hall voltages are linear in B, indicating that only one type of charge carrier dominates the electrical transport. All Hall coefficients $R_H = V_{\mathrm{H}} \cdot d/(B \cdot I)$ measured for the ferecrystals $[(PbSe)_{1+\delta}]_1[NbSe_2]_n$ with $n = 1, 2$ and 3 are positive. The Hall coefficient at $T = 10\,\mathrm{K}$ decreases systematically with increasing n. The values of R_H range from $1.085(6) \times 10^{-3}\,\mathrm{cm^3/As}$ for $n = 3$ to $1.98(1) \times 10^{-3}\,\mathrm{cm^3/As}$

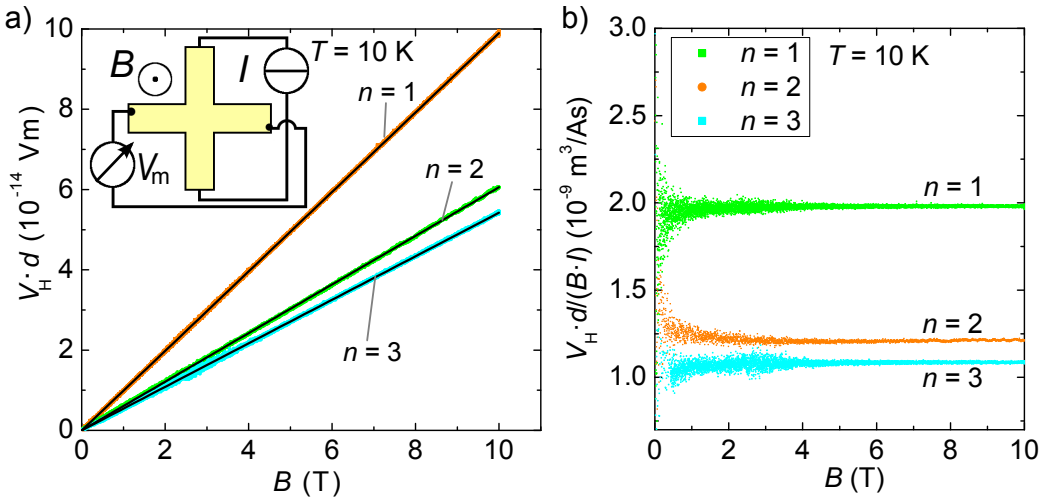

Figure 5.23: a) Hall voltage $V_{\mathrm{H}} = V_m(B) - V_m(0)$ multiplied by thickness d and b) Hall coefficients $R_{\mathrm{H}} = V_{\mathrm{H}} \cdot d/(B \cdot I)$ of $[(\mathrm{PbSe})_{1+\delta}]_1[\mathrm{NbSe_2}]_n$ ferecrystals (batch 3) for $T = 10\,\mathrm{K}$. An additional $B-$independent error of $0.39 \cdot R_{\mathrm{H}}$ due to the contact size has to be considered when calculating R_{H}.

for $n = 1$. Carrier densities calculated from these Hall coefficients are shown in Fig. 5.25. The magnetoresistance measured at $T = 10\,\mathrm{K}$ for the samples $n = 1, 2$ and 3 of batch 3 at $B = 10\,\mathrm{T}$ is lower than 0.4 %. The temperature-dependent Hall coefficients measured for batch 2 are shown in Fig. B.6. At $T = 10\,\mathrm{K}$ these samples show similar R_{H} for $n = 2$ and 3 as for batch 3. The Hall coefficient for $n = 1$ of batch 2 is lower than for batch 3, indicating a slightly higher carrier density for the samples of batch 2, when evaluating R_{H} in a single band model. This might be due to the intermediate and surface layers found for the samples $n = 1$ of batch 2.

5.8 Discussion of resistivity and Hall coefficients of $[(PbSe)_{1+\delta}]_1[NbSe_2]_n$ ferecrystals

5.8.1 The influence of the PbSe layers on the electrical transport properties

In order to analyze the influence of the PbSe layers in the ferecrystals on the electrical transport properties, the in-plane resistivity values of the ferecrystals at room temperature and at $T = 4\,\mathrm{K}$ are compared to the in-plane resistivity values reported for $NbSe_2$ (Figs. B.2 and 5.24a). Bulk $NbSe_2$ single crystals are metallic compounds [52, 56, 60, 63] and their rt in-plane resistivity values range between $(0.7 - 1.6)\,\mu\Omega\mathrm{m}$ [60, 63, 71, 83]. Polycrystalline $NbSe_2$ is reported to show a rt

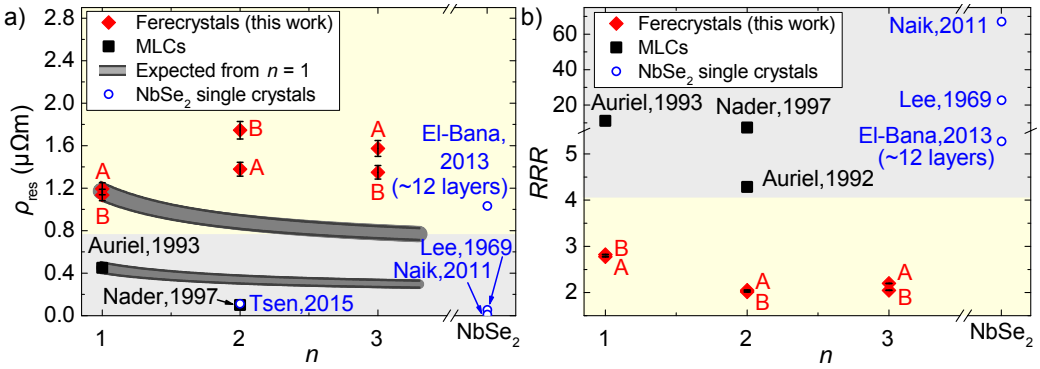

Figure 5.24: a) Residual resistivity measured at $T = 4\,\mathrm{K}$ for the ferecrystals and b) residual resistance ratio of $[(PbSe)_{1+\delta}]_1[NbSe_2]_n$ ferecrystals and data reported for single crystalline MLCs $[(PbSe)_{1+\delta}]_1[NbSe_2]_n$ and $NbSe_2$. The resistivity of the ferecrystals, $NbSe_2$ and the MLCs reported by Auriel *et al.* [40] and Nader *et al.* [41] has been measured within the layer planes. The data reported by Oosawa *et al.* [39] has been measured at pressed pelletized MLCs. The data reported by Lee *et al.* [60] and Soto *et al.* [105] are from bulk $NbSe_2$ single crystals. The data reported by El-Bana *et al.* [9] and Tsen *et al.* [2] are from exfoliated $NbSe_2$ flakes.

resistivity of $2.0\,\mu\Omega\mathrm{m}$ [71]. PbSe is a semiconductor with rt resistivity values of $(30 - 1000)\,\mu\Omega\mathrm{m}$ reported for $(12 - 960)\,\mathrm{nm}$ thin polycrystalline films [118, 119]. As expected, the resistivity values measured for ferecrystals are within this range of values reported for binary $NbSe_2$ and PbSe.

The rt resistivity ρ_{RT} does not change with n within the measurement error (Fig. B.2). These results for the resistivity values are compared to a simple parallel resistors model in which the $NbSe_2$ layers and the PbSe layers are assumed to be independent parallel resistors. In this model, each individual PbSe bilayer is assumed to have a resistance R_{PbSe} and each $NbSe_2$ layer (consisting of 3 atomic monolayers) is assumed to have a resistance $R_{\mathrm{NbSe_2}}$, independent of the stacking sequence (m, n). Consequently, the expected total in-plane resistance R of the ferecrystal sample would be given by

$$\frac{1}{R} = \frac{m \cdot r}{R_{\mathrm{PbSe}}} + \frac{n \cdot r}{R_{\mathrm{NbSe_2}}}, \tag{5.1}$$

where r is the number of repeat units stacked in the sample, m is the number of PbSe layers in the repeat unit and n is the number of $NbSe_2$ layers in the repeat unit. The resistivity ρ is determined by the relation $\rho = RWt/L$, where L is the length, W the width and t the thickness of the sample. For each ferecrystal sample L and W are equal for the PbSe and $NbSe_2$ layers. Therefore, the relation for the

total resistivity $\rho(m,n)$ of the ferecrystal samples with stacking sequence (m,n) is

$$\frac{(t_{\mathrm{NbSe_2}} + t_{\mathrm{PbSe}})}{\rho(m,n)} = \frac{m \cdot t_{\mathrm{PbSe}}}{\rho_{\mathrm{PbSe}}} + \frac{n \cdot t_{\mathrm{NbSe_2}}}{\rho_{\mathrm{NbSe_2}}}, \tag{5.2}$$

where ρ_{PbSe} is the resistivity of the PbSe layers and $\rho_{\mathrm{NbSe_2}}$ is the resistivity of the $NbSe_2$ layers. The thicknesses $t_{\mathrm{PbSe}} = 0.6097(8)$ nm and $t_{\mathrm{NbSe_2}} = 0.6336(3)$ nm are the thickness of a PbSe double layer and a $NbSe_2$ layer (3 atomic monolayers), which have been determined by XRR (Sect. 5.1).

As a first approximation it is assumed that the conductivity of the PbSe layers can be neglected in comparison to the conductivity of the $NbSe_2$ layers ($\rho_{\mathrm{PbSe}} >> \rho_{\mathrm{NbSe_2}}$) and that there is no interaction between the PbSe and $NbSe_2$ layers. Then, the resistivity of the ferecrystals $[(\mathrm{PbSe})_{1+\delta}]_m[\mathrm{NbSe_2}]_n$ would be

$$\rho(m,n) = \rho_{\mathrm{NbSe_2}} \frac{(m \cdot t_{\mathrm{PbSe}} + n \cdot t_{\mathrm{NbSe_2}})}{n \cdot t_{\mathrm{NbSe_2}}} \tag{5.3}$$

$$= \rho(m=n=1) \frac{(m \cdot t_{\mathrm{PbSe}} + n \cdot t_{\mathrm{NbSe_2}})}{n(t_{\mathrm{PbSe}} + t_{\mathrm{NbSe_2}})}, \tag{5.4}$$

where $\rho(m = n = 1)$ is the resistivity of the ferecrystal sample with stacking sequence $(m,n) = (1,1)$. These expected values for ρ are shown as a grey line in Fig. 5.24a for $T = 4\,\mathrm{K}$ and in Fig. B.2 for rt. They have been calculated using Eq. (5.4) with the measured residual and rt resistivity of $[(\mathrm{PbSe})_{1+\delta}]_1[\mathrm{NbSe_2}]_1$. It is expected that the resistivity decreases with increasing n. A deviation from the expected trend in resistivity with n is observed for both temperatures. The assumption that only the $NbSe_2$ layers contribute to the electrical transport is expected to hold better at lower temperatures, because the resistivity of polycrystalline PbSe thin films has been reported to increase with decreasing temperature [118–120], whereas the resistivity of $NbSe_2$ is reported to decrease upon lowering temperature [53, 60, 196]. However, the measurement data at low temperatures shows a higher deviation from the parallel resistors model than at rt. One possible explanation for unexpected increase in resistivity with increasing n could be a decrease in grain size with increasing n, similar as observed for $[(\mathrm{SnSe})_{1+\delta}]_1[\mathrm{NbSe_2}]_n$ ferecrystals [29]. The decrease in RRR with increasing n (Fig. 5.24) supports this hypothesis. A significant change in grain size with n has not been observed in the HAADF-STEM images of batch 3 shown in Sect. 5.4.5. However, only a small sample area has been investigated by HAADF-STEM and not many low-indexed zone axes could be observed to allow for an exact determination of the grain size. Another possible reason for the deviation of the measured data from the parallel resistors model could be a decrease in the carrier density of the $NbSe_2$ or PbSe layers with increasing n. In order to test this, Hall coefficients have been

measured and the charge carrier density of the samples is analyzed using a single-band model. To determine the charge carrier density p of the ferecrystal samples, a single-band model has been applied, i. e. $p = 1/(eR_H)$, Eq. (2.8). The Hall coefficients R_H have been determined by a linear fit of $V_H(B)$, as shown in Fig. 5.23. The resulting carrier densities p are shown in Fig. 5.25. The highest contribution to the errorbars in p are from the error due to the sizes of the contacts on the sample. Using a single-band model seems to be justified as a first approximation, because the Hall coefficient shows a linear dependence on the magnetic field up to high magnetic fields (Fig. 5.23). The Hall coefficients of the $[(PbSe)_{1+\delta}]_1[NbSe_2]_n$ samples measured at $T = 10\,K$ are positive which agrees with positive Hall coefficients reported for bulk $NbSe_2$ with $RRR < 27$ [52, 54] at $T = 10\,K$. For PbSe n-type and p-type samples have been reported for temperatures between $T = 40\,K$ and $T = 500\,K$ [65, 66].

Using the parallel resistors model described above, in which the carrier density p_{PbSe} in the PbSe layers is assumed to be so low that it can be neglected in comparison to the carrier density in the $NbSe_2$ layers, i. e. $p_{PbSe} \ll p_{NbSe_2}$, the expected total carrier density $p(m,n)$ of the ferecrystals $[(PbSe)_{1+\delta}]_m[NbSe_2]_n$ would be

$$p(m,n) = p_{NbSe_2}\frac{n \cdot t_{NbSe_2}}{m \cdot t_{PbSe} + n \cdot t_{NbSe_2}} \tag{5.5}$$

$$= p(m=n=1)\frac{n \cdot (t_{PbSe} + t_{NbSe_2})}{m \cdot t_{PbSe} + n \cdot t_{NbSe_2}}, \tag{5.6}$$

where p_{NbSe_2} is the carrier density of the $NbSe_2$ layers, which is assumed to be independent of the stacking sequence (m,n) and $p(m=n=1)$ is the carrier density of sample $(m,n) = (1,1)$. The expected carrier density is plotted in Fig. 5.25. The expected carrier density for a sample consisting of only $NbSe_2$ layers ($n \to \infty$) calculated from the carrier density of sample $m = n = 1$ is lower than the carrier density reported in [52] for a bulk $NbSe_2$ single crystal. The trend in carrier density p on n obtained for the ferecrystals agrees with the expected trend within the measurement error. However, the error in p is too high in order to exclude a possible influence of the carrier density on the increase in resistivity on n. Within the measurement error it would be possible that p decreases by a factor of 1.5 from $n = 1$ to $n = 2$. This would potentially explain the measured increase in ρ_{res} from $n = 1$ to $n = 2$, since $1/\rho = ep\mu$. A further reason for the unexpected increase in resistivity with increasing n would be a decrease in mobility μ with n. Charge carrier mobility values have been calculated by $\mu = R_H/\rho$. At $T = 10\,K$ they are $\mu = 15(7)\,cm^2/Vs$ for $n = 1$, $9(4)\,cm^2/Vs$ for $n = 2$ and $8(4)\,cm^2/Vs$ for $n = 3$. These values are lower than the values reported for bulk $NbSe_2$ [52, 60] of μ = (48-100) cm^2/Vs at $T = 10\,K$. One possible explanation for this scattering

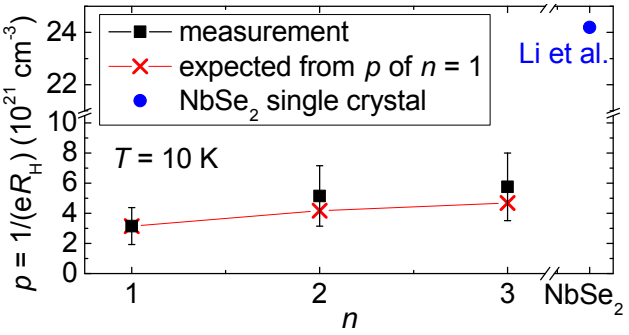

Figure 5.25: Hole density p measured for $[(PbSe)_{1+\delta}]_1[NbSe_2]_n$ ferecrystals in comparison to values expected if the PbSe layers did not contribute to transport and the carrier density of the $NbSe_2$ layers were independent of n.

at grain boundaries due to the polycrystallinity of the ferecrystals. The mean free path calculated using Eq. 2.10 for the ferecrystals is 4(2) nm for $n = 1$ and 3(2) nm for $n = 1$ and $n = 3$, which is similar to the grain sizes of the ferecrystals determined by TEM.

Furthermore, the temperature dependence of the resistivity of the ferecrystals is compared to bulk $NbSe_2$ [53] and 2-3 sheets of $NbSe_2$ [10], as shown in Fig. 5.21. The RRR of the 2-3 sheets of $NbSe_2$ is lower than that of the ferecrystals, which can be due to the two-terminal measurement setup for the $NbSe_2$ flakes reported in [10]. The 2-3 layer thick $NbSe_2$ single crystals and bulk $NbSe_2$ single crystals [9, 10, 52, 53, 60] show a deviation from a linear temperature dependence of R on T, whereas $R(T)$ for the ferecrystals and MLCs is linear between $T = 100\,K$ and rt. The temperature dependence of the resistivity of the ferecrystals is more metal-like than that of $NbSe_2$. This indicates fundamental differences between the transport mechanisms in ferecrystals and $NbSe_2$.

5.8.2 Charge density wave transition

A typical indication for a CDW transition in bulk $NbSe_2$ single crystals is an anomaly in the slope of $\rho(T)$ between $T = 30\,K$ to $60\,K$ [1, 50, 52–56]. Anomalies in the resistivity at the CDW transition temperature have also been observed for VSe_2 single crystals [90, 95, 112, 113] and ferecrystals containing single and few VSe_2 layers [19, 25, 64]. MLCs containing $NbSe_2$ do not show indications for a CDW transition in resistivity [36, 40–43]. For the ferecrystals investigated in this work an anomaly in the slope of $R(T)$ is not observed as shown in Figs. 5.21 and B.3. For few-layer $NbSe_2$ it has been shown that although no indications for a CDW transition are not observed in the electrical properties, a CDW is present as has been verified by Raman measurements [1]. It has been shown for bulk $NbSe_2$ that there is a relation between the sharpness of the resistive anomaly and the

RRR. For bulk $NbSe_2$ single crystals with a *RRR* higher than 27, an anomaly in the slope of the resistivity at about $T = 30\,\mathrm{K}$ to 60 K has been reported. This anomaly is not observed for $NbSe_2$ with a *RRR* of less than 13 [52–54, 56]. The *RRR* values of the ferecrystals are much lower than 13, indicating a higher disorder, which might suppress the charge density wave state or reduce its effect on the resistivity in these samples.

Another typical indication for a CDW transition in $NbSe_2$ can be found in an anomaly of the Hall coefficient below about $T = 30\,\mathrm{K}$ to 60 K [1, 52, 54, 55, 60]. Bulk $NbSe_2$ with high a high *RRR* is known to show a change in the sign of the Hall coefficient in this temperature range [52, 54, 60]. For $NbSe_2$ single crystals with a low *RRR*, no change in sign of the Hall coefficient is observed, it remains *p*-type down to 7 K, where it becomes superconducting [52, 54, 60]. The ferecrystals show a positive Hall coefficient at $T = 10\,\mathrm{K}$. Similar $[(PbSe)_{1.14}]_1[NbSe_2]_1$ ferecrystal samples showed a positive Hall coefficient throughout the temperature range between $T = 20\,\mathrm{K}$ and 300 K [23]. This indicates that the CDW effect is not enhanced in these ferecrystals by a possible enhancement in their quasi-two dimensionality due to their turbostratic disorder. The polycrystallinity of the ferecrystals, leading to a low *RRR*, the change in charge carrier density due to charge transfer or the reduced $NbSe_2$ layer thickness might prevent the CDW state in the ferecrystal or its effect on ρ and R_H. This seems to be different for the VSe_2-containing ferecrystals [19, 64]. A particular difference between the crystal structures of VSe_2 and $NbSe_2$ is that the transition metal atoms in VSe_2 are surrounded by the Se atoms in an octahedral configuration, whereas for $NbSe_2$ they are surrounded in a trigonal-prismatic configuration. However, although no indications for a CDW transition are observed in the electrical properties of the $[(PbSe)_{1+\delta}]_1[NbSe_2]_n$ ferecrystals, it is still possible that a CDW is present, as has been shown for $NbSe_2$ by Raman measurements at few-layer $NbSe_2$ [1].

5.8.3 The influence of turbostratic disorder and polycrystallinity

As shown in Fig. 5.21, the temperature dependencies of the normalized resistances of the ferecrystals are between those reported for 2-3 layers of $NbSe_2$ single crystals [10] and the data reported for conventional MLCs [40, 41]. The temperature dependence of the resistance of the $[(PbSe)_{1+\delta}]_1[NbSe_2]_n$ ferecrystals and MLCs is linear between $T = 100\,\mathrm{K}$ and room temperature. It can be concluded, that the turbostratic disorder, polycrystallinity and the lower thickness of the ferecrystals, do not have an influence on the linear trend between $T = 100\,\mathrm{K}$ and room temperature as observed for the MLC single crystals. However, they have an influence on the slope of $R(T)/R_{290\mathrm{K}}$ and on the absolute resistivity values.

The residual resistivity values of the $[(PbSe)_{1+\delta}]_1[NbSe_2]_n$ ferecrystals, displayed in Fig. B.2, are higher than in-plane resistivity values reported for the analogous conventional MLCs by Nader *et al.* [41] and Auriel *et al.* [40, 42, 43] (Fig. 5.24).

Hall coefficients for these MLCs have only been reported for $n = 1$ with a carrier density of $p = 3 \times 10^{21}\,\mathrm{cm}^{-3}$ at $T = 4\,\mathrm{K}$, determined by $p = 1/(eR_\mathrm{H})$ [42]. This carrier density is similar as obtained for the ferecrystal $n = 1$, Fig. 5.25. At $T = 300\,\mathrm{K}$ the carrier density reported for the MLC with $n = 1$ is $p = 5.7 \times 10^{21}\,\mathrm{cm}^{-3}$, which is similar to the value reported for $[(\mathrm{PbSe})_{1.14}]_1[\mathrm{NbSe_2}]_1$ ferecrystals [23]. The similarity between the Hall coefficients of MLCs and ferecrystals indicates that the differences in resistivity result from differences in the mobility. A possible reason for differences in mobility could be that the polycrystallinity and turbostratic disorder of the ferecrystals in contrast to MLCs which are single crystalline. This hypothesis is also supported by the fact that the RRR values of the MLC with $n = 1$ and 2 are higher than the RRR of the ferecrystals. The in-plane grain size in ferecrystals is few to several tens of nanometers, as observed in the HAADF-STEM images. The cross-plane grain size is only few atomic layers due to the turbostratic disorder. This could explain the observed differences in ρ_{res} and RRR between the ferecrystals and MLCs.

The Debye temperatures θ_D obtained from the Bloch-Grüneisen fits are shown in Fig. 5.22 as a function of n. The values for Θ_D of the ferecrystals are similar as the values reported for the analogous MLCs, suggesting that their phonon spectra are similar, despite of the turbostratic disorder. Debye temperatures of about 200 K are typical for MLCs containing $\mathrm{NbX_2}$ with X=Se or S [38, 40, 41].

5.9 Superconductivity in $[(PbSe)_{1+\delta}]_1[NbSe_2]_n$ ferecrystals

The temperature-dependent normalized resistances of the $[(\mathrm{PbSe})_{1+\delta}]_1[\mathrm{NbSe_2}]_n$ ferecrystals for temperatures down to 300 mK are displayed in Fig. 5.26. The resistances were measured using a lock-in amplifier (DSP 7265) with currents of $I_\mathrm{rms} = 2\,\mu\mathrm{A}$ applied in one of the van der Pauw resistance measurement configurations. Van der Pauw measurements with direct currents of up to 2.4 µA have also been performed in this temperature range and the results are shown in Fig. B.7. All measurements show the same abrupt decrease in resistance with decreasing temperatures for all $[(\mathrm{PbSe})_{1+\delta}]_1[\mathrm{NbSe_2}]_n$ ferecrystals with $n = 1, 2$ and 3. This clearly marks a transition from a normal conducting to a superconducting state. The transition temperatures T_c and transition widths ΔT determined by the lock-in and the van der Pauw and technique are similar. Furthermore, the transition temperatures are similar for both samples measured for each n (samples A and B).

The transition temperature to superconductivity T_c has been determined as $R = 0.9R_n$, where R_n is the resistance in the normal state close to the transition temperature. The values obtained for T_c for the ferecrystals are shown in Fig. 5.27 and Table B.8. For the ferecrystals $T_\mathrm{c} = 1.11(2)\,\mathrm{K}$, $1.91(3)\,\mathrm{K}$ and $2.66(4)\,\mathrm{K}$ for $n = 1, 2$ and 3, respectively. Figure 5.27 shows that T_c of the ferecrystals increases

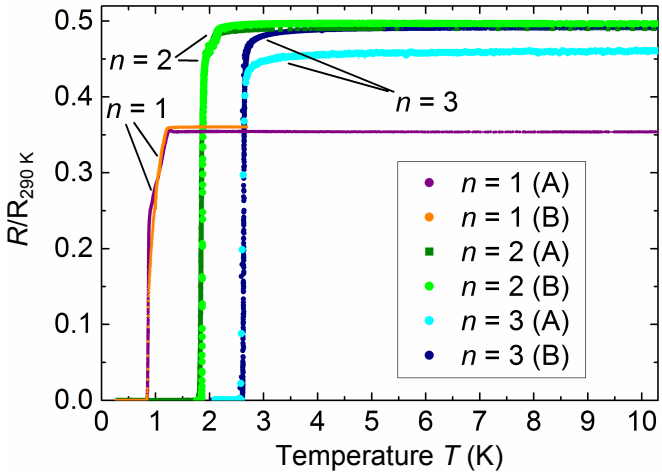

Figure 5.26: Temperature-dependent resistances of $[(PbSe)_{1+\delta}]_1[NbSe_2]_n$ ferecrystals (batch 3) normalized to the resistance at $T = 290\,\mathrm{K}$ for different n between $0.3\,\mathrm{K} \leq T \leq 300\,\mathrm{K}$ showing transitions to the superconducting state. Samples A and B indicate the clover-leaf and the cross-shaped samples, respectively.

monotonously with increasing n.

For $n = 1$ and 2 there is a kink in the $R(T)$-curve at at $R = 0.68R_n$ and $R = 0.91R_n$ at which the slope of $R(T)$ changes. The transition width ΔT has been determined for all samples as the temperature range between $R = 0.1R_\mathrm{n}$ and $R = 0.9R_\mathrm{n}$ and is $0.26(4)\,\mathrm{K}$, $0.07(4)\,\mathrm{K}$ and $0.05(5)\,\mathrm{K}$ for $n = 1, 2$ and 3, respectively (Table B.8). The superconducting transitions in $R(T)$ of batches 1 and 2 are shown in Fig. B.8 and in Fig. B.9 they are compared to those of batch 3. Batches 1 and 2 have shown intermediate layers in the HAADF-STEM images, whereas the samples of batch 3 showed a layer stacking sequence as expected (Fig. 5.4.5).

5.10 Discussion of superconductivity

5.10.1 The transition temperatures in comparison to $NbSe_2$ and their dependence on the thickness of the $NbSe_2$ layers

Fig. 5.27 shows the transition temperature to superconductivity of the ferecrystals in comparison to $NbSe_2$ and MLCs. The value n for the $NbSe_2$ single crystals in Fig. 5.27 depicts the total number of isolated single $NbSe_2$ monolayers along the c-axis of $NbSe_2$ in the sample. The T_c values shown in Fig. 5.27 have been determined from in-plane resistance measurements, except for the T_c reported by Oosawa *et al.* [39], which have been measured at powder compacts. For bulk

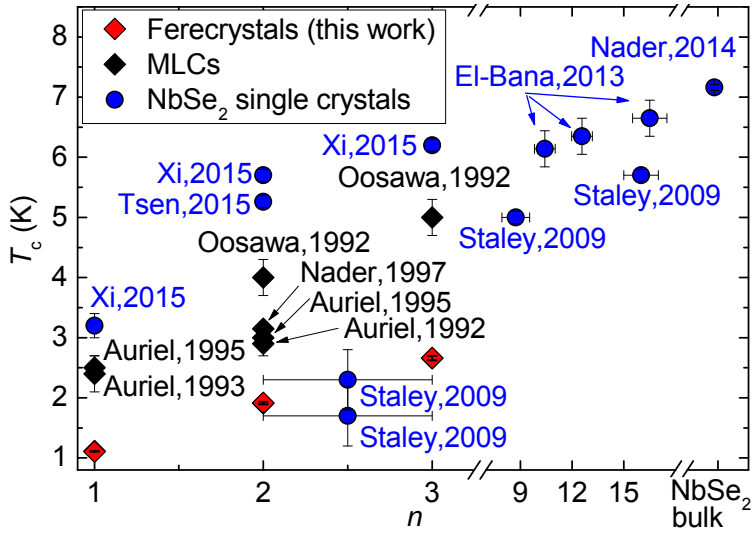

Figure 5.27: T_c of $[(PbSe)_{1+\delta}]_1[NbSe_2]_n$ ferecrystals determined as the temperatures at $R = 0.9R_{res}$. Values for $NbSe_2$ single crystals are reported by Xi *et al.* [1], Staley *et al.* [10], El-Bana *et al.* [9] and Nader *et al.* [58]. Data reported for conventional MLCs are by Oosawa *et al.* [39], Auriel, *et al.*, 1992 [43], Auriel, *et al.*, 1993 [40], Auriel, *et al.*, 1995 [42] and Nader *et al.* [41].

$2H$-$NbSe_2$ transition temperatures of $T_c = 7.0\,K$ to $7.4\,K$ have been reported [1, 58, 59, 61–63, 105], obtained from resistance measurements within the layer plane. Bulk PbSe is reported to become superconducting only under a high pressure of about 300 kbar [121]. The transition temperature of $NbSe_2$ single crystals has been reported to decrease systematically with decreasing sample thickness along the crystallographic c-axis, with the resistance measured within the layer planes [1, 2, 9, 10, 63]. A final explanation for the amount of decrease in T_c of $NbSe_2$ with decreasing thickness has not been found yet [9, 10, 13]. Similar as reported for $NbSe_2$ and MLC, T_c of the ferecrystals also increases with increasing thickness of the $NbSe_2$ layers in the repeat unit. The transition temperature for polycrystalline $NbSe_2$ has been reported to be identical [71] or to show only a reduction by less than 2.5 % (0.15 K) of T_c (0.15 K) of $NbSe_2$ single crystals [72]. Therefore, the thickness dependence of T_c in $NbSe_2$ could be one possible explanation for the lower T_c in ferecrystals compared to bulk $NbSe_2$ and the increase in T_c with increasing n. The T_c values reported for 2-3 monolayers of isolated $NbSe_2$ flakes with $T_c \approx 1\,K$ to 2.5 K [10] are similar to the T_c values measured for the ferecrystals with $n = 2$ and 3. However, recent measurements of single-layer, bilayer and trilayer $NbSe_2$ have shown T_c-values which are 2.5-3 times higher than those of the ferecrystals [1, 2] (Fig. 5.27). This indicates that the thickness effect in $NbSe_2$ alone cannot explain the strong decrease in T_c of the ferecrystals compared to $NbSe_2$. A further possible

effect leading to a lower T_c of the ferecrystals in comparison to $NbSe_2$ would be the proximity effect. This effect describes the lowering of T_c of a superconductor, which is in contact with a normal conductor. It results from the diffusion of charges across the interface between the superconductor and the normal conductor [177]. However, the proximity effect is stronger for a superconductor-normal metal interface than for a superconductor-semimetal interface [177, 197]. Band structure measurements would be necessary to confirm the influence of the PbSe layers on T_c in the ferecrystals.

5.10.2 The transition temperatures in comparison to misfit layer compounds

The transition temperatures for the ferecrystals are only about 44 % to 64 % of the T_c reported for the analogous $[(PbSe)_{1+\delta}]_1[NbSe_2]_n$ MLCs [40–43], for which the resistance has been measured within the layer plane. The T_c values reported for the MLCs by Auriel *et al.* [40, 42, 43] and Nader *et al.* [41] have been obtain from in-plane resistance measurements, similar as for the ferecrystals. In contrast, for the MLCs reported by Oosawa *et al.* [39] the resistance has been measured at pressed powder samples. Due to an anisotropy of the superconducting energy gap of $NbSe_2$ [160, 167] it is not surprising that the results for T_c of these MLCs differ from those of the ferecrystals. However, the strong reduction in T_c of the ferecrystals in comparison to the MLCs reported by Auriel *et al.* [40, 42, 43] and Nader *et al.* [41] cannot be easily explained. The lower T_c of the ferecrystals compared to the MLCs cannot be explained by the in-plane polycrystallinity of the ferecrystals itself. The transition temperature for polycrystalline $NbSe_2$ has been reported to be similar to that of $NbSe_2$ single crystals [71], or only 0.15 K lower than the value of $NbSe_2$ single crystals of $T_c = 7.17$ K (which is only 2 % of T_c) [72]. The transition temperatures for bulk niobium single crystals and bulk polycrystalline niobium do not differ by more than a few 0.1 mK [198, 199], showing that the polycrystallinity does not affect T_c. Superconductivity is connected to the phonons of a material [75]. The Debye-temperatures of ferecrystals and MLCs (Fig. 5.22) indicate similar phonon spectra, which cannot explain the difference in their T_c values either. Another main difference between the MLCs and the ferecrystals is their total thickness. The total thickness of a ferecrystal thin film is about 40 nm, thereof 20 nm of $NbSe_2$ layers, whereas the total thickness of the $NbSe_2$ layers in the MLCs is several micrometers. However, the transition temperature for about 10 nm thick isolated $NbSe_2$ flakes is reported to be already as high as 5.7 K to 6.7 K [9, 10]. The transition temperatures of the MLCs and ferecrystals are much lower than that, indicating that the total sample thickness does not predominantly determine T_c.

A possible reason for the differences in T_c of the ferecrystals in comparison to the MLCs can result from the coordination of the Nb atoms by Se and the

stoichiometry of their $NbSe_2$ layers. The MLCs $[(PbSe)_{1+\delta}]_1[NbSe_2]_n$ have been reported to show a trigonal prismatic coordination of the Nb atoms by Se atoms [40–43, 140] in the $NbSe_2$ layers, similar as in the polytype $2H$-$NbSe_2$. In contrast, for the $NbSe_2$ layers in the ferecrystals $[(SnSe)_{1+\delta}]_1[NbSe_2]_n$ indications for a mixture of a trigonal prismatic and an octahedral coordination have been reported [29]. $NbSe_2$ polytypes containing a mixture of trigonal prismatic and octahedral coordination (e. g. $4H$-$NbSe_2$ [29, 83]) have been reported to show $T_c \leq 6.5$ kelvin [61, 83]), which is lower than for the trigonal prismatic polytype $2H$-$NbSe_2$ with $T_c = 7$ K [58, 59, 61, 83]. Furthermore, T_c has been reported to depend on the stoichiometry of $NbSe_2$, i. e. $Nb_{1+y}Se_2$, which could be realized by interstitial Nb atoms in the van der Waals gaps [61]. T_c is reported to decrease from 7 K for $y = 0$ to approximately 5.5 K for $y = 0.02$ [61]. The occurrence of an octahedral coordination and a higher Nb content in the $NbSe_2$ layers in the ferecrystals would both explain a lower T_c in the ferecrystals in comparison to MLCs. In the HAADF-STEM images sample areas with trigonal prismatic coordination have been observed. However, it cannot be excluded that additional areas with octahedral coordination are present. The kinks in the transition to superconductivity in $R(T)$ might be explained by two distinct transitions, one for the trigonal prismatic and one for the octahedral sample areas. Interstitial Nb in the van der Waals gaps may be detected by measuring the distances between the lattice planes in the $NbSe_2$ layers using X-ray diffraction methods.

If non-stoichiometry and octahedral coordination of the Nb atoms by Se can be excluded in the ferecrystals and MLCs, the most probable reason for a lower T_c in ferecrystals as compared to MLCs is the turbostratic disorder in the ferecrystals. In the MLCs the $NbSe_2$ and PbSe layers are aligned along one direction along which they are commensurate. This alignment leads to lattice strain in the $NbSe_2$ and PbSe layers. In contrast, in ferecrystals the layers are not aligned, but show a turbostratic disorder and independent lattice parameters. In MLCs, this structural coherence between consecutive $NbSe_2$ layers along the stacking direction might lead to a coupling between the superconducting $NbSe_2$ layers across the non-superconducting PbSe layers, which might lead to the observed higher T_c than in ferecrystals. Critical magnetic field measurements [41, 73, 75, 177] would be helpful to confirm a possible decrease of the Ginzburg-Landau cross-plane coherence length of the ferecrystals compared to that of the respective MLCs.

Reports on isolated mono-, bi-, and trilayer flakes of $NbSe_2$ [1, 2], show higher T_c values than both ferecrystals and MLCs. However, for the $NbSe_2$ monolayers a proximity effect is not present, which can be present for ferecrystals and MLCs. Furthermore, according to the BCS theory, the transition temperature increases with increasing density of states at the Fermi level [75]. For bulk $NbSe_2$ the conduction band (d-band) is half filled. A possible electron transfer from PbSe to $NbSe_2$, as suggested in [23], would result in a change in the density of states at the Fermi level compared to $NbSe_2$.

5.10.3 The transition width ΔT

A transition width of $\Delta T \approx 0.04\,\mathrm{K}$ to $0.3\,\mathrm{K}$ has been determined for the ferecrystals $[(\mathrm{PbSe})_{1+\delta}]_1[\mathrm{NbSe_2}]_n$ with $m = 1 - 3$, which is about 2 % to 27 % of T_c, as given in Table B.8. These relative transition widths are similar to the values 6 % to 21 % reported for the MLCs $[(\mathrm{PbSe_{1.12}})_1[\mathrm{NbSe_2}]_2$ [41] and to the approximately 9 % reported for an isolated $\mathrm{NbSe_2}$ monolayer [1]. The relative transition widths for the ferecrystals are higher than for bulk $\mathrm{NbSe_2}$ single crystals, for which $\Delta T/T_\mathrm{c} = 1\,\%$ has been reported [58]. Few-layer $\mathrm{NbSe_2}$ flakes have been reported to show several steps in $R(T)$ during the transition to superconductivity, which might be ascribed to either an inhomogeneous thickness or disorder in the stacking sequence [1, 9, 63]. The transition widths reported for isolated $\mathrm{NbSe_2}$ mono-, bi- and trilayers [1] decrease with increasing number of $\mathrm{NbSe_2}$ layers, similar as for the ferecrystals.

As visible in the temperature-dependent resistance measurements of the ferecrystals in Fig. 5.26, for $n = 1$ and $n = 2$ there are kinks in $R(T)$. These kinks could be due to stacking defects in the samples, which might be present in sample areas, which were not observed by HAADF-STEM. If there are regions in the sample where two or more $\mathrm{NbSe_2}$ layers, which should be separated by a PbSe layer, are connected over a small area, this could lead to local areas with a higher T_c than the rest of the sample. If in addition a saturation in T_c with increasing n was present, with e.g. a decrease in slope of $T_\mathrm{c}(n)$ for $n \geq 3$, this would lead to a lower transition width for $n = 3$ than for $n = 1$ and 2. Furthermore, as mentioned above, sample areas with octahedral or trigonal prismatic coordination might also lead to two distinct transition temperatures.

The indium contacts are unlikely to lead to these kinks, because the superconducting transition temperature of indium has been reported as $T_\mathrm{c} = 3.4\,\mathrm{K}$ [200–202], which is much higher than the observed transition temperatures. Also a possible reduction in T_c for a possible thin indium film across the sample is unlikely, because the kinks and transitions to superconductivity are at identical temperatures for samples A and B, which have different sample and contact geometries. A possible proximity effect could cause the resistance in the ferecrystals to decrease near the indium contacts when the indium becomes superconducting. However, as visible in Figs. 5.26 and B.7, there is no kink in the measured resistivity near the transition temperature of indium and the kinks are at identical temperatures for samples A and B although the samples differ in geometries. This indicates that the indium contacts do not play a major role for the superconductivity measurements of the ferecrystals due to the applied four-terminal sensing technique. Further measurements with non-superconducting contacting materials would be helpful to confirm this.

6 Structural and electrical properties of the ferecrystals $[(SnSe)_{1+\delta}]_m[NbSe_2]_1$

6.1 Synthesis of the ferecrystals $[(SnSe)_{1+\delta}]_m[NbSe_2]_n$

The synthesis of $[(SnSe)_{1+\delta}]_m[NbSe_2]_1$ ferecrystals allows to study the effect of a monochalcogenide with a wider band gap than PbSe in the ferecrystals. For the ferecrystals $[(SnSe)_{1+\delta}]_m[NbSe_2]_1$ the influence of the SnSe layers on the structural and electrical properties is studied by varying the number of SnSe layers m, while keeping the number of $NbSe_2$ monolayers in the repeat unit constant at $n = 1$.

The $[(SnSe)_{1+\delta}]_m[NbSe_2]_n$ ferecrystal samples have been synthesized by Matti B. Alemayehu in the group of Prof. David C. Johnson at the Department of Chemistry, University of Oregon using the MER method [16–20, 22–27], as described in Sect. 5.1. The layers from the elemental sources Sn (99.999 % purity), Nb (99.999 % purity) and Se (99.999 % purity) were deposited on substrates using the physical vapor deposition. Tin and niobium are evaporated using electron beam guns and an effusion cell was used to evaporate Se. The first layers deposited onto the substrates are Sn and Se and the topmost layers are Se-Nb-Se. Subsequently, the samples were annealed for 20 min at 400 °C in a nitrogen atmosphere. The calibration process for the amount of each element required and the optimal annealing temperature is described in [24]. Silicon (100) substrates with a 300 nm thick silicon oxide layer were used for both, the samples for TEM investigations, as well as for electrical transport measurements.

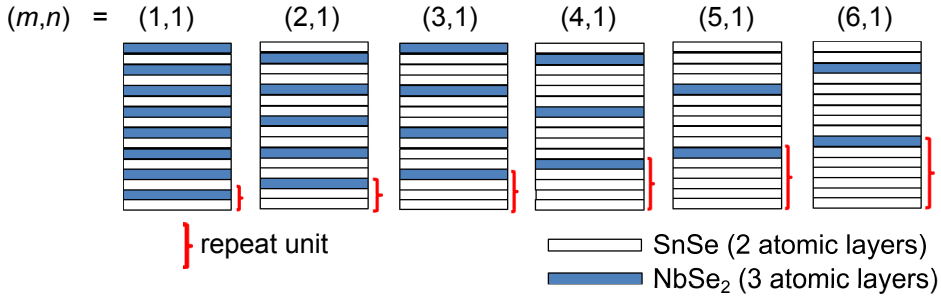

Figure 6.1: Schematic of the stacking sequences of the ferecrystals $[(SnSe)_{1+\delta}]_m[NbSe_2]_n$. The repeat units are stacked repeatedly up to a total sample thickness d, which is given in Table 6.1.

Table 6.1: Total sample thicknesses d of the ferecrystals $[(SnSe)_{1+\delta}]_m[NbSe_2]_n$ determined from X-ray reflectivity by M. Alemayehu.

(m,n)	(1,1)	(2,1)	(3,1)	(4,1)	(5,1)	(6,1)
d (nm)	46.1(3)	48.2(2)	53.0(2)	51.137(2)	42.696(5)	37.812(2)

The samples for the TEM investigations as well as electrical transport measurements are from the same synthesis batches and were annealed in the same load. The stacking sequences of the samples prepared for the $[(SnSe)_{1+\delta}]_m[NbSe_2]_1$ sample system are shown schematically in Fig. 6.1. The substrates for the samples for TEM investigations have a size of about 15 mm x 15 mm and were completely covered by ferecrystals. The size of the substrates for the electrical measurements is 10 mm x 5 mm. The samples have the shape of a clover leaf and a Greek cross deposited using a metal shadow mask. The Greek cross and the clover leaf have the same size as described in Sect. 5.1. In the following the clover leaf shaped sample of each material will be referred to as 'sample A' and the Greek cross shaped sample as 'sample B'. The total film thicknesses d of the ferecrystal samples, given in Table 6.1, were determined from X-ray reflectivity measurements on samples of the same batch at the University of Oregon.

6.2 Structural peculiarities

6.2.1 Sample structure of $[(SnSe)_{1+\delta}]_m[NbSe_2]_1$ ferecrystals

Typical HAADF-STEM overview images of the $[(SnSe)_{1+\delta}]_m[NbSe_2]_1$ samples with $m = 1, 4, 5$ and 6 are shown in Fig. 6.2. The samples exhibit the expected stacking sequence over a large scale. The total film thicknesses measured in the HAADF-STEM images agrees with the thicknesses determined by XRR on samples of the same batch. All four specimens were prepared using a face-to-face gluing temperature of 80 °C, with LN_2-cooling during ion milling and final ion energies of 1.4 keV. For these specimens, no intermediate layers are found. As visible in Figs. 6.2 and A.10 the samples $m = 4 - 6$ show columnar-like regions of bright and dark areas extending from the substrate to the surface of the sample, similar as observed for the $[(PbSe)_{1+\delta}]_1[NbSe_2]_n$ ferecrystals. These columns of similar brightness seem to apply only to the SnSe layers, whereas the $NbSe_2$ layers can have different brightness values within a single column. The observed differences in brightness of individual columns in the HAADF-STEM images can be attributed to slightly different crystal orientations. Consequently, the column width may be used for estimation of the average in-plane grain size. Hence, for the samples $[(SnSe)_{1+\delta}]_m[NbSe_2]_1$ with $m = 1, 4, 5$ and 6 an in-plane grain size of

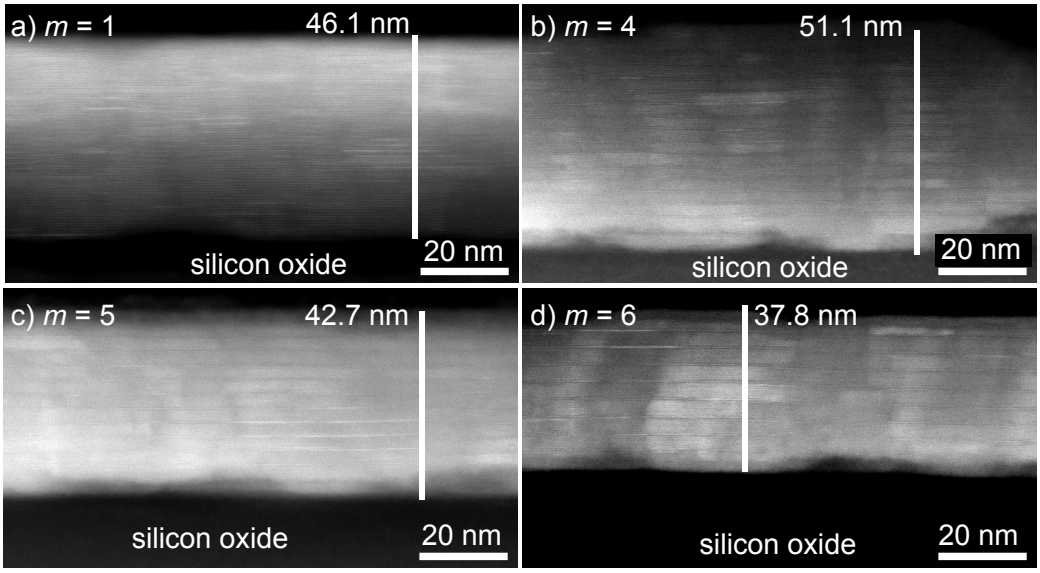

Figure 6.2: HAADF-STEM images of $[(SnSe)_{1+\delta}]_m[NbSe_2]_1$ ferecrystals with $m = 1, 4, 5$ and 6 on 300 nm silicon oxide on Si. Thickness values determined by XRR at respective samples of the same batch are given in each image.

5 nm-50 nm was estimated.

High-resolution HAADF-STEM images from the center of the thin films are shown in Fig. 6.3. They show the expected stacking sequence of $NbSe_2$ single layers alternating with m SnSe bilayers. Some of the layers are oriented along low-indexed zone axes and the atomic columns are visible. These orientations agree with projections of the individual binary compounds SnSe and $2H$-$NbSe_2$. The fact that atomic bilayers can be distinguished in the SnSe layers indicates that all the SnSe layers in the ferecrystals are oriented such that the c-axis of SnSe (assuming the structure is α-SnSe with space group $Pmcn$ [84]) is pointing along the stacking direction, i. e. in the HAADF-STEM images SnSe is projected along the $[u\,v\,0]$ directions. The fact that three atomic layers are visible for $NbSe_2$ means that the c-axis of $NbSe_2$ is also pointing in stacking direction. As in the $[(PbSe)_{1+\delta}]_1[NbSe_2]_n$ samples, the $NbSe_2$ layers in the HAADF-STEM consist of a brighter central (Nb) layer, sandwiched between two darker (Se) layers and show a trigonal prismatic coordination of Nb atoms by Se atoms as visible in the $[1\,0\,.\,0]$ oriented $NbSe_2$ layer in Fig. 6.3a. In some parts of the sample the $NbSe_2$ layers appear brighter than the SnSe layers, although Nb has a lower atomic number than Sn. This effect can appear if the incoming electron beam is parallel to a low-indexed zone axes of the $NbSe_2$ layers, along which there is a high packing density of atoms (channeling effect). As a result, the $NbSe_2$ layer may appear brighter in the image than differently oriented $NbSe_2$ layers (different channeling condition) or

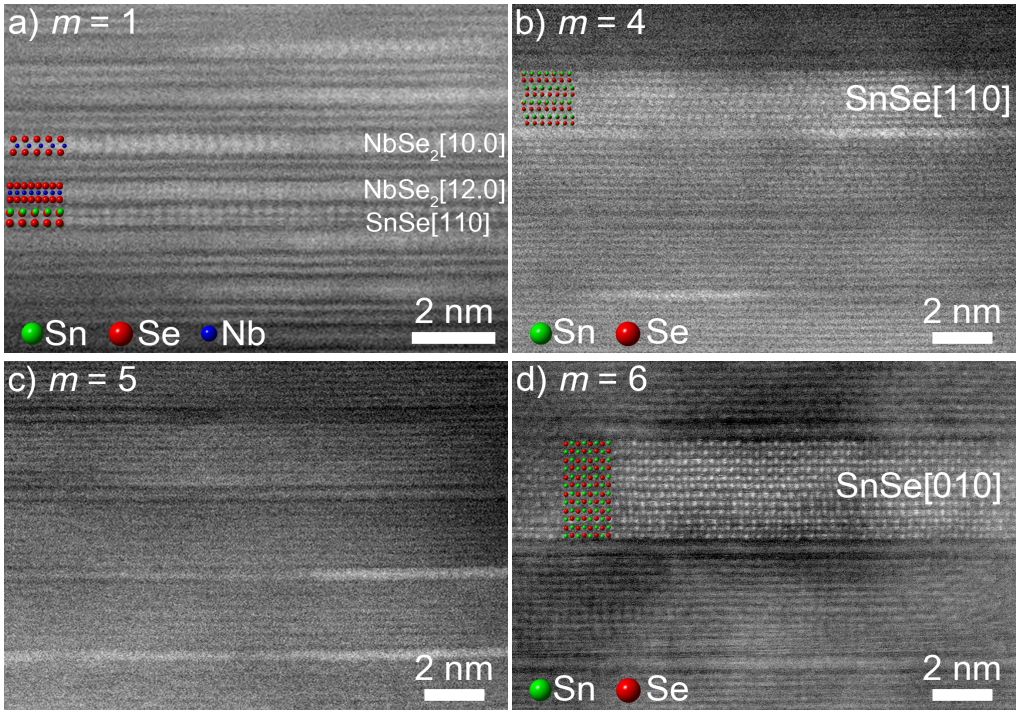

Figure 6.3: High-resolution HAADF-STEM images of $[(SnSe)_{1+\delta}]_m[NbSe_2]_1$ ferecrystals showing turbostratic disorder. Projections of SnSe along [1 1 0] and [0 1 0] and $NbSe_2$ along [1 2 . 0] and [1 0 . 0] are indicated by structure models of the bulk structures of α-SnSe [84] and $NbSe_2$ [82].

even SnSe. Similarly, some of the SnSe layers appear brighter than adjacent SnSe layers and the bright SnSe layers are often aligned along a low-indexed zone axis, as seen e. g. in Figs. 6.3a, b, d and 6.5. The EDXS maps in Fig. 6.6 also confirm the identification of SnSe and $NbSe_2$ layers found in the HAADF-STEM images. The fact that consecutive SnSe or $NbSe_2$ layers along the stacking direction show an abruptly different brightness values shows that their orientation around the c-axis has changed, reflecting the turbostratic disorder.

6.2.2 Defects in $[(SnSe)_{1+\delta}]_m[NbSe_2]_1$ ferecrystals

Several types of stacking defects have been observed in some parts of the ferecrystals $[(SnSe)_{1+\delta}]_m[NbSe_2]_1$. The projected area fraction of defects for sample $m = 1$ has been determined as 1.6 % from the image in Fig. A.11 by calculating the ratio between the defect area (blue dashed boxes) and the total area of 3993 nm^2 (red box). The contrast between the SnSe and the $NbSe_2$ layers is not as high as for the PbSe-$NbSe_2$ system, but bilayers can be identified as the SnSe layers and

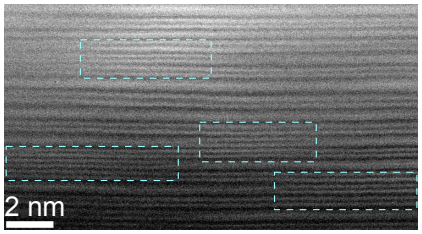

Figure 6.4: HAADF-STEM image of $[(SnSe)_{1+\delta}]_1[NbSe_2]_1$ ferecrystal. Dashed boxes indicate stacking defects where SnSe replaces a part of an $NbSe_2$ layer.

trilayers as $NbSe_2$. A typical type of stacking defect in sample $m = 1$ is shown in Fig. 6.4. In this stacking defect a SnSe bilayer replaces a part of a $NbSe_2$ layer. This is similar to the observation in the $[(PbSe)_{1+\delta}]_1[NbSe_2]_n$ samples, where a PbSe bilayer replaced one or several $NbSe_2$ layers, resulting in a local deviation from the nominal stacking sequence.

For the samples of type $m = 6$ other types of stacking defects are present. Figures 6.5a and b display two different sample areas of sample $m = 6$ and Figs. 6.5c and d show magnified parts of these images. Grain boundaries within the SnSe layers are indicated by arrows. The grain boundaries appear darker than the adjacent SnSe layers, a possible reason being that in the grain boundaries the atoms are less closely packed than inside the grains, and that the channeling conditions for the electrons become different at these specimen positions. In Fig. 6.5c in the grain to the left of the SnSe[010] grain there are only 5 SnSe bilayers present, although 6 SnSe bilayers would be expected for $m = 6$. As a result, below this defect the SnSe layers are offset on both sides of the grain boundary. At the grain boundary, the $NbSe_2$ layer on the left-hand side merges into a SnSe bilayer on the right, indicated by the dashed box in Fig. 6.5c.

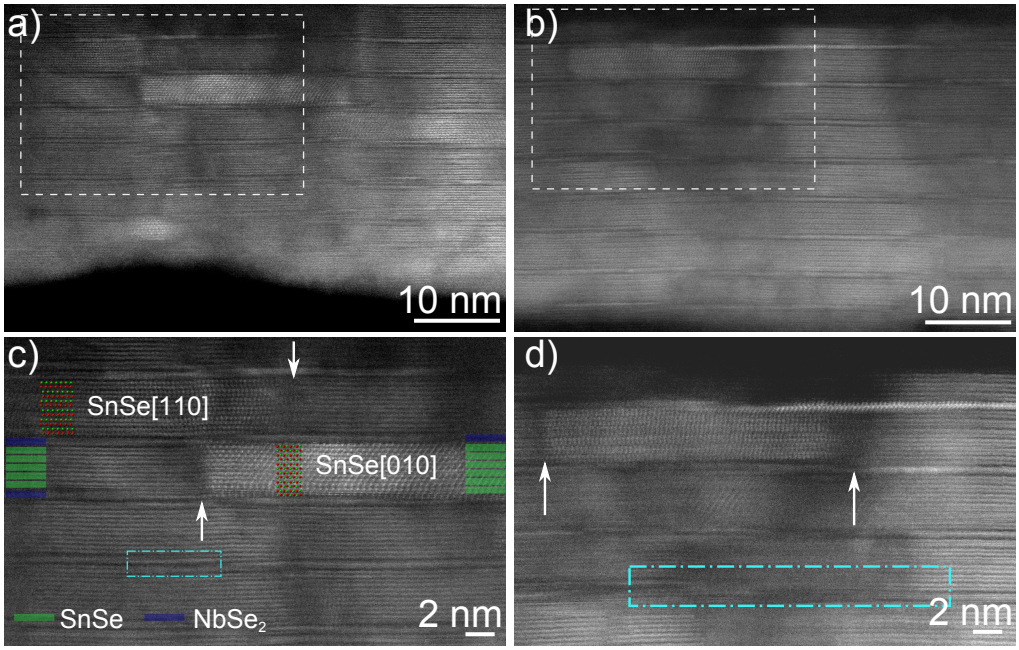

Figure 6.5: HAADF-STEM images of $[(SnSe)_{1+\delta}]_6[NbSe_2]_1$. Boxed areas in a) and b) are shown magnified in c) and d). Arrows indicate grain boundaries. Structure models of $\alpha-$SnSe are from [84]. Boxes in c) and d) indicate stacking defects.

6.3 Compositional analysis of $[(SnSe)_{1+\delta}]_m[NbSe_2]_1$ thin films

Energy-dispersive X-ray spectroscopy was applied to investigate the chemical composition of the $[(SnSe)_{1+\delta}]_m[NbSe_2]_1$ ferecrystals. Fig. 6.6 shows a representative HAADF-STEM images and EDXS maps of sample $m = 5$, all obtained from the same sample area. The alternating thick SnSe and thin $NbSe_2$ layers can be recognized by regions of high Sn and low Nb content alternating with regions of high Nb and low Sn content, respectively.

An EDXS spectrum obtained from the entire specimen area of Fig. 6.6 is shown in Fig. 6.7. The peaks in the spectrum can be ascribed to Nb, Sn, Se, O, Si, C and Cu. Copper and carbon are spurious elements resulting from the TEM specimen preparation. The energy ranges used for the EDXS maps shown in Fig. 6.6 are highlighted in green.

An EDXS linescan through a part of the mapped area in Fig. 6.6 is plotted in Fig. 6.8. The linescan reflects the alternating SnSe and $NbSe_2$ layers more clearly than the maps. In addition, it is depicted that the Se concentration is higher

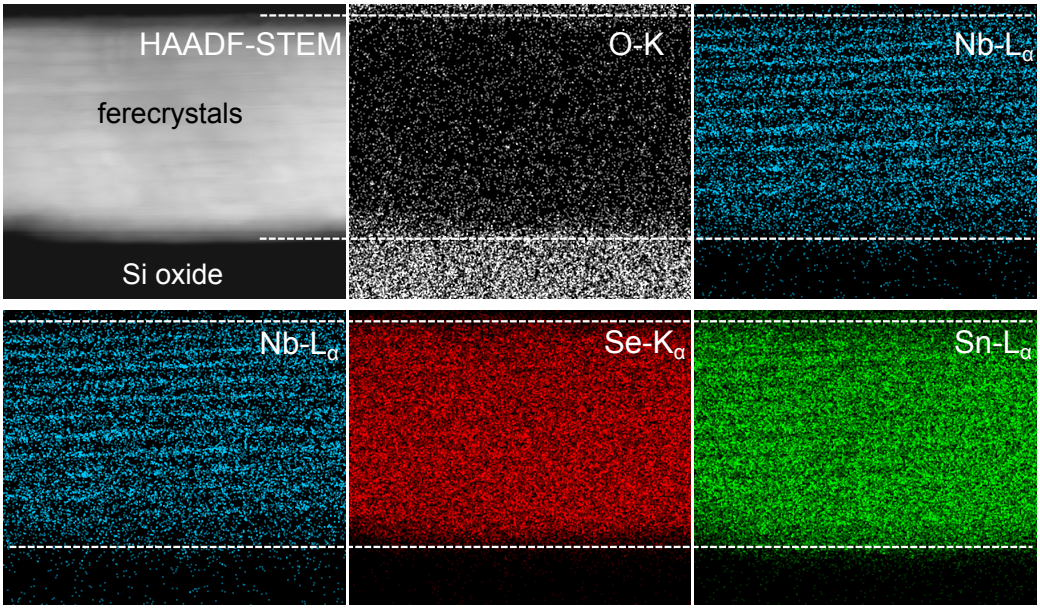

Figure 6.6: HAADF-STEM image and EDXS maps of sample $[(SnSe)_{1+\delta}]_m[NbSe_2]_1$ with $m = 5$. The dashed white lines indicate interfaces between thin film and substrate or surface.

in the same layers in which the Nb concentration is also high, as expected for $NbSe_2$ layers. An apparent decrease of the separation between subsequent $NbSe_2$ layers and a total film thickness lower than the value of 42.7 nm obtained by

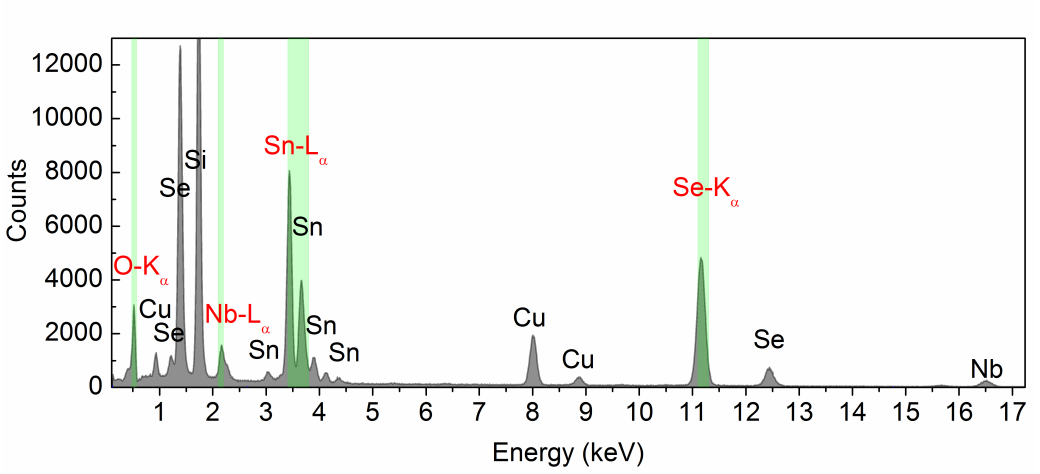

Figure 6.7: EDXS spectrum of sample$[(SnSe)_{1+\delta}]_5[NbSe_2]_1$ in Fig. 6.6.

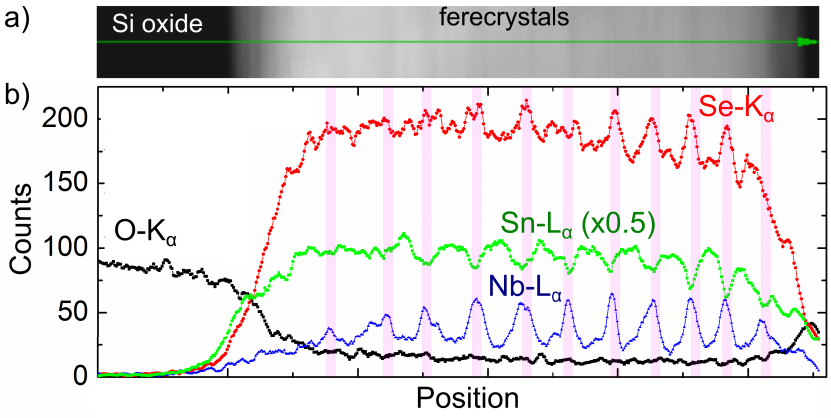

Figure 6.8: a) HAADF-STEM image of $[(SnSe)_{1+\delta}]_5[NbSe_2]_1$, b) EDXS linescan of specimen area in a). The counts for Sn have been multiplied by a factor of 0.5 for a better visibility. The red lines indicate the positions of the $NbSe_2$ layers.

XRR are present in Fig. 6.8. This can be explained by a drift of the sample during the acquisition of the EDXS map, which can lead to artifacts in this length scale. The linescan also shows that the oxygen concentration is increased in the specimen areas near the substrate and at the surface of the film. The increased oxygen concentration at the interface between the ferecrystal and the substrate can stem from the silicon oxide substrate. Near the surface of the film the oxygen concentration is increased within a thickness of a few nanometers, which could result from oxidation of the sample surface and also from the epoxy resin used for face-to-face gluing of the specimens.

6.4 Electron diffraction analysis of $[(SnSe)_{1+\delta}]_m[NbSe_2]_1$ ferecrystals

Figure 6.9 shows selected-area electron diffraction patterns of $[(SnSe)_{1+\delta}]_m[NbSe_2]_1$ ferecrystals. The diffraction spots can be indexed using the crystal structures of bulk SnSe [84] and bulk $NbSe_2$ [82] individually. The reflections for SnSe were indexed according to the structure reported in [84] for bulk α-SnSe at room temperature, using space group $Pmcn$ and lattice parameters obtained by in-plane X-ray diffraction for the $[(SnSe)_{1.16}]_1[NbSe_2]_1$ ferecrystal reported in [24]. The $NbSe_2$ reflections are indexed according to bulk $2H$-$NbSe_2$ [82] at room temperature using lattice parameters obtained by in-plane XRD of the $[(SnSe)_{1.16}]_1[NbSe_2]_1$ ferecrystal [24]. A distinction between the orthorhombic α-SnSe structure and the quasi-tetragonal high-temperature β-SnSe structure from these SAED patterns is not possible due to the insufficient resolution of the SAED patterns. Both pos-

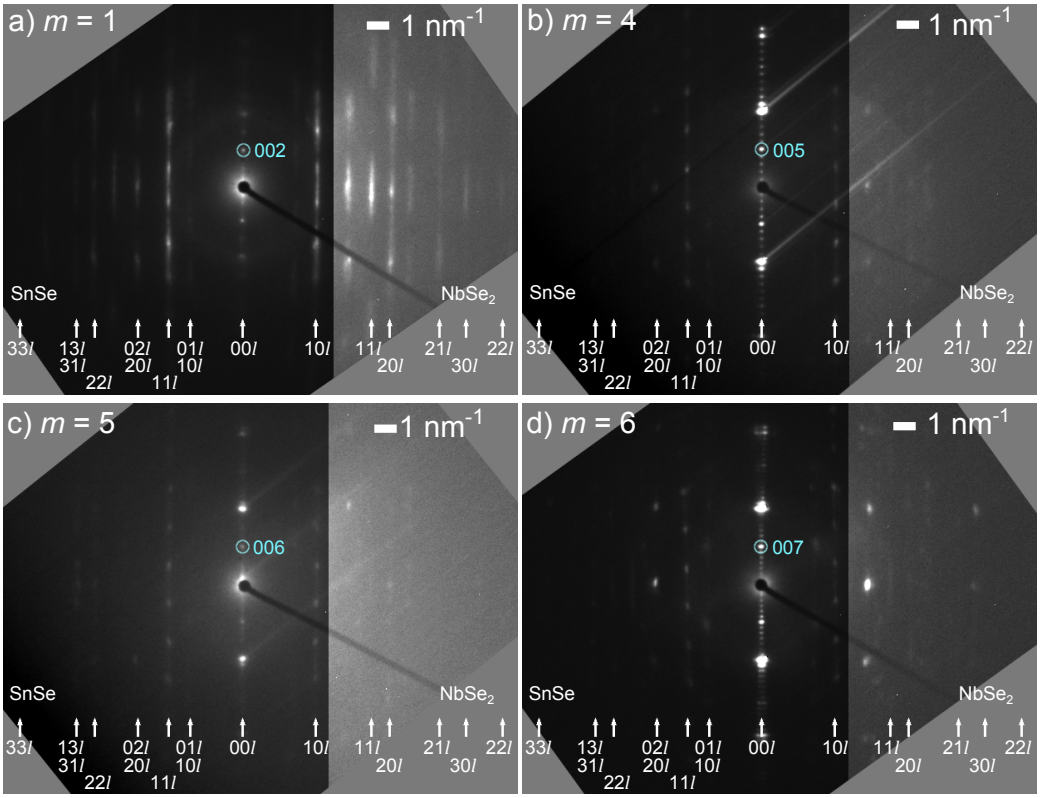

Figure 6.9: Selected-area electron diffraction patterns of ferecrystals $[(SnSe)_{1+\delta}]_m[NbSe_2]_1$ with $m = 1, 4, 5$ and 6. On the right-hand sides of the images the brightness and contrast values were changed in order to enhance the reflections with lower intensity. SnSe is indexed according to binary α-SnSe which is shown on the left-hand side of each diffraction diagram. The indexing of $NbSe_2$ according to binary $2H$- $NbSe_2$ is shown on the right-hand side. The $\{0\,0\,l\}$ ferecrystal reflections along the central vertical line in the diffraction pattern result from the ferecrystal repeat unit (blue circle).

sibilities would fit the measured data. Usually, the SnSe layers in MLCs have a structure similar to the SnSe layers in β-SnSe [35]. A significant change of the in-plane lattice parameters of SnSe with increasing m is not observed either.

The SAED patterns in Fig. 6.9 show a streaking of the lateral reflections instead of diffraction spots. The streaking is more pronounced for lower values of m. The streaks are due to the small size of the $NbSe_2$ and SnSe layers along stacking direction, and due to the lack of orientation relationships between subsequent layers (turbostratic disorder), as depicted in Sect. 3.4. Due to the turbostratic

Table 6.2: Repeat unit thicknesses s of the ferecrystals $[(SnSe)_{1+\delta}]_m[NbSe_2]_1$ with $m = 1, 4, 5$ and 6 determined from SAED patterns.

m	1	4	5	6
Repeat unit thickness s (nm)	1.25(5)	2.98(4)	3.6(1)	4.14(7)

disorder of the ferecrystals the size of the crystallites along the stacking direction is limited to about one repeat unit. For higher m, less repeat units are contained in the observed sample area and thicker SnSe layers are present leading to less intensity streaking in the SAED patterns. The SAED patterns also show discrete $00l$ reflections of the ferecrystals, which result from the periodicity of the repeat unit. The thickness s of the repeat unit along stacking direction was obtained by measuring the distances between the diffraction spots $00l$ and $00\bar{l}$ and using Eq. (3.4). The results are displayed in Table 6.2. The values obtained for s agree with the values observed in the HAADF-STEM images.

6.5 Discussion of structural properties of $[(SnSe)_{1+\delta}]_m[NbSe_2]_1$ ferecrystals

The HAADF-STEM and EDXS analysis reveal that the designated stacking sequences were achieved in most parts of the $[(SnSe)_{1+\delta}]_m[NbSe_2]_1$ ferecrystals with $m = 1, 4, 5$ and 6. Few stacking defects were observed in these samples. A typical defect found in the sample $m = 1$ is one in which a SnSe bilayer replaces a $NbSe_2$ layer. This type of defect is difficult to detect by XRD methods, because the thicknesses of a SnSe bilayer and a $NbSe_2$ layer are very similar (≈ 0.6 nm). Therefore, the layers are almost not bent around these types of defects and adjacent layers can perfectly adapt the originally intended stacking sequence again.

In the samples $m = 6$ defects are present, in which $NbSe_2$ layers merge into an SnSe bilayer instead of an $NbSe_2$ layer. However, for $m = 6$ this defect has shown to have an influence on the surrounding layers, resulting in a local deviation from the designated stacking sequence, sometimes also affecting several surrounding repeat units as seen in Fig. 6.5.

An interruption in the $NbSe_2$ layers can have consequences for the electrical transport properties, because the charge carriers moving along the in-plane direction have to cross the semiconducting SnSe or the van der Waals gap between two metallic $NbSe_2$ layers. This might have an influence on the results of the van der Pauw measurements, since the van der Pauw method requires samples without interruptions. In the superconducting state such interruptions might lead to Josephson junctions. However, the defect density is low, which suggests that the $NbSe_2$ layers are connected somewhere within the layer plane. Therefore, this

should have no influences on the transition temperature to superconductivity T_c obtained from resistance measurements.

In the $NbSe_2$ layers the atomic structure has been resolved in some sample areas and showed a trigonal prismatic coordination of the Nb atoms by Se. Since T_c has been reported to differ for $2H-NbSe_2$ ($T_c = 7.4\,K$) and $4H-NbSe_2$ [71] and $2H-NbSe_2$ contains only trigonal prismatic coordination of Nb whereas $4H-NbSe_2$ also contains octahedral coordination, the coordination might have an influence on T_c. For $[(SnSe)_{1+\delta}]_1[NbSe_2]_n$ ferecrystals trigonal prismatic and octahedral coordination have been reported [29]. The SnSe layers in the ferecrystals showed a similar atomic structure as bulk SnSe. The diffraction spots observed in the SAED patterns can be indexed individually using diffraction patterns of bulk α-SnSe and bulk $NbSe_2$, confirming that their structures have not changed much compared to the bulk structure. A change of the in-plane lattice parameters of SnSe with increasing m has been reported for the SnSe layers in similar $[(SnSe)_{1+\delta}]_m[NbSe_2]_1$ ferecrystals [32] or in $[(SnSe)_{1+\delta}]_m[MoSe_2]_n$ ferecrystals [34]. These changes were measured by in-plane XRD. Upon increasing m these ferecrystals have been reported to show a transition from the quasi-tetragonal high-temperature phase (β-SnSe) to the orthorhombic rt phase (α-SnSe). In the SAED patterns in this work changes in the lattice parameter of SnSe are not resolvable. A higher resolution or in-plane XRD would be necessary to see a possible splitting of the SnSe hkl peaks with $h \neq k$, which would prove the formation of SnSe with an orthorhombic structure.

The repeat unit thicknesses s obtained by SAED agree with the values observed in the HAADF-STEM images and also with values which would be expected from the binary compounds of $NbSe_2$ and SnSe. The repeat unit thickness for $m = 1$ agrees with the value reported for a similar ferecrystal, measured by XRD [24]. Assuming that the thicknesses of the individual SnSe bilayers and $NbSe_2$ monolayers layers do not change with m, the slope of a linear fit with $s = m \cdot t_{SnSe} + t_{NbSe_2}$ yields a thickness of one SnSe bilayer of $t_{SnSe} = 0.579(5)\,nm$. The intercept of the fit yields the thickness of a single $NbSe_2$ layer of $t_{NbSe_2} = 0.67(2)\,nm$. These results will be used in Sect. 6.8.2 for the evaluation of the carrier density and mobility from a two-layer model.

EDXS maps and linescans confirmed the layered distribution of the elements Sn, Nb and Se, which was indicated in the HAADF-STEM images. No other elements were contained in the sample, except for Cu and C, which can be ascribed to the sample preparation process and oxygen. The EDXS linescans and maps revealed that the oxygen concentration is increased in the sample areas near the substrate and at the surface of the sample. The increased oxygen peak near the substrate could also be due to X-ray signals from the adjacent silicon oxide. Near the surface of the film the oxygen concentration is increased for a thickness of a few nanometers. This can be due to oxidation of the sample surface during the time between synthesis, and TEM preparation. However, the total thickness of the ferecrystals

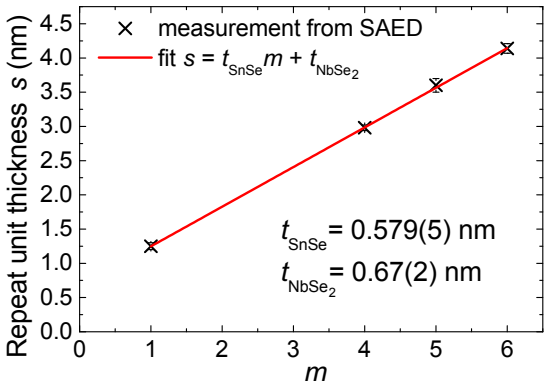

Figure 6.10: Repeat unit thickness s measured from the SAED images for different m and a linear fit to obtain the thickness of the individual SnSe and $NbSe_2$ layers.

in the HAADF-STEM images is consistent with the thickness determined by XRR measurements, which were carried out sooner after synthesis on another sample of the same batch. Between synthesis and TEM sample preparation the samples were stored in air for several days. Assuming that the thickness of all samples of one batch is similar, a possible oxide layer at the surface did not become much thicker during that time, otherwise the thickness of the ferecrystals would have changed. The increased oxygen peak near the surface could also be partly due to the epoxy resin used for gluing the specimens face-to-face.

6.6 Temperature-dependent resistivity and Hall coefficients of $[(SnSe)_{1+\delta}]_m[NbSe_2]_1$ ferecrystals

The resistivity of the ferecrystals $[(SnSe)_{1+\delta}]_m[NbSe_2]_1$ with $m = 1 - 6$ has been measured using the van der Pauw method. The thickness used for the calculation of the resistivity are given in Table 6.1. The temperature-dependent resistivity for $1.4\,\mathrm{K} \leq T \leq 300\,\mathrm{K}$ is shown in Fig. 6.11 (and in Figs. B.10 - B.13). Samples $m = 2$ and $m = 3$ were measured within the bachelor thesis of G. Hoffmann [203]. For each stacking sequence the resistivity of the two samples on each substrate (sample A and B) was measured successively during the same cooling and warming cycles with constant temperatures during the resistance measurements. No differences were observed between the resistivity values measured during the warming and the cooling cycle. For each m samples A and B show the same trend in their temperature-dependent normalized resistivity (Figs. 6.15 and B.11). The temperature dependence and values of the resistivity agree with measurement results obtained at the University of Oregon for different samples of the same type of ferecrystals between between $15\,\mathrm{K} \leq T \leq 300\,\mathrm{K}$ [24, 32]. Error bars in resistivity in Fig. 6.11 resulting from the fit of the I-V curves and the thickness measurement are smaller than the symbol size in Fig. 6.11. The total error including the error due to the contact size (Sect. 4.3) are shown exemplarily only for the highest temperatures in Fig. 6.11. Exemplary I-V curves are shown in Figs. B.14 and B.15.

The residual and rt resistivity values are shown in Fig. 6.14 as a function of m for samples A and B. The error bars shown in Fig. 6.14 for the ferecrystals include the errors due to the size of the contacts. For the samples $m = 2, 3$ and 6 the resistivity values for the samples A and B are very similar. Only for samples $m = 1$ and 4 the two values differed ($m = 1$ sample A: $\rho_{295\mathrm{K}} = 3.8(2)\,\mu\Omega\mathrm{m}$, sample B: $\rho_{295\mathrm{K}} = 7.2(4)\,\mu\Omega\mathrm{m}$; $m = 4$ sample A: $\rho_{295\mathrm{K}} = 14.0(7)\,\mu\Omega\mathrm{m}$, sample B: $\rho_{295\mathrm{K}} = 30(2)\,\mu\Omega\mathrm{m}$). In contrast to the samples A, the samples B of $m = 1$ and $m = 4$ showed several scratches. Since the rt resistivity values measured for the 'samples A' agree with the values measured at the University of Oregon [24, 32] for similar $[(SnSe)_{1+\delta}]_m[NbSe_2]_1$ ferecrystals, the higher resistivity values of the 'samples B' of $m = 1$ and $m = 4$ are ascribed to the scratches and possible holes or inhomogeneities caused by the scratches, which can influence the results of the van der Pauw method [150]. The samples show a metal-like temperature dependence of the resistivity for temperatures between 100 K and rt. At low temperatures there is an increase in resistivity with decreasing T for $m > 2$. In Fig. 6.11 sample $m = 1$ shows an abrupt decrease in resistivity at $T = 1.4\,\mathrm{K}$, indicating a normal to superconducting transition. Further resistivity measurements of the samples $m = 1, 3$ and 6 at temperatures below 1.4 K, performed in the Helium-3-system, show that all of these samples become superconducting at low temperatures as

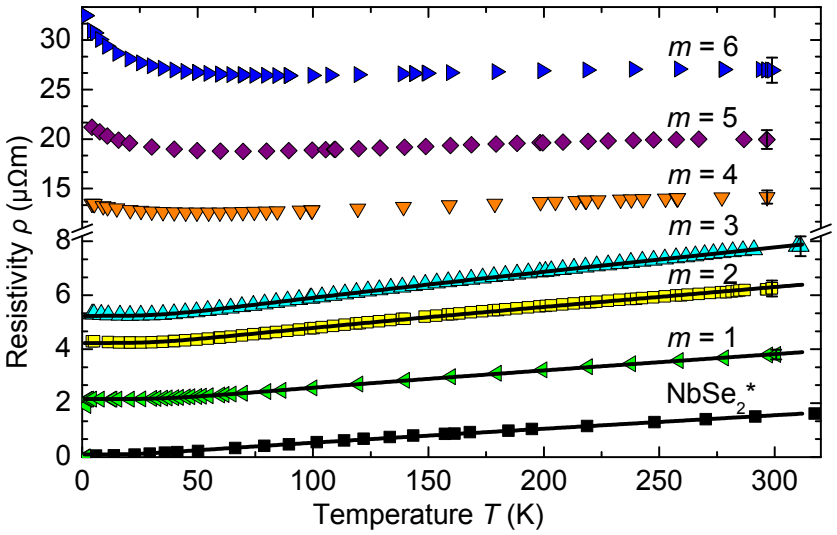

Figure 6.11: Resistivity of $[(SnSe)_{1+\delta}]_m[NbSe_2]_1$ ferecrystals ('samples A') for $1.4\,K \leq T \leq 300\,K$. The resistivity of a bulk $NbSe_2$ single crystal as reported by [60] is also shown (indicated by *). Black solid lines are Bloch-Grüneisen fits. Error bars are given exemplarily for the highest T.

described in Sect. 6.9.

Hall measurements were carried out for temperatures between 4.2 K and 300 K using the van der Pauw technique. The thickness values used for the calculation of the Hall coefficient are given in Table 6.1. The obtained Hall coefficients are shown in Fig. 6.12, together with the Hall coefficient reported for a $NbSe_2$ single crystal [60]. The Hall coefficients of samples $m = 2$ and $m = 3$ were measured within the Bachelor thesis of G. Hoffmann [203]. For each stacking sequence (m) the Hall coefficient was measured for two samples (sample A and B) successively during the same cooling and warming cycles as the resistivity measurements described above. During each Hall measurement the temperature was kept constant. However, small drifts in temperature during the measurement were observed, which had an influence on the measured voltage. Therefore, the magnetic field was set to zero in between measurements with successively increasing magnetic fields and a possible temperature-induced drift in the voltage was subtracted from the voltage measurements for $B = 0$. An exemplary Hall measurement is shown in Fig. B.16. The error bars in Fig. 6.12 are errors due to the linear fit of $V_H(B)$ and the thickness measurement. The errors due to the contact size calculated using the estimation given by van der Pauw [150] amount to about $0.39R_H$, as described in Sect. 4.3.2. However, the errors due to contact size are temperature-independent and do not play a role for the analysis of the temperature dependence of the Hall coefficient. The temperature dependence and values of the Hall coefficients agree with mea-

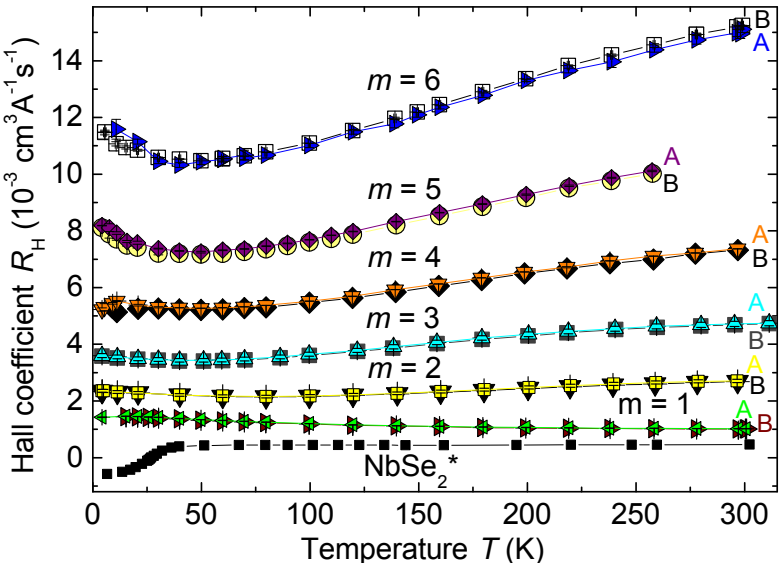

Figure 6.12: Hall coefficients measured for $[(SnSe)_{1+\delta}]_m[NbSe_2]_1$ ferecrystals (samples A and B). The data displayed for $NbSe_2$ (indicated by *) is from [60] for a $NbSe_2$ single crystal. Lines are guides to the eye. An additional temperature-independent error of $0.39R_H$ estimated from [150] is caused by the contat size.

surement results obtained at the University of Oregon for different samples of the same type of ferecrystals between $15\,K \leq T \leq 300\,K$ [24, 32].

For each m the two samples A and B showed similar values and temperature dependencies of the Hall coefficients. All Hall coefficients obtained for the ferecrystals are positive. For $T < 30\,K$ the Hall voltage was not linear in B for magnetic fields up to 660 mT. Therefore, the data $V_H(B)$ in a linear range where $B \leq 400\,mT$ was fitted linearly to obtain the Hall coefficient.

6.7 Magnetoresistance measurement results

The magnetoresistance for sample $[(SnSe)_{1+\delta}]_m[NbSe_2]_1$, $m = 6$ measured at different temperatures is displayed in Fig. 6.13. The measurements were performed in the Helium-3-system using the lock-in amplifier DSP 7265 as described in Sect. 4.4. Similar measurements were performed in the flow-cryostat for sample $m = 2$ within the bachelor thesis of G. Hoffmann [203] and are shown in Fig. B.17.

Simultaneously with the magnetoresistance measurements, Hall measurements have been performed at 'sample B' using a second lock-in amplifier, as described in Sect. 4.4. Due to the sample geometry with a small offset between the Hall voltage contacts at the sample perpendicular to the current direction, the Hall measurements are superimposed by the magnetoresistance which is non-zero at low tem-

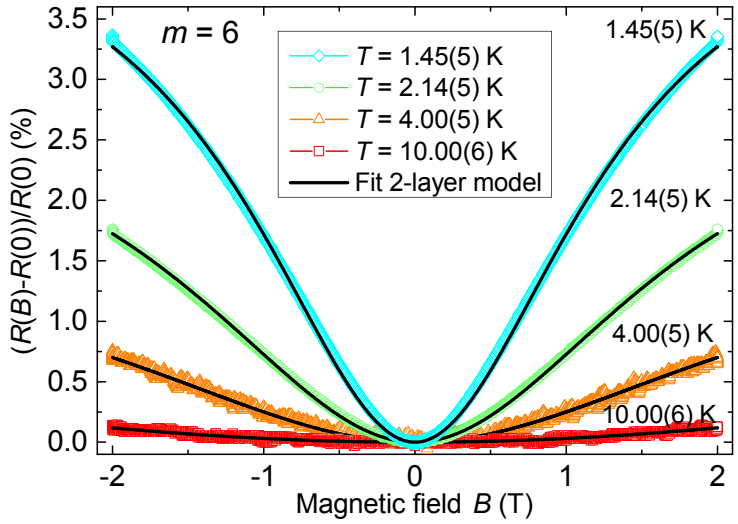

Figure 6.13: Magnetoresistance of sample $[(SnSe)_{1+\delta}]_m[NbSe_2]_1$ with $m = 6$ and fits according to a two-layer model in which $NbSe_2$ is assumed to be n-type and SnSe p-type.

peratures. Therefore, the offset and the magnetoresistance effect were subtracted from the measured voltage V_m, i. e. $V_H(B) = V_m(B) - V_m(0) - V_H(0) \cdot MR(B)$, which is shown in Figs. B.18 - B.21. The resulting Hall coefficient $R_H = V_H \cdot d/(I \cdot B)$ still shows a small dependence on B and therefore, R_H was determined from a linear range of $V_H(B)$ very close to $B = 0$. The resulting Hall coefficients and resistivity values, measured at the same temperatures as the magnetoresistance, agree within error with the Hall coefficients shown in Fig. 6.12 and are listed in Tables B.9 and B.10 for $m = 6$ and $m = 2$, respectively. For $m = 6$ and $m = 2$ the magnetoresistance MR decreases with increasing temperatures and at $T = 10\,\mathrm{K}$, MR is only about 0.1 % for $B = 2\,\mathrm{T}$ for $m = 6$. The magnetoresistance at $T = 315\,\mathrm{K}$ was zero for sample $m = 2$ for magnetic fields up to 660 mT.

6.8 Discussion of resistivity, Hall coefficients and magnetoresistance of $[(SnSe)_{1+\delta}]_m[NbSe_2]_1$ ferecrystals and analysis in a two-layer model

6.8.1 Discussion of temperature-dependent resistivity and Hall coefficients

The residual and room temperature resistivity

The resistivity values of the ferecrystals $[(SnSe)_{1+\delta}]_m[NbSe_2]_1$ at $T = 4\,K$ and at rt are shown in Fig. 6.14 as a function of m, the number of SnSe layers in the repeat unit. An increase in resistivity with increasing m is expected from the resistivity values of binary SnSe and $NbSe_2$. Bulk $NbSe_2$ is reported to be metallic with rt in-plane resistivity values between $(0.7 - 1.6)\,\mu\Omega m$ reported for $NbSe_2$ single crystals [52, 56, 60, 63, 71, 83]. In contrast, SnSe is reported to be semiconducting [123–127, 204, 205]. For polycrystalline SnSe films of thickness 250 nm with the preferential orientation of the c-axis normal to the substrate surface a resistivity of $0.05\,\Omega m$ has been reported [125]. For the ferecrystals the c-axis of SnSe is also normal to the substrate surface. The rt resistivity values measured for the ferecrystals of $3.8(2)\,\mu\Omega m$-$28(2)\,\mu\Omega m$ are within this range of in-plane resistivity values reported for SnSe and $NbSe_2$. The rt resistivity of $3.8(2)\,\mu\Omega m$ measured for the ferecrystal sample $[(SnSe)_{1+\delta}]_1[NbSe_2]_1$ is lower than the rt resistivity of $5.8\,\mu\Omega m$ reported for a powder compact of a conventional misfit layer compound MLC $(SnSe)_{1.16}NbSe_2$ [35]. This difference in ρ can be explained by the high anisotropy in the structure of these compounds resulting in a higher resistivity along the cross-plane direction. For bulk $NbSe_2$ single crystals the cross-plane resistivity has been reported to be two orders of magnitude higher than the in-plane resistivity [56]. The resistivity measured at a powder compact is an average of the in-plane and cross-plane resistivity. Therefore, the resistivity measured on a powder compact of $NbSe_2$ is expected to be higher than the resistivity measured within the layer planes.

To discuss the increase in resistivity as a function of m, the parallel resistors model, introduced in Sect. 5.8.1 will be used as a first approximation, in which the individual $NbSe_2$ monolayers and the SnSe bilayers are assumed as independent parallel resistors. Furthermore, the electrical conductivity of the SnSe bilayers is assumed to be negligible compared to the conductivity of the $NbSe_2$ layers. This assumption appears justified as a first approximation, because the resistivity reported for binary SnSe at rt is about $10^4 - 10^5$ times higher than the resistivity of $NbSe_2$, as described above. The total in-plane resistivity of the ferecrystals $[(SnSe)_{1+\delta}]_m[NbSe_2]_n$ is then given by Eq. (5.4), with t_{PbSe} replaced by t_{SnSe}. The thicknesses $t_{SnSe} = 0.579(5)\,nm$ and $t_{NbSe_2} = 0.67(2)\,nm$ are the thicknesses of the individual $NbSe_2$ and SnSe layers obtained from the SAED analysis of samples

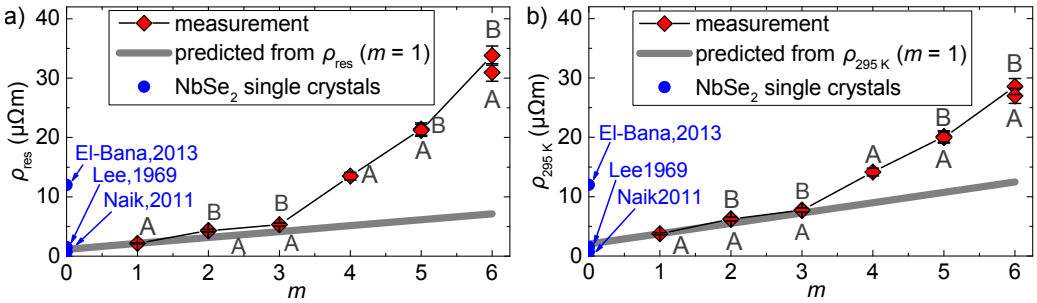

Figure 6.14: Resistivity values of $[(SnSe)_{1+\delta}]_m[NbSe_2]_1$ ferecrystals measured and predicted by Eq. (5.4) for a) $T = 4\,K$ b) $T = 295\,K$. Samples A and B denote the clover-leaf and cross-shaped sample, respectively. Also shown are in-plane resistivity values for bulk $NbSe_2$ single crystals ($m = 0$), reported by Naik *et al.* [83] and Lee *et al.* [60]. Data reported by El-Bana *et al.* is from 9.2 nm thick $NbSe_2$ single crystal layers [9].

$m = 1, 4, 5$ and 6 (Sect. 6.4). The prediction for $\rho(m, n = 1)$ is shown in Fig. 6.14 as a grey line. It shows that the resistivity of the ferecrystals with $m = 4 - 6$ increases more strongly with m than expected from the parallel resistors model in which the conductivity of SnSe layers is assumed zero.

One possible explanation for this deviation from the predicted resistivity might be a non-negligible conductivity of the SnSe layers which decreases with increasing m. The rigid band model described in Sect. 2.2.3 suggests a charge transfer from SnSe to $NbSe_2$. A charge transfer would increase the hole density in SnSe layers, which might therefore also contribute to electrical transport. For higher m charge transfer might be reduced for those SnSe layers with a higher distance to the $NbSe_2$ layers. Although the rigid band model has been applied successfully as an approximation for many MLCs [36], band structure calculations and measurements for $(PbS)(NbS_2)$ MLCs [89] have indicated strong changes in the band structure due to the stacking of the layers. Therefore, a change in the band structure compared to the band structures of SnSe and $NbSe_2$ could also be a reason for the deviations from the predicted values.

Another reason for the increase in resistivity could be an increasing oxidation of the samples with higher m. However, the sample thicknesses observed in the HAADF-STEM images in Fig. 6.2 agree with the thicknesses determined by XRR, although the samples investigated by HAADF-STEM have been stored in air for a longer time before the TEM specimen preparation than the samples used for XRR, indicating that a passivating oxide layer has formed. The rt resistivity values of the samples $m = 4 - 6$ are a factor of 1.5 - 2 times higher than the predicted values. If oxidation and a resulting decrease in effective sample thickness were responsible for this, the effective sample thickness would have to be only 2/3 to 1/2 of the sample

thickness determined by XRR. Such a reduction in sample thickness is not observed in the HAADF-STEM images. The electrical measurements were performed only a few weeks after or before the TEM analysis. In addition, similar results have been found by measurements at the university of Oregon [32]. Therefore, it is unlikely that oxidation is a reason for the unexpected increase in resistivity with increasing m. A further explanation for the stronger increase in resistivity with m than expected would be that the increasing thickness of the barrier material SnSe leads to a reduction in the transmission of holes through SnSe. The transmission through a tunneling barrier depends exponentially on the barrier thickness. For less transmitting barriers, interface scattering is enhanced in the $NbSe_2$ layer and additionally localization of charge carriers becomes feasible.

The temperature dependence of the resistivity

Figure 6.15 shows the temperature dependence of the resistivity of the ferecrystals $[(SnSe)_{1+\delta}]_m[NbSe_2]_1$ normalized to their values at $T = 295\,K$. The error bars are smaller than the symbol sizes and only include the errors due to the linear fits of the I-V-curves, because errors due to contact size and thickness measurements should not play a role for the resistivity. The temperature dependence of the resistivity systematically changes with increasing m from a metal-like behavior for $m = 1$ to a non-metallic temperature dependence for $m = 6$. Surprisingly, the temperature-dependence of sample $m = 2$ is very similar to the temperature-dependence of sample $m = 3$ (Fig. B.11). For $m \leq 2$ there is an increase in resistivity with decreasing temperature below $T \approx 100\,K$. This effect becomes stronger and starts at higher temperatures with increasing m. This is also reflected in the RRR which is displayed in Fig. 6.16a. To obtain the Debye temperature θ_D, fits using the Bloch-Grüneisen equation for metals, Eq. (2.6) were carried out for samples $m = 1 - 3$ for $T \geq 20\,K$. The fits are shown in Figs. 6.11 and B.10-B.13. The results for θ_D are given in Fig. 6.16b. There is a deviation between the fit and the measurement data, which increases with increasing m. For samples $m = 4 - 6$ the deviation from metallic temperature dependence is too strong to obtain an appropriate fit to the Bloch-Grüneisen equation. The Bloch-Grüneisen fit is suitable for metals, for which the carrier density is assumed to be constant with temperature. However, due to the stacking of metallic $NbSe_2$ with semiconducting SnSe in the ferecrystals, the carrier density might become temperature-dependent, as suggested, e. g. by a single-band analysis of the Hall coefficient in Fig. 6.18. The values of θ_D obtained for the ferecrystals are similar to $\theta_D \approx 200\,K$ reported for MLCs containing $NbSe_2$ [38]. Within the error θ_D for the ferecrystals does not change with m and is only slightly higher than θ_D of $NbSe_2$ single crystals and is similar as for typical MLCs [38]. The temperature dependencies of the resistivity reported for bulk $NbSe_2$ single-crystals [60] and for 2-3 layers of $NbSe_2$ [10] are shown in Figs. 6.11 and 6.15. Similar to the temperature-dependence of the $NbSe_2$ single-

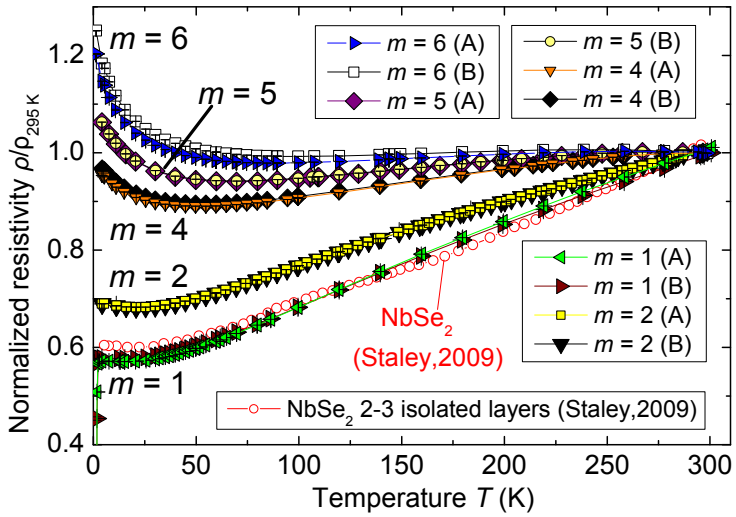

Figure 6.15: Normalized van der Pauw resistivity ρ for temperatures between 1.4 K and 300 K of $[(SnSe)_{1+\delta}]_m[NbSe_2]_1$ ferecrystals normalized to rt resistivity ρ_{295K} and data reported for isolated 2-3 monolayer thick $NbSe_2$ sheets [10].

crystal and 2-3 layers, the ferecrystals $m = 1$ show a slight deviation from a linear temperature dependence of ρ between $100\,K \leq T \leq 300\,K$ (Fig. B.10, 6.15). An upturn in resistivity with decreasing temperature is not typical for metals. A well-known effect leading to an increasing resistance with decreasing temperature is the Kondo effect [206], which is due to magnetic impurities in a metal. However, the EDXS analysis of ferecrystals of the same batch revealed no magnetic impurities. Similar results for the temperature dependence of the resistivity were obtained at the University of Oregon [32]. Therefore, the Kondo-effect seems unlikely to cause the temperature-dependence of the resistivity of the ferecrystals. Further temperature-dependent scattering mechanisms could be present in these ferecrystals, for example, due to disorder in the material, as discussed e. g. in [147, 207]. The ferecrystals, do not only show turbostratic disorder, but also a small in-plane grain size of about 5 nm to 50 nm, increasing the disorder compared to MLCs. A further explanation for the upturn in resistivity with decreasing T would be the opening of an energy gap due to a CDW transition. The highest temperatures at which this upturn in resistivity starts is similar to the CDW transition temperature of bulk $NbSe_2$. A small anomaly in the slope of the temperature-dependent resistivity at the CDW transition temperature is also observed for bulk $NbSe_2$ [1, 10, 50, 52, 53, 105]. A further explanation for the upturn in resistivity with decreasing temperature would be a freeze-out of charge carriers in SnSe, which is a semiconductor. However, no reports on the resistivity of SnSe for temperatures below 40 K have been found for comparison.

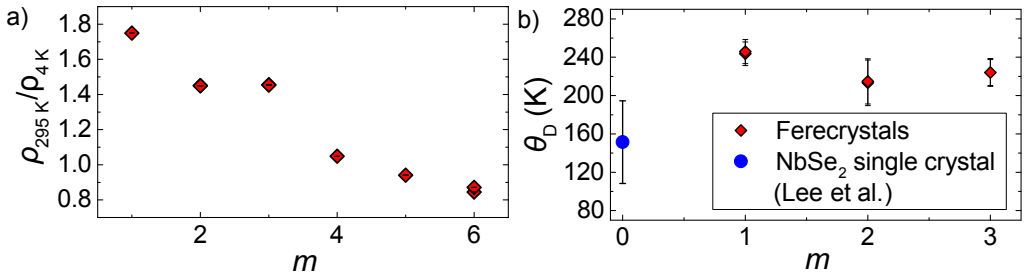

Figure 6.16: a) Residual resistivity ratios , b) Debye temperature θ_D for $[(SnSe)_{1+\delta}]_m[NbSe_2]_1$ ferecrystals and for a $NbSe_2$ single crystal where the temperature-dependence of ρ is reported in [60].

The Hall coefficients at constant temperature

The Hall coefficients measured for the ferecrystals are positive at all temperatures. A positive Hall coefficient between $T = 60\,K$ to $300\,K$ has also been reported for $NbSe_2$ single-crystals [1, 52, 53, 60] and for the MLC $(SnSe)_{1.16}NbSe_2$ [35]. Bulk SnSe is also reported to be p-type [124–126, 128].

The carrier density p has been calculated using a single-band model, i. e. $p = 1/(e{\cdot}R_H)$. The results obtained for different numbers m of SnSe layers in the repeat unit at $T = 4\,K$ and $T = 260\,K$ are shown in Fig. 6.17. The error bars shown in Fig. 6.17 include the errors of the linear fit of $V_H(B)$, the error due to thickness measurement and the error due to the contact sizes, as described in Sect. 4.3.2. As expected, the charge carrier density of the ferecrystals $[(SnSe)_{1+\delta}]_m[NbSe_2]_1$ decreases with increasing m.

In the following, the dependence of the carrier density p on m will be compared to the simple parallel resistors model, described in Sect. 5.8.1 according to which all charge carriers contributing to transport are assumed to be located in the $NbSe_2$ layers. For bulk $NbSe_2$ single-crystals a rt carrier density of about $1.3 \times 10^{22}\,cm^{-3}$ can be calculated from the Hall coefficients measured within the layer planes, reported in [60] and [52]. The Hall measurements of SnSe single crystals reported in [124] were carried out within the layer plane of SnSe (similar as in the ferecrystals) and showed $p = 3 \times 10^{17} - 2 \times 10^{18}\,cm^{-3}$ at rt. The carrier density in SnSe can therefore be assumed to be at least about 3-4 orders of magnitudes lower than in $NbSe_2$. Therefore, the assumption that all charge carriers in the ferecrystals are located in the $NbSe_2$ layers, seems to be justified as a first approximation. Using this parallel resistors model the total carrier density p expected for ferecrystals with the stacking sequence (m, n) is given by Eq. (5.6) with t_{PbSe} replaced by t_{SnSe} and with $p(m = 1, n = 1)$ obtained from sample $m = 1$(A). The carrier densities expected according to this model are plotted in Fig. 6.17 as a function of m. The error boundaries for the expected values are determined from the error boundaries

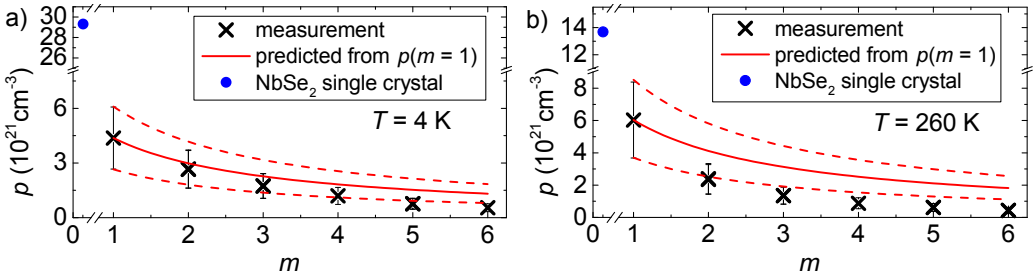

Figure 6.17: Charge carrier density p of $[(SnSe)_{1+\delta}]_m[NbSe_2]_1$ ferecrystals (samples A and B) calculated using a single-band model. Predicted values were calculated using a parallel resistors model, Eq. (5.6). a) $T = 4.2\,K$ with reference value for $NbSe_2$ from [52] and b) at $T = 260\,K$ with reference value for $NbSe_2$ from [60]. The dashed lines indicate the error boundaries of the predicted values.

of the carrier density value for sample $m = 1$. A comparison of the measured data with the values predicted by the parallel resistors model shows that for $T = 260\,K$ the carrier density decreases more strongly with m than expected from the model. This would also explain a stronger increase in the resistivity with m than expected from the parallel resistors model (Fig. 6.14).

The temperature dependence of the Hall coefficients

In Fig. 6.12 the temperature dependence of the Hall coefficient R_H of the ferecrystals is compared to R_H of a $NbSe_2$ single crystal, reported in [60]. All ferecrystal samples show positive Hall coefficients. Bulk $NbSe_2$ with a high residual resistance ratio ($RRR > 27$) is known to show a positive Hall coefficient for temperatures down to about 30 K to 60 K and a drop in the Hall coefficient below about 30 K to 60 K with a change in sign of R_H [1, 52, 54, 60]. Such a change in the sign of the Hall coefficient has been proposed to be accompanied by a charge density wave (CDW) transition at this temperature [1, 52, 54, 55, 57]. For $NbSe_2$ single crystals with a low RRR, no such change in the sign of the Hall coefficient is observed down to 7 K, where it becomes superconducting [52, 53, 55, 56]. A change in the sign of the Hall coefficient is not observed in the ferecrystals either. The Hall coefficient of the ferecrystals remains positive throughout the measured temperature range $4\,K \leq T \leq 300\,K$. However, for $m > 1$ the Hall coefficient shows an upturn with decreasing T below $T \approx 40\,K$ to 60 K, which is near the CDW transition temperature of bulk $NbSe_2$. The upturn in R_H would mean a decrease in the carrier density with decreasing T, as shown in Fig. 6.18. Such a decrease in carrier density would be consistent with the localization of charge carriers and the opening of an energy gap during the CDW transition.

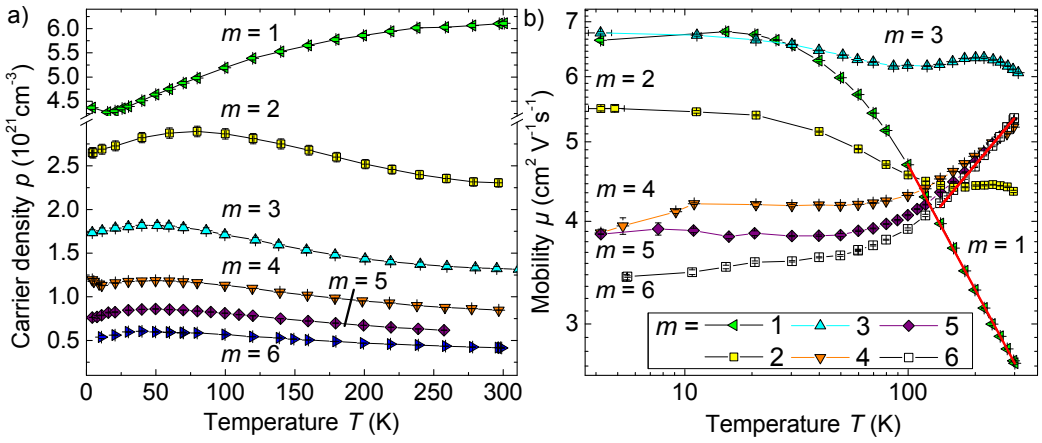

Figure 6.18: a) Temperature-dependent charge carrier density of $[(SnSe)_{1+\delta}]_m[NbSe_2]_1$ (samples A) calculated using a single-band model. The lines are guides to the eye. b) Charge carrier mobility (samples A) in a single-band model of $[(SnSe)_{1+\delta}]_m[NbSe_2]_1$ ferecrystals plotted in double logarithmic scale. The lines are guides to the eye. The red lines indicate linear fits for $m = 1$ and $m = 6$. An additional temperature-independent error of 39 % estimated from [150] is caused by the size of the contacts for both figures.

The temperature-dependent carrier density p, shown in Fig. 6.18a has been calculated assuming a single-band model, $p = 1/(e \cdot R_H)$. The carrier density changes with temperature, which is untypical for metals, for which a constant carrier density would be expected. However, p changes only by a factor of about 1.5 in the temperature range between 4 K and 300 K. For sample $m = 1$ the single-band carrier density p decreases with decreasing temperature. A decrease in p with decreasing temperature could be explained by a freeze-out of charge carriers as binary SnSe is a semiconductor with an exponential decrease of carrier density with decreasing temperature reported for temperatures between $T = 200 - 300$ K [125–127]. For samples $m = 2 - 6$ p increases with decreasing temperature above a certain temperature $T_{p,max}(m)$. An increase in p with decreasing temperatures is unusual for metals as well as semiconductors and might be an effect of using the single-band model. A two-layer model will therefore be discussed in Sect. 6.8.2. Below $T_{p,max}(m)$, p decreases with decreasing T. This would be consistent with a localization of charge carriers. $T_{p,max}$ decreases with decreasing m.

The charge carrier mobility μ, displayed in Fig. 6.18b, has also been calculated using a single band model, i. e. $\mu = R_H/\rho$. The error bars shown here include the error due to the I-V-curve fit and the fit of $V_H(B)$. Due to the large error in mobility the absolute values of μ overlap within the errors. However, the temperature dependence of μ is assumed to be independent of the contact size. For a

Table 6.3: Exponents α for a temperature dependence $\mu \propto T^{\alpha}$ determined from the mobility μ calculated from the Hall coefficient and resistivity using a single-band model.

m	α	**Temperature range for linear fit**
1	-0.506(3)	100 K - 300 K
6	0.324(4)	140 K -300 K

metal with a temperature-independent carrier density, $\mu \propto T^{-1}$ would be expected for temperatures above the Debye temperature and a temperature-independent μ would be expected for low temperatures. For a semiconductor a temperature dependence of $\mu \propto T^{-3/2}$ (due to electron-phonon scattering) would be expected at higher temperatures and $\mu \propto T^{3/2}$ (due to scattering at ionized impurities) at low temperatures. For the ferecrystals none of these behaviors is observed. For the ferecrystals the exponent α in $\mu \propto T^{\alpha}$ has been determined for $m = 1$ and $m = 6$ and is displayed in Table 6.3. There is a striking difference in the temperature dependence of μ between the samples $m = 1$ and $m > 1$. For sample $m = 1$ the mobility decreases with increasing T, which could be due to electron-phonon scattering superposed with another scattering effect which causes the mobility to increase with T, e. g. scattering at ionized impurities. For $m = 4 - 6$ there is an increase in μ with increasing temperatures above about $T_{\mathrm{p,max}}$ which might again be an artifact due to using the single-band model or due to a scattering effect which causes μ to increase with T, such as ionized impurity scattering. Another contribution causing the mobility to increase with increasing T could be from the SnSe layers possibly acting as tunneling barriers. Hence, the with increasing T the charge carriers might have a higher probability to be in the SnSe layers, where the mobility is higher than in $NbSe_2$. This might cause μ to increase with T. The transmission through a tunneling barrier depends exponentially on the barrier thickness, determined by m. For the sample $m = 1$ the barrier is smallest and the charge carriers might overcome this barrier already at very low temperatures $T < 15\,\mathrm{K}$. For $m = 4 - 6$ the tunneling probability might increase with increasing temperatures, because the barrier is thicker.

However, it is also possible that the single-band model assumption made for the calculation of μ is not valid and that more than one type of charge carrier contributes to transport. In spite of the carrier densities differing by 3-4 orders of magnitude for bulk $NbSe_2$ and SnSe, the two types of charge carriers can both contribute significantly to the electrical transport if the difference in the charge carrier mobilities is large enough. A non-zero magnetoresistance measured in sample $m = 6$ at low temperatures supports this possibility and is discussed using a two-band model in Sect. 6.8.2.

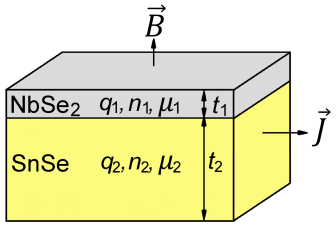

Figure 6.19: Schematic of the two-layer model assumed for the $[(SnSe)_{1+\delta}]_m[NbSe_2]_1$ ferecrystals.

6.8.2 Discussion of magnetoresistance and analysis in a two-layer model

The occurrence of a magnetoresistance effect in the ferecrystals indicates that the simple Drude-Sommerfeld single-band model does not apply at low temperatures. The measured magnetoresistance decreases with increasing temperatures and almost vanishes at $T \geq 10\,\mathrm{K}$ for $m = 6$. The single-band model might therefore still be applicable for higher temperatures. A magnetoresistance effect in the ferecrystals can have several reasons, as described in Sect. 2.3. One obvious reason for a magnetoresistance effect in ferecrystals could be that several types of charge carriers contribute to the electrical transport (Sect. 2.3.3). Since the ferecrystals consist of two different types of layers, a two-layer model is assumed in which one type of carrier is located in the SnSe layers and the other type of carrier is located in the $NbSe_2$ layers. Both layer types are assumed as independent parallel conductors (Fig. 6.19). The parameters of the $NbSe_2$ layers will be denoted with index 1 and the parameters of the SnSe layers will be denoted with index 2. To obtain the charge carrier densities n_1, n_2 and the mobility values μ_1 and μ_2 in the $NbSe_2$ and SnSe layers in the two-layer model, Eqs. (2.17)-(2.19) can been used. The layer thicknesses were determined by SAED of the $[(SnSe)_{1+\delta}]_m[NbSe_2]_1$ samples and are $t_1 = r{\cdot}t_{NbSe_2} = r{\cdot}0.67(2)\,\mathrm{nm}$ and $t_2 = r{\cdot}m{\cdot}t_{SnSe} = r{\cdot}m{\cdot}0.579(5)\,\mathrm{nm}$. The number r of the repeat units contained in the sample cancels in Eqs. (2.17)-(2.19). Furthermore, Eqs. (2.17)-(2.19) require the resistivity and the Hall coefficient, which have been measured at the same temperatures as the magnetoresistance and are given in Tables B.9 and B.10.

Since R_H was determined from a linear range of $V_\mathrm{H}(B)$ close to $B = 0$, Eq. (2.18) can be simplified:

$$R_\mathrm{H}(B \to 0) = \frac{(t_1 + t_2)}{|q_1|^2} \frac{(q_1 n_1 t_1 \mu_1^2 + q_2 n_2 t_2 \mu_2^2)}{(n_1 t_1 \mu_1 + n_2 t_2 \mu_2)^2}. \tag{6.1}$$

The system of Eqs. (6.1) and (2.17) has then been solved for the mobility μ_2 and

the charge carrier density n_2:

$$n_2 = \frac{q_2(t_1 + t_2 - |q_1|n_1 t_1 \rho \mu_1)^2}{|q_1|^2 t_2 (R_\mathrm{H}(t_1 + t_2) - q_1 n_1 t_1 \rho^2 \mu_1^2)} \tag{6.2}$$

$$\mu_2 = \frac{|q_1|(R_\mathrm{H}(t_1 + t_2) - q_1 n_1 t_1 \rho^2 \mu_1^2)}{q_2 \rho (t_1 + t_2 - |q_1| n \rho t_1 \mu_1)} \tag{6.3}$$

These two expressions for n_2 and μ_2 are substituted into equation Eq. (2.19) to obtain the magnetoresistance MR as a function of B, n_1, μ_1, q_1 and q_2. For the signs of q_1 and q_2 there are only 3 possible cases:

- Case 1: n-type $NbSe_2$ layers, p-type SnSe layers.
- Case 2: p-type $NbSe_2$ layers, n-type SnSe layers.
- Case 3: both layers p-type.

The possibility that both layers are n-type (q_1 and q_2 both negative) can be excluded, because the total measured Hall coefficient is positive (Eq. 6.1). The function for $MR(B)$ has been fitted to the data for each of the 3 possible cases individually. The fit function $MR(B)$ then contains only n_1 and μ_1 as fit parameters. A MATLAB program was used to perform a least squares fit for $MR(B)$ with n_1 and μ_1 as fit parameters and is shown in the appendix (B.18 and B.18). Case 3, where both layers are p-type, seems most probable, because the binary materials $NbSe_2$ with low RRR and SnSe are both reported as p-type [52, 54, 60, 124–126, 128, 129]. An electron transfer from the SnSe layers to the $NbSe_2$ layers, as suggested in [23], would also lead to the SnSe and $NbSe_2$ layers both being p-type. However, no fit solution was found for case 3, which fulfills the system of Eqs. (2.17)-(2.19) for any of the temperatures and for $m = 2$ and 6. However, there are fit solutions for case 1 and 2. $MR(B)$ fitted to the data assuming case 1 and 2 leads to two different fit solutions for each case. These two solutions for case 1 and 2 are listed in Table 6.4 for $m = 6$ and $T = 4\,\mathrm{K}$.

As can bee seen in Fig. 6.13, the least-square fit curves match the measured data well. The least-squares fit function obtained for case 1 and 2 both fit the measured data similarly well. The errors of the fit parameters have been calculated considering the 95 % confidence intervals of the nonlinear least squares fit of $MR(B)$ (using the MATLAB program shown in Sect. B.18) as well as the errors resulting from the resistivity, the Hall coefficient and the resolution of the voltage measurement during the magnetoresistance measurement. The error boundaries of the fit results due to the errors in ρ and R_H and the voltage measurement were estimated by varying results of the voltages, ρ and R_H between the upper and lower error boundaries (given in Tables B.9 and B.10) and by determining the upper and lower total error boundaries of the fit parameters from the variation of

Table 6.4: Fit solutions for $T = 4.00(5)$ K for $[(SnSe)_{1+\delta}]_m[NbSe_2]_1$ with $m = 6$. For case 1 the $NbSe_2$ layers are assumed to be n-type and the SnSe layers p-type. For case 2 the $NbSe_2$ layers are assumed p-type and the SnSe layers n-type.

	Parameter	Case 1		Case 2	
		Solution 1	Solution 2	Solution 1	Solution 2
$NbSe_2$	q_1	−e	−e	+e	+e
	n_1 (cm^{-3})	2.1(2)E20	5.6(9)E16	1.9(2)E20	5.6(9)E16
	μ_1 (cm^2/Vs)	67(3)	4158(68)	74(4)	4158(68)
SnSe	q_2	+e	+e	−e	−e
	n_2 (cm^{-3})	9.4(9)E15	3.1(2)E19	9.4(9)E15	3.5(3)E19
	μ_2 (cm^2/Vs)	4158(68)	74(4)	4158(68)	67(3)

all error sources. The errors due to thickness measurement and contact size have been included in the resistivity and Hall coefficient errors.

The fit results for the carrier density n_1 (n_2) of solution 1 of case 1 differ by a factor of m from the respective carrier densities n_2 (n_1) of solution 2 case 2, as shown in Table 6.4. This reflects the equivalence of these two solutions: for case 1 the electrons are assumed to be in the thinner $NbSe_2$ layer and for case 2 they are assumed to be in the m times ticker SnSe layer. The electron and hole mobility values of these two solutions have similar values, since the mobility is unaffected by the thickness in this model. Similarly, solution 2 of case 1 and solution 1 of case 2 differ by a factor of m in their carrier densities and show similar mobility values. Solution 1 of case 1 and solution 1 of case 2 only differ in the signs of the charge carriers for layer 1 and 2, which are unknown. For each of the four solutions shown in Table 6.4, one of the two layers is more semiconductor-like with a low carrier concentration and a high carrier mobility and the other layer is more metal-like with a 3-4 orders of magnitude higher carrier concentration and a lower mobility. The most probable solutions are solution 1 of case 1 and solution 1 of case 2, because $NbSe_2$ is more metal-like and SnSe is more semiconductor-like, similar as in the bulk compounds [52, 60, 124–127]. Then, the only unknown parameter is the sign of the charge carriers. It is not immediately obvious which of the two layers is p-type or n-type. As bulk materials both are reported as p-type and a charge transfer model for ferecrystals, as described in Sect. 2.2.3 would also result in p-type layers. However, $NbSe_2$ as an isolated monolayer has been reported as n-type [8] and bulk $NbSe_2$ has been reported to change sign of the

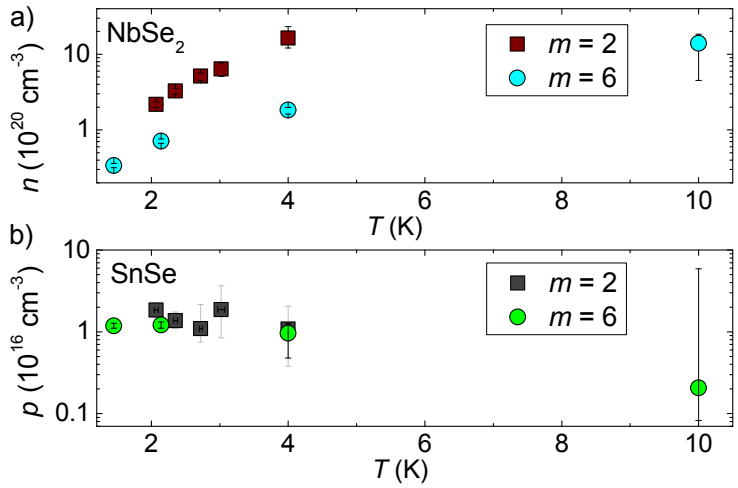

Figure 6.20: Charge carrier densities for a) $NbSe_2$ and b) SnSe obtained from a fit of the two-layer model to $MR(B)$ of samples $[(SnSe)_{1+\delta}]_m[NbSe_2]_1$ with $m = 2$ and $m = 6$ for case 1, solution 1 of Table 6.4.

charge carriers from positive to negative with decreasing temperatures for samples with a high RRR [52, 54, 60], whereas SnSe is only reported as p-type. In addition, the rt Seebeck coefficient of $NbSe_2$ has been reported as n-type [103]. Therefore, solution 1 of case 1 with n-type $NbSe_2$ and p-type SnSe layers seems to be the most probable one among the four solutions shown in Table 6.4.

A similar solution structure with 4 solutions has been obtained for the other temperatures and for sample $m = 2$. The fitted curves for $MR(B)$ of $m = 6$ and $m = 2$ are shown in Figs. 6.13 and B.17. The temperature-dependencies of the fit parameters obtained for solution 1 of case 1 ($NbSe_2$ is n-type and SnSe is p-type) are shown in Figs. 6.20 and 6.21 for $m = 2$ and $m = 6$. Similar as for the results shown in Table 6.4, the error bars shown in Figs. 6.20 and 6.21 were calculated using the error of the fit of $MR(B)$ and the errors estimated from the errors of ρ, R_H and the measurement resolution of the lock-in amplifier.

The carrier density of about $n = (0.045-1.8)\times10^{21}$ cm^{-3} at $T = 10$ K attributed to the $NbSe_2$ layers is about 1-2 orders of magnitude lower than the in-plane carrier density values reported for bulk $NbSe_2$ at $T = 10$ K ($n \approx 2.4 \times 10^{22}$ cm^{-3} [52] and $p \approx 1.1 \times 10^{22}$ cm^{-3} [60]). A similarly low carrier density has been reported for an isolated $NbSe_2$ monolayer, which has been reported to show n-type conductivity with a carrier density 2 orders of magnitude lower than the bulk material [8].

The mobility value of $\mu = 15(11)$ cm^2/Vs for the charge carriers in the $NbSe_2$ layers of $m = 6$ at $T = 10$ K is comparable to the in-plane value reported for bulk $NbSe_2$ single crystals at $T = 10$ K ($\mu = 100$ cm^2/Vs[60]). Similarly, the mobility value for the monolayer of $NbSe_2$ at rt was also reported to be comparable to the

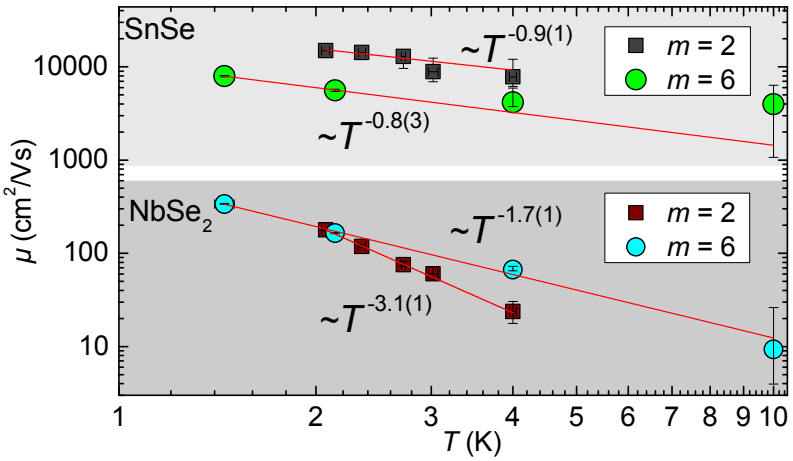

Figure 6.21: Mobility values of SnSe and $NbSe_2$ obtained from a fit of the two-layer model to $MR(B)$ of sample $[(SnSe)_{1+\delta}]_m[NbSe_2]_1$ with $m = 2$ and $m = 6$, for case 1, solution 1 of Table 6.4. The lines are fits of $\mu \propto T^{\alpha}$, where α is the fit parameter.

bulk value [8]. A reason for a slightly lower mobility in the ferecrystals compared to the values reported for bulk $NbSe_2$ single crystals could be the polycrystallinity of the ferecrystals and scattering at the interfaces between the $NbSe_2$ and SnSe layers. These results indicate that the electrical properties of the $NbSe_2$ layers in the ferecrystals are comparable to those reported in [8] for isolated $NbSe_2$ monolayers. The second layer with the lower carrier density and the higher mobility has been assigned to SnSe. No reports for the carrier density in bulk or thin film SnSe at $T = 10\,\mathrm{K}$ have been found. For $T = 77\,\mathrm{K}$ a hole density $p = 0.3 \times 10^{16}\,\mathrm{cm}^{-3}$ to $2 \times 10^{18}\,\mathrm{cm}^{-3}$ [124] has been reported for bulk SnSe averaged over the [0 1 0] and [1 0 0] in-plane directions of SnSe. These carrier densities are similar to those obtained using the two-layer model for the ferecrystals, where $p \approx 10^{16}\,\mathrm{cm}^{-3}$ at $T = 10\,\mathrm{K}$. Mobility values of $\mu = (500-7000)\,\mathrm{cm}^2/\mathrm{Vs}$ at $T = 77\,\mathrm{K}$ [124] have been reported for bulk SnSe single crystals averaged over the [0 1 0] and [1 0 0] in-plane direction. The mobility value of $\mu = (1070 - 6350)\,\mathrm{cm}^2/\mathrm{Vs}$ obtained for SnSe in sample $m = 6$ at $T = 10\,\mathrm{K}$ falls within this range of values reported for binary SnSe. SnSe and $NbSe_2$ in the ferecrystals are polycrystalline with a small grain size and therefore lower mobility values would be expected than those reported for bulk SnSe. However, a channeling effect due to scattering at the interfaces between SnSe and $NbSe_2$ might also lead to increased mobility values.

Figure 6.20a shows that the carrier density of the layer type assigned to $NbSe_2$ for $m = 6$ increases by about one order of magnitude from $n_1 = 0.34(3) \times 10^{20}\,\mathrm{cm}^{-3}$ at $T = 1.4\,\mathrm{K}$ to $8(4) \times 10^{20}\,\mathrm{cm}^{-3}$ at $T = 10\,\mathrm{K}$ and similarly for $m = 2$. This differs from a constant carrier density expected for a typical metal and suggests

that the $NbSe_2$ layers in the ferecrystals are semimetallic, provided the two-layer model assumptions are correct. The isolated $NbSe_2$ monolayers reported in [8] are also reported to be semimetallic. This is also supported by density functional theory calculations reported in [15], which showed that a single isolated $NbSe_2$ monolayer becomes a semimetal in the charge density wave (CDW) state, whereas bulk $NbSe_2$ maintains metallic properties in the CDW state, which sets in at low temperatures. Therefore, the observations in the ferecrystals could result from a CDW in the $NbSe_2$ layers.

For the second layer type, assigned to SnSe, the carrier density n_2 is constant in temperature within measurement error, as shown in Fig. 6.20b. The mobility of the SnSe layers, shown in Fig. 6.21, decreases with increasing temperature for both layer types, and has been fitted with a $\mu \propto T^{\alpha}-$dependence. The exponents $\alpha = -0.8(3)$ to $-0.9(1)$ for the SnSe layers and $\alpha = -1.7(1)$ to $-3.1(1)$ for the $NbSe_2$ layers are not typical for semiconductors, for which roughly $\alpha \approx +1.5$ would be expected at low temperatures and $\alpha \approx -1.5$ at higher temperatures.

In conclusion, the two-layer model analysis shows that the dependence of the magnetoresistance on the magnetic field $MR(B)$ can be explained using a two-layer model for the resistivity, Hall coefficient and magnetoresistance. The values obtained for the carrier density and mobility in each of the two layers are comparable to values reported for single isolated $NbSe_2$ monolayers and bulk SnSe if the assumption is made that $NbSe_2$ is the layer with the higher carrier density and that the signs of the charge carriers differ in the two layers.

However, it could also be possible that the band structure of the ferecrystals differs considerably from the rigid band model and is not only a superposition of the band structures of the individual materials SnSe and $NbSe_2$, making a simple two-layer model invalid. In [87] it has been suggested that a metal cross-substitution (Sect. 2.2) is the reason for stability in the MLCs. Such a non-stoichiometry cannot be excluded for the ferecrystals either and would lead to doped SnSe layers. A higher spatial resolution of EDXS or HAADF-STEM than used in this study would be required to clarify this. However, since the band structure of the $[(SnSe)_{1+\delta}]_m[NbSe_2]_1$ ferecrystals or similar misfit layer compounds is not known so far, the two-band model is a first approximation to explain the observed magnetoresistance effects.

6.9 Superconductivity in $[(SnSe)_{1+\delta}]_m[NbSe_2]_1$ ferecrystals

The resistivity of the ferecrystals $[(SnSe)_{1+\delta}]_m[NbSe_2]_1$ with $m = 1, 3, 4$ and 6 has been measured down to temperatures of $T = 300\,\text{mK}$ and is shown in Fig. 6.22. These resistivity measurements were performed using the van der Pauw method with I-V-curves using direct currents of up to $2\,\mu\text{A}$ for $m = 1$ and 3 and currents up to $0.3\,\mu\text{A}$ for $m = 6$. For currents higher than $0.3\,\mu\text{A}$ the I-V-curves of sample $m = 6$ started to become non-linear near T_c. The critical current for $m = 6$ at $T = 0.62\,\text{K}$ has been determined as $I_c = 18\,\mu\text{A}$ (Fig. B.22). Additionally, temperature-dependent resistance measurements using a lock-in amplifier were performed and are shown in Fig. B.23. The transition temperatures for each stacking sequence are identical within the measurement uncertainty for both measurement techniques (Van der Pauw and lock-in) and for samples A and B. This shows that the normal-to-superconducting transition temperature is not influenced by local sample defects which have led to differences in the resistivity values between samples A and B.

The transition temperature to superconductivity T_c has been defined as the temperature at which the resistivity has decreased to a value of $\rho = 0.9\rho_n$, where

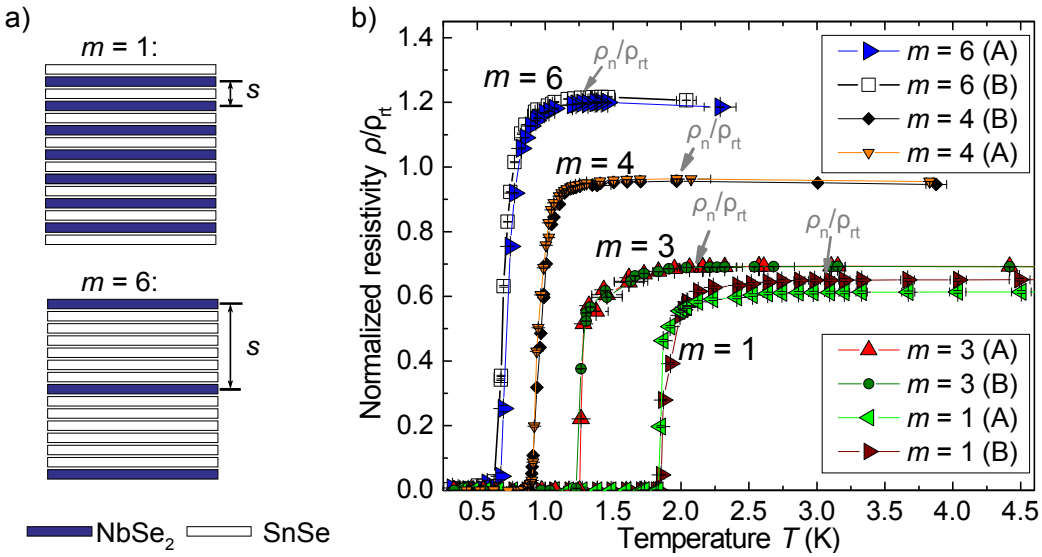

Figure 6.22: a) Schematic structures of the ferecrystal samples $[(SnSe)_{1+\delta}]_m[NbSe_2]_1$ with $m = 1$ and $m = 6$. The distance s between the centers of the superconducting $NbSe_2$ layers is $s = 1.25(5)\,\text{nm}$ for $m = 1$ and $s = 4.14(7)\,\text{nm}$ for $m = 6$. b) Temperature-dependent van der Pauw resistivity ρ at zero magnetic field of $[(SnSe)_{1+\delta}]_m[NbSe_2]_1$ ferecrystals normalized to rt resistivity. Samples A and B indicate the clover and the cross-shaped samples. Lines are guides to the eye.

ρ_n is the residual resistivity, which is indicated in Fig. 6.22b. The transition width ΔT has been determined as the difference between the temperatures at which $\rho = 0.9\rho_n$ and $\rho = 0.1\rho_n$. The resulting values for T_c and ΔT determined from Figs. 6.22 and B.23 are plotted as a function of m in Fig. 6.25 and are given in Table B.11. The resistance of sample $m = 2$ has been measured within the Bachelor thesis of G. Hoffmann [203] down to temperatures of $T = 1.32\,\mathrm{K}$, at which the resistance of the sample dropped to a half of the normal state resistance. It is expected that the resistance of this sample also drops to zero for lower temperatures. The resistances of the sample $m = 5$ has only been measured down to $T = 1.4\,\mathrm{K}$ and no signs for a superconducting transition have been observed down to this temperature. The transition temperature for samples $m = 1 - 4$ and $m = 6$ decreases systematically with increasing m.

In order to determine the in-plane and cross-plane coherence lengths of the ferecrystals and to observe a possible 3D to 2D cross-over in temperature, the in-plane resistance was measured for magnetic fields applied perpendicularly and parallel to the ferecrystal layers. The measurements were performed in one of the van der Pauw resistivity measurement configurations using a lock-in amplifier with an alternating current of 50 nA, as described in Sect. 4.5. Exemplary results of the $R(H)$ are shown in Fig. 6.23. For clarity not all of the measured curves are shown here. More data is shown in Figs. B.24 and B.25. The critical magnetic fields decrease systematically with increasing temperature for $m = 1$ and $m = 6$ for perpendicular and parallel magnetic fields. The parallel critical magnetic fields $H_{c\parallel}$ are considerably higher than the perpendicular critical magnetic fields $H_{c\perp}$. A hysteresis was observed between increasing and decreasing magnetic fields for $m = 6$ with the critical field for an increasing magnetic field being lower than for a decreasing magnetic field. This hysteresis effect was lower for sample $m = 1$. The sweep rate of the magnetic field was 0.1 T/min for both samples. Hysteresis effect were avoided for the subsequent measurements in parallel fields and for the measurements of sample $m = 3$ by keeping the magnetic fields constant until the voltage measured at the sample has settled (within several minutes). The resistance of sample $m = 1$ shows an unusual negative magnetoresistance effect in the normal state with a decreasing resistance for increasing magnetic fields. All samples were cross-shaped and have been measured in similar van der Pauw resistance measurement configurations in which the current was applied between two adjacent arms of the cross and the voltage was measured between the other two contacts, as shown in Fig. 4.2. No such magnetoresistance effect has been observed for $m = 6$.

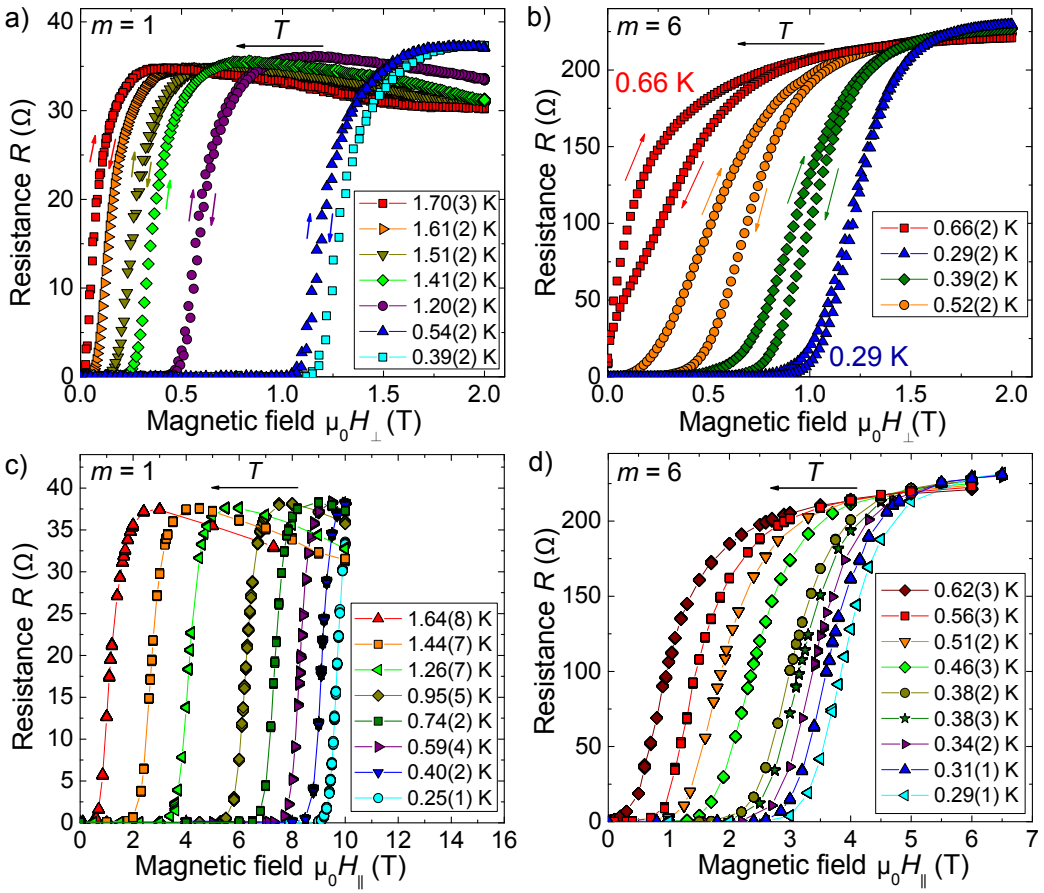

Figure 6.23: Magnetic field dependence of the resistance in a magnetic field perpendicular to the layers of $[(SnSe)_{1+\delta}]_m[NbSe_2]_1$ ferecrystals with a) $m = 1$ (sample B) and b) $m = 6$ (sample B); c) in a magnetic field parallel to the layers for $m = 1$ (sample B) and d) $m = 6$ (sample B). The sweep rate of the magnetic field was 0.1 T/min for a) and b) and for the measurements in c) and d) static magnetic fields were applied. Lines are guides to the eye.

Angle-dependent critical magnetic field measurements were performed at sample $[(SnSe)_{1+\delta}]_m[NbSe_2]_1$ with $m = 1$ at $T = 1.60(1)$ K in a flow-cryostat with magnetic fields of up to 0.66 T. Angle θ has been defined as the angle between the magnetic field and the ferecrystal layer plane. The result is shown in Fig. 6.24. The values for the critical magnetic fields were defined as the magnetic field at which the resistance is 50 % of the normal resistance. Additionally, two values measured in the 10-T-system in perpendicular ($\theta = 90°$) and parallel ($\theta = 0°$) critical magnetic field are also displayed. The error bars for the magnetic field were estimated as 10 mT from the voltage vs. magnetic field curves. The fits shown in

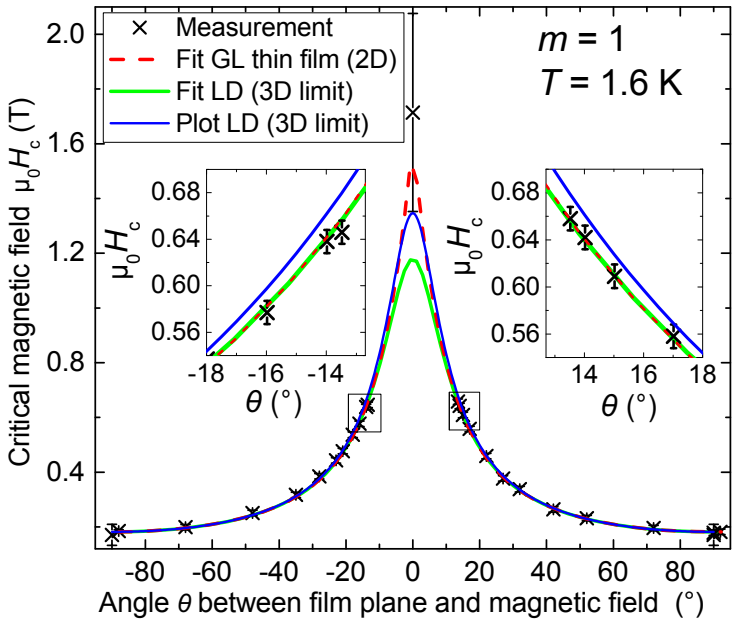

Figure 6.24: Angle-dependent critical magnetic field measurements of $[(SnSe)_{1+\delta}]_m[NbSe_2]_1$ with $m = 1$ and 2D fit (Eq. (2.39), red dahed) and 3D fit (Eq. (2.38), green solid). The blue line is a plot of the LD 3D equation taking into account the lower value for $\theta = 0°$. The insets show details of the plot.

Fig. 6.24 will be discussed in Sect. 6.10.6.

6.10 Discussion of superconductivity in $[(SnSe)_{1+\delta}]_m[NbSe_2]_1$ ferecrystals

6.10.1 The transition temperatures in comparison to $NbSe_2$

The transition temperatures T_c to superconductivity are shown in Fig. 6.25 as a function of m, the number of SnSe bilayers between two $NbSe_2$ monolayers. The transition temperatures reported for isolated $NbSe_2$ monolayers [1], bi/trilayers [10], MLCs and ferecrystals $[(PbSe)_{1+\delta}]_1[NbSe_2]_1$ (this work) are also shown for comparison. Experiments described in [1, 9, 10, 63] have shown that T_c of $NbSe_2$ systematically decreases with decreasing sample thickness. In accordance with this, the T_c values of the ferecrystals are much lower than those reported for bulk $2H$-$NbSe_2$ single crystals, for which T_c values of 7.0 K [58, 61], 7.1 K [62], 7.2 K [83] and 7.39 K [59] have been reported. The T_c values measured for the ferecrystals are similar to $T_c \approx 1.2$ K to 2.75 K reported for 2-3 monolayers of $NbSe_2$ [10] and are lower than T_c reported for a single $NbSe_2$ layer [1]. A possible reason for a lower T_c of the ferecrystals in comparison to $NbSe_2$ monolayers can be differences in the density of states at the Fermi level, e. g. due to charge transfer from SnSe to $NbSe_2$ as described in Sect. 2.2.3, which can lead to changes in T_c according to the BCS theory.

Sample $[(SnSe)_{1+\delta}]_m[NbSe_2]_1$ with $m = 1$ contains a total number of about 36 $NbSe_2$ layers. $NbSe_2$ flakes consisting of only 9-16 monolayers, showed transition temperatures of $T_c \approx 5.0$ K to 6.7 K [9, 10]. Extrapolating the results of the thickness dependence of T_c reported in [9, 10], a sample with the thickness of 36 $NbSe_2$ layers would have a transition temperature close to $T_c \approx 7$ K, similar as bulk $NbSe_2$. The fact that T_c for the ferecrystals $[(SnSe)_{1+\delta}]_m[NbSe_2]_1$ is much lower than this value, suggests that the superconductivity in these ferecrystals is rather determined by the single $NbSe_2$ layers separated by SnSe and not by the total thickness of all $NbSe_2$ layers in the sample. One possible effect leading to a lower T_c is the proximity effect, which describes the lowering of T_c of a superconductor, which is in contact with a normal conductor [177]. However, the proximity effect is higher for a superconductor-metal interface than for a superconductor-semimetal interface [177, 197]. The analysis in a two-layer model has suggested that the carrier density and mobility values of the SnSe layers are semiconductor-like and the SnSe layers have a very low carrier density. Therefore, a strong decrease in T_c due to the proximity effect appears unlikely for these SnSe-based ferecrystals. The fact that T_c decreases with increasing m could be a result of a decrease in coupling between the $NbSe_2$ layers due to the increased $NbSe_2$ layer separation. However, the SnSe between the $NbSe_2$ layers in the ferecrystals could also lead to a decrease in T_c compared to isolated $NbSe_2$ layers due to the proximity effect.

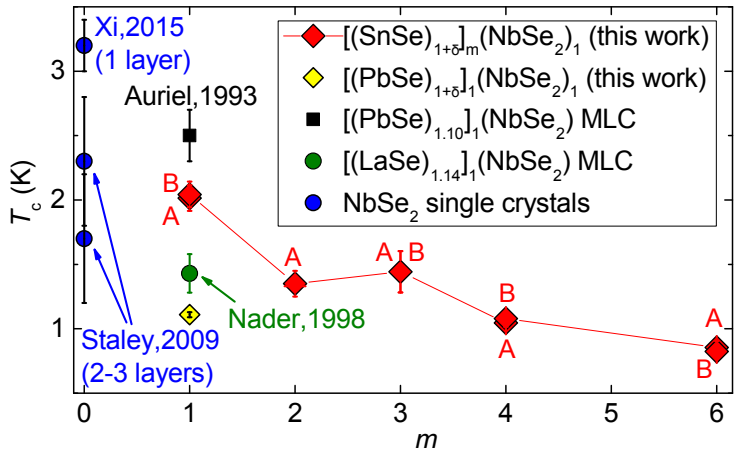

Figure 6.25: Transition temperatures T_c of $[(SnSe)_{1+\delta}]_m[NbSe_2]_1$ ferecrystals determined as the temperatures at which $\rho = 0.9\rho_n$. Values for $NbSe_2$ single crystals are reported by Xi *et al.* [1] and Staley *et al.* [10]. T_c for misfit layer compounds (MLCs) reported by Nader *et al.* [208] and Auriel *et al.* [40].

6.10.2 The transition temperatures in comparison to other misfit layer compounds and ferecrystals

No reports on the transition temperatures of $[(SnSe)_{1+\delta}]_m[NbSe_2]_1$ misfit layer compounds (MLCs) have have been found. However, there are reports on transition temperatures of other MLCs containing single $NbSe_2$ layers, as shown in Fig. 6.25. For the MLC $[(PbSe)_{1.10}]_1[NbSe_2]_1$ $T_c = 2.4\,K$ has been reported [40] and for the MLC $[(LaSe)_{1.14}]_1[NbSe_2]_1$ $T_c \approx 1.4\,K$ has been reported [74, 208]. Measurements of the temperature-dependent critical magnetic field of the MLC $[(LaSe)_{1.14}]_1[NbSe_2]_1$ revealed signatures of 2D-superconductivity [74, 208]. Typically, the $NbSe_2$ layers in MLCs are single crystalline and not turbostratically disordered. The T_c values of the $[(SnSe)_{1+\delta}]_m[NbSe_2]_1$ ferecrystals are in between the values reported for the MLC $[(PbSe)_{1.10}]_1[NbSe_2]_1$ and $[(LaSe)_{1.14}]_1[NbSe_2]_1$. This suggests, that the polycrystallinity and turbostratic disorder do not influence T_c drastically, or that the effect of SnSe instead of LaSe or PbSe cancels the effect of the polycrystallinity or turbostratic disorder on T_c. As shown in Fig. 6.25, the transition temperature of the $[(PbSe)_{1+\delta}]_1[NbSe_2]_1$ ferecrystal is lower than T_c of the $[(SnSe)_{1+\delta}]_1[NbSe_2]_1$ sample. One possible explanation for this could be a stronger proximity effect in the PbSe-based ferecrystals, which would lead to a stronger decrease in T_c compared to the SnSe-based ferecrystals. The stronger proximity effect might be explained by a higher density of states near the Fermi level in the PbSe layers compared to the SnSe layers. This might either be a consequence of bulk PbSe having a narrow band gap of 0.3 eV [65, 66], whereas bulk SnSe has a wider band gap of 0.9 eV [67–69]. A different charge transfer

mechanism between the MSe and $NbSe_2$ layers for M= Pb or Sn could also result in a different density of states at the Fermi level in the normal state and therefore to a different T_c.

6.10.3 The transition width ΔT

The transition width ΔT obtained from the normal-to-superconducting transition in resistivity has been determined as the temperature range between $\rho = 0.9\rho_n$ and $\rho = 0.1\rho_n$ and are given in Table B.11. The transition widths ΔT for the $[(SnSe)_{1+\delta}]_m[NbSe_2]_1$ ferecrystals with $m = 1, 3, 4, 6$ ranges between 0.05 K to 0.28 K, which is 2 % to 25 % of T_c. These relative transition widths are similar to values reported for the MLCs $[(LaSe_{1+x})_1[NbSe_2]_1$ [74], where $\Delta T/T_c$ is about 5 % and for an isolated $NbSe_2$ monolayer, for which $\Delta T/T_c \approx 9\,\%$ has been reported [1]. The relative transition widths for the ferecrystal are higher than for bulk $NbSe_2$ single crystals, for which $\Delta T/T_c = 1\,\%$ has been reported [58]. Few-layer $NbSe_2$ flakes have been reported to show several steps in $R(T)$ during the transition to superconductivity, which might be ascribed to either an inhomogeneous thickness or disorder in the stacking sequence [1, 9, 63]. As visible in the resistance measurements along one van der Pauw measurement configuration in Fig. B.23, for $m = 1, 2, 3$ and $m = 4$ kinks in $R(T)$ appear above the transition temperature to superconductivity which are not present when averaging the resistance measurements along all van der Pauw configurations, as done for the van der Pauw measurement shown in Fig. 6.22. One possible reason for the kinks found in the $R(T)$ curves of the ferecrystals near the transition temperatures could be structural inhomogeneities in the samples, which are not present in the sample areas observed by HAADF-STEM in this study. Another explanation for the kinks would be an influence of the indium contacts. The superconducting transition temperature of indium, which was used for contacting the ferecrystal samples is about $T_c = 3.4$ K [200–202]. A possible proximity effect could cause the resistance in the ferecrystals to decrease near the indium contacts when the indium becomes superconducting. However, as visible in Figs. 5.26 and B.7, there is no kink in the measured resistivity near the transition temperature of indium. Therefore, the indium is not thought to play a major role for the superconductivity measurements of the ferecrystals due to the applied four-terminal sensing measurement technique. Further measurements with different contacting materials, e. g. gold would be necessary to confirm this.

6.10.4 The dependence of the transition temperature on *m*

The measured decrease in transition temperature with increasing m suggests that T_c is not only influenced by the reduced thickness of the $NbSe_2$ layers, but also by the stacking sequence of the SnSe and the $NbSe_2$ layers. Binary SnSe does

usually not become superconducting at normal pressure [130]. However, a possible increased chemical pressure due to the layering in the ferecrystals or a charge transfer between the SnSe and $NbSe_2$ layers could lead to different electron densities of states at the Fermi energy for different m. According to the BCS theory, T_c increases with increasing density of states at the Fermi level [75]. The proximity effect could then lead to a decreased T_c with increasing m in ferecrystals. As an example, intercalation of organic molecules between $NbSe_2$ layers has shown a similar effect of T_c decreasing to below $T_c \leq$ (0.35-3)K for intercalation with different organic molecules of thickness of about 1 nm [106]. Intercalation of semimetallic $TiSe_2$ layers between stacks of six $NbSe_2$ monolayers in ferecrystals has been reported to lead to a decrease in transition temperature from $T_c = 4.4\,K$ to $T_c = 2.6\,K$ as the thickness of the $TiSe_2$ layers is increased [157]. A final explanation for these effects has not been reported so far. A similar effect could be present in the $[(SnSe)_{1+\delta}]_m[NbSe_2]_1$ ferecrystals. A decrease in interlayer coupling between the $NbSe_2$ layers for increasing the distance between the $NbSe_2$ layers appears conceivable. Therefore, in the following the dependence of the Ginzburg-Landau coherence lengths obtained from the temperature dependence of the critical magnetic fields of the samples will be discussed.

6.10.5 The temperature dependence of the critical magnetic fields

In order to obtain the in-plane and cross-plane coherence lengths ξ_{ab} and ξ_c, the critical magnetic fields are plotted against the reduced temperature $t = T/T_c$ as shown in Fig. 6.26 for $m = 1$ and $m = 6$ and in Fig. B.26 for $m = 3$. The critical magnetic fields $H_{c\parallel}$ and $H_{c\perp}$ denote the critical magnetic fields for an orientation of the magnetic field parallel and perpendicular to the ferecrystal layers, respectively. The values for the critical magnetic fields were defined as the magnetic field at which the resistance is 50 % of the maximum resistance measured in normal state near T_c. The error bars for the critical magnetic fields were defined to include the values obtained for the increasing and the decreasing magnetic fields. Because of the hysteresis effect observed in sample $m = 6$, the error bars for $H_{c\perp}$ of this sample are larger than for $m = 1$. According to the anisotropic Ginzburg-Landau theory, a linear relationship between the upper critical perpendicular magnetic field $H_{c2\perp}$ and the temperature is expected near T_c, for a 2D as well as a 3D superconductor, Eq. (2.34). Since $NbSe_2$ is a type-II superconductor, the ferecrystals are also expected to be type-II superconductors and the measured critical magnetic fields $H_{c\perp}$ and $H_{c\parallel}$ are assumed to be the upper critical magnetic fields $H_{c2\perp}$ and $H_{c2\parallel}$ of the ferecrystals. The solid and dashed lines shown in Fig. 6.26 indicate the estimated boundaries for linear fits of $H_{c\perp}(t)$ and $H_{c\parallel}(t)$ (Eqs. (2.34) and (2.35)) near $t = 1$. From the slopes of these boundaries, the boundaries for $\xi_{ab}(0)$ and $\xi_c(0)$ are calculated using Eqs. (2.34) and (2.35). The results for $\xi_{ab}(0)$ and $\xi_c(0)$ and the respective error ranges are given in Table 6.5 for $m = 1, 3$ and

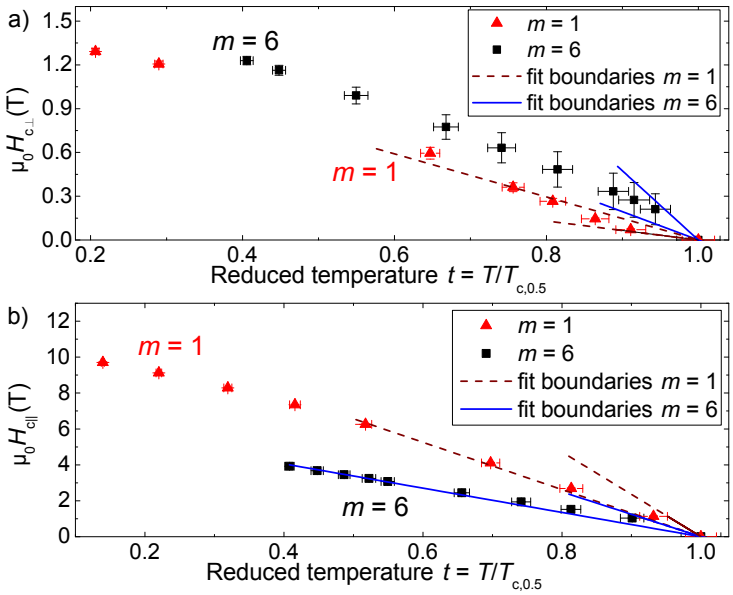

Figure 6.26: Critical magnetic field a) perpendicular and b) parallel to the layers of the $[(SnSe)_{1+\delta}]_m[NbSe_2]_1$ ferecrystals. The solid and dashed lines indicate the boundaries for linear fits of $H_{c\perp}(t)$ and $H_{c\parallel}(t)$, Eqs. (2.34) and (2.35) near $t = 1$. The transition temperature $T_{c,0.5}$ has been determined at $\rho = 0.5\rho_n$.

6. They are a first approximation, since only few data points have been measured for $H_{c\perp}(T)$ and for $m = 6$ large error bars are present due to the hysteresis effect. More measurements in the vicinity of T_c at static magnetic fields would be necessary to obtain more precise values for ξ_{ab} and ξ_c.

The obtained values for ξ_{ab} range between 11(3) nm and 23 nm. To estimate whether these values for ξ_{ab} indicate a clean or a dirty limit, the carrier mean free paths l have been calculated using equation Eq. (2.10). For samples $m = 1$ and $m = 3$ the normal state carrier density obtained by the Hall measurements, calculated using the single-band model, has been used. For $m = 6$ the carrier density obtained from the two-layer model has been used. The temperature dependencies of the mean free paths l for the three samples are plotted in Fig. B.27. From these graphs the values of l extrapolated to low temperatures were estimated and are given in Table 6.5. This is only a rough estimation for the mean free paths, because Eq. (2.10) holds for quasi-free electrons in metals with a single band which might not be appropriate for ferecrystals, especially for sample $m = 6$, in which $NbSe_2$ shows a semi-metallic temperature dependence of the carrier density at low temperatures. The calculated mean free paths are lower than the BCS coherence lengths $\xi_{ab}(0)$ by about two orders of magnitude for all 3 samples. Therefore, the samples are assumed to be in the dirty limit and the in-plane BCS-coherence

Table 6.5: In-plane coherence length ξ_{ab}, in-plane mean free path l, in-plane BCS-coherence length $\xi_{0\parallel}$, cross-plane coherence length ξ_c, repeat unit distance s determined by TEM, normal resistivity ρ_n and T_c of $[(SnSe)_{1+\delta}]_m[NbSe_2]_1$ ferecrystals, determined at $\rho = 0.9\rho_n$.

m	$\xi_{ab}(0)$ (nm)	l (nm)	$\xi_{0\parallel}$ (nm)	$\xi_c(0)$ (nm)	Repeat unit distance s (nm)	ρ_n (μΩm)	T_c (K)
1	18(5)	≈ 1.2	≈ 356	1.3(8)	1.25(5)	4.7(3)	1.9(1)
3	14(1)	≈ 1.7	≈ 146	not meas.	2.37(1)	5.3(3)	1.49(6)
6	11(3)	≈ 0.6	≈ 258	4(3)	4.14(7)	35(2)	0.82(4)

length $\xi_{0\parallel}$ is derived from Eq. (2.27) and is also given in Table 6.5.

A 3D to 2D crossover or 2D behavior could not be identified from the measured data of the temperature-dependent parallel critical magnetic fields. A 3D to 2D crossover is either not present in these ferecrystal samples or the distance in temperature between the measurement points does not allow for an identification of the 3D to 2D crossover effect. For a 2D superconductor a strong upturn in $H_{c\parallel}(t)$ would be expected with $\mu_0 H_{c\parallel}(t) \propto (1-t)^{1/2}$ (Eq. (2.36)) below a crossover temperature T^*, as e. g. reported in [73, 77, 78], which is not observed in Fig. 6.26b. An estimation of an upper boundary for a possible T^* from the measured data is given in the Appendix (Fig. B.29). The values of ξ_c obtained for the ferecrystals are 1.3(8) nm for $m = 1$ and 4(3) nm for $m = 3$. These values are similar to the distances s between the superconducting $NbSe_2$ layers for each sample. This indicates that along the stacking direction the superconducting order parameter ψ is limited by the repeat unit distance s. This would mean that two $NbSe_2$ layers are coupled across one SnSe layer, but not across three or more repeat units. For $m > 6$ larger distances between superconducting layers are present, which might lead to a loss of coherence along the cross-plane direction and to a 3D to 2D transition with increasing m. In Table 6.6 the coherence lengths obtained for the ferecrystals are compared to reported coherence lengths for single-crystalline $2H$-$NbSe_2$ and several MLCs. The coherence lengths for the MLCs listed in Table 6.6 and for $NbSe_2$ reported in [209] have been determined from the slopes of $H_{c\parallel}$ and $H_{c\perp}$, which were also determined from resistance measurements. None of these reported materials fulfills the condition $\xi_c < s/\sqrt{2}$ for 2D behavior. However, the ferecrystals are closest to this condition. For $NbSe_2$ the cross-plane coherence length ξ_c is about 8.8 times higher than $s/\sqrt{2}$. For the MLC $[(LaSe)_{1.14}]_1[NbSe_2]_2$ it is at least 3.2 times higher than $s/\sqrt{2}$. For the ferecrystals $[(SnSe)_{1+\delta}]_m[NbSe_2]_1$ with $m = 1$ and $m = 6$ ξ_c is about 1.4(7) times higher than $s/\sqrt{2}$. The lower co-

Table 6.6: Critical temperatures T_c, determined at $\rho \approx 0.9\rho_n$, in-plane and cross-plane coherence lengths $\xi_{ab}(0)$ and $\xi_c(0)$ and $\xi_c(0)/(s/\sqrt{2})$, where s is the largest distance between two consecutive superconducting layers. For a 2D superconductor $\xi_c \leq s/\sqrt{2}$. For the ferecrystals s was determined using TEM. For $NbSe_2$ and the misfit layer compounds (MLCs), s was approximated assuming similar thicknesses of the individual SnSe and $NbSe_2$ layers as in ferecrystals.

Compound	T_c (K)	$\xi_{ab}(0)$ (nm)	$\xi_c(0)$ (nm)	$\frac{\xi_c(0)}{s/\sqrt{2}}$ (nm)	Ref.
$[(SnSe)_{1+\delta}]_1[NbSe_2]_1$	1.9(1)	18(5)	1.3(8)	1.4(7)	this work
$[(SnSe)_{1+\delta}]_6[NbSe_2]_1$	0.82(4)	11(3)	4(3)	1.4(7)	this work
$2H$-$NbSe_2$ single crystal	6.90-7.02	9.9	4.0	≈ 9.4	[210]
$2H$-$NbSe_2$ single crystal	7.11	11.0	3.7	≈ 8.7	[211]
$2H$-$NbSe_2$ single crystal	7.4	9.0	2.7	≈ 6.4	[209]
$[(PbSe)_{1.12}]_1(NbSe_2)_2$ MLC	2.9	16.8	3.4	≈ 4	[41]
$[(SnS)_{1.17}]_1(NbS_2)$ MLC	2.88	26.7	2.8	3.35	[212]
$[(LaSe)_{1.14}]_1(NbSe_2)_2$ MLC	5.43	9.3	2.7	≈ 3.2	[213]

herence lengths ξ_c for the ferecrystals compared to the misfit layer compounds could be a result of the semiconducting large-band gap SnSe layers in ferecrystals, which are not present in the $NbSe_2$ single crystals and the MLCs.

The trend in the temperature dependence of the perpendicular critical magnetic field $H_{c\perp}(T)$ for the ferecrystals is similar to the trend of $H_{c\perp}$ in $NbSe_2$ single crystals [58, 59]. The parallel critical magnetic field $H_{c\parallel}(T)$, however, reported for $NbSe_2$ single crystals, decreases with a different (positive) curvature as temperature is increased near T_c [59]. This differs from the $H_{c\parallel}(T)$ curve measured for the ferecrystals. Fig. 6.27 shows the trend of the temperature dependence of the critical magnetic fields for the ferecrystals fitted to the empirical equation $H_c(t) = \mu_0 H_c(0)(1-at^2)$, Eq. (2.32), where $\mu_0 H_c(0)$ and a are fit parameters. Bulk $NbSe_2$ is reported to show a temperature dependence $H_{c\perp}(t) = \mu_0 H_{c\perp}(0)(1-at^2)$ with an empirical parameter $a \approx 2.02$ [167]. This type of temperature dependence is observed for the ferecrystals with $m = 6$, whereas for the ferecrystals $m = 1$ a different behavior is observed. Using $a = 1$, usually applied for type-I-superconductors, does not show a better agreement with the measured data for $m = 1$, as is displayed in Fig. B.28. The values for the fit parameter a obtained for the ferecrystals are close to the value 1 for type-I superconductors and differ

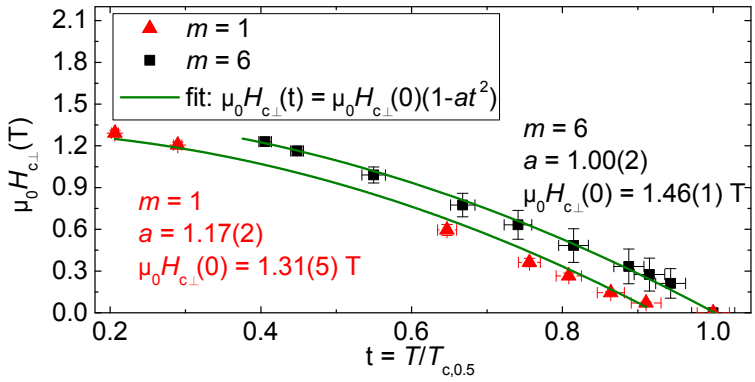

Figure 6.27: Critical magnetic fields perpendicular to the $[(SnSe)_{1+\delta}]_m[NbSe_2]_1$ ferecrystal layers. The fits are according to the empirical parabolic law, Eq. (2.32), with fit parameters $\mu_0 H_c(0)$ and a. The least-square fit curves match the data for $m = 6$ well, but do not match the data for $m = 1$.

from the value $a = 2.02$ for $NbSe_2$ [167]. This result is unexpected, because the ferecrystals are probably type-II superconductors, because $NbSe_2$ is a type-II superconductor. The temperature dependence of the parallel critical magnetic field for bulk $NbSe_2$ has been fitted and explained in [59] using the Takanaka theory [214], which fits to the $NbSe_2$ data in a small range near T_c. The Takanaka theory takes into account anisotropy of the energy gap and nonlocal effects next to the simple effective mass model and was applied in [59] to explain the unusual $H_{c\parallel}(T)$ behavior and it was concluded that the energy gap of single-crystalline $NbSe_2$ is anisotropic. An ansiotropic energy gap in $NbSe_2$ has also been found in [196]. In addition, the discussion of a fit of the $H_{c\parallel}(T)$ of $NbSe_2$ to the Josephson coupling model developed by Klemm [176] in [59] led to the conclusion that the coupling strength in bulk $NbSe_2$ single crystals is too strong to fit to the Josephson coupling model [59].

6.10.6 The angle dependence of the critical magnetic fields

The angle-dependent critical magnetic field measured in the cryostat with a rotating system (black crosses in Fig. 6.24) was fitted to the LD equation in the 3D anisotropic limit, Eq. (2.38) using γ as fit parameter. This fit yields a critical parallel magnetic field much lower than the measured $H_{c\parallel}$. For demonstration, a plot of the LD equation in the 3D anisotropic limit, Eq. (2.38), is also shown, for which the parameter γ is chosen such that the plot includes the lower boundary of the measured parallel critical magnetic field measured in the 10-T-system. This plot then does not match the data measured in the flow-cryostat, which is visible in the insets of Fig. 6.24. A possible misalignment of a few degrees of the sample in

the 10-T-system with respect to the magnetic field would result in measured critical fields lower than the true parallel critical magnetic field due to an additional perpendicular component of the magnetic field. This would mean that the true parallel critical magnetic field would be even higher than the measured one and that would make the disagreement with the LD formula in the 3D anisotropic limit even higher. The data was also fitted to the 2D GL thin film equation, Eq. (2.39), which is shown in red in Fig. 6.24. For this purpose Eq. (2.39) was solved for $H_c(\theta)$ and the anisotropy parameter γ was used as a fit parameter. The parallel critical magnetic field resulting from the fit agrees well with the measured parallel critical magnetic field. The result that the 2D GL fit matches the measured data for $H_c(\theta)$ and the 3D fit does not, is in contrast to the result obtained from $H_{c\parallel}(T)$, where the 3D anisotropic Lawrence-Doniach model matched the data better. A similar systematic deviation of the measured data from a fit to the 3D anisotropic GL model, Eq. (2.38), was also reported for $2H$-$NbSe_2$ single crystals in [59], where the measured critical parallel fields are also systematically lower than the fit for angles between $\theta \approx 5° - 20°$. However, for the angle-dependent measurement shown in Fig. 6.24 there is only one data point for $\theta = 0°$ from the measurement in the 10-T-system supporting this statement, which might not be sufficient. A measurement with a rotating system in a Helium-3-system and high magnetic fields would be more advantageous to make a more clear statement about the result of the angle-dependent critical magnetic field and also to get more precise results for the measurements of ξ_c. In addition, a possible anisotropy in the energy gap of $NbSe_2$ can also lead to deviations in the $H_c(T)$ and $H_c(\theta)$ behavior compared to the simple effective mass model, as discussed in [59].

6.10.7 The anisotropy parameter

According to the Lawrence-Doniach model for 3D anisotropic superconductors, the square of the ratios between the parallel and the perpendicular critical magnetic fields equals the effective mass ratio m_c/m_{ab}, Eq. (2.33), where m_{ab} and m_c are the in-plane and cross-plane components of the effective mass components of the quasi-particles in the LD model. This is plotted in Fig. 6.28. For comparison, the data reported for $2H$-$NbSe_2$ from [59] are also shown. For a 3D anisotropic superconductor a temperature-independent effective mass ratio would be expected (Eqs. (2.34) and (2.35)). This is the case for $m = 6$. However, for $m = 1$ the effective mass ratio increases with increasing t. In contrast to the ferecrystals, $NbSe_2$ shows a decreasing effective mass ratio with increasing temperatures. The effective mass ratio for $m = 1$ is higher than for $m = 6$ and bulk $NbSe_2$ single crystals.

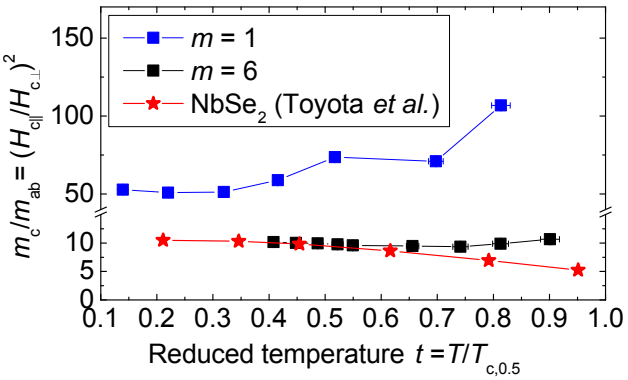

Figure 6.28: Effective mass ratios for $[(SnSe)_{1+\delta}]_m[NbSe_2]_1$ ferecrystals from the ratios between parallel and perpendicular critical magnetic fields and data reported for $2H$-$NbSe_2$ [59]. Lines are guides to the eye.

7 Comparison of ferecrystals with M = Pb and Sn

7.1 Structural differences between ferecrystals $[(MSe)_{1+\delta}]_m[NbSe_2]_n$ with M = Pb and Sn

In contrast to the $[(SnSe)_{1+\delta}]_m[NbSe_2]_1$ ferecrystals, the samples of the system $[(PbSe)_{1+\delta}]_1[NbSe_2]_n$ have shown defect layers between the substrate and the ferecrystals and also defect layers near the surface of the thin films for the first two synthesis batches investigated in this work. A third batch of $[(PbSe)_{1+\delta}]_1[NbSe_2]_n$ samples did not show the defect layers. In the center of the thin films of the first two batches of $[(PbSe)_{1+\delta}]_1[NbSe_2]_n$ the chemical composition and atomic structure are mainly as expected for the ferecrystals. However, also in the center of the thin films the $[(PbSe)_{1+\delta}]_1[NbSe_2]_n$ ferecrystals of batch 1 and 2 exhibit a much higher stacking defect area fraction than the ferecrystals containing SnSe. In an image showing a projected area of about 4000 nm^2 the samples of $[(PbSe)_{1+\delta}]_1[NbSe_2]_1$ showed a fraction of defect area of 13 %, whereas the $[(SnSe)_{1+\delta}]_1[NbSe_2]_1$ ferecrystals showed a fraction of defect area of only 1.6 %. The type of defect observed for the (m,n)=(1,1) samples was similar for SnSe- and the PbSe-containing ferecrystals: over a distance of several nanometers a $NbSe_2$ layer is interrupted and replaced by a PbSe or SnSe bilayer. The adjacent layers around these defects are almost not bent due to the similar c-lattice parameters of SnSe (or PbSe) and $NbSe_2$.

Both, the PbSe- and the SnSe-based ferecrystal samples might be susceptible to the loss of selenium, due to the high vapor pressure of selenium. The top layers of the PbSe-type ferecrystals of batch 1 and 2 show a decreased selenium concentration compared to the selenium concentration in the ferecrystals. The EDXS maps of the SnSe type of ferecrystals show no depletion of selenium, neither next to the substrate, nor next to the surface. However, the $[(SnSe)_{1+\delta}]_m[NbSe_2]_1$ samples have been prepared for TEM sooner after synthesis than the $[(PbSe)_{1+\delta}]_1[NbSe_2]_n$ samples and therefore a direct comparison is difficult. Annealing of the samples in an atmosphere containing additional Se vapor might prevent a selenium depletion near the surface of the samples [21].

The differences in the sample quality between the PbSe-based and the SnSe-based ferecrystal systems can have several reasons, e. g. the synthesis process, the substrate material, aging between synthesis and TEM analysis, TEM sample

Table 7.1: Melting point, heat of fusion and Gibbs free energy of formation for PbSe and SnSe [216].

Properties	PbSe	SnSe
Melting point (K)	1351(2)	1149(2)
Heat of fusion (kJ/mol)	42.3(4)	35.5(4)
Gibbs free energy of formation at 298 K, 1 bar (kJ/mol)	-143	-135

preparation or a fundamental difference in their synthesizability as ferecrystals. For the synthesis process, the chemical composition and the annealing temperature have been optimized for both sample systems using electron probe microanalysis and X-ray diffraction for analysis [23, 24, 32]. The TEM analysis led to the conclusion that the substrate material, aging and TEM sample preparation did not influence the thickness of the intermediate and surface defect layers.

Indications for a difference in the synthesizability of SnSe and PbSe containing ferecrystals are given in an article by Hernán *et al.* [215], which describes an experiment in which the MLCs $[(PbSe)_{1+\delta}]_1(NbSe_2)_2$ and $[(SnSe)_{1+\delta}]_1(NbSe_2)_2$ were tried to be intercalated with lithium using an n-butyl-lithium solution. This experiment was successful for the $[(SnSe)_{1+\delta}]_1(NbSe_2)_2$ MLCs. In contrast, the MLCs $[(PbSe)_{1+\delta}]_1(NbSe_2)_2$ decomposed into the phases $NbSe_2$ and PbSe. The authors ascribed this to the higher thermodynamical stability of PbSe compared to SnSe. Several parameters giving information on the thermodynamic stability of PbSe and SnSe are given in Table 7.1. These parameters show that PbSe is thermodynamically more stable than SnSe, and that PbSe might therefore be less suitable for being alternately layered with $NbSe_2$ in the ferecrystals. Furthermore, SnSe itself is a layered compound with bilayers of SnSe alternately stacked along the *c*-direction, with a shift between the bilayers perpendicular to the stacking direction (Sect. 2.1). This *c*-direction is the same as the stacking direction in ferecrystals. This layered structure of bulk SnSe might be more favorable for the formation of SnSe bilayers in ferecrystals. Bulk PbSe is not a layered compound and the formation of bilayers might be less favorable than for SnSe. Another indication for the validity of this hypothesis is that for the SnSe-based ferecrystals a lower annealing temperature of only 20 min at 400 °C was sufficient for the formation of ferecrystals [24, 32]. In contrast, the PbSe-based ferecrystals had to be annealed for 1 h at 450 °C for an optimal formation of ferecrystals [23].

Both, the SnSe- and the PbSe- based samples show column-like regions of bright and dark areas extending from the bottom to the top of the layer (Figs. 5.7, A.2 and A.10) indicating a columnar crystallization of both types of ferecrystals and

similar in-plain grain sizes of about 5 nm to 50 nm.

7.2 Electrical properties of ferecrystals with M = Pb or Sn

A comparison between electrical properties measured for the $[(PbSe)_{1+\delta}]_1[NbSe_2]_1$ and $[(SnSe)_{1+\delta}]_1[NbSe_2]_1$ ferecrystals is given in Table 7.2. The rt resistivity values and the carrier densities evaluated in a single-band model are similar for both sample systems. The residual resistance ratio (RRR) is higher for the PbSe-based than for the SnSe-based ferecrystals. This indicates that the defect density for batch 3 of the PbSe-based ferecrystals is lower than for the SnSe-based ferecrystals. More HAADF-STEM images of $[(PbSe)_{1+\delta}]_1[NbSe_2]_1$ of batch 3 would be necessary to confirm this. In contrast, the defect density observed by HAADF-STEM of batches 1 and 2 of the $[(PbSe)_{1+\delta}]_1[NbSe_2]_1$ ferecrystals investigated in this study was higher than for the $[(SnSe)_{1+\delta}]_1[NbSe_2]_1$ ferecrystal. The Debye temperature θ_D of the $[(SnSe)_{1+\delta}]_1[NbSe_2]_1$ ferecrystals is higher than for the $[(PbSe)_{1+\delta}]_1[NbSe_2]_1$ ferecrystals and the error is higher, due to the deviation in linearity of $\rho(T)$ observed for these ferecrystals, as described below.

The temperature-dependent resistances of the PbSe- and SnSe-based ferecrystals with $(m, n) = (1, 1)$ are shown in Fig. 7.1 together with data reported for $NbSe_2$ single crystals of different thicknesses. Both ferecrystal types show a metal-

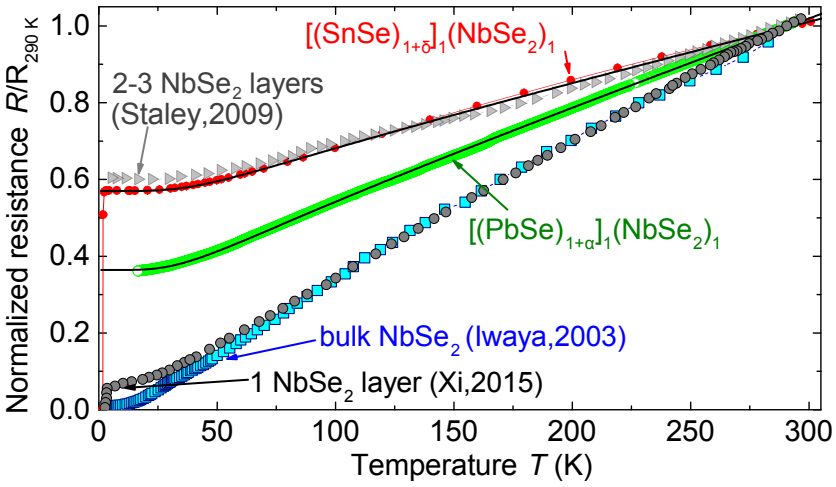

Figure 7.1: Temperature-dependent normalized resistance of ferecrystals $[(SnSe)_{1+\delta}]_1[NbSe_2]_1$ and $[(PbSe)_{1+\delta}]_1[NbSe_2]_1$ (batch 3) for $1.4\,K \leq T \leq 300\,K$ and the resistivity of 1 $NbSe_2$ monolayer (4-terminal measurement) [1], 2-3 isolated sheets of $NbSe_2$ (2-terminal measurement) [10] and of bulk $NbSe_2$ single crystals (4-terminal measurement) [53] are also shown. Solid lines are Bloch-Grüneisen fits to the data measured for the ferecrystals.

Table 7.2: Comparison between room temperature resistivity ρ_{rt}, residual resistance ration RRR, Debye temperature θ_{D} and transition temperature to superconductivity T_{c} of $[(\mathrm{PbSe})_{1+\delta}]_1[\mathrm{NbSe_2}]_1$ and $[(\mathrm{SnSe})_{1+\delta}]_1[\mathrm{NbSe_2}]_1$ ferecrystals.

Parameter	$[(\mathrm{PbSe})_{1+\delta}]_1[\mathrm{NbSe_2}]_1$	$[(\mathrm{SnSe})_{1+\delta}]_1[\mathrm{NbSe_2}]_1$
ρ_{rt} (µΩ m)	3.3(3)	3.8(2)
ρ_{4K} (µΩ m)	1.17(9)	2.1(2)
$p(T = 10\,\mathrm{K})$ (cm^{-3})	$3(2) \times 10^{21}$	$4(2) \times 10^{21}$
RRR	2.80(3)	1.750(3)
θ_{D} (K)	209(1)	244(14)
T_{c} (K)	1.11(2)	2.04(8)

like temperature dependence of the resistivity. However, for $100\,\mathrm{K} \leq T \leq 300\,\mathrm{K}$ the ferecrystals $[(\mathrm{SnSe})_{1+\delta}]_1[\mathrm{NbSe_2}]_1$ show a larger deviation from a linear temperature dependence of the resistivity than the $[(\mathrm{PbSe})_{1+\delta}]_1[\mathrm{NbSe_2}]_1$ samples. The $\mathrm{NbSe_2}$ single crystals also show a deviation from a linear temperature dependence of the resistivity in this temperature range. This indicates that the PbSe layers introduced between the $\mathrm{NbSe_2}$ layers result in a stronger deviation in the electrical transport properties of the ferecrystals compared to $\mathrm{NbSe_2}$ than SnSe. One explanation for this effect might be lower band gap of PbSe in comparison to SnSe. Reported resistivity values for PbSe single crystals at $T = 77\,\mathrm{K}$ ranges from 1 µΩm - 3 µΩm [65], whereas for SnSe single crystals at $T = 77\,\mathrm{K}$ resistivity values of 60 µΩm-8900 µΩm [123, 124] have been reported. Lower residual resistivity observed for the $[(\mathrm{PbSe})_{1+\delta}]_1[\mathrm{NbSe_2}]_1$ compound in comparison to $[(\mathrm{SnSe})_{1+\delta}]_1[\mathrm{NbSe_2}]_1$. Resistivity values for $T \leq 77\,\mathrm{K}$ have not been reported for SnSe. This would also be a possible explanation why the temperature-dependence of the resistivity of the $[(\mathrm{SnSe})_{1+\delta}]_m[\mathrm{NbSe_2}]_1$ ferecrystals resembles more closely the resistivity behavior of $\mathrm{NbSe_2}$ single crystals [52, 60], with a decreasing slope of $\rho(T)$ with increasing temperature for $T \gtrsim 100\,\mathrm{K}$, whereas $[(\mathrm{PbSe})_{1+\delta}]_1[\mathrm{NbSe_2}]_n$ shows a mainly linear, more metal-like temperature dependence. A higher carrier density and mobility of PbSe might lead to a higher contribution of high-mobility charge carriers from the PbSe layers to the electrical transport in the PbSe-based ferecrystals.

The transition temperature T_{c}, determined at 90 % of the residual resistance is $T_{\mathrm{c}} = 1.11(2)\,\mathrm{K}$ for the $[(\mathrm{PbSe})_{1+\delta}]_1[\mathrm{NbSe_2}]_1$ ferecrystals and $T_{\mathrm{c}} = 2.04(8)\,\mathrm{K}$ for the ferecrystals $[(\mathrm{SnSe})_{1+\delta}]_1[\mathrm{NbSe_2}]_1$. One possible explanation for the lower transition temperature of the $[(\mathrm{PbSe})_{1+\delta}]_1[\mathrm{NbSe_2}]_1$ ferecrystal is, as discussed in Sect. 6.10.2 a stronger proximity effect in the PbSe-based ferecrystals compared to the SnSe-based ferecrystals in connection with the lower normal state conductivity

of PbSe.

7.3 Comparison to electrical properties of SnSe-based ferecrystals

A comparison between the temperature-dependent resistivity values of three different ferecrystals containing SnSe in combination with different group V transition metal diselenides is shown in Fig. 7.2. The transition metal dichalcogenides VSe_2, $NbSe_2$, and $TaSe_2$ are group V transition metals. Therefore, the ferecrystals are expected to show roughly similar electrical properties [4]. However, below $T \approx 100\,\mathrm{K}$ the temperature-dependent resistivity of $[(SnSe)_{1+x}]_1[VSe_2]_1$ shows a striking difference to that of the other ferecrystals. Below about $T = 100\,\mathrm{K}$ the resistivity of this ferecrystal strongly increases with decreasing T [19]. This has been suggested to be an effect of a charge density wave (CDW) transition [19, 25, 64], because at $T_{\mathrm{CDW}} \approx 100\,\mathrm{K} - 140\,\mathrm{K}$ bulk VSe_2 single crystals show a CDW transition [90, 95, 112, 113]. During the CDW transition the resistivity increases with decreasing T for $T \leq T_{\mathrm{CDW}}$ and the carrier density decreases due to the localization of charge carriers and the opening of an energy gap in the CDW state. This localization of the charge carriers would also explain the increase of the Hall coefficient R_{H} of $[(SnSe)_{1+x}]_1[VSe_2]_1$ shown in Fig. 7.3. Bulk $NbSe_2$ is reported to show a charge density wave transition at $T_{\mathrm{CDW}} \approx 35\,\mathrm{K}$ accompanied by a change in the slope of ρ and R_{H} [44, 50–54, 54, 55, 55, 57, 172]. However, such changes in the slope of ρ or R_{H} are not observed for the $NbSe_2$-based ferecrystals. Bulk $TaSe_2$ is reported to have a CDW transition with an onset temperature of $T_{\mathrm{CDW}} \approx 85\,\mathrm{K} - 110\,\mathrm{K}$ [91, 109–111]. In this temperature range no indications for a CDW transition have been observed for the $TaSe_2$-based ferecrystals either. An important difference in atomic structure between the three different transition metal dichalcogenides is that VSe_2 usually shows an octahedral coordination of the transition metal atom by Se atoms [95, 218], whereas in $2H$-$NbSe_2$ and $2H$-$TaSe_2$ (the most common polytypes at rt) the coordination of the transition metal atom by Se atoms is trigonal prismatic [82, 218]. In contrast, the polytype $4H$-$NbSe_2$ contains alternately octahedral and trigonal prismatic coordination and shows an increased CDW transition temperature observed by an anomaly in the resistivity compared to $2H$-$NbSe_2$ [83]. This indicates that this structural difference can have an influence on the formation of a CDWs or on its effect on resistivity in the different types of ferecrystals.

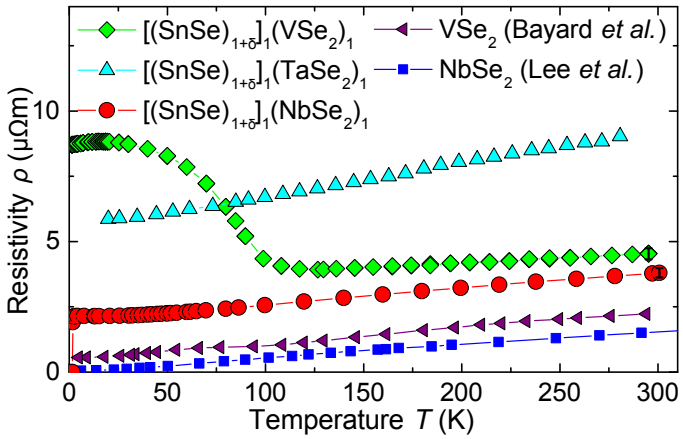

Figure 7.2: Temperature-dependent resistivity of $[(SnSe)_{1+\delta}]_1[NbSe_2]_1$ ferecrystals in comparison to other SnSe-based ferecrystals. The ferecrystal $[(SnSe)_{1+x}]_1[VSe_2]_1$ has been measured in this work and is reported in [19, 25]. The sample $[(SnSe)_{1+\beta}]_1[TaSe_2]_1$ has been measured by R. Atkins at the University of Oregon [33]. The resistivity of bulk $NbSe_2$ and VSe_2 single crystals as reported in [60] and [95] are also shown. Lines are guides to the eye.

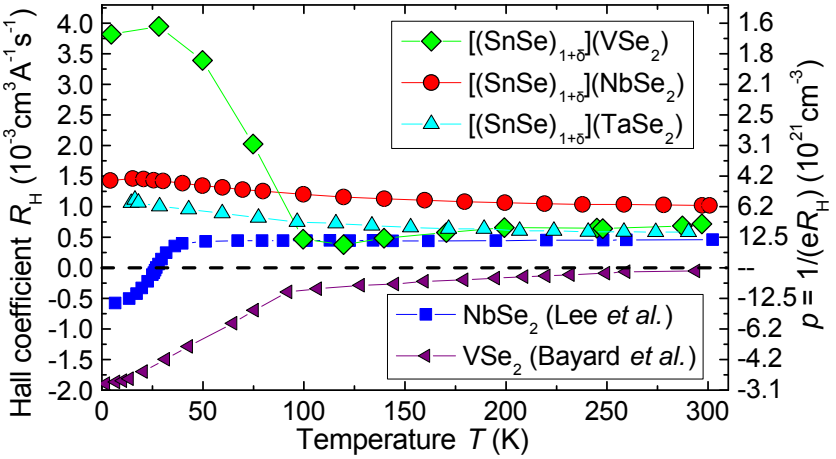

Figure 7.3: Temperature-dependent Hall coefficients R_H for $[(SnSe)_{1+\delta}]_m[NbSe_2]_1$ ferecrystals in comparison to other SnSe-based ferecrystals. The resistivity of bulk $NbSe_2$ and VSe_2 single crystals as reported in [60] and [95] are also shown. Lines are guides to the eye. The sample $[(SnSe)_{1+\beta}]_1[TaSe_2]_1$ has been measured by R. Atkins at the University of Oregon [217]. The ferecrystal $[(SnSe)_{1+x}]_1[VSe_2]_1$ has been reported in [19, 25].

8 Summary

The structural and electrical properties of the novel $[(PbSe)_{1+\delta}]_1[NbSe_2]_n$ and $[(SnSe)_{1+\delta}]_m[NbSe_2]_1$ ferecrystals have been investigated. For the structural characterization high-angle annular dark-field scanning transmission electron microscopy (HAADF-STEM), energy-dispersive X-ray spectroscopy (EDXS) and selected-area electron diffraction (SAED) have been used. For an electrical analysis temperature-dependent in-plane resistivity, Hall coefficients, magnetoresistance and normal-to-superconducting transitions were determined. Some of the main results are

- The atomic structure of the PbSe, SnSe and $NbSe_2$ layers in the ferecrystals is similar to the structure reported for the respective bulk binary compounds.
- A grain size of 5 nm to 50 nm and defects, in which PbSe or SnSe replaces parts of the $NbSe_2$ layers, were observed for the ferecrystals.
- The room temperature resistivity values of 2.5(2) µΩm to 28(2) µΩm, are within the range of values reported for bulk $NbSe_2$, PbSe or SnSe.
- The dependence of the resistivity on m and n deviates from a parallel resistors model in which PbSe and SnSe do not contribute to transport.
- A quantitative analysis using a two-layer model yields n-type conductivity for the $NbSe_2$ layers with a carrier density of $\approx 10^{20}$, which differs from bulk $NbSe_2$ (p-type) and is consistent with reports on isolated $NbSe_2$ monolayers.
- Possible indications for a charge density wave transition are observed in resistivity and Hall coefficient for the ferecrystals $[(SnSe)_{1+\delta}]_m[NbSe_2]_1$ with $m > 1$, but not for the ferecrystals $[(PbSe)_{1+\delta}]_1[NbSe_2]_n$.
- The transition temperatures to superconductivity T_c for the ferecrystals $[(PbSe)_{1+\delta}]_1[NbSe_2]_n$ with $n = 1, 2, 3$ are only 44 % to 64 % of T_c of analogous MLCs. This high reduction in T_c can be ascribed to the turbostratic disorder if non-stoichiometry and octahedral coordination of the Nb atoms by Se can be excluded.
- An increase in the cross-plane distance between $NbSe_2$ layers s in the ferecrystals $[(SnSe)_{1+\delta}]_m[NbSe_2]_1$ is found to lead to an increase in the cross-plane Ginzburg-Landau coherence length ξ_c. The ratio ξ_c/s is lower for these ferecrystals than for bulk $NbSe_2$ and MLCs containing $NbSe_2$.

These and further results will be described in more detail below.

The atomic structure

The TEM analysis has shown that the applied cross-sectional TEM preparation parameters and the substrate materials do not influence the structure of the ferecrystal thin films substantially. The HAADF-STEM images of the ferecrystals show an arrangement of atomic columns in the $NbSe_2$ and SnSe layers similar as in the respective bulk $2H$-$NbSe_2$ and α- or β-SnSe compounds with the c-axes parallel to the stacking direction in the ferecrystals. A trigonal prismatic coordination of the Nb atoms by Se is observed. Furthermore, the ferecrystals show a turbostratic disorder between the individual layers. The SAED diffraction patterns confirm the turbostratic disorder, visible as a streaking of the diffraction spots along the stacking direction. The in-plane diffraction spots in the SAED pattern can be indexed using the individual crystal structures of bulk SnSe (space group $Pmcn$) [84] and bulk $NbSe_2$ (space group $P6_3/mmc$) [82]. A difference between the a and b-lattice parameters of SnSe, indicating an orthorhombic unit cell and a significant change in the in-plane lattice parameters with increasing m, as reported for SnSe in ferecrystals containing $MoSe_2$- and VSe_2 [19, 25, 34], are not observed. Columns of in-plane width 5 nm to 50 nm with similar brightness of the PbSe or SnSe layers in some of the samples reaching from the substrate to the surface of the ferecrystals in the HAADF-STEM images suggest a common alignment of subsequent PbSe or SnSe layers along the stacking direction. The $NbSe_2$ layers within these columns show a turbostratic disorder. In some sample areas the PbSe or SnSe layers are oriented similarly as in MLCs.

Structural defects

The ferecrystals show a grain size of 5 nm to 50 nm. Several types of other defects were observed in low concentrations in the ferecrystals. The PbSe- and SnSe-based samples with $(m, n) = (1, 1)$ contained defects in which parts of the $NbSe_2$ layers were replaced by PbSe or SnSe layers. In contrast, the $[(SnSe)_{1+\delta}]_m[NbSe_2]_1$ samples with $m = 6$ showed defects in which two $NbSe_2$ layers of adjacent grains are offset along the stacking direction. The SnSe- and PbSe-based samples have shown an increased oxygen content within a layer of a few nanometers below the surface, which was similar for samples prepared for TEM after different periods of time after synthesis, indicating the formation of a passivating oxide. The first two batches of PbSe-based ferecrystals showed intermediate layers and a higher defect density in the center of the thin films in contrast to the SnSe-based ferecrystals. This indicates that the layered structure of bulk SnSe might be more favorable for the formation of SnSe bilayers in ferecrystals than bulk PbSe, which is not a layered compound.

The influence of MSe on electrical properties

The room temperature (rt) in-plane resistivity values measured for the ferecrystals $[(PbSe)_{1+\delta}]_1[NbSe_2]_n$ with $n = 1-3$ range from 2.5(2) µΩm to 3.6(2) µΩm. For the ferecrystals $[(SnSe)_{1+\delta}]_m[NbSe_2]_1$ with $m = 1-6$ the rt resistivity values range from 3.8(2) µΩm to 28(2) µΩm. As expected, these values are within the range of in-plane resistivity values reported for bulk $NbSe_2$ and PbSe or SnSe. The Hall coefficients of the ferecrystals are higher than those reported for bulk $NbSe_2$ and lower than those reported for PbSe or SnSe. The resistivity values and Hall coefficients of the PbSe- and SnSe-based ferecrystals with $(m, n) = (1, 1)$ are the same within measurement error and both show a metal-like temperature-dependence of their resistances.

However, unlike the PbSe-based ferecrystals, the SnSe-based ferecrystals with $m = 1$ show a deviation from a linear temperature dependence of the resistivity between $T = 100\,\mathrm{K}$ and 300 K. The temperature-dependent resistivity of the SnSe-based ferecrystals with $m = 1$ resembles more closely that of bulk and few-layer $NbSe_2$ [10, 60], indicating that the PbSe layers in ferecrystals contribute more strongly to the electrical transport than the SnSe layers. This corresponds to the lower band gap of PbSe in comparison to SnSe. Samples with $m > 1$ show an increasingly semiconductor-like temperature dependence of their resistivity with increasing m.

The Debye temperature of the ferecrystal $[(PbSe)_{1+\delta}]_1[NbSe_2]_1$, $\theta_D = 209(1)\,\mathrm{K}$, is slightly lower than $\theta_D = 244(14)\,\mathrm{K}$ for the ferecrystal $[(SnSe)_{1+\delta}]_1[NbSe_2]_1$. The Debye temperatures of the PbSe-based ferecrystals with $n = 1-3$ and the SnSe-based ferecrystals with $m = 1-3$ range between 190 K and 259 K and are within the range of values reported for bulk and few-layer $NbSe_2$ and are similar to values reported for Nb-containing MLCs.

The residual resistivity as a function of n for the $[(PbSe)_{1+\delta}]_1[NbSe_2]_n$ ferecrystals and as a function of m for the $[(SnSe)_{1+\delta}]_m[NbSe_2]_1$ ferecrystals increases more strongly than expected from a parallel resistors model in which the conductivity of the PbSe or SnSe layers is neglected in comparison to the conductivity of the $NbSe_2$ layers. This suggests that the PbSe or SnSe layers also contribute to the electrical transport in the ferecrystals. A non-zero magnetoresistance measured for the $[(SnSe)_{1+\delta}]_m[NbSe_2]_1$ ferecrystals at $T \leq 10\,\mathrm{K}$ has been analyzed quantitatively using a two-layer model. The analysis yielded n-type conductivity in one of the layer types and p-type conductivity in the other layer type, although bulk $NbSe_2$ and SnSe are usually reported as p-type. Based on the report for an isolated $NbSe_2$ monolayer, which has been found to show n-type conductivity [8], the $NbSe_2$ layers in the ferecrystals are assumed to be n-type. Using the two-layer model yields a semimetallic temperature dependence of the carrier density of the $NbSe_2$ layers in the ferecrystals, a carrier density 1-2 orders of magnitude lower than $\approx 10^{22}$ for bulk $NbSe_2$ and a mobility of $(10-400)\,\mathrm{cm}^2/(\mathrm{Vs})$ similar as for

bulk $NbSe_2$. This is consistent with reports on single $NbSe_2$ layers [8]. One explanation for the semimetallic behavior at low temperatures can be the occurrence of a CDW which has been calculated to lead to semiconducting properties in $NbSe_2$ monolayers, whereas for bulk $NbSe_2$ it leads to metallic properties [15].

For the SnSe layers the two-layer model yielded carrier densities of $\approx 10^{16}$ and mobility values of $(10^3 - 10^4)\,\mathrm{cm}^2/(\mathrm{Vs})$, similar as reported for bulk or thin film SnSe. Lower mobility values would be expected for the SnSe and the $NbSe_2$ layers in the ferecrystals compared to bulk compounds, since in the ferecrystals they are polycrystalline with a small in-plane grain size. However, a channeling effect due to scattering at the interfaces between the SnSe and $NbSe_2$ layers might lead to increased mobility values.

Charge density wave transition

No indications for a charge density wave (CDW) transition were observed for the PbSe-based ferecrystals. In contrast, the ferecrystals $[(SnSe)_{1+\delta}]_m[NbSe_2]_1$ show an increasing resistivity and Hall coefficient with decreasing temperatures for $m > 1$ starting below $T \approx 60\,\mathrm{K}$, where a CDW transition is expected for $NbSe_2$. This non-metal-like behavior results in a ratio $\rho_{295\mathrm{K}}/\rho_{4\mathrm{K}}$ lower than 1 for $m = 5$ and 6. These effects are similar to the effects observed for the $[(SnSe)_{1+\beta}]_m[VSe_2]_1$ ferecrystals at about $T = 110\,\mathrm{K}$, where a CDW transition has been suggested to take place [19, 64].

The influence of turbostratic disorder and polycrystallinity

A comparison between $[(PbSe)_{1+\delta}]_1[NbSe_2]_n$ ferecrystals with $n = 1, 2$ and 3 and analogous MLCs $[(PbSe)_{1+\delta}]_1[NbSe_2]_n$ shows that the turbostratic disorder, polycrystallinity and the lower thickness of the ferecrystals, have an influence on the value of the resistivity and the value of the slope of $R(T)$. However, ferecrystals and MLCs both show a linear trend in $\rho(T)$ between $T = 100\,\mathrm{K}$ and rt, unlike bulk and few-layer $NbSe_2$. The Debye temperatures are similar for ferecrystals and the analogous MLCs, suggesting that their phonon spectra are similar, despite the turbostratic disorder. In contrast to the MLCs, the residual resistance of the ferecrystals increases with increasing n. A possible explanation can be made in analogy to ferecrystals $[(SnSe)_{1.16}]_1[NbSe_2]_n$ [29], which have been reported to show a decrease in grain size with increasing n. The residual resistivity values reported for the MLCs are lower and the residual resistance ratios higher than those for the ferecrystals which can be explained by the polycrystallinity and turbostratic disorder of the ferecrystals.

Superconductivity

For the first time superconductivity has been detected for ferecrystals. The transition temperatures of the $[(SnSe)_{1+\delta}]_m[NbSe_2]_1$ and $[(PbSe)_{1+\delta}]_1[NbSe_2]_n$ ferecrystals range from $T_c \approx 0.82(5)$ K to 2.66(4) K. The transition widths ΔT range from 2 % to 25 % of T_c, similar as reported for MLCs. Upon increasing the thickness of the $NbSe_2$ layers in the repeat unit, as done for the $[(PbSe)_{1+\delta}]_1[NbSe_2]_n$ ferecrystals, T_c increases systematically from $T_c = 1.11(2)$ K for $n = 1$ to 2.66(4) K for $n = 3$. For the $[(SnSe)_{1+\delta}]_m[NbSe_2]_1$ ferecrystals T_c decreases systematically upon increasing the cross-plane distance between the $NbSe_2$ layers from $T_c = 2.04(8)$ K for $m = 1$ to $T_c = 0.84(7)$ K for $m = 6$. These results show that the ferecrystals can serve as model systems with systematically varying superconducting properties upon changing the stacking sequence and the material combination.

The transition temperatures of the $[(PbSe)_{1+\delta}]_1[NbSe_2]_n$ ferecrystals are reduced to about 34 % to 43 % of T_c of the analogous isolated $NbSe_2$ single-, bi- and trilayers. The observed trend of increasing T_c upon increasing the thickness of the $NbSe_2$ layers is as expected from reports on single- and few-layer $NbSe_2$ single crystals [1, 2]. One possible explanation for the effect of decreasing T_c upon increasing m is that the increase in separation of the $NbSe_2$ layers with increasing m leads to a reduction in the coupling between the individual $NbSe_2$ layers in the ferecrystals and to T_c approaching the value for a single $NbSe_2$ layer embedded in SnSe for increasing m.

A possible explanation for the about 50 % lower T_c of the PbSe-based ferecrystals with $(m, n) = (1, 1)$ compared to the SnSe-based ferecrystals with $(m, n) = (1, 1)$ is a stronger proximity effect for the PbSe-based ferecrystals due to the lower band gap of PbSe.

Surprisingly, the transition temperatures of the $[(PbSe)_{1+\delta}]_1[NbSe_2]_n$ ferecrystals are drastically reduced to 44 % to 64 % of T_c of the analogous MLCs. If a non-stoichiometry and an octahedral coordination of the Nb by Se atoms in the $NbSe_2$ layers can be excluded, this large reduction of T_c can be attributed to the turbostratic disorder in the ferecrystals, which is not present in the MLCs.

A hysteresis effect was observed for the magnetic field dependent resistances of $[(SnSe)_{1+\delta}]_m[NbSe_2]_1$ ferecrystals. The hysteresis effect was much higher for the samples with $m = 6$ than for $m = 1$. This can be attributed to the larger fraction of interrupted $NbSe_2$ layers for $m = 6$ than for $m = 1$ observed in the HAADF-STEM images, since defects can act as flux pinning centers.

First measurements of the temperature- and angle-dependent parallel and perpendicular critical magnetic fields of ferecrystals have been carried out. The analysis shows that the cross-plane Ginzburg-Landau (GL) coherence lengths of the ferecrystals $[(SnSe)_{1+\delta}]_m[NbSe_2]_1$ with $m = 1$ and $m = 6$ are equal to the cross-plane distances between the superconducting $NbSe_2$ layers in these samples, within

the error boundaries. A cross-plane GL coherence length smaller than the cross-plane distance between superconducting layers would be a signature of 2D superconductivity [73–75] and the ferecrystals are close to this condition. The ratio between the coherence length and the distance between the $NbSe_2$ layers for the ferecrystals is closer to that of 2D superconductors than the ratios reported for MLCs and bulk $NbSe_2$. This can be explained by the cross-plane incoherence of the structure of the ferecrystals in contrast to MLCs and bulk $NbSe_2$ single crystals, reflecting the relation of the structural peculiarities to the physical properties of these materials.

9 Outlook

Ferecrystals are novel materials and the structural and electrical properties of many ferecrystals are still unknown. Furthermore, the origin of their stability and their bonding mechanisms is still an open question. For a prediction of the electrical properties of the many possible material combinations and stacking sequences for ferecrystals and to investigate the origin of their stability, charge transfer and bonding mechanisms, band structure measurements using angle-resolved photoemission spectroscopy would be helpful.

The findings of intermediate layers in some batches of the ferecrystals in this work has lead to the question how their formation process can be optimized and how their properties can be stabilized. In order to learn more about the formation process of the ferecrystals and possible intermediate layers, an *in-situ* annealing study of the as-deposited ferecrystal precursors using high-resolution TEM could be used to detect whether an onset temperature exists, at which possible intermediate layers start to form or whether an intermediate layer is already present in the as-deposited layers. Since the $[(PbSe)_{1+\delta}]_1[NbSe_2]_n$ samples have shown a decreased selenium content at the surface and in the intermediate layers, another possible way to improve the sample quality would be to anneal the samples in selenium vapor, as shown in [21, 219] or to increase the selenium layer thickness during deposition of the first and last precursor layers.

Comparing the transition temperatures of the PbSe-based ferecrystals to analogous misfit layer compounds allows for the direct detection of the influence of turbostratic disorder on T_c, if a non-stoichiometry of the $NbSe_2$ layer and an octahedral coordination of the Nb atoms can be excluded. The detection of non-stoichiometry, e. g. due to interstitial atoms in the van der Waals gaps between two $NbSe_2$ layers, can be achieved by X-ray diffraction and refinement methods by determining cross-plane distances between lattice planes and a comparison to bulk $NbSe_2$. In addition high-resolution TEM on more sample areas would help to detect the coordination of the Nb atoms by Se or interstitial atoms.

Another open question is whether a charge density wave is present in the ferecrystals. Optical methods using Raman spectroscopy would be helpful to clarify this, similar as reported for $NbSe_2$ mono-, bi- and trilayers [1]. Possibly, selected-area electron diffraction or X-ray diffraction methods could be used to observe the appearance of superlattice peaks below the CDW transition temperature, similar as described in [49, 50, 96].

Furthermore, the characteristics of the cross-plane electrical resistivity of the

ferecrystals in the normal and superconducting state are still unknown. Due to their layered superconductor-non-superconductor-superconductor structure, the ferecrystals might show an intrinsic Josephson junction behavior in the superconducting state [144, 220, 221]. To show whether an intrinsic Josephson junction effect can be observed, cross-plane resistivity measurements could be used, similar as for the misfit layer compound $(LaSe)_{1.14}NbSe_2$ [144, 220, 221].

Additional information on the type of charge carriers contributing to the electrical transport and their properties in terms of a two-band model could be obtained by Seebeck measurements. Experiments applying a back-gate voltage to vary the carrier density in the samples, as reported in [9, 10, 15] to analyze their normal state or superconducting properties would give further information on the type and density of charge carriers in the ferecrystals.

With the measurements of the critical magnetic fields of superconductivity in this work a starting point was set for further measurements of the temperature-dependence of the critical magnetic field to determine a possible crossover from 3D to 2D-superconducting properties. This study has shown that further, more detailed measurements of the temperature dependent critical magnetic fields are required to determine whether a possible 3D- to 2D transition in temperature takes place. Furthermore, susceptibility measurements to characterize their superconducting properties would be interesting. Finally, measuring the temperature-dependent critical magnetic fields of samples with an even higher separation of the $NbSe_2$ layers, e. g. $m = 10$, or even a single layer of $NbSe_2$ buried in semiconducting or insulating layers, seem promising experiments for the observation of 2D properties.

List of symbols and acronyms

List of symbols

m	Number of metal chalcogenide bilayers (two atomic monolayers) in the repeat unit of a ferecrystal.
n	Number of transition metal dichalcogenide layers (three atomic monolayers) in the repeat unit of a ferecrystal.
s	Repeat unit thickness.
e	Elementary charge.
d	Total sample thickness.
d_{sc}	Thickness of a superconducting thin film or a length scale for the spatial distribution of the order parameter.
p	Hole density.
RRR	Residual resistance ratio.
ρ	Electrical resistivity.
ρ_{res}	Residual resistivity.
$\rho_{4\mathrm{K}}$	Resistivity at $T = 4\,\mathrm{K}$.
ρ_n	Normal state resistivity close to transition temperature to superconductivity.
R_n	Normal state resistance close to transition temperature to superconductivity.
R_{rt}	Room temperature resistance.
ρ_{rt}	Room temperature resistivity.
MR	Magnetoresistance.
I	Current.
V	Voltage.
V_m	Measured voltage in Hall measurement experiment.
q	Charge of a charge carrier (for electrons: $q = -e$, for holes: $q = e$, where $e = 1.602 \times 10^{-19}\,\mathrm{C}$).
I_{rms}	Root mean square current.
R_{res}	Residual resistance.
MX	Metal chalcogenide (M: metal, X: Se, Te or S).
TX_2	Transition metal dichalcogenide (T: transition metal, X: Se, Te or S).

T_c	Transition temperature to the superconducting state at which $R = 0.9R_n$.
ΔT	Transition width determined as the temperature range between $R = 0.1R_\mathrm{n}$ and $R = 0.9R_\mathrm{n}$.
$T_{\mathrm{c},0.5}$	Transition temperature to the superconducting state at which $R = 0.5R_n$.
H_c	Critical magnetic field.
ξ_0	BCS-coherence length.
T_CDW	Charge density wave transition temperature.
ξ	Ginzburg-Landau coherence length.
ξ_{ab}	In-plane Ginzburg-Landau coherence length.
ξ_c	Cross-plane Ginzburg-Landau coherence length.
$H_{c\parallel}$	Critical magnetic field with magnetic field applied parallel to the layers.
$H_{c\perp}$	Critical magnetic field with magnetic field applied perpendicular to the layers.
θ_D	Debye temperature.
R_H	Hall coefficient.
V_H	Hall voltage.

Acronyms

2D	Two-dimensional.
BCS	Bardeen-Cooper-Schrieffer.
CDW	Charge density wave.
EDXS	Energy dispersive X-ray spectroscopy.
FIB	Focused ion beam.
GL	Ginzburg-Landau.
HAADF-STEM	High-angle annular dark-field scanning transmission electron microscopy.
LD	Lawrence-Doniach.
MER	Modulated elemental reactants.
MLC	Misfit layer compound.
rt	Room temperature.
SAED	Selected-area electron diffraction.
TEM	Transmission electron microscopy.
TMDC	Transition metal dichalcogenide.
XRD	X-ray diffraction.
XRR	X-ray reflectivity.

Appendix

A Details for structural analyses

A.1 TEM preparation parameters

$[(PbSe)_{1+\alpha}]_1(NbSe_2)_1$ ferecrystals

Table A.1: TEM preparation parameters for sample $[(PbSe)_{1+\alpha}]_1(NbSe_2)_1$. All samples were prepared on silicon with native silicon oxide.

Sample name	Synthesis batch No.	Face-to-face gluing/ gluing into tube temperature, time	Ion milling LN_2 cooling: energy, time	Time between synthesis and TEM
1	1	150 °C, 2 h/ 80 °C, 1.5 h	not cooled 5 kV, 5.5 h 3 kV, 15 min 2 kV, 10 min 1.4 kV, 5 min	≈ 22 months
2	2	150 °C, 2 h/ 80 °C, 1.5 h	not cooled 5 kV, 3.5 h 3 kV, 5 min 2 kV, 20 min 1.6 kV, 17 min	≈ 10 months
3	2	150 °C, 2 h/ 80 °C, 1.5 h	cooled 5 kV, 4.5 h 3 kV, 60 min 2 kV, 10 min 1.4 kV, 5 min	≈ 10 months
4	2	150 °C, 2 h/ 80 °C, 1.5 h	cooled 3 kV, 6.5 h 1.5 kV, 20 min 0.75 kV, 20 min	≈ 13 months

Continued on next page

Table A.1 – *Continued from previous page*

Sample name	Synthesis batch No.	Face-to-face gluing/ gluing into tube temperature, time	Ion milling LN_2 cooling: energy, time	Time between synthesis and TEM
			0.2 kV, 20 min	
5	2	80 °C, 2 h/ 80 °C, 1.5 h	cooled 5 kV, 3.5 h 3 kV, 15 min 2 kV, 5 min 1.4 kV, 5 min	≈ 21 months
6	2	80 °C, 2 h/ 80 °C, 1.5 h	cooled 5 kV, 2.6 h 3 kV, 5 min 2 kV, 5 min 1.4 kV, 10 min	≈ 24 months

$[(PbSe)_{1+\alpha}]_1(NbSe_2)_2$ ferecrystals

Table A.2: TEM preparation parameters for sample $[(PbSe)_{1+\alpha}]_1(NbSe_2)_2$. All samples were prepared on silicon with native silicon oxide.

Sample name	Synthesis batch No.	Face-to-face gluing/ gluing into tube temperature, time	Ion milling LN_2 cooling: energy, time	Time between synthesis and TEM
1	1	100 °C, 3 h/ 80 °C, 1.5 h	cooled 5 kV, 4 h 3 kV, 15 min 2 kV, 5 min 1.4 kV, 5 min	≈ 10.5 months

Continued on next page

Table A.2 – *Continued from previous page*

Sample name	Synthesis batch No.	Face-to-face gluing/ gluing into tube temperature, time	Ion milling LN_2 cooling: energy, time	Time between synthesis and TEM
2	2	100 °C, 3 h/ 80 °C, 1.5 h	cooled 5 kV, 4 h 3 kV, 5 min 2 kV, 10 min 1.4 kV, 5 min	≈ 14 months
3	2	100 °C, 3 h/ 80 °C, 1.5 h	cooled 5 kV, 7 h 3 kV, 5 min 2 kV, 5 min 1.4 kV, 5 min	≈ 15.5 months

$[(PbSe)_{1+\alpha}]_1(NbSe_2)_3$ ferecrystals

Table A.3: TEM preparation parameters for sample $[(PbSe)_{1+\alpha}]_1(NbSe_2)_3$. All samples were prepared on silicon with native silicon oxide.

Sample name	Synthesis batch No.	Face-to-face gluing/ gluing into tube temperature, time	Ion milling LN_2 cooling: energy, time	Time between synthesis and TEM
1	1	100 °C, 3 h/ 80 °C, 1.5 h	cooled 5 kV, 3.6 h 3 kV, 10 min 2 kV, 10 min 1.4 kV, 10 min	≈ 11.5 months
2	2	150 °C , 0.3 h/	cooled	≈ 14 months

Continued on next page

Table A.3 – *Continued from previous page*

Sample name	Synthesis batch No.	Face-to-face gluing/ gluing into tube temperature, time	Ion milling LN_2 cooling: energy, time	Time between synthesis and TEM
		150 °C , 0.3 h	5 kV, 9 h	
			3 kV, 25 min	
			2 kV, 5 min	
			1.4 kV, 5 min	

$[(PbSe)_{1+\alpha}]_1(NbSe_2)_4$ ferecrystals

Table A.4: TEM preparation parameters for sample $[(PbSe)_{1+\alpha}]_1(NbSe_2)_4$. All samples were prepared on silicon with native silicon oxide.

Sample name	Synthesis batch No.	Face-to-face gluing/ gluing into tube temperature, time	Ion milling LN_2 cooling: energy, time	Time between synthesis and TEM
1	1	100 °C, 3 h/	cooled	≈ 13.5 months
		80 °C, 1.5 h	5 kV, 3 h	
			3 kV, 15 min	
			2 kV, 5 min	
			1.4 kV, 5 min	

$[(SnSe)_{1+\delta}]_m[NbSe_2]_1$ ferecrystals

Table A.5: TEM preparation parameters for sample $[(SnSe)_{1+\delta}]_m(NbSe_2)_1$. All samples were prepared on 300 nm silicon oxide on silicon.

m	**Synthesis batch No.**	**Face-to-face gluing/ gluing into tube temperature, time**	**Ion milling LN_2 cooling: energy, time**	**Time between synthesis and TEM**
1	1	80 °C, 2 h/ 80 °C, 1.5 h	cooled 5 kV, 12 h 3 kV, 16 min 2 kV, 5 min 1.4 kV, 5 min	≈ 2 months
4	2	80 °C, 2 h/ 80 °C, 1.5 h	cooled 5 kV, 10.5 h 3 kV, 25 min 2 kV, 20 min 1.4 kV, 5 min	≈ 3 months
5	2	80 °C, 2 h/ 80 °C, 1.5 h	cooled 5 kV, 7.8 h 3 kV, 30 min 2 kV, 10 min 1.4 kV, 10 min	≈ 1.5 months
6	2	80 °C, 2 h/ 80 °C, 1.5 h	cooled 5 kV, 22.5 h 3 kV, 9 min 2 kV, 5 min 1.4 kV, 5 min	≈ months

A.2 HAADF-STEM of $[(PbSe)_{1+\alpha}]_1(NbSe_2)_n$ ferecrystals

Intermediate layers in $[(PbSe)_{1+\alpha}]_1(NbSe_2)_1$

Figure A.1 shows a high-angle annular dark-field (HAADF-STEM) overview image of specimen 4 of $[(PbSe)_{1+\delta}]_1(NbSe_2)_1$. The intermediate and surface layers are present throughout the image over a range of about 2.56 µm. The intermediate layer is also found at the other side of the TEM specimen at the top of the image. The specimen part seen at the top of the image originates from a specimen area which was at least several hundreds of micrometers away from the lower specimen part in the original as-synthesized specimen.

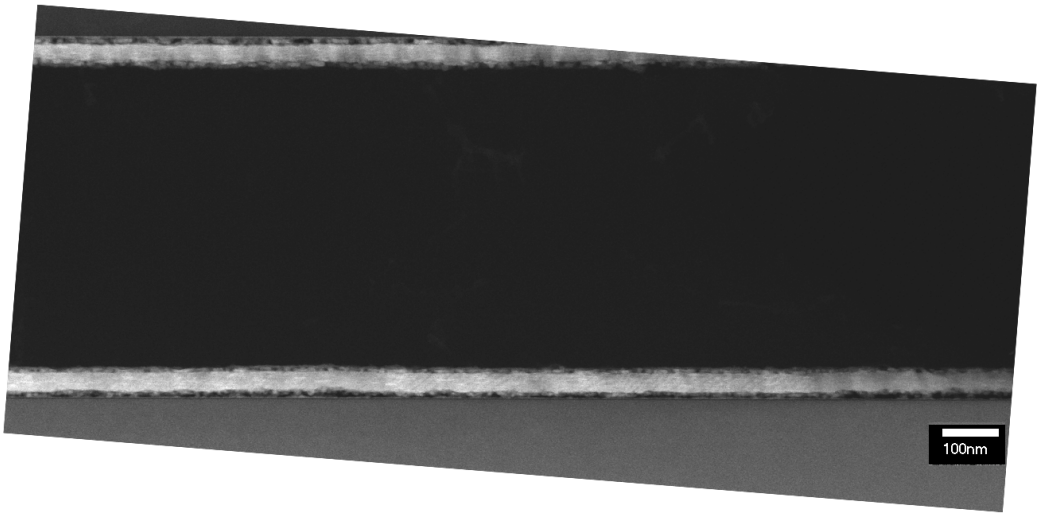

Figure A.1: HAADF-STEM image of $[(PbSe)_{1+\delta}]_1(NbSe_2)_1$ specimen 4 showing the specimen along a length of about 2.56 µm. The defect intermediate and surface layers are present throughout the whole analyzed area.

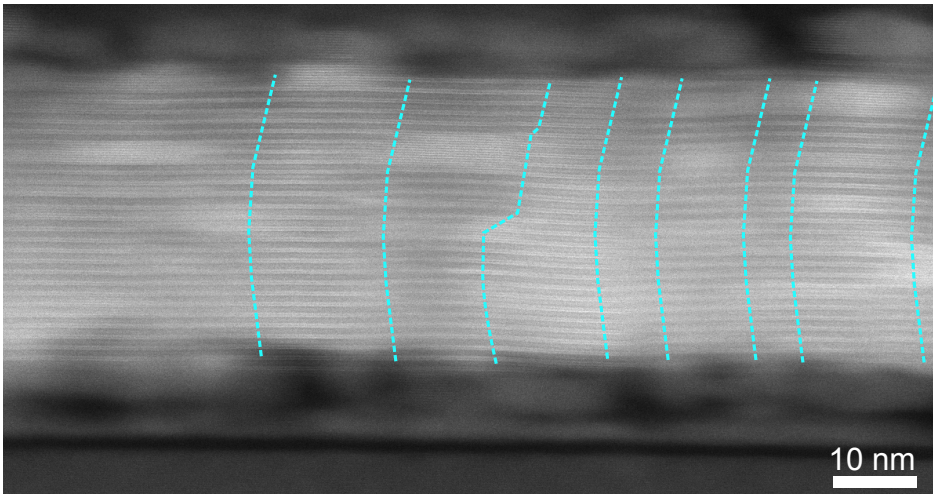

Figure A.2: HAADF-STEM image of sample $[(PbSe)_{1+\delta}]_1[NbSe_2]_1$ (specimen 4) showing column-like areas which are slightly darker or brighter than the neighboring areas. The approximate positions of the boundaries between the columns are highlighted by light blue lines.

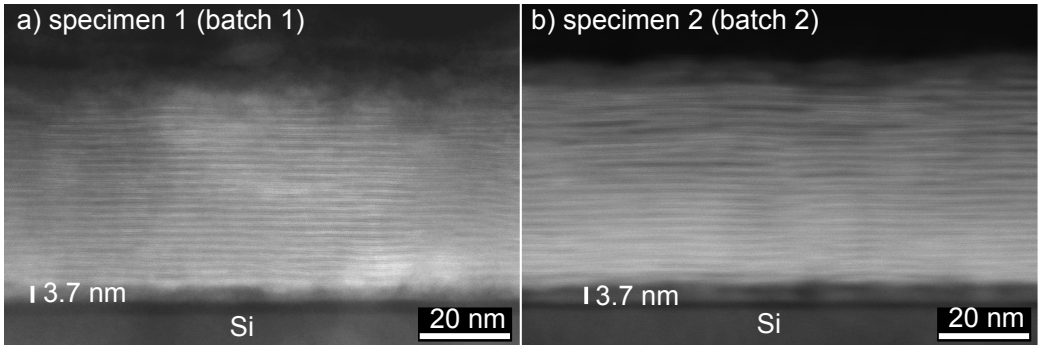

Figure A.3: HAADF-STEM image of $[(PbSe)_{1+\delta}]_1(NbSe_2)_1$ specimen 4 showing the specimen along a length of about 2.56 µm. The defect intermediate and surface layers are present throughout the whole analyzed area.

Stacking defects in $[(PbSe)_{1+\alpha}]_1(NbSe_2)_1$

The defect density of these stacking defects in the ferecrystals has been estimated from the HAADF-STEM image shown in Fig. A.4. The defect density has been calculated by relating the sum of the areas boxed in blue to the total area of the ferecrystals boxed in red. The defects density then amounts to 13 %.

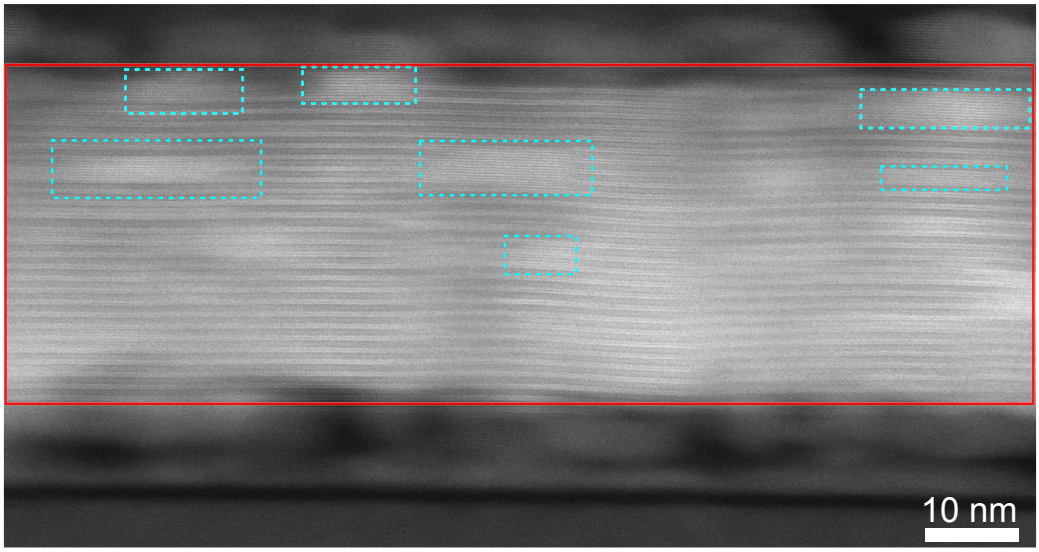

Figure A.4: HAADF-STEM image of specimen 2 of $[(PbSe)_{1+\delta}]_1(NbSe_2)_1$. The areas boxed in dashed blue boxes indicate stacking defects, the area boxed in red was used for calculating the defect density.

A.3 EDX analysis of $[(PbSe)_{1+\alpha}]_1(NbSe_2)_n$ ferecrystals

EDX spectra and maps of $[(PbSe)_{1+\alpha}]_1(NbSe_2)_2$ ferecrystal

Table A.6: Composition of the different specimen regions of $[(PbSe)_{1+\delta}]_1[NbSe_2]_2$, specimen 2, determined from the EDX spectra in Fig. A.6. The errors given are the 3σ errors. For comparison, the chemical composition of an ideal MLC $[(PbSe)_{1.10}]_1(NbSe_2)_2$ is also given.

Element	Ferecrystals	Intermediate layer	Surface layer	Ideal MLC ($\delta = 0.1$)
	at.%	at.%	at.%	at.%
Nb	24(3)	31(6)	27(4)	24.4
Se	60(6)	33(5)	51(6)	62.2
Pb	14(5)	10(4)	15(5)	13.4
O	2(1)	25(7)	8(3)	0

For EDX maps acquired in this study (Fig. A.5) the K-series of Nb ($E \approx 16.5$ keV), the K-series of Se ($E \approx 11.2$ keV), the K-series of O ($E \approx 0.5$ keV) and the L-series of Pb ($E \approx 10.5$ keV) were used. The oxygen content is increased and the selenium content is reduced in the bottom and surface layer.

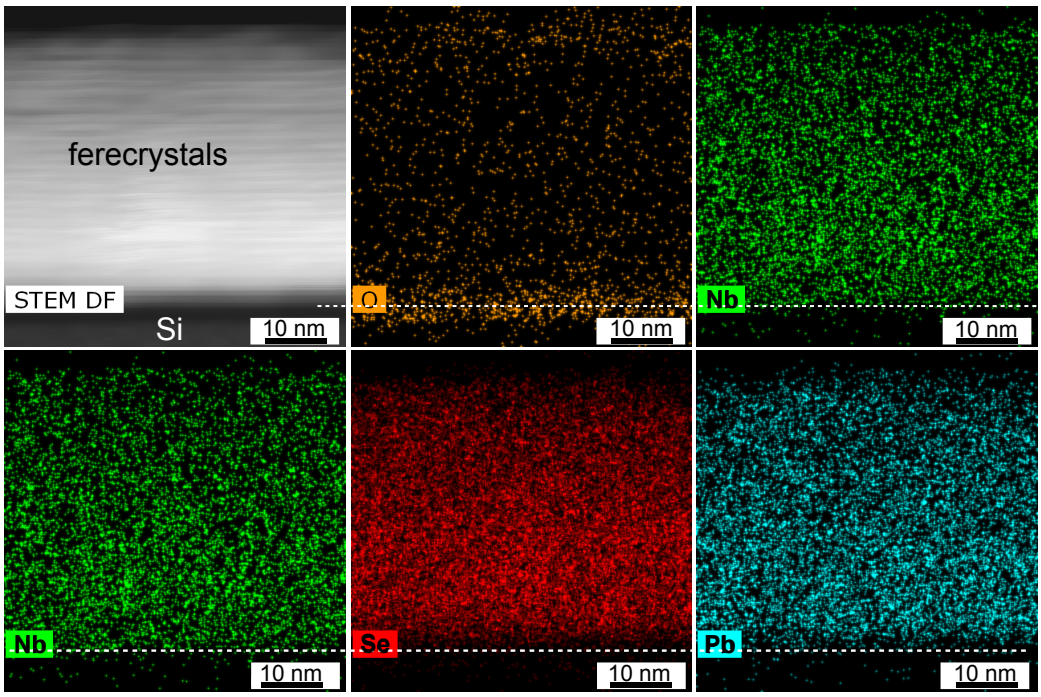

Figure A.5: EDX maps of $[(PbSe)_{1+\delta}]_1(NbSe_2)_2$, specimen 2. The figures show the HAADF-STEM image and the simultaneously measured EDX maps of oxygen (O), niobium (Nb), selenium (Se) and lead (Pb). The dashed line indicates the interface between silicon oxide and intermediate layer, estimated from the HAADF-STEM image.

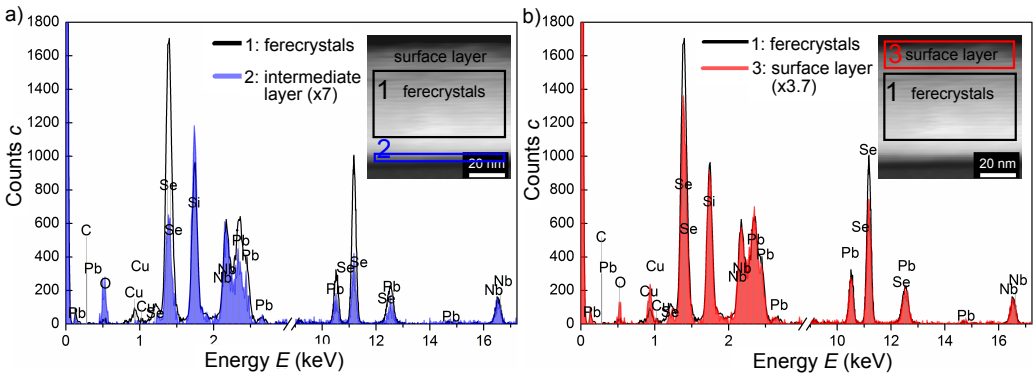

Figure A.6: EDX spectra of $[(PbSe)_{1+\delta}]_1[NbSe_2]_2$, specimen 2. The background has been removed. a) Spectrum of the intermediate layer (blue, filled), b) Spectrum of the surface layer (red, filled). Insets show HAADF-STEM images with the specimen areas from which the spectra originate (colored rectangles). The spectra from the ferecrystal layers are displayed in black.

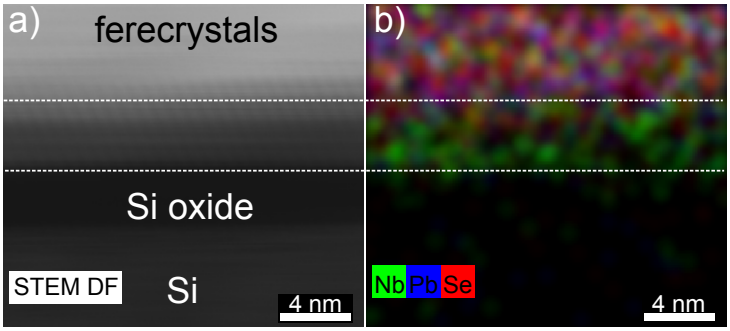

Figure A.7: EDXS maps of $[(PbSe)_{1+\delta}]_1[NbSe_2]_2$, specimen 2, batch 2 on Si with native oxide. The figures show the HAADF-STEM image and the simultaneously measured EDXS map for Nb, Se and Pb. The dashed line indicates the interface between silicon oxide and intermediate layer, estimated from the HAADF-STEM image.

EDX spectra and maps of $[(PbSe)_{1+\alpha}]_1(NbSe_2)_3$ ferecrystal

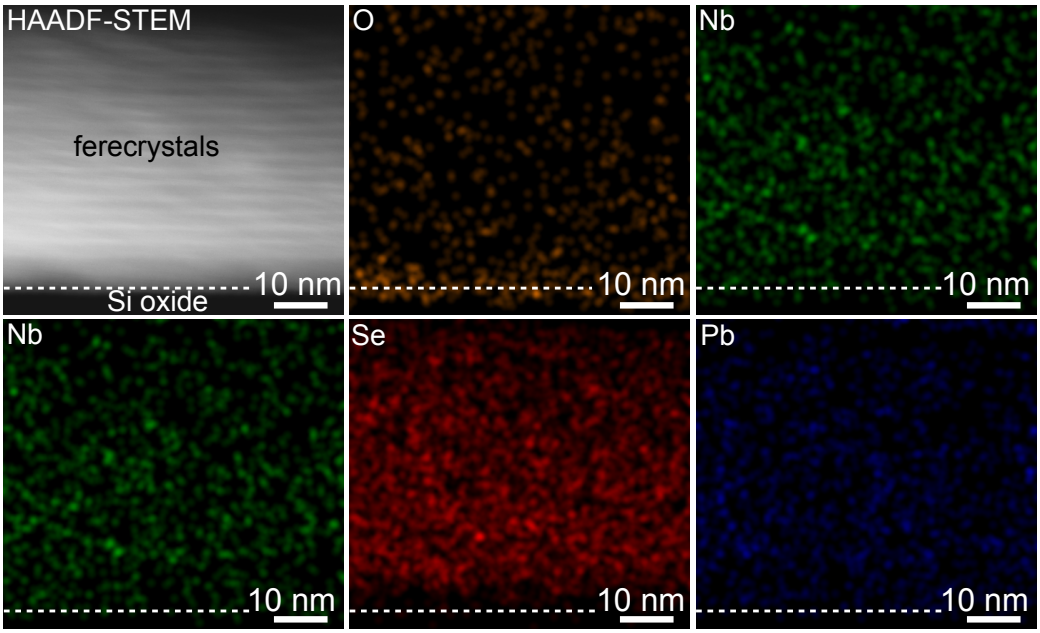

Figure A.8: HAADF-STEM and EDXS maps of $[(PbSe)_{1+\delta}]_1(NbSe_2)_3$, specimen 2 (batch 2). The dashed lines indicate the interface between silicon oxide and intermediate layer.

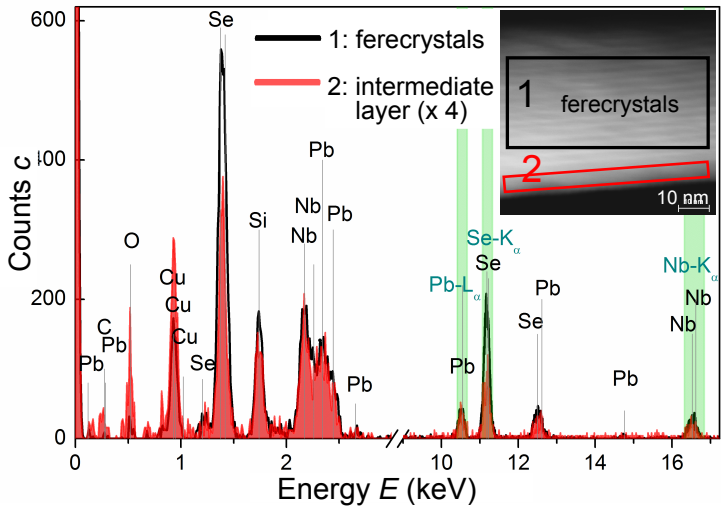

Figure A.9: EDX spectra of $[(PbSe)_{1+\delta}]_1(NbSe_2)_3$, specimen 2 (batch 2). The background has been removed from the spectra. The inset shows the HAADF-image with the specimen areas from which the spectra originate marked with colored rectangles. The spectrum from the ferecrystal layers is displayed in black. The spectrum of the bottom layer is displayed in red.

Table A.7: Composition of the different specimen regions of $[(PbSe)_{1+\delta}]_1[NbSe_2]_3$, specimen 2 (batch 2), determined from the EDX spectra in Fig. A.9. The errors are given in parenthesis as 3σ errors. For comparison, the chemical composition of an ideal MLC $[(PbSe)_{1.10}]_1(NbSe_2)_3$ is also given.

Element	Ferecrystals	Intermediate layer	Ideal MLC ($\delta = 0.1$)
	at.%	at.%	at.%
Nb	25(4)	17(6)	26.8
Se	59(7)	30(6)	63.4
Pb	10(4)	11(4)	9.8
O	6(3)	45(12)	0

A.4 HAADF-STEM of $[(SnSe)_{1+\alpha}]_m(NbSe_2)_1$ ferecrystals

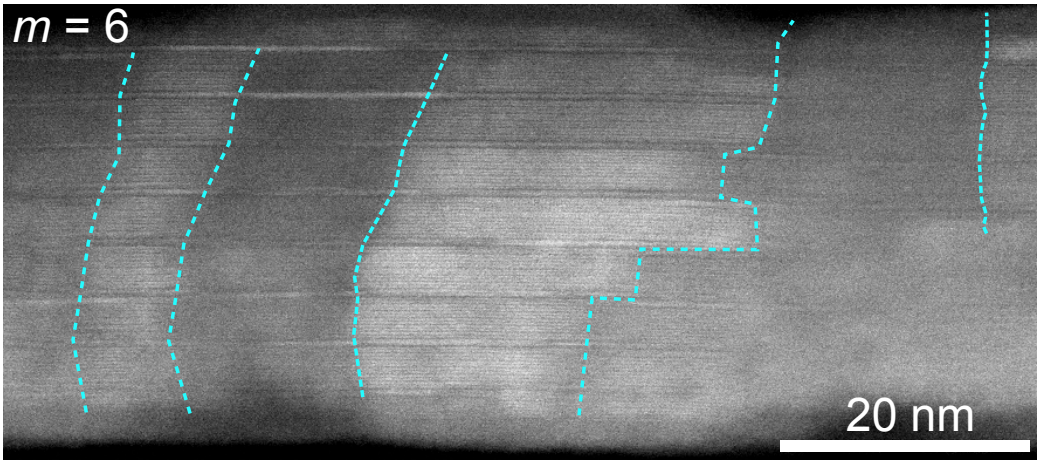

Figure A.10: HAADF-STEM image of sample $[(SnSe)_{1+\delta}]_6(NbSe_2)_1$ showing column-like areas which are slightly darker or brighter than the neighboring areas. The boundaries of the columns are indicated by light blue lines.

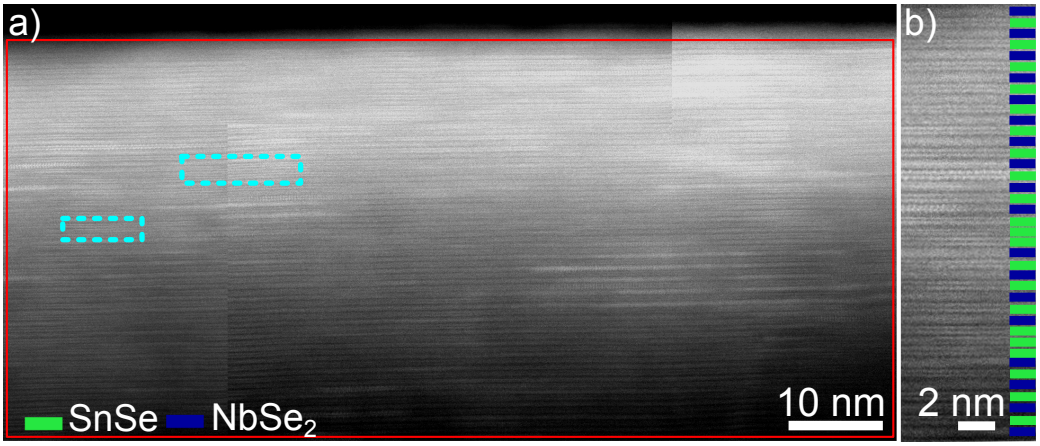

Figure A.11: HAADF-STEM images of $[(SnSe)_{1+\delta}]_m[NbSe_2]_1$ ferecrystal with $m = 1$. The image in Fig. A.11 a) is set of two images of two adjacent sample areas, which were acquired at the same magnification. a) The boxed areas indicate stacking defects in which a SnSe layer replaces a part of a $NbSe_2$ layer. b) a magnified part of a) is shown with the stacking sequence indicated by green (SnSe) and blue ($NbSe_2$) rectangles.

B Details for electrical analyses

B.1 Temperature-dependent resistivity of $[(PbSe)_{1+\alpha}]_1(NbSe_2)_n$

Batch 3

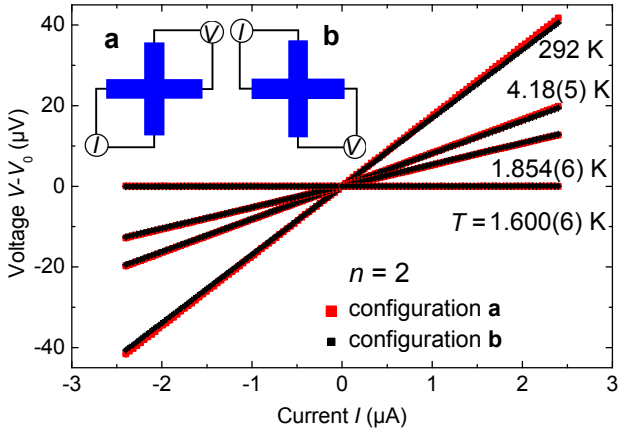

Figure B.1: Exemplary I-V curves for four temperatures for sample $[(PbSe)_{1+\delta}]_1[NbSe_2]_n$ with $n = 2$ (A) of batch 3. The schematics on the upper left-hand side show the two van der Pauw measurement configurations (a, b).

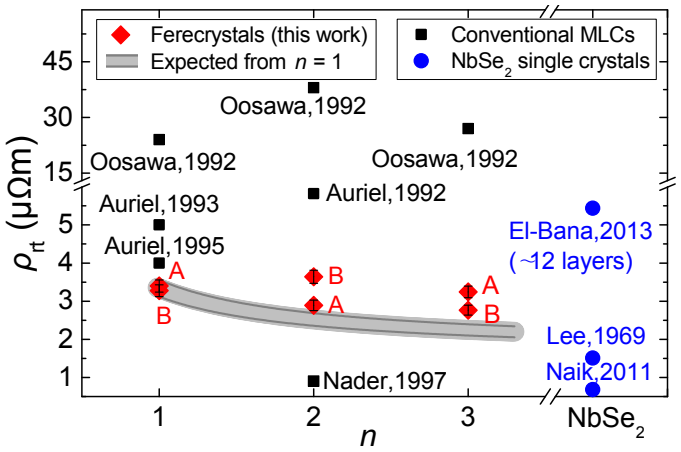

Figure B.2: Room temperature (T = (292.3 - 295.8) K) resistivity for $[(PbSe)_{1+\delta}]_1[NbSe_2]_n$ ferecrystals and values for $[(PbSe)_{1+\delta}]_1[NbSe_2]_n$ misfit layer compounds (MLCs) reported by Nader *et al.* [41], Oosawa *et al.* [39], Auriel *et al.*, 1993 [40], Auriel *et al.*, 1995 [42], Auriel *et al.*, 1992 [43] and bulk $NbSe_2$ single crystals reported by Lee *et al.* [60] and Naik *et al.* [83] and for 12 layer thick $NbSe_2$ reported by El-Bana *et al.* [9].

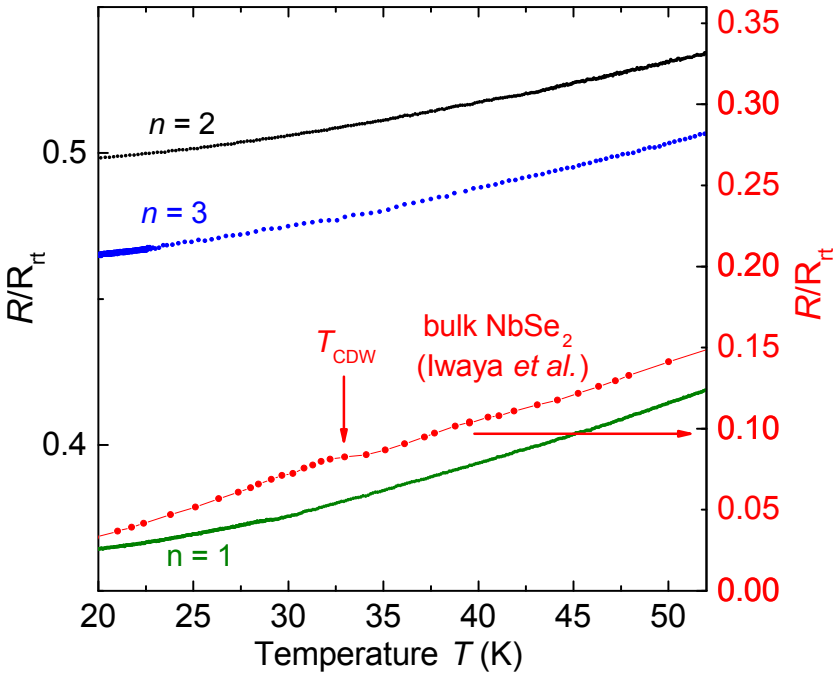

Figure B.3: Temperature-dependent resistance R normalized to room temperature resistance R_{rt} of $[(PbSe)_{1+\delta}]_1[NbSe_2]_n$ ferecrystals (batch 3) for $20\,K \leq T \leq 50\,K$. The resistivity values of a bulk $NbSe_2$ single crystal as reported in [53] are shown on the right-hand scale.

Batches 1 and 2

The STEM-HAADF images for the samples of type $n = 1$ of batch 1 and 2 have shown non-layered intermediate and top layers. The STEM-HAADF images of samples of type $n = 2$ of batch 2 have shown untypical thin Nb rich layers below the ferecrystals and the STEM-HAADF images of a sample of type $n = 4$ showed mostly amorphous layers (section 5.4).

The rt resistivity values of the $[(PbSe)_{1+\delta}]_1[NbSe_2]_n$ samples are displayed in Fig. B.2. The error bars in resistivity shown in Fig. B.2 for the ferecrystals measured in this work (red and green symbols) include the errors due the fit of $I(V)$, due to thickness measurement and due to contact size, as described in section 4.3.1. The measured resistivity values are between $\rho_{295K} = 3.3\,\mu\Omega\,m$ and $4.9\,\mu\Omega\,m$. These values are within the range of resistivity values reported for the respective conventional misfit layer compounds reported by Nader *et al.* [41], Oosawa *et al.* [39], Auriel *et al.* [40]. A direct interpretation of the measurement results in terms of the influence of the increasing $NbSe_2$ layer thickness or the turbostratic disorder and polycrystallinity on the electrical properties of the ferecrystals is not possible,

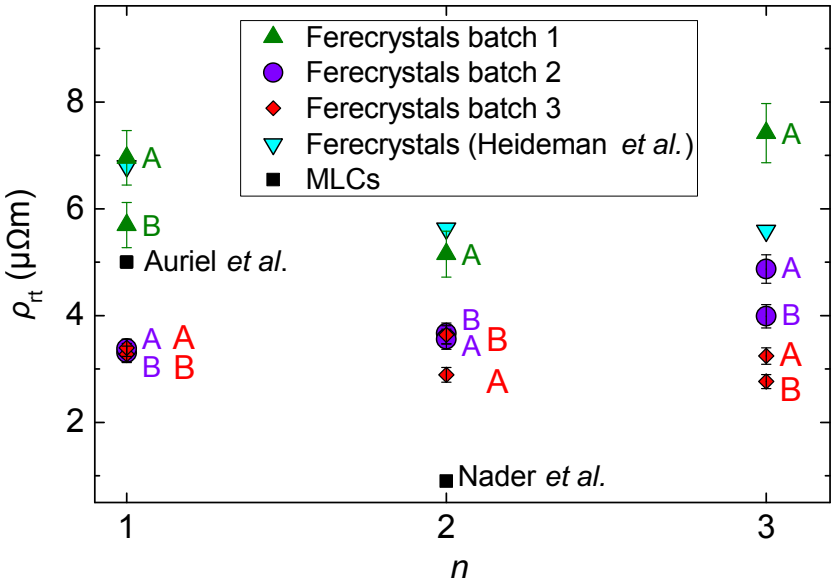

Figure B.4: Room temperature resistivity determined from van der Pauw measurements for $[(PbSe)_{1+\delta}]_1[NbSe_2]_n$ samples compared to reported values of other $[(PbSe)_{1+\delta}]_1[NbSe_2]_n$ ferecrystals [31], In-plane resistivity data for crystalline $[(PbSe)_{1+\delta}]_1[NbSe_2]_n$ misfit layer compounds (MLCs) reported by Nader *et al.* [41] and Auriel *et al.* [40] is shown for comparison. The ferecrystal samples of type $n = 1$ have shown non-layered intermediate and surface layers for batch 1 and 2. Samples with $n = 2$ showed a Nb rich intermediate layer. Samples with $n = 4$ showed an amorphous layer structure and sample $n = 3$ of batch 1 showed large voids. The samples of batch 3 showed a layer stacking sequence as expected and no intermediate or surface layers.

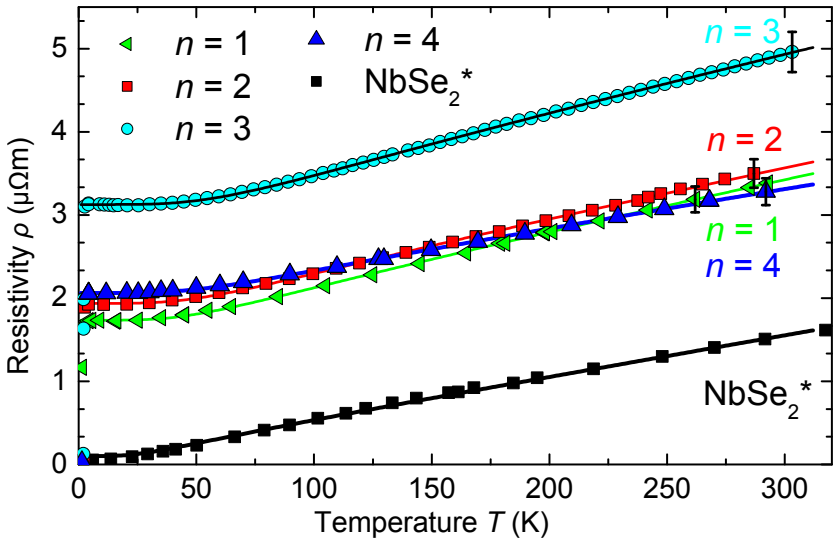

Figure B.5: Temperature-dependent resistivity of $[(PbSe)_{1+\delta}]_1[NbSe_2]_n$ ferecrystals (batch 2, 'samples A') for $1.4\,K \leq T \leq 300\,K$. The resistivity of a bulk $NbSe_2$ single crystal as reported in [60] is also shown (indicated by *). Solid lines are Bloch-Grüneisen fits. Error bars are shown exemplarily for the highest temperatures. The resistivity measurements of the samples $m = 2$ and 3 in Fig. B.5 were performed by A. Simon and A. Fiedler in the Novel Materials Group at HU Berlin.

due to the different defect layers which were observed for the different n. Only for the sample $n = 3$, sample A of batch 1 the increased resistivity can be expected due to the large voids found across the TEM sample. The resistivity values of the other samples measured in this work are similar or lower than the values reported for similar $[(PbSe)_{1+\delta}]_1[NbSe_2]_n$ ferecrystals in [31]. This difference to the previously measured ferecrystals might be due to the about 10 nm thick intermediate layers which were observed for samples of the type $n = 1$ in this work and which might not be present for the reported ferecrystals. However, no TEM images were shown in [31] indicating whether intermediate layers are present in those ferecrystals or not. Assuming that these layers have not been present in the previously reported samples, a lower resistivity would mean that the intermediate layers contribute to the electrical transport. However, the scattering of the resistivity values of batch 1 and 2 is larger than the difference to ρ_{295K} of the previously reported ferecrystals. The large scattering in the resistivity values for the samples of the same batch indicates that the samples are inhomogeneous.

The error bars shown for ρ of the ferecrystals in Fig. B.5 are only shown for one temperature for each n. These errors include the errors due the fit of $I(V)$, due to thickness measurement and due to contact size, as described in section 4.3.1.

The error due to contact size causes the largest part of the error $\approx 4.7\,\%$ of ρ). The error bars due to the linear fits of the I-V-curves are smaller than the sizes of the symbols. Several samples show a drop to zero resistivity at temperatures below 4 K. This is shown in more detail in Fig. B.8.

B.2 Temperature-dependent Hall coefficients of $[(PbSe)_{1+\alpha}]_1(NbSe_2)_n$

The carrier (hole) density calculated assuming a single-band model (2.8) is shown on the right-hand side axis in Fig. B.6 a). At RT these carrier density values are about $p \approx 810^{21}\,\mathrm{cm}^{-3}$. This value is similar to the value for $NbSe_2$ single crystals for which a room temperature carrier density of about $1.3 \times 10^{22}\,\mathrm{cm}^{-3}$ can be calculated from the Hall coefficients measured within the layer planes ([60] and [52]). The RT carrier density of $\approx 10^{18}\,\mathrm{cm}^{-3}$ [65, 66] reported for PbSe films is clearly lower. The Hall coefficients of the samples $[(PbSe)_{1+\delta}]_1[NbSe_2]_n$ in Fig. B.6 a) show a similar temperature dependence for the samples $n = 1 - 3$ between $T = 4\,\mathrm{K}$ and $T = 300\,\mathrm{K}$. In this temperature range there is only a small variation in carrier density which similar to metals, for which no temperature dependence in the carrier density is expected. The small increase in R_H with decreasing temperature would be associated with a slight decrease in charge carrier density with decreasing temperatures in a single-band model.
At about $T = 4\,\mathrm{K}$, R_H of sample $n = 3$ (sample B) shows a decreased value and at $T = 4\,\mathrm{K}$ a change in sign (Fig. B.6 b)). A change in sign of R_H has also been reported for bulk $NbSe_2$ with a high RRR. In $NbSe_2$ R_H changes from positive to negative with decreasing temperatures at about 30 K to 60 K [52, 54, 60]. An example for R_H reported for $NbSe_2$ bulk single crystals is shown in Fig. B.6 b). This change in sign of the Hall coefficient has been proposed to be accompanied by a charge density wave transition at this temperature [54, 55, 57]. However, it has also been reported that this change in sign of R_H is only observed for $NbSe_2$ samples with a high RRR value of the $NbSe_2$ material [52, 53]. The ferecrystals do not show a high RRR value. A change in sign of R_H can also occur if two or more types of charge carriers with different signs (electrons and holes) contribute to the electrical transport, as can be seen in Eq. (2.18). Due to the similarity between the RT resistivity values of binary $NbSe_2$ and PbSe this seems probable. There have been reports on n-type and p-type PbSe and therefore, PbSe could contribute electrons and $NbSe_2$ holes to the electrical transport, which can lead to the observed change in sign of the total Hall coefficient. Magnetoresistance or Seebeck measurements would give more information necessary to analyze carrier densities and mobility values in terms of a two-band model. The carrier densities obtained in the single-band model assumption have to be treated with caution, because of these findings, the single-band model might not be applicable for these ferecrystals, at least at low temperatures.

The error bars shown in Fig. B.6 are due to the linear fits of the curves $R_\mathrm{H}(B)$.

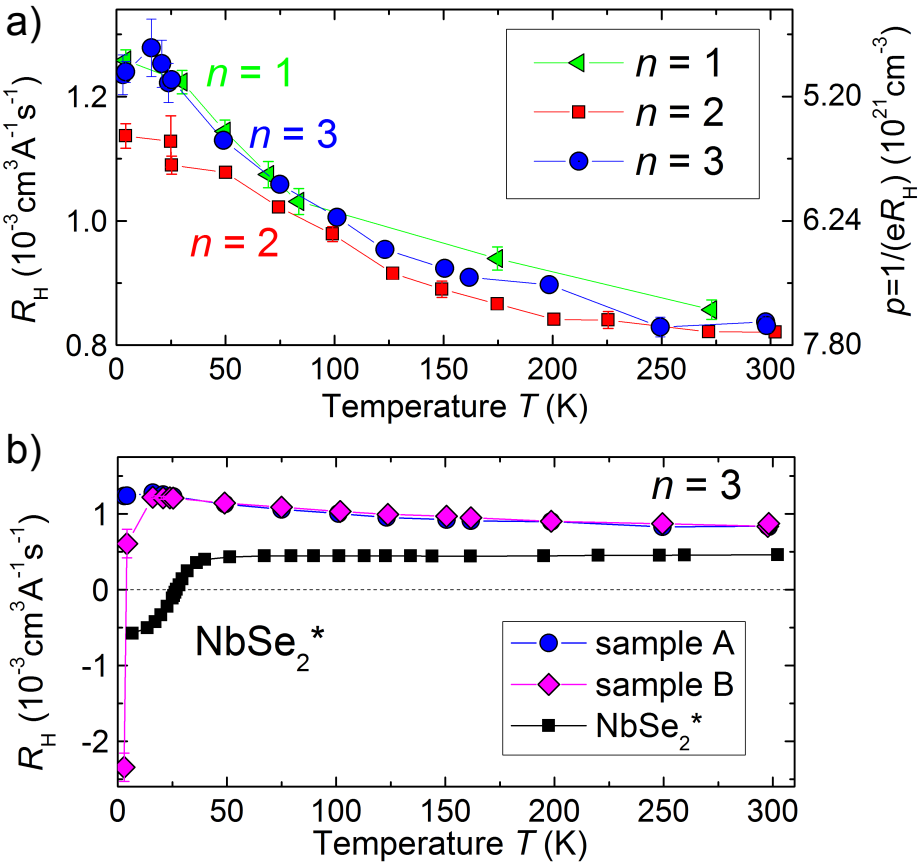

Figure B.6: Temperature-dependent Hall coefficients of $[(PbSe)_{1+\delta}]_1[NbSe_2]_n$ ferecrystals (batch 2) for $2\,K \leq T \leq 300\,K$. Lines are guides to the eye. a) samples $n = 1 - 3$ ('samples A'). The carrier density calculated using a single-band model is shown on the right-hand axis. b) Ferecrystal samples $n = 3$ in comparison to a $NbSe_2$ single crystal reported in [60]. The dashed line indicates $R_H = 0$. The Hall measurements measurements of the samples $m = 2$ and 3 were performed by A. Simon and A. Fiedler in the Novel Materials Group at HU Berlin.

An additional systematic error of 39 % due to the size of the contacts (Sect. 4.3.2) has to be considered when comparing the absolute values of the R_{H}. At about $T \leq 2.6\,\mathrm{K}$ the 'sample B' of $n = 3$ shows a change in the sign of the Hall coefficient, whereas the 'sample A' does not. This change in sign occurs very close to the superconducting transition temperature in sample B ($T_{\mathrm{c}} = 2.6\,\mathrm{K}$), which is higher than for sample A. This change in the Hall coefficient can therefore also be an effect of a canceling of superconductivity rather than a Hall effect.

B.3 Superconductivity in $[(PbSe)_{1+\alpha}]_1(NbSe_2)_n$

Batch 3

Table B.8: Transition temperatures T_{c} determined at 90 % of the residual resistance R_n of $[(\mathrm{PbSe})_{1+\delta}]_1[\mathrm{NbSe_2}]_n$ ferecrystals. The transition width was determined from the temperature values at 90 % and 10 % of R_n. Samples A and B are the clover and the cross-shaped samples, respectively.

n (Sample)	T_{c} (K) (K)	Transition width ΔT (K)	$\Delta T/T_c$ (%)
1 (A)	1.113(7)	0.27(3)	24(3)
1 (B)	1.104(5)	0.25(3)	23(3)
2 (A)	1.91(2)	0.07(3)	4(2)
2 (B)	1.92(2)	0.06(4)	3(2)
3 (A)	2.66(4)	0.04(4)	2(2)
3 (B)	2.66(3)	0.05(5)	2(2)

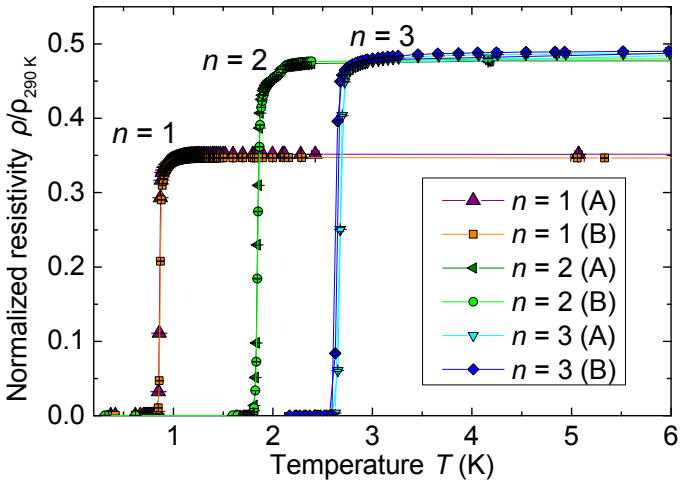

Figure B.7: Temperature-dependent resistivity measured using the Van der Pauw method of $[(PbSe)_{1+\delta}]_1[NbSe_2]_n$ ferecrystals (batch 3) for the temperature range $0.3\,\mathrm{K} \leq T \leq 6\,\mathrm{K}$.

Batches 1 and 2 in comparison to batch 3

For the samples $n = 1$ of batch 1 and 2 about 10 nm thick intermediate layers have been observed, which are shown schematically as orange rectangles in Fig. B.8. In samples $n = 2$ an about 5 nm thin Nb-rich film has been observed between the ferecrystals and the substrate.

Due to the presence of different intermediate layers in samples $n = 1$ and $n = 2$ of batch 1 and 2, the measured T_c do not have to be representative for the ferecrystals with the stacking sequences $n = 1$ and $n = 2$, but can be influenced by the intermediate layers, e. g. due to a parallel conduction or a proximity effect.

Sample $n =$ has shown intermediate layers with a high niobium concentration. Niobium is also a superconductor and transition temperatures of e. g. 9 K have been reported for bulk single crystals [198] and 4 K for thin films with a thickness of 2 nm [76]. The thickness of the Nb-rich layer in the ferecrystals is about 2 nm-5 nm and therefore the intermediate layer could have a significant influence on the transition temperature measured for the samples.

Furthermore, the resistivity measurements show that samples with the same nominal stacking sequences become superconducting at different transition temperatures. In general, is can be seen that samples with a higher resistivity show a lower T_c. There are especially large differences between the T_c values of batch 1 and 2 and for $n = 2$ and $n = 3$ of batch 2 the values also differ for the two samples which were on the same substrates. This shows that in spite of the TEM images showing a locally a similar structure for two batches, the superconducting properties differ. This might be due to structural inhomogeneities in the samples.

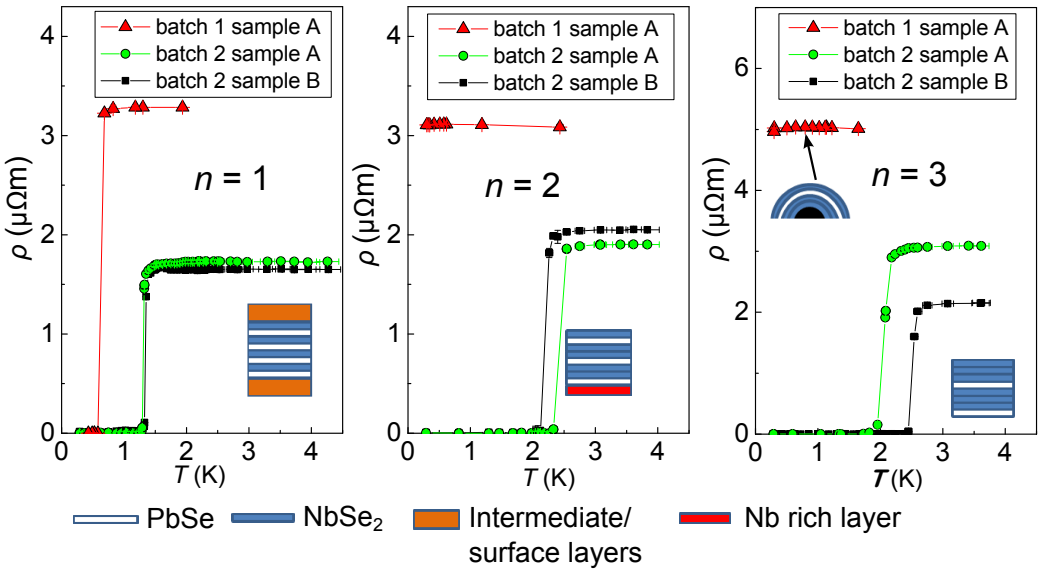

Figure B.8: Temperature-dependent resistivity ρ for $0.3\,\mathrm{K} \leq T \leq 5\,\mathrm{K}$ of $[(\mathrm{PbSe})_{1+\delta}]_1[\mathrm{NbSe_2}]_n$ ferecrystal samples with $n = 1-3$ of batch 1 and 2 showing superconducting transitions in some of the samples. The insets show schematics of the layer structures.

For sample $n = 3$ of batch 1 many round voids have been found throughout the sample viewed in HAADF-STEM and these might have led to a canceling of superconductivity. It is not clear whether the Nb-rich layer found in both batches of sample type $n = 2$ has an influence on T. Superconducting thin films of pure Nb are reported to have a transition temperature of $T = 3.7\,\mathrm{K}$ [76], which is much higher than the transition temperature observed for the $n = 2$ sample of batch 1.

Figure B.9 shows the measured transition temperatures for all three batches of the ferecrystals $[(\mathrm{PbSe})_{1+\delta}]_1[\mathrm{NbSe_2}]_n$ in comparison to values reported for conventional misfit layer compounds. The values of T_c measured for the ferecrystal samples are lower than the values reported for the respective MLCs. Furthermore, they are lower than T_c of bulk $\mathrm{NbSe_2}$ and are also lower than T_c of few-layer $\mathrm{NbSe_2}$ thin films consisting of only 9-16 monolayers of $\mathrm{NbSe_2}$, which showed transition temperatures of $T_c \approx 5.0\,\mathrm{K}$ to $6.7\,\mathrm{K}$ [9, 10]. The T_c values of the ferecrystals of batch 2 are similar to the values reported in [10] for 2-3 monolayers of $\mathrm{NbSe_2}$ after a high-current cleaning technique of $T_c = 2\,\mathrm{K}$ to $2.5\,\mathrm{K}$. The 2-3 monolayer thick $\mathrm{NbSe_2}$ flakes reported in [9] did not become superconducting down to $2.0\,\mathrm{K}$. However, for the $[(\mathrm{PbSe})_{1+\delta}]_1[\mathrm{NbSe_2}]_n$ samples of batch 1 and 2, it is difficult to draw conclusions for the influence of the stacking sequence of the $\mathrm{NbSe_2}$ and PbSe layers on the electrical properties. This is on the one hand, this is due to the scattering in T_c for the 2 batches and on the other hand it is due to the defect

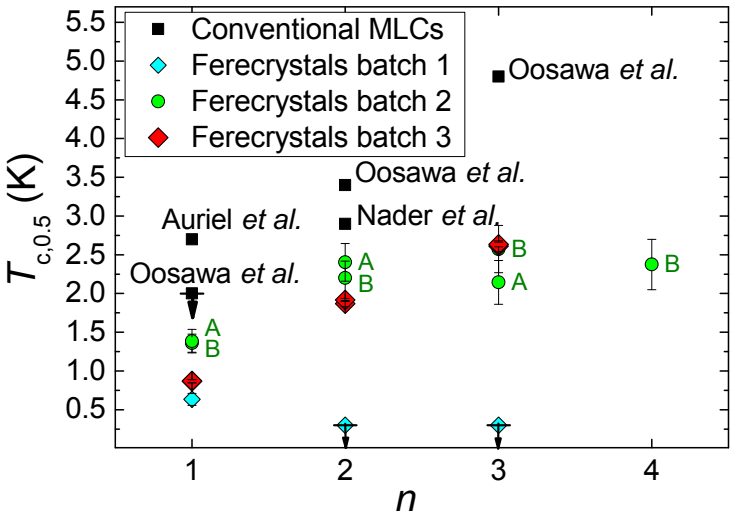

Figure B.9: Transition temperatures $T_{c,0.5}$ of $[(PbSe)_{1+\delta}]_1[NbSe_2]_n$ ferecrystals determined as the temperatures at which $R = 0.5R_{res}$ in comparison to those of conventional misfit layer compounds (MLCs). The labels A and B indicate the clover- and cross leaf shaped samples. The symbols with arrows for $n = 2$ and 3 of batch 1 and the MLC with $n = 1$ indicate that no transition to superconductivity is observed down to this temperature.

layers (intermediate and top layers, Nb-rich layers) differ for each value of n. Since neither the influence of n nor the influence of the layers stacking sequence is known an interpretation is difficult.

B.4 Temperature-dependent resistivity of $[(SnSe)_{1+\delta}]_m(NbSe_2)_1$

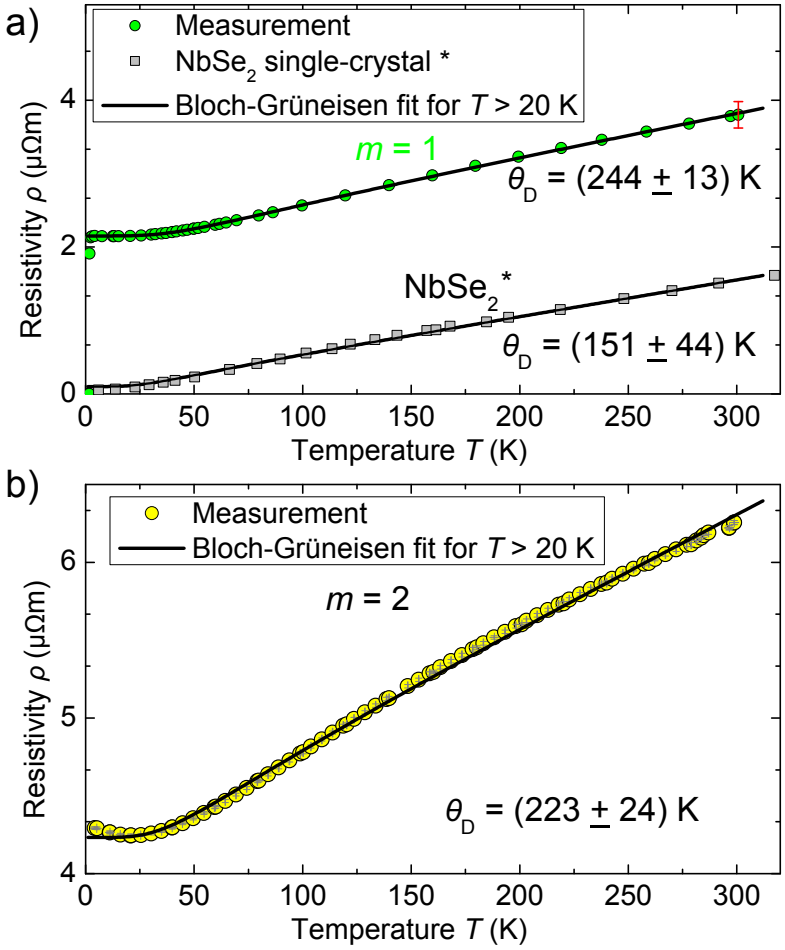

Figure B.10: a) Temperature-dependent van der Pauw resistivity ρ measured for temperatures $1.4\,\mathrm{K} \leq T \leq 300\,\mathrm{K}$ of $[(SnSe)_{1+\delta}]_m[NbSe_2]_1$ ferecrystal with $m = 1$ (sample A, clover leaf) and reported for a $NbSe_2$ single crystal [60]. An error bar is shown exemplarily for $T \approx 300\,\mathrm{K}$, which includes the error due to the contact size and thickness measurement. Black lines are Bloch-Grüneisen fits. b) for $m = 2$ (samples A, clover leaf shaped). The error bars shown here are due to the resistivity measurement and the thickness measurement. This error and the error in temperature are smaller than the size of the symbols. The resistivity measurements of the sample $m = 2$ were performed within the bachelor thesis by G. Hoffmann [203].

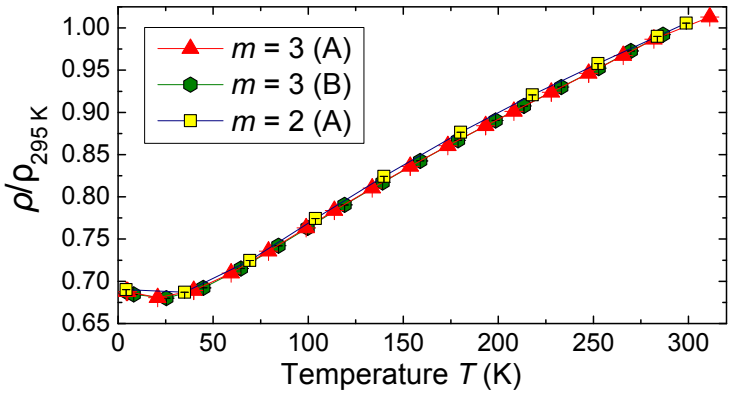

Figure B.11: Temperature-dependent normalized van der Pauw resistivity ρ for temperatures $1.4\,\mathrm{K} \leq T \leq 300\,\mathrm{K}$ of $[(\mathrm{SnSe})_{1+\delta}]_m[\mathrm{NbSe_2}]_1$ ferecrystals with $m = 2$ and $m = 3$ normalized to the room temperature resistivity $\rho_{295\mathrm{K}}$. The lines are guides to the eye. The resistivity measurements of the sample $m = 2$ and $m = 3$ were performed within the bachelor thesis by G. Hoffmann [203].

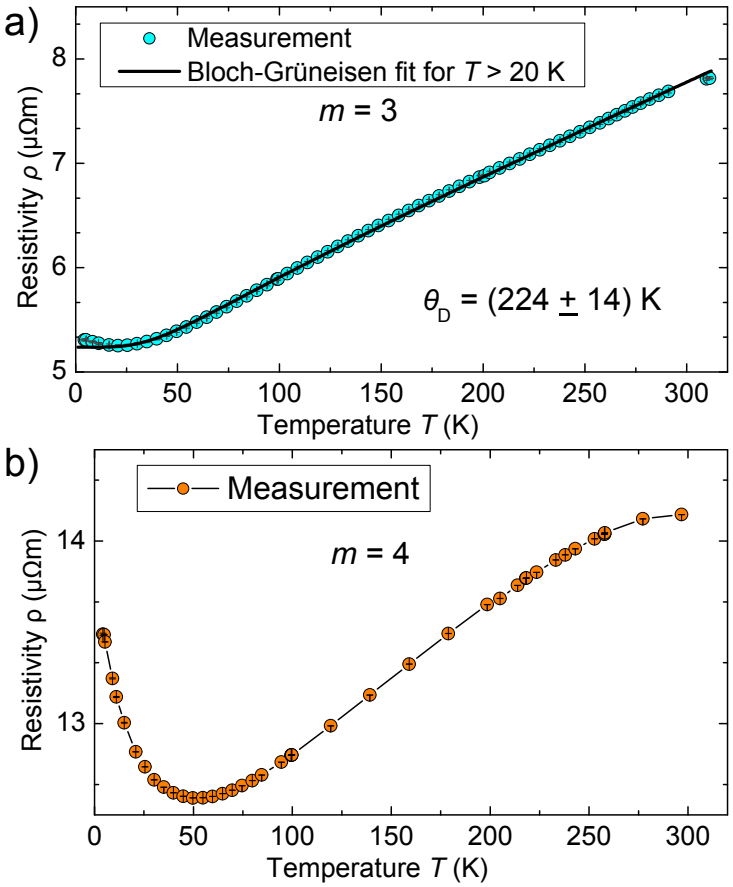

Figure B.12: a) and b) Temperature-dependent van der Pauw resistivity ρ for temperatures $1.4\,\mathrm{K} \leq T \leq 300\,\mathrm{K}$ of $[(SnSe)_{1+\delta}]_m[NbSe_2]_1$ ferecrystals with $m = 3$ and 4 (samples A, clover leaf shaped). The error bars shown here are due to the resistivity measurement and the thickness measurement. This error and the error in temperature are smaller than the size of the symbols. Black lines are Bloch-Grüneisen fits.The resistivity measurements of the sample $m = 3$ were performed within the bachelor thesis by G. Hoffmann [203].

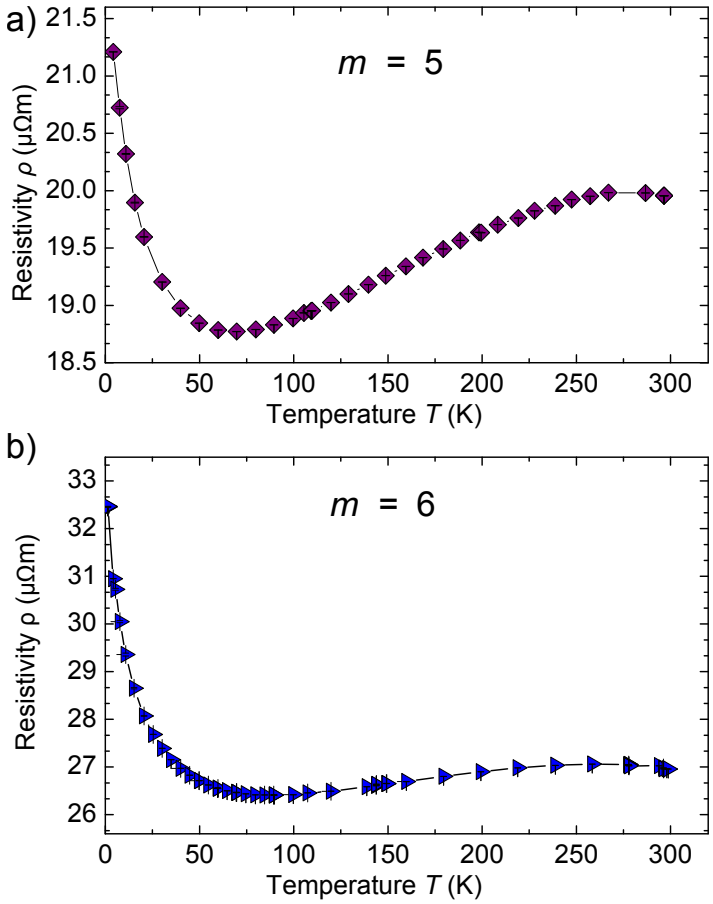

Figure B.13: Temperature-dependent van der Pauw resistivity ρ for temperatures $1.4\,\mathrm{K} \leq T \leq 300\,\mathrm{K}$ of $[(\mathrm{SnSe})_{1+\delta}]_m[\mathrm{NbSe_2}]_1$ ferecrystals with $m = 5$ and 6 (samples A, clover leaf shaped). The error bars shown here are due to the resistivity measurement and the thickness measurement. This error and the error in temperature are smaller than the size of the symbols.

B.5 Exemplary I-V curves of $[(SnSe)_{1+\delta}]_m(NbSe_2)_1$

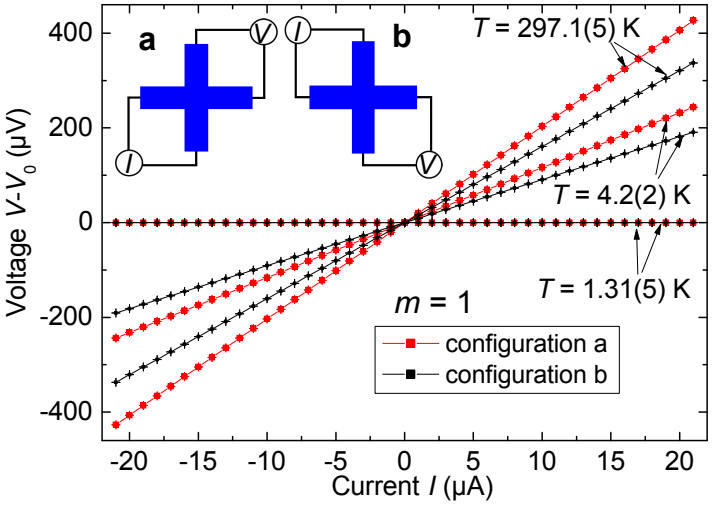

Figure B.14: Exemplary I-V curves for different temperatures for sample $[(SnSe)_{1+\delta}]_m[NbSe_2]_1$ with $m = 1$ (A). The schematics on the upper left-hand side show two exemplary van der Pauw measurement configurations (a and b).

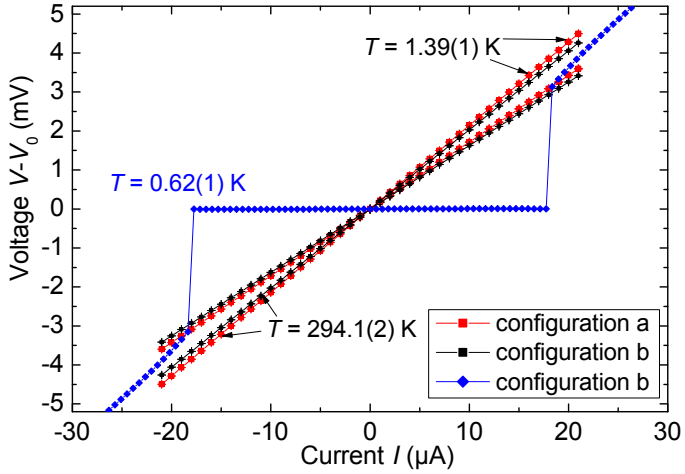

Figure B.15: Exemplary I-V curves for different temperatures for sample $[(SnSe)_{1+\delta}]_m[NbSe_2]_1$ with $m = 6$ (B). The schematics on the upper left-hand side show two exemplary van der Pauw measurement configurations (a and b). For $T = 0.62(1)$ K /(blue diamonds) the sample shows a transition from the superconducting to the normal conducting state at $I_c = \pm 17.76\,\mu A$.

B.6 Exemplary Hall measurement results of $[(SnSe)_{1+\delta}]_m(NbSe_2)_1$

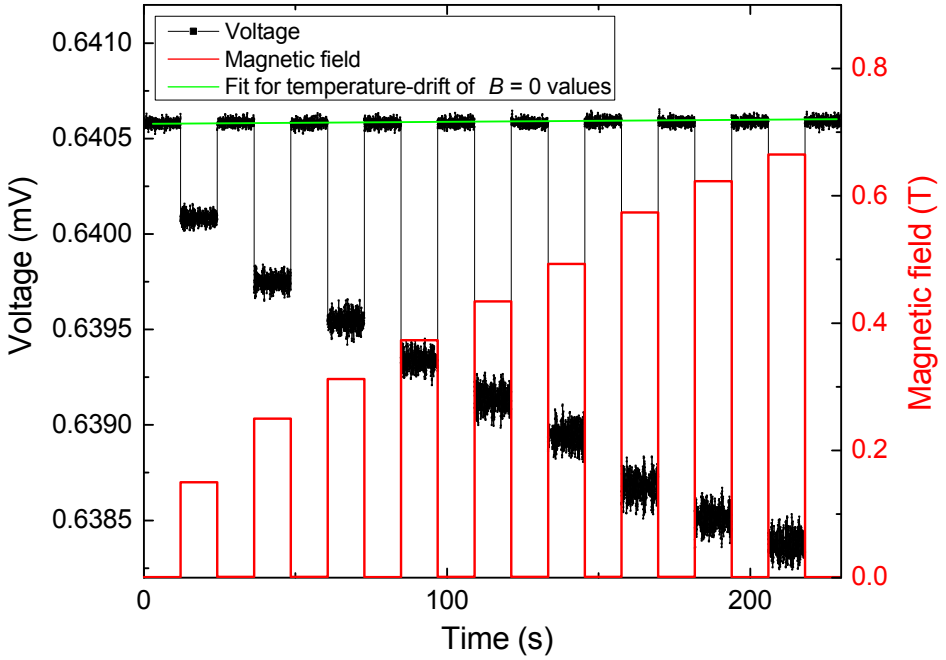

Figure B.16: Exemplary Hall measurement for $[(SnSe)_{1+\delta}]_m[NbSe_2]_1$ $m = 1$(A) using Keithley 6221 and 2182 instruments with a constant current of $I = 150\,\mu A$ at $T = 297\,K$ and varying magnetic field B. The measurement setup is shown in Fig. 2.6 c). It can be concluded that the Hall coefficient is p-type.

B.7 Magnetoresistance measurements of $[(SnSe)_{1+\delta}]_2(NbSe_2)_1$ and analysis in a two-layer model

The magnetoresistance measurements shown in Fig. B.17 were performed within the Bachelor thesis of G. Hoffmann [203]. These measurements were performed in one of the van der Pauw resistance measurement configurations using the flow-cryostat and a lock-in amplifier SR830 with a current of $I_{rms} = 50\,nA$.

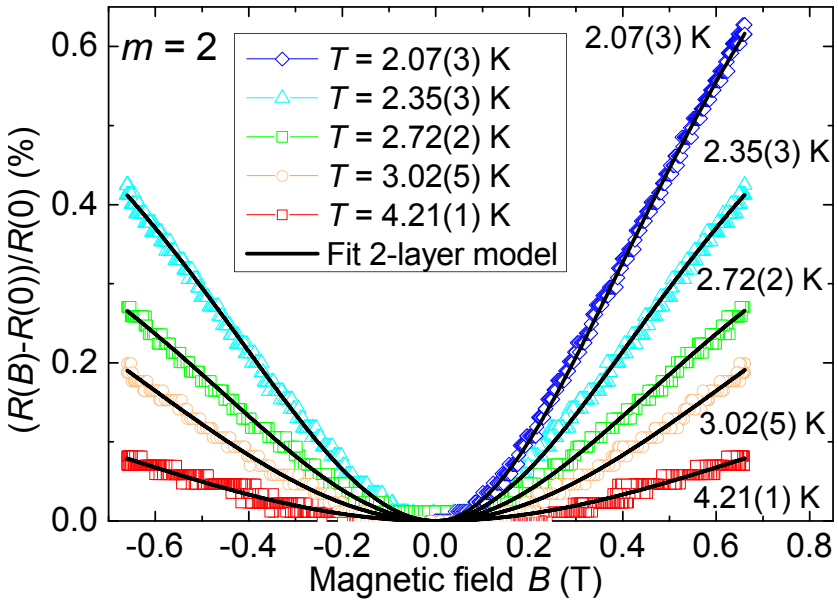

Figure B.17: Magnetoresistance of sample $[(SnSe)_{1+\delta}]_m[NbSe_2]_1$ with $m = 2$ and fits according to a two-band model discussed in section 6.8.2 in which $NbSe_2$ is assumed to be n-type and SnSe p-type.

B.8 Hall coefficients and resistivity of $[(SnSe)_{1+\delta}]_6(NbSe_2)_1$ for analysis in a two-layer model

The measured voltages for the Hall measurement have been corrected for magnetoresistance effects and have been fitted near $B = 0$, as shown in Figs B.18, B.19, B.20 and B.21. The fit results are shown in Table B.9.

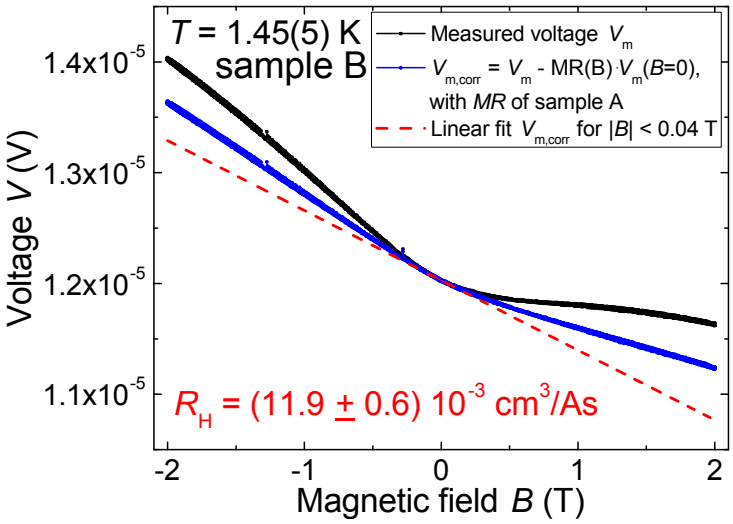

Figure B.18: Hall measurement of sample $[(SnSe)_{1+\delta}]_m[NbSe_2]_1$ with $m = 6$. The measured Hall voltage (black) has been corrected for the magnetoresistance (blue). A linear fit (red, dashed) has been made to this corrected Hall voltage.

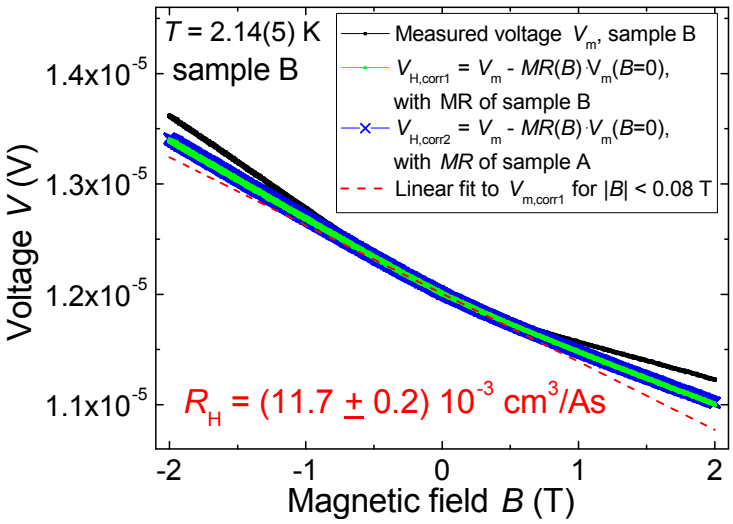

Figure B.19: Hall measurement of sample $[(SnSe)_{1+\delta}]_m[NbSe_2]_1$ with $m = 6$. The measured Hall voltage (black) has been corrected for the magnetoresistance (blue). A linear fit (red, dashed) has been made to this corrected Hall voltage.

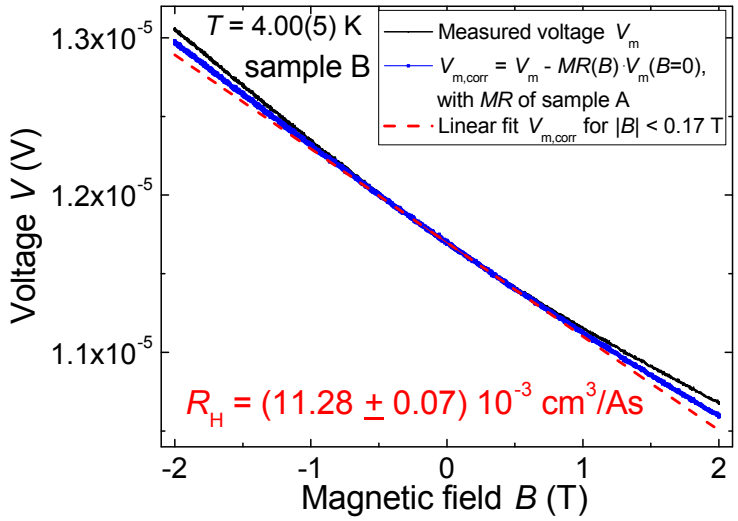

Figure B.20: Hall measurement of sample $[(\mathrm{SnSe})_{1+\delta}]_m[\mathrm{NbSe_2}]_1$ with $m = 6$. The measured Hall voltage (black) has been corrected for the magnetoresistance (blue). A linear fit (red, dashed) has been made to this corrected Hall voltage.

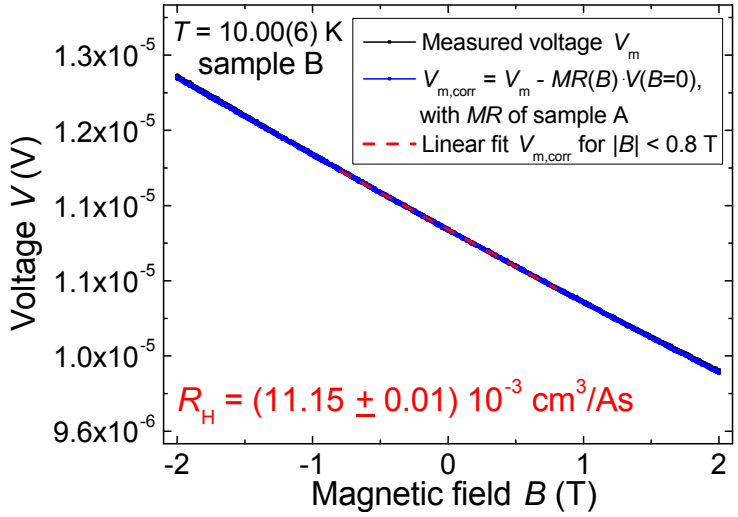

Figure B.21: Hall measurement of sample $[(\mathrm{SnSe})_{1+\delta}]_m[\mathrm{NbSe_2}]_1$ with $m = 6$. The measured Hall voltage (black) has been corrected for the magnetoresistance (blue). A linear fit (red, dashed) has been made to this corrected Hall voltage.

Table B.9: Resistance $R(B = 0)$, resistivity ρ and Hall coefficient R_{H} of the ferecrystal $[(\mathrm{SnSe})_{1+\delta}]_m[\mathrm{NbSe_2}]_1$ $m = 6$ for different temperatures T. The errors given for ρ and R_{H} result from the error in the linear fit of $V(I)$ and $V_{\mathrm{H}}(B)$ and from the error in thickness measurement and size of the contacts.

T	$R(B = 0)$	$\rho(B = 0)$	R_{H}
(K)	(Ω)	($\mu\Omega\,$m)	(10^{-3} cm^3/(As))
1.45(5)	311	32.40 ± 1.61	11.9 ± 4.8
2.14(5)	308	32.03 ± 1.61	11.7 ± 4.7
4.00(5)	299	31.04 ± 1.51	11.28 ± 4.6
10.00(6)	284	29.53 ± 1.41	11.15 ± 4.5

Table B.10: Resistance $R(B = 0)$, resistivity ρ and Hall coefficient R_{H} of the ferecrystal $[(\mathrm{SnSe})_{1+\delta}]_m[\mathrm{NbSe_2}]_1$ $m = 2$ for different temperatures T. The errors given for ρ and R_{H} result from the error in the linear fit of $V(I)$ and $V_{\mathrm{H}}(B)$ and from the error in thickness measurement and size of the contacts.

T	$R(B = 0)$	$\rho(B = 0)$	R_{H}
(K)	(Ω)	($\mu\Omega\,$m)	(10^{-3} cm^3/(As))
2.07(3)	20.1	4.34 ± 0.21	2.37 ± 0.96
2.35(3)	20.2	4.36 ± 0.21	2.41 ± 0.96
2.72(2)	20.2	4.36 ± 0.21	2.41 ± 0.96
3.02(5)	20.3	4.37 ± 0.21	2.41 ± 0.96
4.21(1)	20.2	4.36 ± 0.21	2.40 ± 0.95

B.9 Critical current for normal-superconducting transition in $[(SnSe)_{1+\delta}]_6(NbSe_2)_1$

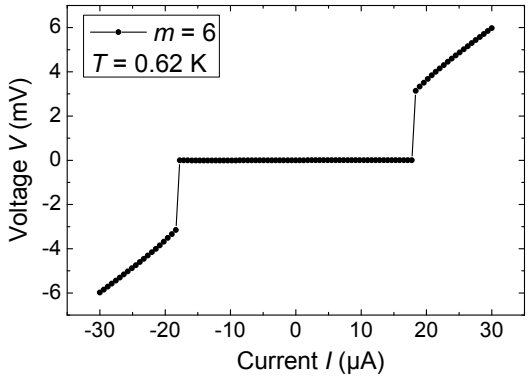

Figure B.22: Current-voltage plot of $[(SnSe)_{1+\delta}]_m[NbSe_2]_1$ with $m = 6$ showing a transition from the superconducting to the normal state at $I_c = \pm 17.76\,\mu A$.

B.10 Normal-to-superconducting transition temperature in $[(SnSe)_{1+\delta}]_m(NbSe_2)_1$

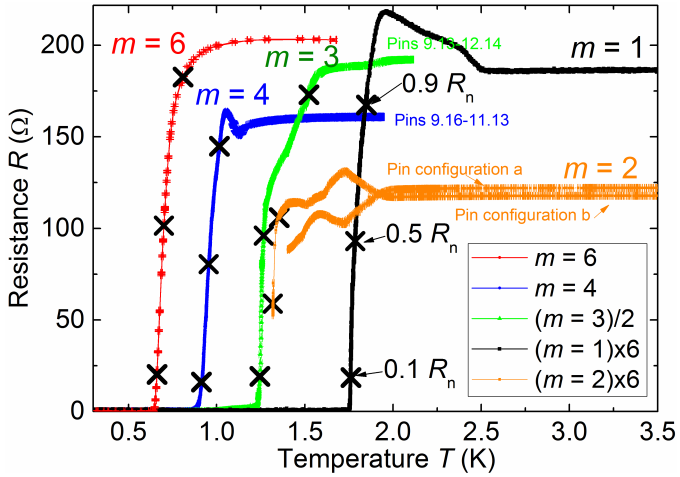

Figure B.23: Temperature-dependent resistance measured using a lock-in amplifier in one of the van der Pauw resistance measurement configurations. Crosses indicate the 10 %, 50 % and 90 % values of the residual resistances R_n.

Figure B.23 shows temperature-dependent resistance measurements performed using a lock-in amplifier (DSP 7265) with $I_{rms} = 50\,nA$ for $m = 1$ and 6 and

$I_{rms} = 500\,\mathrm{nA}$ for $m = 3$ and $I_{rms} = 50\,\mu\mathrm{A}$ for $m = 2$. The measurements of $m = 2$ have been performed by G. Hoffmann within the Bachelor thesis [203]. The resulting values for T_c are given in Table B.11.

Table B.11: Transition temperatures T_c determined at 90 % of the normal resistivity ρ_n (near T_c of $[(SnSe)_{1+\delta}]_m[NbSe_2]_1$ ferecrystals with $m = 1, 3$ and $m = 6$ (samples B). The transition width ΔT was determined as the temperature range between the temperatures at which the resistance is 90 % and 10 % of R_n obtained from the lock-in measurements.

m	Sample	T_c (K)	ΔT (K)	$\Delta T/T_c$ (%)
1	A	2.01 ± 0.10	0.10 ± 0.05	5 ± 3
1	B	2.04 ± 0.10	0.10 ± 0.05	5 ± 3
2	A	1.35 ± 0.10	not measured	
3	A	1.44 ± 0.16	0.23 ± 0.05	16 ± 4
3	B	1.44 ± 0.16	0.23 ± 0.05	16 ± 4
4	A	1.05 ± 0.03	0.10 ± 0.04	10 ± 4
4	B	1.08 ± 0.03	0.10 ± 0.04	10 ± 4
6	A	0.86 ± 0.05	0.15 ± 0.02	17 ± 3
6	B	0.82 ± 0.05	0.15 ± 0.05	18 ± 7

B.11 Critical magnetic field $[(SnSe)_{1+\delta}]_6(NbSe_2)_1$

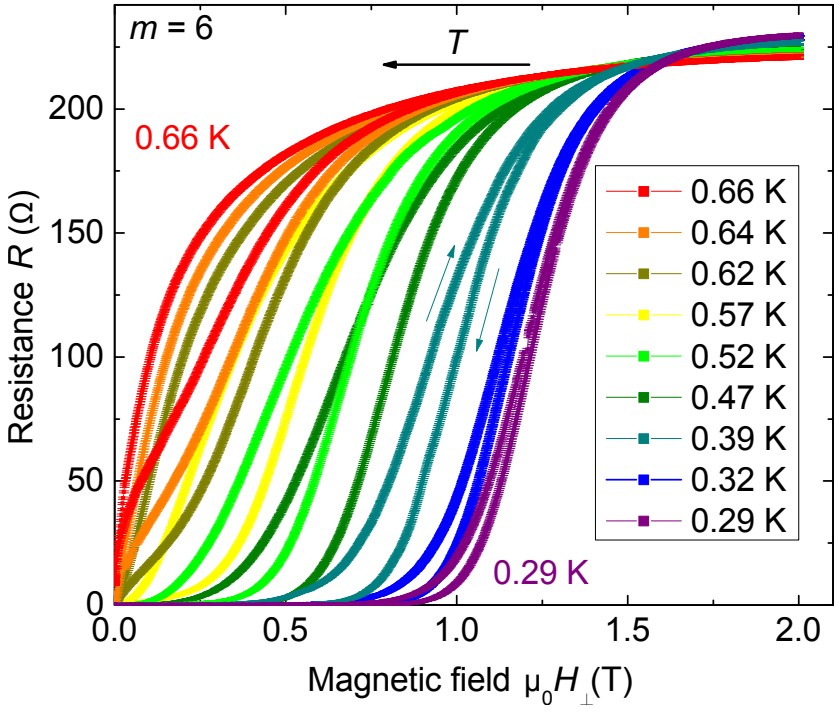

Figure B.24: Magnetic-field-dependent resistance of $[(SnSe)_{1+\delta}]_m[NbSe_2]_1$ ferecrystals with $m = 6$ (sample B) in a magnetic field perpendicular to the layers. The error in temperature is 0.02 K.

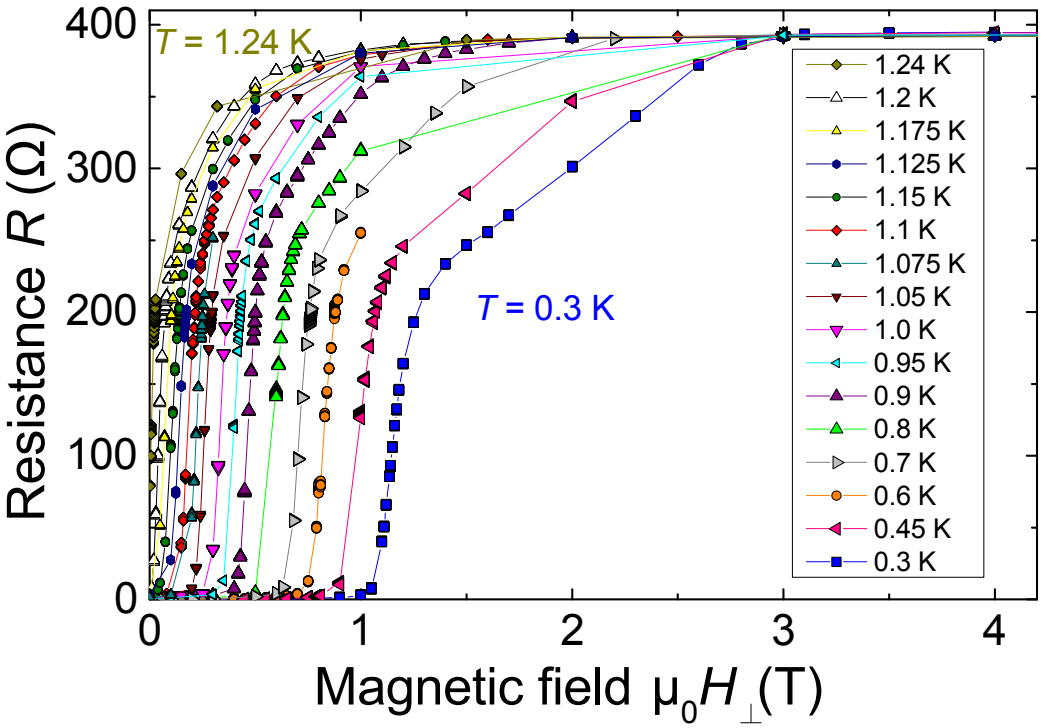

Figure B.25: Magnetic-field-dependent resistance of $[(SnSe)_{1+\delta}]_m[NbSe_2]_1$ ferecrystals with $m = 3$ in a magnetic field perpendicular to the layers. The error in temperature is 0.02 K.

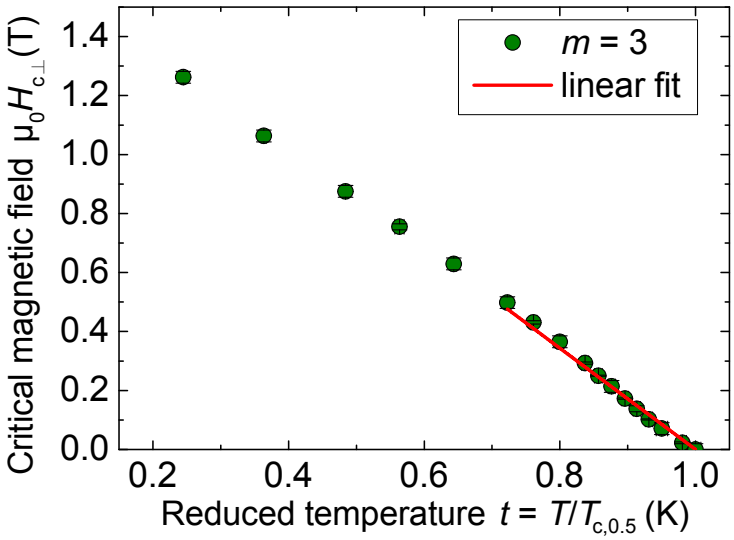

Figure B.26: Temperature-dependent critical perpendicular magnetic field for $[(SnSe)_{1+\delta}]_m[NbSe_2]_1$ ferecrystals with $m = 3$.

B.12 Mean free path of $[(SnSe)_{1+\delta}]_m(NbSe_2)_1$

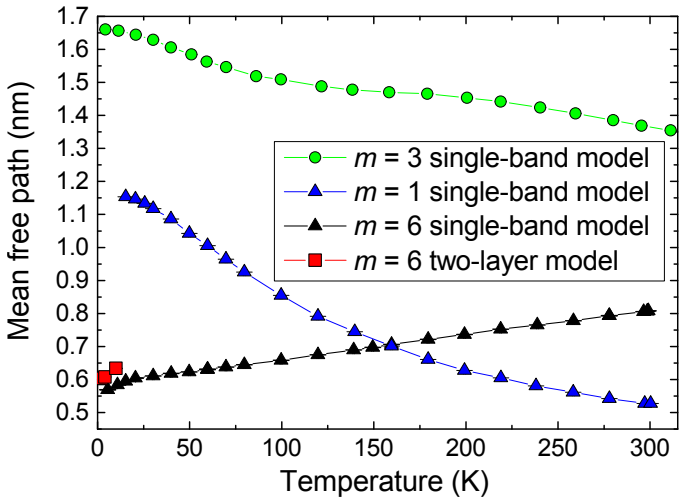

Figure B.27: Mean free paths calculated for $[(SnSe)_{1+\delta}]_m[NbSe_2]_1$ ferecrystals from the single-band carrier density using the quasi-free charge carrier model. For $m = 6$ the result using the carrier density for $NbSe_2$ obtained using two-layer model is also shown.

B.13 Temperature dependence of the critical magnetic fields

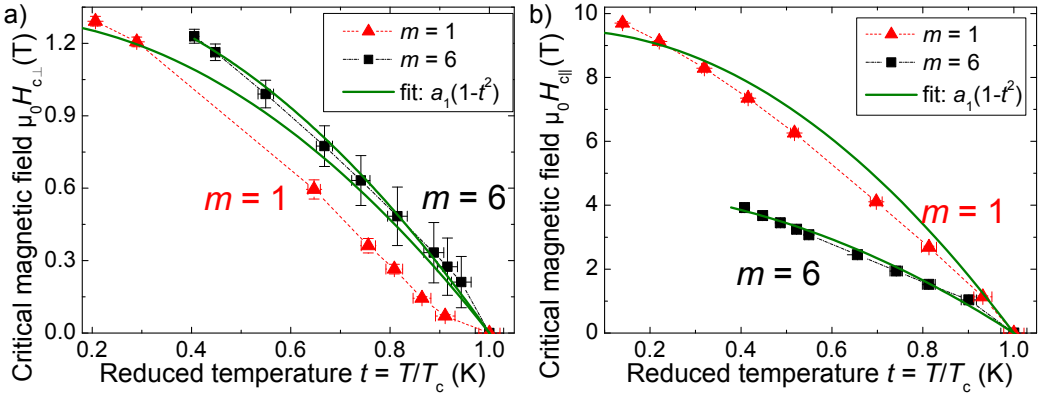

Figure B.28: a) Perpendicular and b) parallel critical magnetic field for $[(SnSe)_{1+\delta}]_m[NbSe_2]_1$ ferecrystals with $m = 1$ and $m = 6$. The fits are according to the empirical parabolic law found for type-I superconductors, Eq. (2.30), with fit parameter a_1.

B.14 Example for Ginzburg-Landau 2D fit to temperature-dependent parallel critical magnetic field

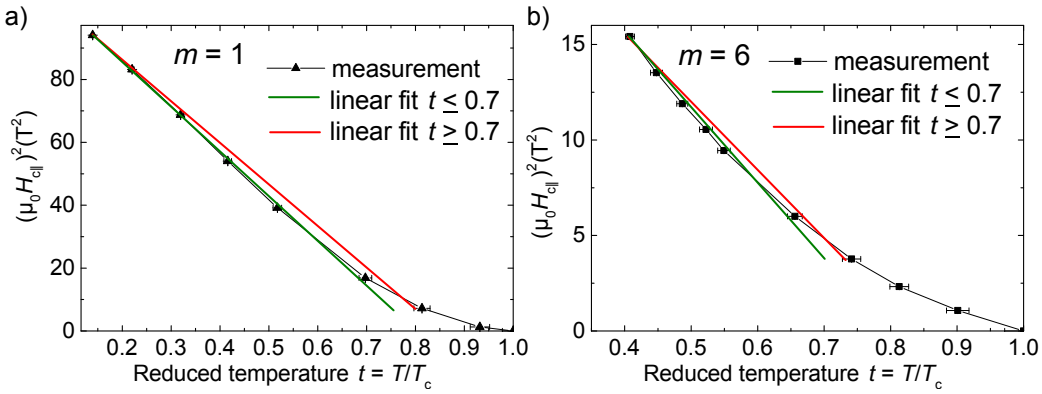

Figure B.29: Square of parallel critical magnetic field plotted against reduced temperature t for $[(SnSe)_{1+\delta}]_m[NbSe_2]_1$ ferecrystals with a) $m = 1$ and b) $m = 6$. The green line is a schematic line showing that a linear dependence $H^2_{c\|}(t)$ (2-D behavior) might be present in the measured data for t up to $t \approx 0.75$ for $m = 1$ and up to $t \approx 0.7$ for $m = 6$. The red line is a schematic line showing that no linear dependence $H^2_{c\|}(t)$ (2-D behavior) is present in the measured data if measured values for $t \geq 0.72$ are included. If there was a 3-D to 2-D crossover, then the upper boundary for T^* estimated from the measured data would be between $t \approx 0.68$ and $t \approx 0.75$ for sample $m = 1$ and it would be between $t \approx 0.65$ and $t \approx 0.75$ for $m = 6$.

B.15 MATLAB code for the calculation of the van der Pauw sheet resistance

```
%program requires files to be in this sequence: R1,R1,R2,R2,R1,R1,R2...
    ,R2
%requires herrorbar.m in same folder

clear all
hold off
format long
close

%%  Enter Input data:

% 1. Enter path for input files and result files:

filelocation = 'C:\'; %location of input files
filelocationresults = 'C:\';
```

```
diary(fullfile(filelocationresults,'diary.dat'))

% 2. Enter number of header lines in measurement .txt- files:

headerlines = 29

% 3. Enter voltage measurement ranges :

Vrange2401 = 200*10^(-3) % in V, possible ranges in Volt: ...
    200*10^(-3) ; 2 ; 20
Vrange2182 = 10*10^(-3)  % in V, possible ranges in Volt: 10*10^(-3)...
     ; 100*10^(-3) ; 1 ; 10 ; 100

% 4. Was a magnetic field applied and measured?

Bfieldmeasured=0  % yes=1; no=0

%End input data

%% Finds all txt-file names in the input folder
locexist=exist(filelocation,'dir');
 if locexist==0
     disp('file location does not exist.')
 end

wildcard='\*';
fileending='.txt';
directory=[filelocation,wildcard,fileending];

namesoffiles = dir (directory); %structure array of all .txt ...
    filenames

%% check if 8 txt files per van der Pauw measurement

nufiles = size(namesoffiles,1); % Number of txtfiles in folder
if mod(nufiles,8) == 0
else
    disp('Number of files not multiple of 8!')
end

%% create cell-array for filenames

Files={zeros(nufiles,1)};

for fileno =1:nufiles
Files(fileno)={namesoffiles(fileno).name};%fill cell array with ...
    filenames
end

%% get filenumbers from filenames to check if 8 have same number

```

```
nufilesmultipleof8=nufiles+8-mod(nufiles,8);
Nocheck=zeros(nufilesmultipleof8,1);
for k=1:nufiles
filenamess=char(Files(k));
C = textscan(filenamess, '%s %f %s %f %s');
Nocheck(k,1)=C{2};
end
countPauw=nufiles/8;  % number of van der Pauw measurements
No=zeros(8,1);
%a=0; %starts at 3rd row of results-cell (first 2rows are header)
for a=0:8:nufiles-mod(nufiles,8)
        for y=1:8
         No(y,1)=Nocheck(a+y); %to test if fileno is equal for all 8 ...
             files
        end
         q=No(1,1);
          if No(2,1)==q && No(3,1)==q && No(4,1)==q && No(5,1)==q && ...
              No(6,1)==q && No(7,1)==q && No(8,1)==q
            else
            warn3=sprintf('For file 00%8.0f there are not 8 files ...
                present.',No(1,1));
            disp(warn3);
          return
         end
end

%% create a matrix for I-V-curve fit results and enter 2 header ...
    lines
result=cell(length(Files)+2,4); %+2 due to 2 header lines
result(1,1)={'Filename'};
result(1,2)={'Resistance'};
result(1,3)={'Error Resistance'};
result(1,4)={'Pearsons r'};
result(2,1)={' '};
result(2,2)={'Ohm'};
result(2,3)={'Ohm'};
result(2,4)={' '};

%% make I-V-curve fits and plots for each input file:

for x=1:length(Files)
fid=0;  %file identifier
while fid < 1 % get current filename, while-loop for error message ...
    if file does not exist
     filename=char(Files(x));
     fullfilename=[filelocation,'\',filename];
        [fid,message] = fopen(fullfilename, 'r');
    if fid == -1
      disp('file does not exist.')
      return
    end
```

```
end

%% ----------------------open contents of the file...
    ------------------------------------
GPIB=textscan(fid,'GPIB0::%2f');
GPIBadd=GPIB{1}; %e.g. GPIB0::16::INSTR

measure = textscan(fid, '%f %f %f %f %f ', 'headerlines', ...
    headerlines);

status = fclose('all');

I = measure{1,1};
V = measure{1,2};
Vcorr=V-V(1,1); % V(1,1) has to be the zero point
Powercorr=Vcorr.*I;
Resistcorr=Vcorr./I;
figure('visible','off')
plot(Powercorr(2:length(Powercorr)),Resistcorr(2:length(Resistcorr))...
    ,'.-')%do not plot for Power=0
xlabel('Power P [W]')
ylabel('Resistance R [\Omega]')
fnam=sprintf('%s%s%s_%s',filelocationresults,'\',char(Files(x)),'...
    _roverp.jpg');
print('-dpng',fnam)
close

%-----------------linear fit-------------------
%% Keithley 2401  systematic errors
% assuming systematic errors have the value of the next-to-last ...
    digit:
if GPIBadd == 24 || GPIBadd == 25 || GPIBadd == 23 || GPIBadd == 26
    if Vrange2401 == 200*10^(-3)
        error=10^(-5)*ones(length(V),1);
    elseif Vrange2401 == 2
        error=10^(-4)*ones(length(V),1);
    elseif Vrange2401 == 20
        error=10^(-3)*ones(length(V),1);
    else
        display('Enter correct Voltage range.')
    end
%%Keithley 2182 systematic errors
% assuming systematic errors have the value of the next-to-last ...
    digit:

elseif GPIBadd == 12 || GPIBadd == 16
    if Vrange2182 == 10*10^(-3)
        error=5*10^(-8)*ones(length(V),1);
    elseif Vrange2182 == 100*10^(-3)
        error=10^(-7)*ones(length(V),1);
    elseif Vrange2812 == 1
```

```
        error=10^(-6)*ones(length(V),1);
    elseif Vrange2812 == 10
        error=10^(-5)*ones(length(V),1);
    elseif Vrange2182 == 100
        error=10^(-4)*ones(length(V),1);
    else
        display('Enter correct Voltage range.')
    end
else
    display('GPIB-adress not found!')
end
[fitresult,gof] = fit(I,V,'poly1','Weight',1./(error.^2));
R_intervals = confint(fitresult,0.95);
error_R=max(fitresult.p1-R_intervals(1,1),fitresult.p1-R_intervals...
    (2,1));
V_fit = feval(fitresult,I); %calculate fit values

%% ----------check if IV-curve is linear----------


Pearsonsr=gof.rsquare; %Pearson's r
if Pearsonsr<0.98
    warn=sprintf('%s: Pearsons r < 0.98 ! Data not linear.',char(...
        Files(x)));
    disp(warn)
end
%% plot I-V curve and fit
figure('visible','off')
plot(I,V,'.',...
      I,V_fit,'r-');
xlabel('Current I [A]');
ylabel('Voltage V [V]');
grid on
hold on
errorbar(I,V,error,'.')
legend('Data','Linear Fit','Location','Best');
hold off
fnam=sprintf('%s%s%s_%s',filelocationresults,'\',char(Files(x)),'....
    jpg');
print('-dpng','-r300',fnam)
close

%% Check if residuals are high and plot residuals over current
residuals=zeros(length(Files),1);

res = V - V_fit;
for k=1:length(V)
    if abs(res(k)) >= 2*error(k);
    warn4=sprintf('Residual high for file %s.',char(Files(x)));
            disp(warn4);
    residuals(x,1)=1;
```

```
    end
end

figure('visible','off')
plot(I,res,'.','MarkerSize',25)
xlabel('Current I [A]');
ylabel('Residuals [V]');
legend('Residuals','Location','Best');
fnam=sprintf('%s%s%s_%s',filelocationresults,'\',char(Files(x)),'...
    _res.jpg');
print('-dpng',fnam)
close

%% fill matrix with I-V-curve fit results
%filename, resistance, error resistance  %x+2 because of header
result(x+2,1)={filename};
result(x+2,2)={fitresult.p1};
result(x+2,3)={error_R};
result(x+2,4)={Pearsonsr};
end

%% save single I-V-fit results in result.dat

[nrows,ncols]= size(result);

fnam=sprintf('%s%s%s_%s',filelocationresults,'\',char(Files(1)),'...
    _result.dat');
fid = fopen(fnam, 'w');

for row=1:2
    fprintf(fid, '%s; %s; %s; %s\n', result{row,:});
end

for row=3:nrows
    fprintf(fid, '%s; %f; %f; %f\n', result{row,:});
end

fclose('all');


%% Calculate van der Pauw sheet resistance and errors out of 8 I-V-...
    curves for each temperature:
resultPauw=zeros(countPauw,2);% dummy for averages of 8 R's and ...
    errors
Avgres=zeros(8,1);
Errorsquare=zeros(countPauw,1);
x=2; %starts at 3rd row of results-cell (first 2 rows are header ...
    lines)
for count=1:countPauw
        for y=1:8
```

```
245         Avgres(y,1)=result{x+y,2}; %starts at first of 8 files at 3...
                rd row of results-cell
            Errorsquare(y,1)=result{x+y,3}.^2;
            end
            resultPauw(count,1)=sum(Avgres); %sum of all 8 resistances
            resultPauw(count,2)=sqrt(sum(Errorsquare)); %pythagorean ...
                addition of all 8 resistance-errors (error_R's)
250         x=x+8;
    end

    %calculate Pauw correction factor f
    R1=zeros(4,1);
255 R2=zeros(4,1);
    fresult=zeros(countPauw,1);
    x=2;
    for count=1:countPauw
            for y=1:4
260         R1(2*y-1,1)=abs(result{x+2*y-1,2}); %line 1,3,5,7; abs ...
                because for superconducting samples R becomes negative ...
                sometimes
            R2(2*y,1)=abs(result{x+2*y,2}); %line 2,4,6,8
            end
    RRatio=sum(R1)/sum(R2);
    if RRatio<=1
265     RRatio=sum(R2)/sum(R1); %in Van der Pauw paper plotted for ...
            RRatio>1
    end
    Pauwequation=@(f)cosh(((RRatio-1)./(RRatio+1))*(log(2)/f))-0.5*exp((...
        log(2)/f));
    f = fsolve(Pauwequation,0.5);
    fresult(count,1)=f;
270 char(Files(x))
    x=x+8;
    end

    %Calculate sheet resistance R_s:
275 resultPauw(:,1)=resultPauw(:,1).*pi./log(2).*fresult(:,1)./8;%sheet ...
        resistance
    resultPauw(:,2)=resultPauw(:,2).*pi./log(2).*fresult(:,1)./8;%errors...
         sheet resistance

    %% get temperatures from filenames
    Temp=zeros(nufiles,1);
280 for k=1:nufiles
    filenamess=char(Files(k));
    C = textscan(filenamess, '%*s␣%*s␣%*s␣%*s␣T2=%7.4f␣%*s');
    Temp(k,1)=C{1};
    end
285 %% get Bfield from filename:

    Bfield=zeros(nufiles,1);
```

```
if Bfieldmeasured==1
for k=1:nufiles  %25
    filenamess=char(Files(k));
    C = textscan(filenamess, '%*s %*s %12s B=%3.0fmT %*s %*s');
        if length(C{2})==1
        Bfield(k,1)=C{2}/1000;
       end
end
end

%% Determine average temperatures, temperature errors, Bfields, ...
    filenames, R^2's, high-residuals-warnings
resultTemp=zeros(countPauw,2);  % 2 columns for temps and error ...
    temps
resultB=zeros(countPauw,1);
eightsfilename={zeros(countPauw,1)};
eighttemps=zeros(8,1);
eightBs=zeros(8,1);
eightresid=zeros(8,1);
residualalarm=zeros(countPauw,1);
t=0;
for tcount=1:countPauw
    for y=1:8
       eighttemps(y,1)=Temp(t+y,1); %starts at first of 8 files
       eightBs(y,1)=Bfield(t+y,1);
       eightresid(y,1)=residuals(t+y,1);
    end
      resultTemp(tcount,1)=min(eighttemps)+(max(eighttemps)-min(...
          eighttemps))/2; %temperature
      resultTemp(tcount,2)=(max(eighttemps)-min(eighttemps))/2; % ...
          error of temperature
      resultB(tcount,1)=(sum(eightBs))/8;
      eightsfilename(tcount,1)={Files{1,t+1}};
      residualalarm(tcount,1)=sum(eightresid);
      t=t+8;
end

%% save Pauw-sheet resistance and AverageTemp and B-field and ...
    filename in dat-file
fnam=sprintf('%s%s%s_%s',filelocationresults,'\',char(Files(1)),'...
    _Pauw.dat');
fid = fopen(fnam, 'wt');

fprintf(fid, '%s;%s;%s;%s;%s;%s;%s;%s\n', 'Temperature', '...
    Error Temperature','Sheet Resistance','Error Sheet Resistance','...
    Magnetic Field','Filename','Pauw correction factor f','Warning ...
    high residuals');
fprintf(fid, '%s;%s;%s;%s;%s;%s;%s;%s\n', 'K','K','Ohm','...
    Ohm','T',' ',' ',' ');
for row=1:countPauw
```

```
    fprintf(fid, '%f;␣%f;␣%f;␣%f;␣%f;␣%s;␣%f;␣%f␣\n', resultTemp(row...
        ,1:2),resultPauw(row,1:2),resultB(row,1),char(eightsfilename...
        (row,1)),fresult(row,1),residualalarm(row,1));
end
fclose('all');
close


%% plot sheet resistance vs Temp
figure('visible','off')
errorbar(resultTemp(:,1),resultPauw(:,1),resultPauw(:,2),'b.')
xlabel('Temperature␣T␣[K]');
ylabel('Sheet␣Resistance␣R_s␣[Ohm]');
legend('Measurement','Location','Best');
hold on
herrorbar(resultTemp(:,1),resultPauw(:,1),resultTemp(:,2),'b.')
hold off
fnam=sprintf('%s%s%s_%s',filelocationresults,'\',char(Files(1)),'...
    _Pauw.png');
print('-dpng','-r1200', fnam)
close
%%
diary off
```

B.16 MATLAB code for the Bloch-Grüneisen fits

The following MATLAB code for the Bloch-Grüneisen fits has been written on the basis of a MATLAB code written by Martin Handwerg and Georg Hoffmann.

```
function [ R ] = Bloch(TT, kappa, R0, theta)

 fun = @(x) x.^5./((exp(x)-1).*(1-exp(-x)));

 for x=1:size(TT)
  T=TT(x);
  inte=quadgk(fun,0,theta/T);
  RR(x)=R0+kappa*((T./theta).^5).*inte;
 end

 R=RR';
end
```

```
% Bloch-Grüneisen fit function
% requires function Bloch
% input file: column 1: temperatures; column 2: resistivities or ...
    sheet
% resistances

clear all
hold off
```

```
format long
digits(50)
clc
clf
close
%% Input Filelocation

filelocationMRfile = 'D:\BGinput.txt';


headerlines = 2;

fid = fopen(filelocationMRfile);
    MRfile = textscan(fid, '%f %f ', 'headerlines', 2, 'delimiter', ...
        ';');
    T2 = MRfile{1}
    R2 = MRfile{2}
fclose(fid);

%% Fitfunction
myfun=@(b,x) Bloch(x,b(1),b(2),b(3));
opts = statset('MaxIter',1000000,'Display','notify','TolX',eps,'...
    TolFun',eps);

%% nonlinear fit
[af,r,J,cov,mse] = nlinfit(T2,R2,myfun,[100 50 200],opts);

%% Fitparameters
kappa=af(1) % factor
R0=af(2)    % residual resistivity
t0=af(3)    % Debye-Temperature

%% Confidence intervalls (ci):
ci = nlparci(af,r,'covar',cov,'alpha',0.05)%0.05 for 95% confidence ...
    interv.
af_up=[af(1),af(2),ci(3,2)]
af_low=[af(1),af(2),ci(3,1)]

%% calculate fitted points
for vv=1:312
    TTT(vv)=vv;
 Theo1(vv)=myfun(af,vv);
 Upperbound(vv)=myfun(af_up,vv);
 Lowerbound(vv)=myfun(af_low,vv);
end;

%% Plot
figure(1)
plot(TTT,Theo1,T2,R2,'o',...
 TTT,Upperbound,'r-',...
 TTT,Lowerbound,'g-')
```

```
55
%% Save fitted data
fid=fopen('Blochgrüneisen.txt','w');
fprintf(fid,'%5.9f %8.12f \r\n',[TTT; Theo1;]);
fclose(fid);
60
result=[t0, (ci(3,2)-ci(3,1))/2 R0 (ci(2,2)-ci(2,1))/2]
```

B.17 MATLAB code for the analysis of van der Pauw Hall measurements

The following MATLAB source code for the analysis of the Hall measurements has been written on the basis of a MATLAB code written by Andreas Fiedler at group Novel Materials, HU Berlin.

```
0  %% Hallmeasurement
   %only works for measurement data of the profile in magnetic field:
   %valley-plateau-valley-plateau-...-plateau-valley
   %the data has to be adapted to this profile
   %the current is read from the filename between the third _ "...
       underscore" and
5  %the "\microA"
   clear all
   hold off
   format long
   clc
10 clf
   close
   %% Input Filelocation

   filelocation = 'D:\'; %=input('Enter file location ','s')%'C:\Users\...
       GNM_06\Documents\Grosse\Promotion\Electrical\Matlab\Matlab' %...
       filelocation = input('Path ');
15 filelocationresults = 'D:\'; %=input('Enter file location for ...
       results ','s')%'C:\Users\GNM_06\Documents\Grosse\Promotion\...
       Electrical\Matlab\Matlab' %filelocation = input('Path ');
   headerlines = 17; % Number of rows over the measurement data in the ...
       measurement file

   %%-------------------------------Input Parameters...
       ---------------------------------
   % it is often necessary to measure with the 2182 because the ...
       resolution is much higher
20 Vrange2401 = 200*10^(-3); % possible ranges in Volt: 200*10^(-3) ; 2...
       ; 20
   Vrange2182 = 10*10^(-3); % possible ranges in Volt: 10*10^(-3) ; ...
       100*10^(-3) ; 1 ; 10 ; 100
   d=48.209*10^(-9); % thicknes of the sample in meter
   d_Er=0.0*10^(-9); % uncertainty of the thicknes in meter
```

```
elementarycharge=1.60217656535*10^(-19); % the elementary charge (...
    assuming no uncertainity)
%Current = 5*10^(-5); % applied current (uncomment if the current is...
    not writen in the filename)

%...
    ------------------------------------------------------------------------...

%% insert the parameters for the smoothing and the derivation
% the smoothing factor "GLATT" and the "AnstiegsKriterium" which ...
    defines
% the boundarie for the derivation of the Magnetic Field to be ...
    treated as zero

GLATT=1; % smoothing factor ranges from 1(no smoothing) to about ...
    1/10 of plateau length(strong smoothing)
%Number of elements which were averaged in the convolution function ...
    (GLATT-1 overlap)
AnstiegsKriterium=0.007; % defines the boundary for the derivation ...
    to be treated as zero


%% sort Files
locexist=exist(filelocation,'dir');
 if locexist==0
     disp('file location does not exist.')
 end

wildcard='\*';
fileending='.txt';
directory=[filelocation,wildcard,fileending];

namesoffiles = dir (directory); %structure-array with all filenames

numberoffiles = size(namesoffiles,1);  % Number of .txt-files in ...
    folder

Files={zeros(numberoffiles,1)}; %dummy cell-array for filenames(...
    reserve storage space)

%% structure array -> string-array
for fileno =1:numberoffiles
Files(fileno)={namesoffiles(fileno).name}; % fill dummy with ...
    filenames (column "vector")
end

%% reserve storage space
Temp=zeros(numberoffiles,1);
residuals=zeros(length(Files),1);
HallKoeffizient=zeros(numberoffiles,1);
HallKoeffizient_Er=zeros(numberoffiles,1);
```

```
Hallcoefficient_without_thickness=zeros(numberoffiles,1);
Hallcoefficient_without_thickness_Er=zeros(numberoffiles,1);
chargedensity=zeros(numberoffiles,1);
chargedensity_Er=zeros(numberoffiles,1);
Rsquare=zeros(numberoffiles,1);
Rsquareindicator=zeros(numberoffiles,1);

%% Loop over all files
for x=1:numberoffiles
    %% get Temps from filenames
    filenamess=char(Files(x));
    C = textscan(filenamess, '%*s %*s %*s T2=%7.4f %*s');
    Temp(x,1)=C{1};
    %% get Currents from filenames
    Plotmeasuretime=strfind(filenamess,'_');
    bbbb=strfind(filenamess,'microA');
    Current=str2double(filenamess((Plotmeasuretime(3)+1):(bbbb-1)))...
        *10^(-6);
    %% open File
    fid=0; %file identifier
    while fid < 1 % get current filename, while loop for error ...
        message if file does not exist
        filename=char(Files(x));
        fullfilename=[filelocation,'\',filename];
        [fid,message] = fopen(fullfilename, 'r');
       if fid == -1
         disp('file does not exist.')
         return
       end
    end
    %% read GPIB
    GPIB=textscan(fid,'GPIB0::%2f');
    GPIBadd=GPIB{1}; %GPIB0::16::INSTR, GPIB0::12::INSTR, GPIB0...
        ::24::INSTR

    %% read measurement data
    Hallmessung = textscan(fid, '%s %f %f %f ', 'headerlines', ...
        headerlines);
    fclose('all');
    Date = Hallmessung{1};
    Measuretime = Hallmessung{2};
    Voltage = Hallmessung{3};
    MagneticField = Hallmessung{4};

    %% smooth measurement data
    %measurement time
    Measuretime=Measuretime/60000;
    Measuretime2=conv(Measuretime,1/GLATT*ones(GLATT,1));%smoothing
    Measuretime3=Measuretime2(GLATT:(length(Measuretime2)-(GLATT-1)))...
        );%cut off the boundaries
```

```
    %Voltage
110 Voltage2=conv(Voltage,1/GLATT*ones(GLATT,1));%smoothing
    Voltage3=Voltage2(GLATT:(length(Voltage2)-(GLATT-1)));%cut off ...
        boundaries

    %magnetic field
    MagneticField2=conv(MagneticField,1/GLATT*ones(GLATT,1));%...
        smoothing
115 MagneticField3=MagneticField2(GLATT:(length(MagneticField2)-(...
        GLATT-1)));%cut of boundaries

    %% derivation to find the plateaus
    slopeMagnetic = diff(MagneticField3)./diff(Measuretime3);

120 % the x values of the derivation has to be shifted, too
    x_slopeMagnetic=(Measuretime3(1:(end-1))+diff(Measuretime3)./2);

    % find the indeces for x:
    % reserve storage space and set all indices 0("false"):
125 Indiz_plateau=zeros(size(x_slopeMagnetic));
    Indiz_valley=zeros(size(x_slopeMagnetic));
    %set the positions where the derivation=0 to 1("true"):
    Indiz_plateau((AnstiegsKriterium>slopeMagnetic&slopeMagnetic>-...
        AnstiegsKriterium)&(MagneticField3(1:1:(end-1))>0.03))=1;
    Indiz_valley((AnstiegsKriterium>slopeMagnetic&slopeMagnetic>-...
        AnstiegsKriterium)&(MagneticField3(1:1:(end-1))<=0.03))=1;
130 %find the positions where the plateaus starts and ends
    B=[];
    for i=1:length(Indiz_plateau)-2
        if (Indiz_plateau(i+1)-Indiz_plateau(i)~= 0);
            B=[B i+1];
135     end
    end
    %find the positions where the valleys starts and ends
    A=[];
    for i=1:length(Indiz_valley)-2
140     if (Indiz_valley(i+1)-Indiz_valley(i)~= 0);
            A=[A i+1];
        end
    end
    %set the first point of the data to the starting point of the ...
        first
145 %valley (the profile described at the top is necessary)
    A=[1 A length(Indiz_valley)];
    %sort the boundaries in pairs (starting and ending point of the ...
        i-th
    %plateau/valley)
    Valley_Limits=reshape(A,2,[]);
150 Plateau_Limits=reshape(B,2,[]);

    %% temperature fit
```

```
% set this variables back to an empty matrix
TempVoltage=[];
TempMeasuretime=[];
% temperature-fit limits (assuming a constant Temperature T1 and...
    a
% equaling temperature T2)
for i=1:length(Valley_Limits);
    TempVoltage = [TempVoltage Voltage3(Valley_Limits(1,i):...
        Valley_Limits(2,i)) '];
    TempMeasuretime =[TempMeasuretime Measuretime3(Valley_Limits...
        (1,i):Valley_Limits(2,i)) '];
end
% defines the temperatur fit function
if ((TempVoltage(end)-TempVoltage(1))/(TempMeasuretime(end)-...
    TempMeasuretime(1)))<=0
tempfit = @(y,a) (y(1)+exp(y(2)-(y(3).*a)));
else
tempfit = @(y,a) (y(1)-exp(y(2)-(y(3).*a)));
end
%set the starting coefficients for the fit
coeffstart = [TempVoltage(end),TempMeasuretime(1),1];
%set fit options
opts = statset('MaxIter',10000,'Display','notify','TolX',eps,'...
    TolFun',eps);
%perform the fit
Temperaturefit = nlinfit(TempMeasuretime,TempVoltage,tempfit,...
    coeffstart,opts);

Plotmeasuretime=Measuretime3;
if ((TempVoltage(end)-TempVoltage(1))/(TempMeasuretime(end)-...
    TempMeasuretime(1)))<=0
funct = (Temperaturefit(1)+exp(Temperaturefit(2)-(Temperaturefit...
    (3).*Plotmeasuretime)));
funct2 = (coeffstart(1)+exp(coeffstart(2)-(coeffstart(3).*...
    Plotmeasuretime)));
else
funct = (Temperaturefit(1)-exp(Temperaturefit(2)-(Temperaturefit...
    (3).*Plotmeasuretime)));
funct2 = (coeffstart(1)-exp(coeffstart(2)-(coeffstart(3).*...
    Plotmeasuretime)));
end

%plot the Temperature fit
figure('visible','off')
plot(TempMeasuretime,TempVoltage,'b.',...
      Plotmeasuretime,funct,'r-');
xlabel('Measuretime [min]');
ylabel('Voltage [V]')
grid on
legend('Measurement','Temperature Fit','Location','Best');
fnam=sprintf('%s%s%s_%s',filelocationresults,'\',char(Files(x)),...
```

```
        'Temperaturfit.png');
    print('-dpng','-r300',fnam)
    close

    %recalculate the Voltage with the temperature
    Voltage3=Voltage3-funct;

    % plot the smoothed and temperaturefitted measuring data ...
        including the
    % plateau and valley limits (always check this plots to be sure ...
        that
    % the analysis works)
    figure('visible','off')
    [AX,H1,H2]=plotyy(Measuretime,MagneticField,...
          Measuretime3,Voltage3.*1000);hold on;
    set(get(AX(1),'Ylabel'),'String','Magnetic Field [T]');
    set(get(AX(2),'Ylabel'),'String','Voltage [mV]');
    set(H1,'Color','b');
    set(H2,'Color','k');
    plot(x_slopeMagnetic,Indiz_plateau,'g--',...
          x_slopeMagnetic,Indiz_valley,'m.-'); hold off;
    xlabel('Measuretime [min]');
    grid on
    legend('Magnetic Field','Plateau Limits','Valley Limits','...
        smoothed Voltage','Location','Best');
    fnam=sprintf('%s%s%s_%s',filelocationresults,'\',char(Files(x)),...
        'plateaus.png');
    print('-dpng','-r300',fnam)
    close


    %Uncertainty of the Voltage
    %% Keithley 2401
    if GPIBadd == 24 ||  GPIBadd == 25 || GPIBadd == 23 || GPIBadd ...
        == 26
        if  Vrange2401 == 200*10^(-3)
            weights=10^(-6)*ones(length(Voltage3),1);
        elseif Vrange2401 == 2
            weights=10^(-5)*ones(length(Voltage3),1);
        elseif Vrange2401 == 20
            weights=10^(-4)*ones(length(Voltage3),1);
        else
            display('Enter correct Voltage range.')
    end
    %%Keithley 2182
    elseif GPIBadd == 12 ||  GPIBadd == 16
        if  Vrange2182 == 10*10^(-3)
            weights=10^(-9)*ones(length(Voltage3),1);
        elseif Vrange2182 == 100*10^(-3)
            weights=10^(-8)*ones(length(Voltage3),1);
        elseif Vrange2812 == 1
```

```
            weights=10^(-7)*ones(length(Voltage3),1);
        elseif Vrange2812 == 10
            weights=10^(-6)*ones(length(Voltage3),1);
        elseif Vrange2182 == 100
            weights=10^(-5)*ones(length(Voltage3),1);
        else
            display('Enter correct Voltage range.')
        end
    else
        display('GPIB-adress not found!')
    end
    weights = weights/sqrt(GLATT); % error propagation for smoothing

    % get the length of all valleys
    Length_Valleys = 0;
    for i = 1:length(Valley_Limits)
        Length_Valleys = Length_Valleys+(Valley_Limits(2,i)-...
            Valley_Limits(1,i));
    end
    %Magnetic field and Hallvoltage at the zero point
    Mag=zeros(1);
    HallVoltage=zeros(1);
    HallVoltage_Er=sum(weights)/length(weights)/sqrt(Length_Valleys)...
        ;
    %Hall Voltage between the plateaus and the valleys
    for i=1:length(Plateau_Limits)
        % calculate the Magnetic field at the plateaus
        Mag=[Mag sum(MagneticField(Plateau_Limits(1,i):...
            Plateau_Limits(2,i)))/length(MagneticField(...
            Plateau_Limits(1,i):Plateau_Limits(2,i)))];
        % calculate the Hall-Voltage
        % linear Fit through the valleys to calculate the Valley-...
            Voltage
        % and the erros
        [fitVoltage_Valley,fun] = fit(...
            [Measuretime3(Valley_Limits(1,i):Valley_Limits(2,i))' ...
                Measuretime3(Valley_Limits(1,i+1):Valley_Limits(2,i...
                +1))']',...
            [Voltage3(Valley_Limits(1,i):Valley_Limits(2,i))' ...
                Voltage3(Valley_Limits(1,i+1):Valley_Limits(2,i+1))...
                ']',...
            'poly1','Weight', ...
            1./([weights(Valley_Limits(1,i):Valley_Limits(2,i))' ...
                weights(Valley_Limits(1,i+1):Valley_Limits(2,i+1))...
                ']'.^2));
        fitVoltage_Valley_Er = confint(fitVoltage_Valley);
        % get the mean Plateau-Voltage for each Plateau and the ...
            errors
        Plateau_Voltage = (sum(Voltage3(Plateau_Limits(1,i):1:...
            Plateau_Limits(2,i))))/length(Voltage3(Plateau_Limits(1,...
            i):1:Plateau_Limits(2,i)));
```

```
        Plateau_Voltage_Er = sqrt(sum(weights(Plateau_Limits(1,i):1:...
            Plateau_Limits(2,i)).^2))/(length(Plateau_Limits(1,i):1:...
            Plateau_Limits(2,i)));
        % get the values of the Valley-Voltages from the fit
        Valley_Voltage =    fitVoltage_Valley.p1*Measuretime((...
            Plateau_Limits(1,i)+floor((Plateau_Limits(2,i)-...
            Plateau_Limits(1,i))/2)))+fitVoltage_Valley.p2;
        Valley_Voltage_Er = sqrt(((fitVoltage_Valley_Er(2,1)-...
            fitVoltage_Valley_Er(1,1))/2*Measuretime(Plateau_Limits...
            (1,i)+floor((Plateau_Limits(2,i)-Plateau_Limits(1,i))/2)...
            ))^2+((fitVoltage_Valley_Er(2,2)-fitVoltage_Valley_Er...
            (1,2))/2)^2);
        % Calculate the Hall-Voltages from the plateaus and valleys
        HallVoltage=[HallVoltage (Plateau_Voltage-Valley_Voltage)];
        HallVoltage_Er=[HallVoltage_Er sqrt((Plateau_Voltage_Er)^2+(...
            Valley_Voltage_Er)^2)];
    end

    %% Liniear Fit to calculate the Hall coefficient
    % defines the fit function
    Hallfit = fittype(@(p1,x) (p1.*x));
    %set the starting coefficients for the fit
    coeffstart = HallVoltage(end);
    %perform the fit
    [fitresult,gof] = fit(Mag',HallVoltage',Hallfit,'Start',...
        coeffstart,'Weights',1./(HallVoltage_Er'.^2));
    R_intervals = confint(fitresult);
    PearsonRsquare = gof.rsquare;
    Fit_p1 = fitresult.p1;
    Fit_error = max(abs(fitresult.p1-R_intervals(1)),abs(fitresult....
        p1-R_intervals(2)));
    % Calculating the fit points for the plot
    HallVoltage_fit = Mag*Fit_p1;

    %% ----------------calculating the Hall coeffizient...
        ----------------
    HallKoeffizient(x,1) = -Fit_p1*d/Current*(100^3); % 100^3 to get...
        the Unit: cm^3/As
    HallKoeffizient_Er(x,1) = sqrt((d/Current*Fit_error)^2+(Fit_p1/...
        Current*d_Er)^2)*(100^3); % 100^3 to get the Unit: cm^3/As
    Hallcoefficient_without_thickness(x,1) = -Fit_p1/Current;
    Hallcoefficient_without_thickness_Er(x,1) = Fit_error/Current;
    Rsquare(x,1)=PearsonRsquare;
    if PearsonRsquare < 0.999945
    Rsquareindicator(x,1)=1;
    end
    %% Plot the linear fit of the Hall coefficient
    figure('visible','off')
    plot(Mag,HallVoltage,'.',...
          Mag,HallVoltage_fit,'r-');
    xlabel('Magnetic Field B [T]');
```

```
    ylabel('HallVoltage V_H [V]');
    grid on
    hold on
    errorbar(Mag,HallVoltage,HallVoltage_Er,'.')
    legend('Data','Linear Fit','Location','Best');
    hold off
    fnam=sprintf('%s%s%s_%s',filelocationresults,'\',char(Files(x)),...
        '.png');
    print('-dpng','-r300',fnam)
    close

    %Residuals
    res = HallVoltage' - HallVoltage_fit';
    figure('visible','off')
    plot(Mag,res,'.','MarkerSize',25)
    xlabel('Magnetic Field B [T]');
    ylabel('Residuals [V]');
    legend('Residuals','Location','Best');

    for i=1:length(res)
        if abs(res(i)) >= 3*HallVoltage_Er(i)
         warn4=sprintf('Residual high for file %s at Magnetic Field ...
            %3.0f mT.',char(Files(x)), Mag(i)*1000);
                disp(warn4);
        residuals(x,1)=residuals(x,1)+1;
        end
    end
    fnam=sprintf('%s%s%s_%s',filelocationresults,'\',char(Files(x)),...
        '_res.png');
    print('-dpng',fnam)
    close
end

%% plot Hall coefficient vs Temp
HallKurve = [Temp HallKoeffizient HallKoeffizient_Er];
HallKurve = sortrows(HallKurve,1);
figure('visible','off')
errorbar(HallKurve(:,1),HallKurve(:,2),HallKurve(:,3),'b.')
xlabel('Temperature T [K]');
ylabel('Hall-Coefficient R_H [cm^{3} A^{-1} s^{-1}]');
legend('Measurement','Location','Best');
hold on
plot(HallKurve(:,1),HallKurve(:,2))
hold off
fnam=sprintf('%s%s%s_%s',filelocationresults,'\',char(Files(1)),'...
    _Hallcoefficient.png');
print('-dpng','-r1200', fnam)
close

%% ----------------calculate the charge carrier density----------------
% only saves the charge carrier density when there is no change in ...
```

```
    sign in
% the temperature dependent hall coefficient(single band model)
if (abs(sum(sign(HallKoeffizient)))==numberoffiles)
    chargedensity = 1./(elementarycharge.*abs(HallKoeffizient));
    chargedensity_Er = sqrt((HallKoeffizient_Er./(elementarycharge.*...
        abs(HallKoeffizient).^2)).^2);


    %plot chrage carrier density vs Temp
    chargedensityKurve = [Temp chargedensity chargedensity_Er];
    chargedensityKurve = sortrows(chargedensityKurve,1);
    figure('visible','off')
    errorbar(chargedensityKurve(:,1),chargedensityKurve(:,2),...
        chargedensityKurve(:,3),'b.')
    xlabel('Temperature T [K]');
    ylabel('charge density [cm^{-3}]');
    legend('Measurement','Location','Best');
    hold on
    plot(chargedensityKurve(:,1),chargedensityKurve(:,2))
    hold off
    fnam=sprintf('%s%s%s_%s',filelocationresults,'\',char(Files(1)),...
        '_chargedensity.png');
    print('-dpng','-r1200', fnam)
    close
    %save Pauw-resistivity and AverageTemp and B-field and 1...
        stfilename in dat-file
    fnam=sprintf('%s%s%s_%s',filelocationresults,'\',char(Files(1)),...
        '_Hall.dat');
    fid = fopen(fnam, 'wt');

    fprintf(fid, '%s;%s;%s;%s;%s;%s;%s;%s;%s;%s;%s;%s;%s...
        ;\n', 'Temperature','Error Temperature', 'Hall Coefficient'...
        ,'Error Hall Coefficient','Charge Carrier Density','Error ...
        Charge Carrier Density','RSquare','non linear?','Residuals ...
        high?','Thickness','Error thickness','Hall without thickness...
        ','Error Hall without thickness');
    fprintf(fid, '%s;%s;%s;%s;%s;%s;%s;%s;%s;%s;%s;%s;%s...
        ;\n', 'K','K','cm^{3} A^{-1} s^{-1}','cm^{3} A^{-1} s^{-1}'...
        ,'cm^{-3}','cm^{-3}',' ','(Rsquare<0.999945)','(res>3*...
        HallVoltage_Er)','nm','nm','m^{2} A^{-1} s^{-1}','m^{2} A...
        ^{-1} s^{-1}');
    for row=1:numberoffiles
        fprintf(fid, '%.8f;%.8f;%.8f;%.8f;%.8f;%.8f;%.8f;%.8f...
            ;%.8f;%.12f;%.12f;%.8f;%.8f;\n', Temp(row),0.5,...
            HallKoeffizient(row),HallKoeffizient_Er(row),...
            chargedensity(row),chargedensity_Er(row),Rsquare(row),...
            Rsquareindicator(row),residuals(row),d*10^9,d_Er*10^9,...
            Hallcoefficient_without_thickness(row),...
            Hallcoefficient_without_thickness_Er(row));
    end
    fclose('all');
```

```
    close
else
    display('There is a change in sign in Hall coefficient , the ...
        charge carrier density is not calculated.')
    %save Pauw-resistivity and AverageTemp and B-field and 1...
        stfilename in dat-file
    fnam=sprintf('%s%s%s_%s',filelocationresults,'\',char(Files(1)),...
        '_Hall.dat');
    fid = fopen(fnam, 'wt');

    fprintf(fid, '%s;,%s; %s; %s; %s; %s; %s; %s; %s; %s; %s; \n', '...
        Temperature','Error Temperature', 'Hall Coefficient','Error ...
        Hall Coefficient','RSquare','non linear?','Residuals high?',...
        'Thickness','Error thickness','Hall without thickness','...
        Error Hall without thickness');
    fprintf(fid, '%s; %s; %s; %s; %s; %s; %s; %s; %s; %s; %s; \n', '...
        K','K','cm^{3} A^{-1} s^{-1}','cm^{3} A^{-1} s^{-1}','','(...
        Rsquare<0.999945)','(res>3*HallVoltage_Er)','nm','nm','m^{2}...
        A^{-1} s^{-1}','m^{2} A^{-1} s^{-1}');
    for row=1:numberoffiles
    fprintf(fid, '%.8f %.8f; %.8f; %.8f; %.8f; %.8f; %.8f; %.12f; ...
        %.12f; %.8f; %.8f; \n', Temp(row),0.5,HallKoeffizient(row),...
        HallKoeffizient_Er(row),Rsquare(row),Rsquareindicator(row),...
        residuals(row),d*10^9,d_Er*10^9,...
        Hallcoefficient_without_thickness(row),...
        Hallcoefficient_without_thickness_Er(row));
    end
    fclose('all');
    close
end

allresults=[Mag',HallVoltage',HallVoltage_Er']
```

B.18 Mathematica and code for the analysis of magnetic-field-dependent magnetoresistance measurements

Resistivity tensor in two-band model

Calculation of resistivity tensor, Hall coefficient and magnetoresistance in two-band model (2 layers) using the Mathematica:

$q1 = -e;$

$q2 = e;$

$\mathrm{A1} = n * e * \mathrm{u1}/(1 + \mathrm{u1\hat{}2} * B\hat{}2);$

$\mathrm{A2} = p * e * \mathrm{u2}/(1 + \mathrm{u2\hat{}2} * B\hat{}2);$

$\mathrm{B1} = n * \mathrm{q1} * \mathrm{u1\hat{}2} * B/(1 + \mathrm{u1\hat{}2} * B\hat{}2);$

$$\text{B2} = p * \text{q2} * \text{u2}\hat{}2 * B/(1 + \text{u2}\hat{}2 * B\hat{}2);$$

$$\text{rho} = \text{Inverse}\left[\left(\text{t1} * \begin{pmatrix} \text{A1} & \text{B1} & 0 \\ -\text{B1} & \text{A1} & 0 \\ 0 & 0 & \text{s1} \end{pmatrix} + \text{t2} * \begin{pmatrix} \text{A2} & \text{B2} & 0 \\ -\text{B2} & \text{A2} & 0 \\ 0 & 0 & \text{s2} \end{pmatrix}\right) \Big/ (\text{t1} + \text{t2})\right];$$

$$\text{Factor}[\text{Simplify}[\text{rho}[[2,1]]]]/B$$

$$-\frac{(\text{t1}+\text{t2})\left(n\text{t1u1}^2 - p\text{t2u2}^2 + B^2 n\text{t1u1}^2\text{u2}^2 - B^2 p\text{t2u1}^2\text{u2}^2\right)}{e\left(n^2\text{t1}^2\text{u1}^2 + 2np\text{t1t2u1u2} + p^2\text{t2}^2\text{u2}^2 + B^2 n^2\text{t1}^2\text{u1}^2\text{u2}^2 - 2B^2 np\text{t1t2u1}^2\text{u2}^2 + B^2 p^2\text{t2}^2\text{u1}^2\text{u2}^2\right)}$$

$$\text{rhoxx} = \text{Factor}[\text{Simplify}[\text{rho}[[1,1]]]]$$

$$\frac{(\text{t1}+\text{t2})\left(n\text{t1u1} + p\text{t2u2} + B^2 p\text{t2u1}^2\text{u2} + B^2 n\text{t1u1u2}^2\right)}{e\left(n^2\text{t1}^2\text{u1}^2 + 2np\text{t1t2u1u2} + p^2\text{t2}^2\text{u2}^2 + B^2 n^2\text{t1}^2\text{u1}^2\text{u2}^2 - 2B^2 np\text{t1t2u1}^2\text{u2}^2 + B^2 p^2\text{t2}^2\text{u1}^2\text{u2}^2\right)}$$

$$\text{rhoxx0} = \text{With}[\{B = 0\}, \text{Evaluate}[\text{rhoxx}]]$$

$$\frac{(\text{t1}+\text{t2})(n\text{t1u1} + p\text{t2u2})}{e\left(n^2\text{t1}^2\text{u1}^2 + 2np\text{t1t2u1u2} + p^2\text{t2}^2\text{u2}^2\right)}$$

$$\text{Magnetoresistance} = \text{Factor}[\text{Simplify}[(\text{rhoxx} - \text{rhoxx0})/\text{rhoxx0}]]$$

$$\frac{B^2 np\text{t1t2u1u2}(\text{u1}+\text{u2})^2}{n^2\text{t1}^2\text{u1}^2 + 2np\text{t1t2u1u2} + p^2\text{t2}^2\text{u2}^2 + B^2 n^2\text{t1}^2\text{u1}^2\text{u2}^2 - 2B^2 np\text{t1t2u1}^2\text{u2}^2 + B^2 p^2\text{t2}^2\text{u1}^2\text{u2}^2}$$

Create fitfunction for magnetoresistance vs. B

```
% solve_equation_system_u1_n1.m
% creates a fit for Magnetoresistance vs. B in a two-layer model ...
    with u1
% (mobility of layer1) and n1 (carrier density of layer 1) as ...
    fitparameters

syms n1 u1 u2 n2 hall rho t1 t2 el B q1 q2
% Solve equation system of rho and Hallcoefficient for n2 and u2:
Sol = solve(rho == (t1 + t2)./(el.*n1.*t1.*u1 + el.*n2.*t2.*u2),hall...
    == ((t1 + t2).*(q1.*n1.*t1.*u1.^2 + q2.*n2.*t2.*u2.^2))./(el...
    .^2*(n1.^2.*t1.^2.*u1.^2 + 2.*n1.*n2.*t1.*t2.*u1.*u2 + n2.^2.*t2...
    .^2.*u2.^2)),n2,u2)
n2= Sol.n2
u2= Sol.u2
% Substitute the results for n2 and u2 into two-band equation for
% magnetoresistance:
Magnetores =(B.^2.*n1.*n2.*t1.*t2.*u1.*u2.*(u1 - u2.*(q1./q2)).^2)...
    ./((n1.*t1.*u1 + n2.*t2.*u2).^2 + B.^2.*u1.^2.*u2.^2.*(n1.*t1 + ...
    n2.*t2.*(q1./q2)).^2)
% Change the name of the variables n1 and u2 for use in the program
% MagnetoresistanceBfitu1n1.m:
MRneu=subs(Magnetores, u1, 'a(1)'); % name u1 a(1) for the fit
MRneu2=subs(MRneu, n1, 'a(2)') % name n1 a(2) for the fit
```

Fit to magnetic-field-dependent magnetoresistance with MATLAB

```
% MagnetoresistanceBfitu1n1.m
% Makes a fit to data magnetoresistance vs magnetic field using two-band
% model with n1 and u1 as fit parameters.
% The input file must contain magnetic field (in Tesla) as 1st
% column and Magnetoresistance (in Percent) in second column.

clear all, hold off, format long, digits(50), clc, clf, close

%% Enter input filelocation

headerlines = 2; % Number of headerlines of input file
filelocationMRfile = 'D:\m=6_2K.txt';
filelocationresults = 'D:\fits';

%% Enter input values (all lengths in micrometer):
el = 1.602176565*10^(-19); % elementary charge

q1=-el; %for electrons: q1=-el; for holes: q1=el
q2=el;  %for electrons: q2=-el; for holes: q2=el
rho = 33.9528 ; %in uWm
hall =6.659 *10^(9); %(um)^3/As
t1 = 5.4*10^-4; %
t2 = 32.4*10^-4; %

%% Read values from .txt file

fid = fopen(filelocationMRfile);
    MRfile = textscan(fid, '%f␣%f␣', 'headerlines', 2, 'delimiter', ...
        ';');
    B = MRfile{1};
    B=B./(10^(12));
    MR = MRfile{2}./100;
fclose(fid);

%% fit
% fitparameters are in vector a:  a(1)=u1; a(2)=n1, fitfunction ...
    created by
% "solve_equation_system_u1_n1.m" and replace *  /  and ^  by .*  ./... and .^
MRfitfc = @(a,B) ((B.^2.*t1.*a(1).*a(2).*(a(1) - (el.*q1.*(- q1.*t1...
    .*a(1).^2*a(2).*rho.^2 + hall.*t1 + hall.*t2))./(q2.^2.*rho.*(t1...
     + t2 - el.*rho.*t1.*a(1).*a(2)))).^2.*(t1 + t2 - el.*rho.*t1.*a...
    (1).*a(2))).^2./(el.*rho.*((t1.*a(1).*a(2) + (t1 + t2 - el.*rho.*t1...
    .*a(1).*a(2))./(el.*rho)).^2 + (B.^2.*el.^2.*a(1).^2.*(t1.*a(2) ...
    + (q1.*(t1 + t2 - el.*rho.*t1.*a(1).*a(2)).^2)./(el.^2.*(- q1.*...
```

```
    t1.*a(1).^2.*a(2).*rho.^2 + hall.*t1 + hall.*t2))).^2.*(- q1.*t1...
    .*a(1).^2.*a(2).*rho.^2 + hall.*t1 + hall.*t2).^2)./(q2.^2.*rho...
    .^2.*(t1 + t2 - el.*rho.*t1.*a(1).*a(2)).^2))));
 %set the starting coefficients for the fit
  coeffstart = [80*10^(8),10^7] % if u1, n1 for Nbse2: [80*10^(8)...
      ,10^7]; for SnSe: 4*10^11,5*10^4
    %set fit options
    opts = statset('MaxIter',500000,'Display','notify','TolX',eps,'...
        TolFun',eps);
    %perform the fit
[MRfit,r,J,cov,mse] = nlinfit(B,MR,MRfitfc,coeffstart,opts);

%results for u1 and n1 in suitable units
u1res=MRfit(1)/(10^8); %in cm^2/Vs
n1res=MRfit(2)*(10^12); %in cm^-3

%errors of fitresults:
ci = nlparci(MRfit,r,'covar',cov,'alpha',0.05);
erroru1=(ci(1,2)-ci(1,1))/2/(10^8);
errorn1=(ci(2,2)-ci(2,1))/2*(10^12);

%function for u2 and n2 (created by "solve_equation_system_u1_n1.m...
    ")
u2=@(u1,n1)((el*(- n1*q1*t1*rho^2*u1^2 + hall*t1 + hall*t2))/(q2*rho...
    *(t1 + t2 - el*n1*rho*t1*u1)));
n2=@(u1,n1)((q2*(t1 + t2 - el*n1*rho*t1*u1)^2)/(el^2*t2*(- n1*q1*t1*...
    rho^2*u1^2 + hall*t1 + hall*t2)));

u2res=u2(MRfit(1),MRfit(2))/(10^8);%in cm^2/Vs
n2res=n2(MRfit(1),MRfit(2))*(10^12);%in cm^-3

allresults=cell(8,2)';
allresults(1,1)={'u1 (cm^2/Vs)'};
allresults(1,2)={'error_u1 (cm^2/Vs)'};
allresults(1,3)={'n1 (cm^-3)'};
allresults(1,4)={'error n1 (cm^-3)'};
allresults(1,5)={'u2 (cm^2/Vs)'};
allresults(1,6)={'error u2 (cm^2/Vs)'};
allresults(1,7)={'n2 (cm^-3)'};
allresults(1,8)={'error n2 (cm^-3)'};

allresults(2,1)={u1res};
allresults(2,2)={erroru1};
allresults(2,3)={n1res};
allresults(2,4)={errorn1};
allresults(2,5)={u2res};
allresults(2,6)={0};
allresults(2,7)={n2res};
allresults(2,8)={0};
allresults=allresults';
```

```
figure('visible','off')
plot(B,MR,'.',...
      B,MRfitfc(MRfit,B),'r-');
xlabel('Magnetic field B [T]');
ylabel('Magnetoresistance');
grid on
hold on
legend('Data','Fit','Location','Best');
hold off
fnam=sprintf('%s%s%s_%s',filelocationresults,'\','4K_eh','_MRfit.jpg...
    ');
print('-dpng','-r300',fnam)
close

%% Save fitted data
MRfitted=MRfitfc([MRfit(1),MRfit(2)],B)*100; % in Percent;
B=B.*(10^(12));
%1st column: B(T), 2nd column: fitted magnetoresistance(%)
fnam=sprintf('%s%s%s',filelocationresults,'\','_MR.txt');
fid = fopen(fnam, 'w');
fprintf(fid,'%f %f\r\n',[B'; MRfitted';]);
fclose('all');
close
```

Bibliography

[1] Xiaoxiang Xi, Liang Zhao, Zefang Wang, Helmuth Berger, László Forró, Jie Shan and Kin Fai Mak, Strongly enhanced charge-density-wave order in monolayer $NbSe_2$. *Nature Nanotechnology* **10**, (2015), 765–769.

[2] A. W. Tsen, B. Hunt, Y. D. Kim, Z. J. Yuan, S. Jia, R. J. Cava, J. Hone, P. Kim, C. R. Dean and A. N. Pasupathy, Evidence for a Bose Metal in a Two-Dimensional Crystalline Superconductor. *arXiv* **1507.08639**, (2015), 1–8.

[3] A. K. Geim and I. V. Grigorieva, Van der Waals heterostructures. *Nature* **499**, (2013), 419–425.

[4] Manish Chhowalla, Hyeon Suk Shin, Goki Eda, Lain-Jong Li, Kian Ping Loh and Hua Zhang, The chemistry of two-dimensional transition metal dichalcogenide (TMDC) layers. *Nature Chemistry* **5**, (2013), 263–275.

[5] Qing Hua Wang, Kourosh Kalantar-Zadeh, Andras Kis, Jonathan N. Coleman and Michael S. Strano, Electronics and optoelectronics of two-dimensional transition metal dichalcogenides. *Nature Nanotechnology* **5**, (2012), 699–712.

[6] Qing Tang and Zhen Zhou, Graphene-analogous low-dimensional materials. *Progress in Materials Science* **58** (8), (2013), 1244–1315.

[7] Kin Fai Mak, Changgu Lee, James Hone, Jie Shan and Tony F. Heinz, Atomically Thin MoS_2: A New Direct-Gap Semiconductor. *Physical Review Letters* **105**, (2010), 136805.

[8] K. S. Novoselov, D. Jiang, F. Schedin, T. J. Booth, V. V. Khotkevich, S. V. Morozov and A. K. Geim, Two-dimensional atomic crystals. *Proceedings of the National Academy of Sciences of the United States of America* **102** (30), (2005), 10451–10453.

[9] Mohammed S. El-Bana, Daniel Wolverson, Saverio Russo, Geetha Balakrishnan, Don Mck Paul and Simon J. Bending, Superconductivity in two-dimensional $NbSe_2$ field effect transistors. *Superconductor Science and Technology* **26** (12), (2013), 125020.

[10] Neal Staley, Jian Wu, Peter Eklund, Ying Liu, Linjun Li and Zhuan Xu, Electric field effect on superconductivity in atomically thin flakes of $NbSe_2$. *Physical Review B* **80**, (2009), 184505.

[11] Masaro Yoshida, Yijin Zhang, Jianting Ye, Ryuji Suzuki, Yasuhiko Imai, Shigeru Kimura, Akihiko Fujiwara and Yoshihiro Iwasa, Controlling charge-density-wave states in nano-thick crystals of $1T$-TaS_2. *Scientific Reports* **4**, (2014), 7302.

[12] Felix Flicker and Jasper van Wezel, Charge order from orbital-dependent coupling evidenced by $NbSe_2$. *Nature Communications* **6**, (2015), 1–6.

[13] Y. Cao, A. Mishchenko, G. L. Yu, E. Khestanova, A. P. Rooney, E. Prestat, A. V. Kretinin, P. Blake, M. B. Shalom, C. Woods, J. Chapman, G. Balakrishnan, I. V. Grigorieva, K. S. Novoselov, B. A. Piot, M. Potemski, K. Watanabe, T. Taniguchi, S. J. Haigh, A. K. Geim and R. V. Gorbachev, Quality heterostructures from two-dimensional crystals unstable in air by their assembly in inert atmosphere. *Nano Letters* **15(8)** (0), (2015), 4914–4921.

[14] Richard A. Klemm, Pristine and intercalated transition metal dichalcogenide superconductors. *Physica C: Superconductivity and its Applications* **514**, (2015), 86–94.

[15] Matteo Calandra, I. I. Mazin and Francesco Mauri, Effect of dimensionality on the charge-density wave in few-layer $2H$-$NbSe_2$. *Physical Review B* **80**, (2009), 241108.

[16] Matt Beekman, Colby L. Heideman and David C. Johnson, Ferecrystals: non-epitaxial layered intergrowths. *Semiconductor Science and Technology* **29** (6), (2014), 064012.

[17] M. Beekman, C. Heideman, M. Anderson, M. Smeller, R. Atkins, Q. Lin, N. Nguyen, and D. C. Johnson, Modules, Systems, and Applications in Thermoelectrics, chapter Design and Realization of Nanostructured Inorganic Intergrowths, 1–20. CRC (2012).

[18] Marco Esters, Matti B. Alemayehu, Zachary Jones, Ngoc T. Nguyen, Michael D. Anderson, Corinna Grosse, Saskia F. Fischer and David C. Johnson, Synthesis of inorganic structural isomers by diffusion-constrained self-assembly of designed precursors: A novel type of isomerism. *Angewandte Chemie International Edition* **54** (4), (2015), 1130–1134.

[19] Ryan Atkins, Michelle Dolgos, Andreas Fiedler, Corinna Grosse, Saskia F. Fischer, Sven P. Rudin and David C. Johnson, Synthesis and Systematic

Trends in Structure and Electrical Properties of $[(SnSe)_{1.15}]_m(VSe_2)_1$, m = 1, 2, 3, and 4. *Chemistry of Materials* **26** (9), (2014), 2862–2872.

[20] Colby Heideman, Families of metastable misfit layered compounds prepared by modulated elemental precursors and the resulting physical properties. Ph.D. thesis, University of Oregon (2010).

[21] Colby L Heideman and David C Johnson, Structural influence on transport properties in $[(PbSe)_{1.00}]_m(MoSe_2)_n$ misfit layered compounds. *Semiconductor Science and Technology* **29** (6), (2014), 064007.

[22] Q. Lin, M. Smeller, C. L. Heideman, P. Zschack, M. Koyano, M. D. Anderson, R. Kykyneshi, D. A. Keszler, I M. Anderson and D.C. Johnson, Rational Synthesis and Characterization of a New Family of Low Thermal Conductivity Misfit Layer Compounds $[(PbSe)_{0.99}]_m(WSe_2)_n$. *Chemistry of Materials* **22**, (2010), 1002–1009.

[23] Matti B. Alemayehu, Gavin Mitchson, Jeffery Ditto, Ben E. Hanken, Mark Asta and David C. Johnson, Charge Transfer between PbSe and $NbSe_2$ in $[(PbSe)_{1.14}]_m[NbSe_2]_n$ Ferecrystalline Compounds. *Chemistry of Materials* **26** (5), (2014), 1859–1866.

[24] Matti B. Alemayehu, Matthias Falmbigl, Corinna Grosse, Kim Ta, Saskia F. Fischer and David C. Johnson, Structural and electrical properties of a new $[(SnSe)_{1.16}]_1[NbSe_2]_1$ polytype. *Journal of Alloys and Compounds* **619**, (2015), 861–868.

[25] Ryan Atkins, Sabrina Disch, Zachary Jones, Ines Haeusler, Corinna Grosse, Saskia F. Fischer, Wolfgang Neumann, Paul Zschack and David C. Johnson, Synthesis, structure and electrical properties of a new tin vanadium selenide. *Journal of Solid State Chemistry* **202**, (2013), 128–133.

[26] Myungkeun Noh, Christopher D. Johnson, Marc D. Hornbostel, James Thiel and David C. Johnson, Control of reaction pathway and the nanostructure of final products through the design of modulated elemental reactants. *Chemistry of Materials* **8** (8), (1996), 1625–1635.

[27] David C. Johnson, Controlled synthesis of new compounds using modulated elemental reactants. *Current Opinion in Solid State and Materials Science* **3** (2), (1998), 159–167.

[28] Daniel B. Moore, Matt Beekman, Sabrina Disch and David C. Johnson, Telluride misfit layer compounds: $[(PbTe)_{1.17}]_m(TiTe_2)_n$. *Angewandte Chemie International Edition* **53** (22), (2014), 5672–5675.

[29] Matti B. Alemayehu, Matthias Falmbigl, Kim Ta and David C. Johnson, Effect of local structure of $NbSe_2$ on the transport properties of $([SnSe]_{1.16})_1(NbSe_2)_n$ ferecrystals. *Chemistry of Materials* **27** (6), (2015), 2158–2164.

[30] Corinna Grosse, Ryan Atkins, Holm Kirmse, Anna Mogilatenko, Wolfgang Neumann and David C. Johnson, Local structure and defect chemistry of $[(SnSe)_{1.15}]_m(TaSe_2)$ ferecrystals – A new type of layered intergrowth compound. *Journal of Alloys and Compounds* **579** (0), (2013), 507–515.

[31] C. Heideman, N. Nguyen, D. C. Johnson, J. Hanni, Q. Lin, S. Duncombe and P. Zschack, The synthesis and characterization of new $[(BiSe)_{1.10}]_m[NbSe_2]_n$, $[(PbSe)_{1.10}]_m[NbSe_2]_n$, $[(CeSe)_{1.14}]_m[NbSe_2]_n$ and $[(PbSe)_{1.12}]_m[TaSe_2]_n$ misfit layered compounds. *Journal of Solid State Chemistry* **181**, (2008), 1701–1706.

[32] Matti B. Alemayehu, Matthias Falmbigl, Kim Ta, Corinna Grosse, Richard D. Westover, Sage R. Bauers, Saskia F. Fischer and David C. Johnson, Structural and electrical properties of $[(SnSe)_{1+\delta}]_m[NbSe_2]_1$ compounds: single $NbSe_2$ layers separated by increasing thickness of SnSe. *Chemistry of Materials* **27**, (2015), 867–875.

[33] Ryan Atkins, Jason Wilson, Paul Zschack, Corinna Grosse, Wolfgang Neumann and David C. Johnson, Synthesis of $[(SnSe)_{1.15}]_m(TaSe_2)_n$ Ferecrystals: Structurally Tunable Metallic Compounds. *Chemistry of Materials* **24** (23), (2012), 4594–4599.

[34] Matt Beekman, Sabrina Disch, Sergei Rouvimov, Deepa Kasinathan, Klaus Koepernik, Helge Rosner, Paul Zschack, Wolfgang S. Neumann and David C. Johnson, Controlling size-induced phase transformations using chemically designed nanolaminates. *Angewandte Chemie International Edition* **52** (50), (2013), 13211–13214.

[35] G. A. Wiegers and W. Y. Zhou, The misfit layer compound $(SnSe)_{1.16}NbSe_2$. *Materials Research Bulletin* **26** (9), (1991), 879–885.

[36] G. A. Wiegers, Misfit layer compounds: Structures and physical properties. *Progress in Solid State Chemistry* **24**, (1996), 1–139.

[37] Alain Meerschaut, Misfit layer compounds. *Current Opinion in Solid State and Materials Science* **1** (2), (1996), 250– 259.

[38] J. Rouxel, A. Meerschaut and G. A. Wiegers, Chalcogenide misfit layer compounds. *Journal of Alloys and Compounds* **229**, (1995), 144–157.

[39] Y. Oosawa, Y. Gotoh, J. Akimoto, T. Tsunoda, M. Sohma and M. Onoda, Three Types of Ternary Selenides with Layered Composite Crystal Structures Formed in the Pb-Nb-Se System. *Japanese Journal of Applied Physics* **31**, (1992), L1096–L1099.

[40] C. Auriel, R. Roesky, A. Meerschaut and J. Rouxel, Structure determination and electrical properties of a new misfit layered selenide $(PbSe)_{1.10}NbSe_2$. *Materials Research Bulletin* **28**, (1993), 247–254.

[41] A. Nader, A. Briggs, A. Meerschaut and A. Lafond, Superconductivity in the misfit layer compound $(PbSe)_{1.12}(NbSe_2)_2$. *Solid State Communications* **102** (5), (1997), 401– 403.

[42] C. Auriel, A. Meerschaut, C. Deudon, G.A. Wiegers, J. Baas, J. Chen and P. Monceau, Electrical transport properties of mono-and bilayers misfit compounds $(MX)_{1+x}(TX_2)_m$, M= Sn, Pb; T=Ti, Nb; X=S,Se. *European Journal of Solid State and Inorganic Chemistry* **32**, (1995), 947–962.

[43] C. Auriel, A. Meerschaut, R. Roesky and J. Rouxel, Crystal structure determination and transport properties of a new misfit layer compound $(PbSe)_{1.12}(NbSe_2)_2$: "$PbNb_2Se_5$". *European Journal of Solid State and Inorganic Chemistry* **29**, (1992), 1079–1091.

[44] C. J. Arguello, S. P. Chockalingam, E. P. Rosenthal, L. Zhao, C. Gutiérrez, J. H. Kang, W. C. Chung, R. M. Fernandes, S. Jia, A. J. Millis, R. J. Cava and A. N. Pasupathy, Visualizing the charge density wave transition in $2H$-$NbSe_2$ in real space. *Physical Review B* **89**, (2014), 235115.

[45] Robert E. Thorne, Charge Density Wave Conductors. *Physics Today* **49** (5), (1996), 42–47.

[46] R. E. Peierls, Quantum Theory of Solids. Oxford University Press, London (1955).

[47] G. Grüner, The dynamics of charge-density waves. *Reviews of Modern Physics* **60**, (1988), 1129–1181.

[48] Hans-Martin Eiter, Michela Lavagnini, Rudi Hackl, Elizabeth A. Nowadnick, Alexander F. Kemper, Thomas P. Devereaux, Jiun-Haw Chu, James G. Analytis, Ian R. Fisher and Leonardo Degiorgi, Alternative route to charge density wave formation in multiband systems. *Proceedings of the National Academy of Sciences* **110** (1), (2013), 64–69.

[49] J. A. Wilson, F. J. Di Salvo and S. Mahajan, Charge-density waves in metallic, layered, transition-metal dichalcogenides. *Physical Review Letters* **32**, (1974), 882–885.

[50] U. Chatterjee, J. Zhao, M. Iavarone, R. Di Capua, J. P. Castellan, G. Karapetrov, C. D. Malliakas, M. G. Kanatzidis, H. Claus, J. P. C. Ruff, F. Weber, J. van Wezel, J. C. Campuzano, R. Osborn, M. Randeria, N. Trivedi, M. R. Norman and S. Rosenkranz, Emergence of coherence in the charge-density wave state of $2H$-$NbSe_2$. *Nature Communications* **6**, (2015), 6313.

[51] Christos D. Malliakas and Mercouri G. Kanatzidis, Nb-Nb Interactions Define the Charge Density Wave Structure of $2H$-$NbSe_2$. *Journal of the American Chemical Society* **135** (5), (2013), 1719–1722, pMID: 23336213.

[52] L. Li, Z. Xu, J. Shen, L. Qiu and Z. Gan, The effect of a charge-density wave transition on the transport properties of $2H$-$NbSe_2$. *Journal of Physics: Condensed Matter* **17**, (2005), 493–498.

[53] K. Iwaya, T. Hanaguri, A. Koizumi, K. Takaki, A. Maeda and K. Kitazawa, Electronic state of $NbSe_2$ investigated by STM/STS. *Physica B: Condensed Matter* **329–333**, (2003), 1598–1599, proceedings of the 23rd International Conference on Low Temperature Physics.

[54] R. C. Morris, Connection between charge-density waves and superconductivity in $NbSe_2$. *Physical Review Letters* **34** (18), (1975), 1164–1166.

[55] H. Mutka, N. Housseau, J. Pelissier, R. Ayroles and C. Roucau, Effects of defects on charge density waves in layered dichalcogenides. *Solid State Communications* **50** (2), (1984), 161–164.

[56] A. LeBlanc and A. Nader, Resistivity anisotropy and charge density wave in $2H$-NbS_2 and $2H$ -$TaSe_2$. *Solid State Communications* **150** (29-30), (2010), 1346–1349.

[57] W. Higemoto, K. Nagamine, S. Kuroda and K. Takita, Charge density wave in $2H$-$NbSe_2$ probed by muons. *Physica B: Condensed Matter* **326** (1–4), (2003), 540– 544.

[58] Adel Nader and Pierre Monceau, Critical field of $2H$-$NbSe_2$ down to 50mK. *SpringerPlus* **3** (1), (2014), 1–5.

[59] N. Toyota, H. Nakatsuji, K. Noto, A. Hoshi, N. Kobayashi, Y. Muto and Y. Onodera, Temperature and angular dependences of upper critical fields for the layer structure superconductor $2H$-$NbSe_2$. *Journal of Low Temperature Physics* **25** (3-4), (1976), 485–499.

[60] H. N. S. Lee, H. McKinzie, D.S. Tannhauser and A. Wold, The Low-Temperature Transport Properties of $NbSe_2$. *Journal of Applied Physics* **40** (2), (1969), 602–604.

[61] E. Revolinsky, G.A. Spiering and D.J. Beerntsen, Superconductivity in the niobium-selenium system. *Journal of Physics and Chemistry of Solids* **26** (6), (1965), 1029–1034.

[62] R. E. Schwall, G. R. Stewart and T. H. Geballe, Low-temperature specific heat of layered compounds. *Journal of Low Temperature Physics* **22** (5-6), (1976), 557–567.

[63] R. F. Frindt, Superconductivity in Ultrathin $NbSe_2$ Layers. *Physical Review Letters* **28**, (1972), 299–301.

[64] Matthias Falmbigl, Andreas Fiedler, Ryan E. Atkins, Saskia F. Fischer and David C. Johnson, Suppressing a charge density wave by changing dimensionality in the ferecrystalline compounds $([SnSe]_{1.15})_1(VSe_2)_n$ with $n = 1$, 2, 3, 4. *Nano Letters* **15** (2), (2015), 943–948.

[65] Robert S. Allgaier and Wayne W. Scanlon, Mobility of Electrons and Holes in PbS, PbSe, and PbTe between Room Temperature and 4.2°K. *Physical Review* **111**, (1958), 1029–1037.

[66] Jay N. Zemel, James D. Jensen and Richard B. Schoolar, Electrical and Optical Properties of Epitaxial Films of PbS, PbSe, PbTe, and SnTe. *Physical Review* **140**, (1965), A330–A342.

[67] Li-Dong Zhao, Shih-Han Lo, Yongsheng Zhang, Hui Sun, Gangjian Tan, Ctirad Uher, C. Wolverton Vinayak P. Dravid and Mercouri G. Kanatzidis, Ultralow thermal conductivity and high thermoelectric figure of merit in SnSe crystals. *Nature* **508**, (2014), 373–377.

[68] I. Lefebvre, M. A. Szymanski, J. Olivier-Fourcade and J. C. Jumas, Electronic structure of tin monochalcogenides from SnO to SnTe. *Physical Review B* **58**, (1998), 1896–1906.

[69] H. S. Soliman, D. A. Abdel Hady, K. F. Abdel Rahman, S. B. Youssef and A. A. El-Shazly, Optical properties of tin-selenid films. *Physica A: Statistical Mechanics and its Applications* **216**, (1995), 77–84.

[70] S.S. Banerjee, S. Saha, N.G. Patil, S. Ramakrishnan, A.K. Grover, S. Bhattacharya, G. Ravikumar, P.K. Mishra, T.V.C. Rao, V.C. Sahni, C.V. Tomy, G. Balakrishnan, D. Mck. Paul and M.J. Higgins, Generic phase diagram for vortex matter via a study of peak effect phenomenon in crystals of $2H$-$NbSe_2$. *Physica C: Superconductivity* **308** (1-2), (1998), 25–32.

[71] I. Naik and A. K. Rastogi, Transport properties of $2H$-NbS_2: Effect of Ga-intercalation. *Physica B: Condensed Matter* **405** (3), (2010), 955– 957.

[72] T. F. Smith, R. N. Shelton and R. E. Schwall, Pressure enhanced superconductivity in $NbSe_2$. *Journal of Physics F: Metal Physics* **4** (11), (1974), 2009.

[73] Hisashi Inoue, Minu Kim, Christopher Bell, Yasuyuki Hikita, Srinivas Raghu and Harold Y. Hwang, Tunable coupling of two-dimensional superconductors in bilayer $SrTiO_3$ heterostructures. *Physical Review B* **88**, (2013), 241104.

[74] P. Samuely, P. Szabó, J. Kačmarčík, A.G.M. Jansen, A. Lafond, A. Meerschaut and A. Briggs, Two-dimensional behavior of the naturally layered superconductor $(LaSe)_{1.14}(NbSe_2)$. *Physica C: Superconductivity* **369** (1-4), (2002), 61– 67.

[75] Michael Tinkham, Introduction to Superconductivity. Dover Publications, Inc., Second edition (2004).

[76] J. Hsu and A. Kapitulnik, Superconducting transition, fluctuation, and vortex motion in a two-dimensional single-crystal Nb film. *Physical Review B* **45**, (1992), 4819–4835.

[77] S. Ruggiero, T. Barbee and M. Beasley, Superconductivity in Quasi-Two-Dimensional Layered Composites. *Physical Review Letters* **45**, (1980), 1299–1302.

[78] D. Neerinck, K. Temst, C. Van Haesendonck, Y. Bruynseraede, A. Gilabert and Ivan K. Schuller, Crossover in the critical field of Pb/Ge multilayers: from single-film to coupled behavior. *Physical Review B* **43**, (1991), 8676–8678.

[79] A. Meerschaut, R. Roesky, A. Lafond, C. Deudon and J. Rouxel, Misfit layered compounds: polytypism, multilayer stages, non-stoichiometry and electronic structure, self-misfit compounds. *Journal of Alloys and Compounds* **219**, (1995), 157–160, eleventh international conference on solid compounds of transition elements.

[80] N. Giang, Q. Xu, Y.S. Hor, A.J. Williams, S.E. Dutton, H.W. Zandbergen and R.J. Cave, Superconductivity at 2.3 K in the misfit compound $(PbSe)_{1.16}(TiSe_2)_2$. *Physical Review B* **82**, (2010), 024503.

[81] A. Kikuchi and S. Tsuneyuki, Electronic structure and charge density wave state in polytypes of $NbSe_2$. *Surface Science* **409** (3), (1998), 458–464.

[82] B. E. Brown and D. J. Beerntsen, Layer Structure Polytypism Among Niobium and Tantalum Selenides. *Acta Crystallographica* **18**, (1965), 31–36.

[83] I. Naik and A. K. Rastogi, Charge density wave and superconductivity in $2H$- and $4H$-$NbSe_2$: A revisit. *Pramana* **76** (6), (2011), 957–963.

[84] T. K. Chattopadhyay, J. Pannetier and H. G. von Schnering, Neutron Diffraction Study of the Structural Phase Transition in SnS and SnSe. *Journal of Physics and Chemistry of Solids* **47**, (1986), 879–885.

[85] Yasutoshi Noda, Katashi Masumoto, Shigeru Ohba, Yoshihiko Saito, Koshiro Toriumi, Yutaka Iwata and Iwao Shibuya, Temperature Dependence of Atomic Thermal Parameters of Lead Chalcogenides, PbS, PbSe and PbTe. *Acta Crystallographica C* **43**, (1987), 1443–1445.

[86] Evgeniya Kabliman, Peter Blaha and Karlheinz Schwarz, Ab initio study of stabilization of the misfit layer compound $(PbS)_{1.14}TaS_2$. *Physical Review B* **82**, (2010), 125308.

[87] M. Kalläne, K. Rossnagel, M. Marczynski-Bühlow, L. Kipp, H. I. Starnberg and S. E. Stoltz, Stabilization of the Misfit Layer Compound $PbS_{1.13}TaS_2$ by Metal Cross Substitution. *Physical Review Letters* **100**, (2008), 065502.

[88] Y. Moëlo, A. Meerschaut, J. Rouxel and C. Auriel, Precise Analytical Characterization of Incommensurate Sandwiched Layered Compounds $[(Pb,Sn)S]_{1+x}[(Nb,Ti)S_2]_m$, $(0.08 \leq x \leq 50.28, m = 1-3)$. Role of Cationic Coupling on the Properties and the Structural Modulation. *Chemistry of Materials* **7** (10), (1995), 1759–1771.

[89] J. Brandt, J. Kanzow, K. Rossnagel, L. Kipp, M. Skibowski, E. Krasovskii, W. Schattke, M. Traving, J. Stettner, W. Press, C. Dieker and W. Jäger, Band structure of the misfit compound $(PbS)NbS_2$ compared to $NbSe_2$: experiment and theory. *Journal of Electron Spectroscopy and Related Phenomena* **114-116** (0), (2001), 555–561, proceeding of the Eight International Conference on Electronic Spectroscopy and Structure.

[90] Lynn F. Schneemeyer, Angelica Stacy and M. J. Sienko, Effect of nonstoichiometry on the periodic lattice distortion in vanadium diselenide. *Inorganic Chemistry* **19** (9), (1980), 2659–2662.

[91] Ph. Leininger, D. Chernyshov, A. Bosak, H. Berger and D. S. Inosov, Competing charge density waves and temperature-dependent nesting in $2H$-$TaSe_2$. *Physical Review B* **83**, (2011), 233101.

[92] L. F. Mattheiss, Band Structures of Transition-Metal-Dichalcogenide Layer Compounds. *Physical Review B* **8**, (1973), 3719–3740.

[93] J. A. Wilson and A. D. Yoffe, The transition metal dichalcogenides discussion and interpretation of the observed optical, electrical and structural properties. *Advances in Physics* **18**, (1969), 193–335.

[94] Tomohisa Kumakura, Hiroki Tan, Tetsuya Handa, Masashi Morishita and Hiroshi Fukuyama, Charge density waves and superconductivity in $2H$-$TaSe_2$. *Czechoslovak Journal of Physics* **46** (5), (1996), 2611–2612.

[95] Michel Bayard and M.J. Sienko, Anomalous electrical and magnetic properties of vanadium diselenide. *Journal of Solid State Chemistry* **19** (4), (1976), 325–329.

[96] D J Eaglesham, R L Withers and D M Bird, Charge-density-wave transitions in $1T-VSe_2$. *Journal of Physics C: Solid State Physics* **19** (3), (1986), 359.

[97] D W Bullett, Electronic band structure and bonding in transition metal layered dichalcogenides by atomic orbital methods. *Journal of Physics C: Solid State Physics* **11** (22), (1978), 4501.

[98] Ashok Kumar and P.K. Ahluwalia, Effect of quantum confinement on electronic and dielectric properties of niobium dichalcogenides NbX_2 (X=S, Se, Te). *Journal of Alloys and Compounds* **550** (0), (2013), 283–291.

[99] J. V. Acrivos, W. Y. Liang, J. A. Wilson and A. D. Yoffe, Optical studies of metal-semiconductor transmutations produced by intercalation. *Journal of Physics C: Solid State Physics* **4** (1), (1971), L18.

[100] Th. Straub, Th. Finteis, R. Claessen, P. Steiner, S. Hüfner, P. Blaha, C. S. Oglesby and E. Bucher, Charge-Density-Wave Mechanism in $2H$-$NbSe_2$: Photoemission Results. *Physical Review Letters* **82**, (1999), 4504–4507.

[101] D. Berner, H. Leihenseder, K. Widder, H. P. Geserich, V. M. Burlakov, B. N. Mavrin, V. N. Denisov, R. Roesky, P. Gressier and A. Meerschaut, $LaSe_{1.14}(NbSe_2)$ - a metal - insulator quantum well crystal? *Journal of Physics: Condensed Matter* **9** (47), (1997), 10545.

[102] G. Leveque, S. Robin-Kandare and L. Martin, Band structure of layer crystals $NbSe_2$ and MoS_2 and an interpretation of their optical spectra. *physica status solidi (b)* **63** (2), (1974), 679–690.

[103] L. H. Brixner, Preparation and properties of the single crystalline $AB2$-type selenides and tellurides of niobium, tantalum, molybdenum and tungsten. *Journal of Inorganic and Nuclear Chemistry* **24** (3), (1962), 257–263.

[104] D. S. Inosov, V. B. Zabolotnyy, D. V. Evtushinsky, A. A. Kordyuk, B. Büchner, R. Follath, H. Berger and S. V. Borisenko, Fermi surface nesting in

several transition metal dichalcogenides. *New Journal of Physics* **10** (12), (2008), 125027.

[105] F. Soto, H. Berger, L. Cabo, C. Carballeira, J. Mosqueira, D. Pavuna, P. Toimil and F. Vidal, Electric and magnetic characterization of $NbSe_2$ single crystals: Anisotropic superconducting fluctuations above T_c. *Physica C: Superconductivity* **460-462, Part 2**, (2007), 789–790, proceedings of the 8th International Conference on Materials and Mechanisms of Superconductivity and High Temperature SuperconductorsM2S-HTSC {VIII}.

[106] S. F. Meyer, R. E. Howard, G. R. Stewart, J. V. Acrivos and T. H. Geballe, Properties of intercalated $2H$-$NbSe_2$, $4H$-TaS_2, and $1T$-TaS_2. *The Journal of Chemical Physics* **62** (11), (1975), 4411–4419.

[107] Ken-ichi Yokota, Gouo Kurata, Tomohiro Matsui and Hiroshi Fukuyama, Superconductivity in the quasi-two-dimensional conductor $2H$-$TaSe_2$. *Physica B: Condensed Matter* **284-288** (0), (2000), 551–552.

[108] K. Tsutsumi, Y. Ishihara and H. Suzuki, Survey of Superconductivity in a Layered Compound $1T-VSe_2$. In: Takehiko Ishiguro and Koji Kajimura, eds., Advances in Superconductivity II, 533–536, Springer Japan (1990).

[109] R. A. Craven and S. F. Meyer, Specific heat and resistivity near the charge-density-wave phase transitions in $2H$-$TaSe_2$ and $2H$-TaS_2. *Physical Review B* **16**, (1977), 4583–4593.

[110] A. E. Jacobs and M. B. Walker, Theory of the incommensurate charge-density-wave phases of the $2H$-$TaSe_2$ structure. *Physical Review B* **26**, (1982), 206–218.

[111] S. V. Borisenko, A. A. Kordyuk, A. N. Yaresko, V. B. Zabolotnyy, D. S. Inosov, R. Schuster, B. Büchner, R. Weber, R. Follath, L. Patthey and H. Berger, Pseudogap and Charge Density Waves in Two Dimensions. *Physical Review Letters* **100**, (2008), 196402.

[112] C. F. van Bruggen and C. Haas, Magnetic susceptibility and electrical properties of VSe_2 single crystals. *Solid State Communications* **20** (3), (1976), 251–254.

[113] A. H. Thompson and B. G. Silbernagel, Correlated magnetic and transport properties in the charge-density-wave states of VSe_2. *Physical Review B* **19**, (1979), 3420–3426.

[114] Richard A. Klemm, Layered Superconductors, volume 1. Oxford University Press (2012).

[115] G. Martinez, M. Schlüter and Marvin L. Cohen, Electronic structure of PbSe and PbTe. I. band structures, densities of states, and effective masses. *Physical Review B* **11**, (1975), 651–659.

[116] Xin Chen, David Parker and David J. Singh, Importance of non-parabolic band effects in the thermoelectric properties of semiconductors. *Scientific Reports* **3**, (2013), 3168.

[117] S. E. Kohn, P. Y. Yu, Y. Petroff, Y. R. Shen, Y. Tsang and M. L. Cohen, Electronic band structure and optical properties of PbTe, PbSe, and PbS. *Physical Review B* **8**, (1973), 1477–1488.

[118] V. D. Das and K. S. Bhat, Electrical conductivity of air-exposed and unexposed lead selenide thin films: Temperature and size effects. *Physical Review B* **40**, (1989), 7696–7703.

[119] M. Shandalov, Z. Dashevsky and Y. Golan, Microstructure related transport phenomena in chemically deposited PbSe films. *Materials Chemistry and Physics* **112** (1), (2008), 132–135.

[120] S. K. Datta and A. K. Chaudhuri, On the mechanism of photoconductivity in polycrystalline lead selenide films. *Semiconductor Science and Technology* **4** (5), (1989), 376.

[121] N. B. Brandt, D. V. Gitsu, N. S. Popovich, V. I. Sidorov and S. M. Chudinov, Superconductivity of the compounds PbTe and PbSe under high pressure. *ZhETF Pis. Red.* **22**, (1975), 104–106.

[122] Z. Nabi, A. Kellou, S. MéÇabih, A. Khalfi and N. Benosman, Opto-electronic properties of rutile SnO_2 and orthorhombic SnS and SnSe compounds. *Materials Science and Engineering: B* **98** (2), (2003), 104–115.

[123] T. Abraham, C. Juhasz, J. Silver, J. D. Donaldson and M. J. K. Thomas, A TIN-119 Mössbauer and electrical conductivity study of the system $Sn_xGe_{1-x}Se$ ($0 \leq x \leq 1$). *Solid State Communications* **27** (11), (1978), 1185–1187.

[124] H. Maier and D. R. Daniel, SnSe single crystals: Sublimation growth, deviation from stoichiometry and electrical properties. *Journal of Electronic Materials* **6** (6), (1977), 693–704.

[125] Dang Tran Quan, SnSe thin films synthesized by solid state reactions. *Thin Solid Films* **149** (2), (1987), 197–203.

[126] Dang Tran Quan, Electrical properties and optical absorption of SnSe evaporated thin films. *physica status solidi (a)* **86** (1), (1984), 421–426.

[127] J. P. Singh and R. K. Bedi, Electrical properties of flash-evaporated tin selenide films. *Thin Solid Films* **199** (1), (1991), 9–12.

[128] N. Kumar, V. Sharma, N. Padha, N. M. Shah, M. S. Desai, C. J. Panchal and I. Yu. Protsenko, Influence of the substrate temperature on the structural, optical, and electrical properties of tin selenide thin films deposited by thermal evaporation method. *Crystal Research and Technology* **45** (1), (2010), 53–58.

[129] N. Kumar, U. Parihar, R. Kumar, K. J. Patel, C. J. Panchal and N. Padha, Effect of film thickness on optical properties of tin selenide thin films prepared by thermal evaporation for photovoltaic applications. *American Journal of Materials Science* **2** (2), (2012), 41–45.

[130] Yu. A. Timofeev, B. V. Vinogradov and V. B. Begoulev, Superconductivity of tin selenide at pressures up to 70 GPa. *Physics of the Solid State* **39** (2), (1997), 207–207.

[131] Yan Sun, Zhicheng Zhong, Tomonori Shirakawa, Cesare Franchini, Dianzhong Li, Yiyi Li, Seiji Yunoki and Xing-Qiu Chen, Rocksalt SnS and SnSe: Native topological crystalline insulators. *Physical Review B* **88**, (2013), 235122.

[132] Zhenyu Wang, Jianfeng Wang, Yunyi Zang, Qinghua Zhang, Jin-An Shi, Tian Jiang, Yan Gong, Can-Li Song, Shuai-Hua Ji, Li-Li Wang, Lin Gu, Ke He, Wenhui Duan, Xucun Ma, Xi Chen and Qi-Kun Xue, Molecular beam epitaxy-grown SnSe in the rock-salt structure: An artificial topological crystalline insulator material. *Advanced Materials* **27** (28), (2015), 4150–4154.

[133] R. H. Friend and A. D. Yoffe, Electronic properties of intercalation complexes of the transition metal dichalcogenides. *Advances in Physics* **36** (1), (1987), 1–94.

[134] A. R. H. F. Ettema, G. A. Wiegers, C. Haas and T. S. Turner, Resonant and Core Level Photoemission Spectroscopy of the Misfit Layer Compound $(SnS)_{1.20}TiS_2$. *Physica Scripta* **1992** (T41), (1992), 265.

[135] A. R. H. F. Ettema, C. Haas and T. S. Turner, Strong multiple resonances in the photoemission spectra of transition-metal-layer and misfit-layer compounds. *Physical Review B* **47**, (1993), 12794–12805.

[136] A. R. H. F. Ettema and C Haas, An X-ray photoemission spectroscopy study of interlayer charge transfer in some misfit layer compounds. *Journal of Physics: Condensed Matter* **5** (23), (1993), 3817.

[137] Youichi Ohno, Core-electron spectra and electronic structure of $CeNbS_3$. *Physical Review B* **48**, (1993), 5515–5524.

[138] Youichi Ohno, Electronic structure of the misfit-layer compounds $PbTiS_3$ and $SnNbS_3$. *Physical Review B* **44**, (1991), 1281–1291.

[139] C. M. Fang, A. R. H. F. Ettema, C. Haas, G. A. Wiegers, H. van Leuken and R. A. de Groot, Electronic structure of the misfit-layer compound $(SnS)_{1.17}NbS_2$ deduced from band-structure calculations and photoelectron spectra. *Physical Review B* **52**, (1995), 2336–2347.

[140] P. Monceau, J. Chen, O. Laborde, A. Briggs, C. Auriel, R. Roesky, A. Meerschaut and J. Rouxel, Anisotropy of the superconducting properties of misfit layer compounds $(MX)_n(NbX2)_m$. *Physica B* **194-196**, (1994), 2361–2362.

[141] P. Blood and J.W. Orton, The electrical characterization of semiconductors: Majority carriers and electron states. Academic Press (1992).

[142] Rudolf Gross and Achim Marx, Festkörperphysik, volume 2., aktualisierte Aufl. De Gruyter (2014).

[143] Charles Kittel, Introduction to Solid State Physics. John Wiley & Sons (2005).

[144] Harald Ibach and Hans Lüth, Festkörperphysik-Einführung in die Grundlagen. Springer (2009).

[145] K. Seeger, Semiconductor Physics - An Introduction. Springer Berlin Heidelberg New York (2002).

[146] F. Bloch, Zum elektrischen Widerstandsgesetz bei tiefen Temperaturen. *Zeitschrift für Physik* **59** (3-4), (1930), 208–214.

[147] Jack Bass, William Pratt and Peter Schroeder, The temperature-dependent electrical resistivities of the alkali metals. *Reviews of Modern Physics* **62**, (1990), 645–744.

[148] N. W. Ashcroft and N. D. Mermin, Solid State Physics. Saunders College (1976).

[149] Gerd Czycholl, Theoretische Festkörperphysik. Springer (2008).

[150] L. J. van der Pauw, A method of measuring specific resistivity and Hall effect of discs of arbitrary shape. *Philips Research Reports* **13** (1), (1958), 1–9.

[151] L. J. van der Pauw, A method of measuring the resistivity and hall coefficient on lamellae of arbitrary shape. *Philips Technical Review* **20** (8), (1958/59), 220–224.

[152] HI Starnberg, HE Brauer, L.J. Holleboom and H.P. Hughes, 3D-to-2D transition by Cs intercalation of VSe_2. *Physical review letters* **70** (20), (1993), 3111–3114.

[153] S. Lebègue and O. Eriksson, Electronic structure of two-dimensional crystals from *ab initio* theory. *Physical Review B* **79**, (2009), 115409.

[154] Yi Ding, Yanli Wang, Jun Ni, Lin Shi, Siqi Shi and Weihua Tang, First principles study of structural, vibrational and electronic properties of graphene-like MX_2 (M=Mo, Nb, W, Ta; X=S, Se, Te) monolayers. *Physica B: Condensed Matter* **406** (11), (2011), 2254–2260.

[155] Lun Li, Zhong Chen, Ying Hu, Xuewen Wang, Ting Zhang, Wei Chen and Qiangbin Wang, Single-Layer Single-Crystalline SnSe Nanosheets. *Journal of the American Chemical Society* **135** (4), (2013), 1213–1216, pMID: 23311291.

[156] Arunima K. Singh and Richard G. Hennig, Computational prediction of two-dimensional group-IV mono-chalcogenides. *Applied Physics Letters* **105**, (2014), 042103.

[157] Myungkeun Noh, David C. Johnson and Greg S. Elliott, Variations in the conductive and superconductive properties of $([TiSe_2]_l[NbSe_2]_m)_n$ superlattices as a function of superlattice structure. *Chemistry of Materials* **12** (10), (2000), 2894–2901.

[158] S. V. Borisenko, A. A. Kordyuk, V. B. Zabolotnyy, D. S. Inosov, D. Evtushinsky, B. Büchner, A. N. Yaresko, A. Varykhalov, R. Follath, W. Eberhardt, L. Patthey and H. Berger, Two energy gaps and fermi-surface "arcs" in $NbSe_2$. *Physical Review Letters* **102**, (2009), 166402.

[159] R. Peierls, Zur Theorie der elektrischen und thermischen Leitfähigkeit von Metallen. *Annalen der Physik* **396** (2), (1930), 121–148.

[160] R. C. Morris and R. V. Coleman, Tunneling measurement of the superconducting energy gap in $NbSe_2$. *Physics Letters A* **43** (1), (1973), 11–12.

[161] H. Kamerlingh Onnes, Further experiments with liquid helium. C. On the change of electric resistance of pure metals at very low temperatures etc. IV. The resistance of pure mercury at helium temperatures. In: Kostas

Gavroglu and Yorgos Goudaroulis, eds., Through Measurement to Knowledge, volume 124 of *Boston Studies in the Philosophy of Science*, 261–263, Springer Netherlands (1991).

[162] F. London and H. London, The Electromagnetic Equations of the Supraconductor. *Proceedings of the Royal Society of London A: Mathematical, Physical and Engineering Sciences* **149** (866), (1935), 71–88.

[163] V. L Ginzburg and L. D. Landau, On the theory of superconductivity. *Zhurnal Eksperimental'noi i Teoreticheskoi Fiziki* **20**, (1950), 1064–1082.

[164] J. Bardeen, L. Cooper and J. Schrieffer, Theory of superconductivity. *Physical Review* **108**, (1957), 1175–1204.

[165] J. G. Bednorz and K. A. Müller, Possible high T_c superconductivity in the Ba-La-Cu-O system. *Zeitschrift für Physik B Condensed Matter* **64** (2), (1986), 189–193.

[166] A. Schilling, M. Cantoni, J. D. Guo and H. R. Ott, Superconductivity above 130 K in the Hg-Ba-Ca-Cu-O system. *Nature* **363**, (1993), 56–58.

[167] P. de Trey, Suso Gygax and J.-P. Jan, Anisotropy of the Ginzburg-Landau parameter κ in $NbSe_2$. *Journal of Low Temperature Physics* **11** (3-4), (1973), 421–434.

[168] D. Saint-James, G. Sarma and E. J. Thomas, Type II Superconductivity. Pergamon Press, London (1968).

[169] I. Guillamón, H. Suderow, S. Vieira, L. Cario, P. Diener and P. Rodière, Superconducting Density of States and Vortex Cores of $2H$-NbS_2. *Physical Review Letters* **101**, (2008), 166407.

[170] H. F. Hess, Scanning tunneling spectroscopy of vortices in a superconductor. *Physica C: Superconductivity* **185-189, Part 1** (0), (1991), 259– 263.

[171] H. F. Hess, R. B. Robinson, R. C. Dynes, J. M. Valles and J. V. Waszczak, Scanning-Tunneling-Microscope Observation of the Abrikosov Flux Lattice and the Density of States near and inside a Fluxoid. *Physical Review Letters* **62**, (1989), 214–216.

[172] R. Corcoran, P. Meeson, Y. Onuki, P. A. Probst, M. Springford, K. Takita, H. Harima, G. Y. Guo and B. L. Gyorffy, Quantum oscillations in the mixed state of the type II superconductor $2H$-$NbSe_2$. *Journal of Physics: Condensed Matter* **6** (24), (1994), 4479.

[173] D. E. Prober, R. E. Schwall and M. R. Beasley, Upper critical fields and reduced dimensionality of the superconducting layered compounds. *Physical Review B* **21**, (1980), 2717–2733.

[174] W. Lawrence and S. Doniach, Theory of layer structure superconductors. *Proc. 12 th Inter. Conf. on Low Temperature Physics, Academic Press of Japan, Kyoto* **24**, (1971), 361–362.

[175] B. D. Josephson, Possible new effects in superconductive tunnelling. *Physics Letters* **1** (7), (1962), 251– 253.

[176] R. A. Klemm, M.R. Beasley and A. Luther, The upper critical field of layered superconductors. *Journal of Low Temperature Physics* **16** (5-6), (1974), 607–613.

[177] Werner Buckel and Reinhold Kleiner, Superconductivity: Fundamentals and Applications, Second Edition. Wiley-VCH Verlag GmbH (2007).

[178] M. Tinkham, Effect of Fluxoid Quantization on Transitions of Superconducting Films. *Physical Review* **129**, (1963), 2413–2422.

[179] F. E. Harper and M. Tinkham, The Mixed State in Superconducting Thin Films. *Physical Review* **172**, (1968), 441–450.

[180] Ctirad Uher, Joshua L. Cohn and Ivan K. Schuller, Upper critical field in anisotropic superconductors. *Physical Review B* **34**, (1986), 4906–4908.

[181] D. B Williams and C. B. Carter, Transmission Electron Microscopy - A Textbook for Materials Science. Springer (2009).

[182] D. E. Newbury, Electron beam-specimen interactions in the analytical electron microscope. In: DavidC. Joy, Jr. Romig, AltonD. and JosephI. Goldstein, eds., Principles of Analytical Electron Microscopy, 1–27, Springer US (1986).

[183] A. Jablonski, F. Salvat and C. J. Powell, Differential cross sections for elastic scattering of electrons by atoms and solids. *Journal of Electron Spectroscopy and Related Phenomena* **137-140**, (2004), 299–303.

[184] M. Haruta, H. Kurata, H. Komatsu, Y. Shimakawa and S. Isoda, Effects of electron channeling in HAADF-STEM intensity in La_2CuSnO_6. *Ultramicroscopy* **109** (4), (2009), 361–367.

[185] C. J. Rossouw, L. J. Allen, S. D. Findlay and M. P. Oxley, Channelling effects in atomic resolution STEM. *Ultramicroscopy* **96** (3-4), (2003), 299–312, proceedings of the International Workshop on Strategies and Advances in Atomic Level Spectroscopy and Analysis.

[186] Noel S Gunning, Joseph Feser, Matthias Falmbigl, Matt Beekman, David G Cahill and David C Johnson, Synthesis, structure, and thermal conductivity of $[(SnSe)_{1+y}]_n[MoSe_2]_n$ compounds. *Semiconductor Science and Technology* **29** (12), (2014), 124007.

[187] Devin R Merrill, Daniel B Moore, Mark N Coffey, Adam W Jansons, Matthias Falmbigl and David C Johnson, Synthesis and characterization of turbostratically disordered $(BiSe)_{1.15}TiSe_2$. *Semiconductor Science and Technology* **29** (6), (2014), 064004.

[188] Brent Fultz and James Howe, Transmission Electron Microscopy and Diffractometry of Materials. Springer (2008).

[189] A. Winkelmann, Electron Backscatter Diffraction in Materials Science, chapter 2, Dynamical Simulation of Electron Backscatter Diffraction Patterns, 21–33. Springer (2009).

[190] A. R. Landa-Cánovas, A. Gómez-Herrero and L. Carlos Otero-Díaz, Electron microscopy study of incommensurate modulated structures in misfit ternary chalcogenides. *Micron* **32** (5), (2001), 481–495.

[191] Mohammed Kars, Daniel C. Fredrickson, A. Gómez-Herrero, Sven Lidin, Allaoua Rebbah and L.C. Otero-Diáz, Structural study by X-ray diffraction and transmission electron microscopy of the misfit compound $(SbS_{1-x}Se_x)_{1.16}(Nb_{1.036}S_2)_2$. *Materials Research Bulletin* **45** (8), (2010), 982– 988.

[192] E. Spiecker, M. Garbrecht, W. Jaeger. and K. Tillmann, Advantages of aberration correction for HRTEM investigation of complex layer compounds. *Journal of Microscopy* **237**, (2010), 341–346.

[193] S. Kuypers and J. Van Landuyt, Electron microscopy study of incommensurate intergrowth structures MTS_3. *Materials Science Forum* **100-101**, (1992), 223–272.

[194] Ryan Atkins, Daniel B. Moore and David C. Johnson, Insights into the self-assembly of ferecrystalline compounds from designed amorphous precursors. *Chemistry of Materials* **25** (9), (2013), 1744–1750.

[195] Carl L. Yaws, Vapor pressure graphs for inorganic compounds and elements. In: Carl L. Yaws, ed., Inorganic Compounds and Elements, volume 4 of *Handbook of Vapor Pressure*, 1 – 343, Gulf Professional Publishing (1995).

[196] P. Diener, P. Rodiére, J.D. Fletcher, A. Carrington, J.P. Brison, R. Prozorov, T. Olheiser and R.W. Giannetta, Anisotropic superconductivity in $NbSe_2$

probed by magnetic penetration depth. *Physica C: Superconductivity* **460-462** (0), (2007), 700–701, proceedings of the 8th International Conference on Materials and Mechanisms of Superconductivity and High Temperature Superconductors M2S-HTSC {VIII}.

[197] P. G. De Gennes, Boundary effects in superconductors. *Reviews of Modern Physics* **36**, (1964), 225–237.

[198] B. Fellmuth, H. Maas and D. Elefant, Investigation of the superconducting transition point of niobium as a reference temperature. *Metrologia* **21**, (1985), 169–180.

[199] B. Fellmuth, D. Elefant and J.-I. Mönch, Investigation of the superconducting transition of ultra-high-purity niobium. *physica status solidi (a)* **100** (2), (1987), 597–605.

[200] Susumu Matsuo, Hideo Sugiura and Seiichiro Noguchi, Superconducting transition temperature of aluminum, indium, and lead fine particles. *Journal of Low Temperature Physics* **15** (5-6), (1974), 481–490.

[201] D. K. Finnemore and D. E. Mapother, Superconducting properties of tin, indium, and mercury below 1° K. *Physical Review* **140**, (1965), A507–A518.

[202] C. A. Bryant and P. H. Keesom, Low-temperature specific heat of indium and tin. *Physical Review* **123**, (1961), 491–499.

[203] Georg Hoffmann, Bachelor thesis: Elektrische Transportmessungen an $[(SnSe)_{1+\delta}]_m[NbSe_2]_1$ Ferekristallschichtsystemen, Humboldt-Universität zu Berlin (2015).

[204] B. Subramanian, T. Mahalingam, C. Sanjeeviraja, M. Jayachandran and Mary Juliana Chockalingam, Electrodeposition of Sn, Se, SnSe and the material properties of SnSe films. *Thin Solid Films* **357** (2), (1999), 119–124.

[205] B. B. Nariya, A. K. Dasadia, M. K. Bhayani, A. J. Patel and A. R. Jani, Electrical transport properties of SnS and SnSe single crystals grown by direct vapor transport technique. *Chalcogenide Letters* **6** (10), (2009), 549–554.

[206] J. Kondo, Resistance Minimum in Dilute Magnetic Alloys. *Progress of Theoretical Physics* **32**, (1964), 37–49.

[207] Wei-Che Hsu, Chao-Chun Chen, Yong-Han Lin, Huang-Kai Lin, Hsin-Tien Chiu and Juhn-Jong Lin, Metallic conduction and large electron-phonon-impurity interference effect in single TiSi nanowires. *Nanoscale Research Letters* **7** (1), (2012), 500.

[208] A. Nader, A. Lafond, A. Briggs, A. Meerschaut and R. Roesky, Structural characterization and superconductivity in the misfit layer compound $(LaSe)_{1.14}(NbSe_2)$. *Synthetic Metals* **97** (2), (1998), 147–150.

[209] S. Foner and E.J. McNiff Jr., Upper critical fields of layered superconducting $NbSe_2$ at low temperature. *Physics Letters A* **45** (6), (1973), 429–430.

[210] P. Molinié, D. Jérome and A. J. Grant, Pressure-enhanced superconductivity and superlattice structures in transition metal dichalcogenide layer crystals. *Philosophical Magazine* **30** (5), (1974), 1091—1103.

[211] P. Garoche, J.J. Veyssié, P. Manuel and P. Molinié, Experimental investigation of superconductivity in $2H$-$NbSe_2$ single crystal. *Solid State Communications* **19** (5), (1976), 455–460.

[212] A. Nader, A. Lafond, A. Briggs and A. Meerschaut, Critical Magnetic Field Measurements of the Misfit Layer Compound $(SnS)_{1.17}(NbS_2)$ down to 50 mK. *Physica Scripta* **57** (2), (1998), 310.

[213] A. Nader, A. Lafond, A. Briggs, A. Meerschaut and G. Remenyi, Upward curvature of the perpendicular resistive critical magnetic field in the highly layered superconductor $(LaSe)_{1.14}(NbSe_2)_2$. *Synthetic Metals* **89** (2), (1997), 87– 89.

[214] K. Takanaka, Magnetic properties of superconductors with uniaxial symmetry. *physica status solidi (b)* **68** (2), (1975), 623–631.

[215] L. Hernán, J. Morales, J. Pattanayak and J.L. Tirado, Lithium intercalation into $PbNb_2S_5$, $PbNbS_3$, $SnNb_2Se_5$, $BiVS_3$, $SnVSe_3$, and $PbNb_2Se_5$ misfit layer chalcogenides. *Journal of Solid State Chemistry* **100** (2), (1992), 262–271.

[216] Katsunori Yamaguchi, Kazuo Kameda, Yoichi Takeda and Kimio Itagaki, Measurements of High Temperature Heat Content of the II-VI and IV-VI (II: Zn, Cd IV: Sn, Pb VI: Se, Te) Compounds. *Materials Transactions, JIM* **35** (2), (1994), 118–124.

[217] Ryan Atkins, *Synthesizing New* $[(SnSe)_{1.15}]_m(TSe_2)_n$, $[(SnSe)_{1.16}]_m(VSe_2)_n[(SnSe)_{1.16}]_p(TaSe_2)_q$ *and* $(SnSe)_{1.16}(V_{.51}Ta_{.49}Se_2)$ *Intergrowth Compounds (T = V and Ta)*. Ph.D. thesis, University of Oregon (2013).

[218] Miklos Kertesz and Roald Hoffmann, Octahedral vs. trigonal-prismatic coordination and clustering in transition-metal dichalcogenides. *Journal of the American Chemical Society* **106** (12), (1984), 3453–3460.

[219] Qiyin Lin, Sara Tepfer, Colby Heideman, Clay Mortensen, Ngoc Nguyen, Paul Zschack, Matt Beekman and David C. Johnson, Influence of selenium vapor postannealing on the electrical transport properties of PbSe-WSe_2 nanolaminates. *Journal of Materials Research* **26**, (2011), 1866–1871.

[220] P. Szabó, P. Samuely, J. Kačmarčík, A. G. M. Jansen, A. Briggs, A. Lafond and A. Meerschaut, Interlayer transport in the highly anisotropic misfit-layer superconductor $LaSe_{1.14}NbSe_2$. *Physical Review Letters* **86**, (2001), 5990–5993.

[221] J. Kačmarčík, P. Szabó, P. Samuely, J.G. Rodrigo, H. Suderow, S. Vieira, A. Lafond and A. Meerschaut, Intrinsic Josephson junction behaviour of the low T_c superconductor $(LaSe)_{1.14}(NbSe_2)$. *Physica C: Superconductivity* **468**, (2008), 543–546.

Publications

Matti B. Alemayehu, Matthias Falmbigl, Kim Ta, Corinna Grosse, Richard D. Westover, Sage R. Bauers, Saskia F. Fischer and David C. Johnson. Structure and electrical properties of $[(SnSe)_{1+\delta}]_m[NbSe_2]_1$ compounds: single $NbSe_2$ layers separated by increasing thickness of SnSe. *Chemistry of Materials* **27**, (2015), 867–875.

Marco Esters, Matti B. Alemayehu, Zachary Jones, Ngoc T. Nguyen, Michael D. Anderson, Corinna Grosse, Saskia F. Fischer, and David C. Johnson. Synthesis of inorganic structural isomers by diffusion-constrained self-assembly of designed precursors: A novel type of isomerism. *Angewandte Chemie International Edition*, **54**(4), (2015), 1130–1134.

Matti B. Alemayehu, Matthias Falmbigl, Corinna Grosse, Kim Ta, Saskia F. Fischer and David C. Johnson. Structural and electrical properties of a new $[(SnSe)_{1.16}]_1[NbSe_2]_1$ polytype. *Journal of Alloys and Compounds* **619**, (2015), 861–868.

Ryan Atkins, Michelle Dolgos, Andreas Fiedler, Corinna Grosse, Saskia F. Fischer, Sven. P. Rudin, and David C. Johnson. Synthesis and systematic trends in structure and electrical properties of $[(SnSe)_{1.15}]_m[VSe_2]_1$, $m = 1$, 2, 3, and 4. *Chemistry of Materials* **26**(9), (2014), 2862–2872.

Corinna Grosse, Ryan Atkins, Holm Kirmse, Anna Mogilatenko, Wolfgang Neumann and David C. Johnson. Local structure and defect chemistry of $[(SnSe)_{1.15}]_m(TaSe_2)$ ferecrystals - a new type of layered intergrowth compound. *Journal of Alloys and Compounds* **579**, (2013), 507–515.

Ryan Atkins, Sabrina Disch, Zachary Jones, Ines Häusler, Corinna Grosse, Saskia F. Fischer, Wolfgang Neumann, Paul Zschack and David C. Johnson. Synthesis, structure and electrical properties of a new tin vanadium selenide. *Journal of Solid State Chemistry* **202**, (2013), 128–133.

Ryan Atkins, Jason Wilson, Paul Zschack, Corinna Grosse, Wolfgang Neumann and David C. Johnson. Synthesis of $[(SnSe)_{1.15}]_m(TaSe_2)_n$ ferecrystals: structurally tunable metallic compounds. *Chemistry of Materials* **24**, (2012), 4594–4599.

Wolfgang Neumann, Holm Kirmse, Ines Häusler, Corinna Grosse, Peter Moeck, Sergej Rouvimov, Matt Beekman, Ryan Atkins, David C. Johnson and Kerstin Volz. Methods of electron crystallography as tools for materials analysis, invited lecture: XIVth International Conference on Electron Microscopy, Wisla, Poland, June 26-30, 2011, *Solid State Phenomena* **186** 1–6, 2012.

Holm Kirmse, Corinna Grosse, Ines Häusler, Peter Moeck, Sergej Rouvimov, Matt Beekman, Daniel Moore, Ryan Atkins, David C. Johnson and Wolfgang Neumann. Structural investigations of "ferecrystals" by scanning nanobeam transmission electron diffraction, lecture at symposium: Advances in Electron Crystallography for material Research, M&M2011, Nashville Tennessee, USA, 2011.

Sergej Rouvimov, Corinna Grosse, Matt Beekman, Ryan Atkins, Holm Kirmse, Paul Zschack, David C. Johnson and Wolfgang Neumann. Structural investigations of ferecrystals $[(SnSe)_{1+\delta}]_m(TSe_2)_n$ (T = Mo, Ta) by means of transmission electron microscopy, *11th IEEE International Conference on Nanotechnology - IEEE-Nano*, (2011), 398–403.

Holm Kirmse, Corinna Grosse, Ines Häusler, Peter Moeck, Sergej Rouvimov, Matt Beekman, Daniel Moore, Ryan Atkins, David C. Johnson und Wolfgang Neumann. Structural investigations of 'Ferecrystals' by scanning nanobeam transmission electron diffraction. Microscopy and Microanalysis **17**, 1070-1071 (2011).

In preparation:

Corinna Grosse, Matti B. Alemayehu, Matthias Falmbigl, David C. Johnson and Saskia F. Fischer. Normal-to-Superconducting Transition in $(PbSe)_{1.14}(NbSe_2)_n$ Ferecrystals with n = 1, 2, 3 in comparison to crystalline misfit layer compounds. In preparation.

Corinna Grosse, Georg Hoffmann, Matti B. Alemayehu, Olivio Chiatti, Anna Mogilatenko, David C. Johnson and Saskia F. Fischer. Low-temperature transport properties of $[(MSe)_{1.16}]_m(NbSe_2)_n$ ferecrystals with M = Sn and Pb. In preparation.

Selbständigkeitserklärung

Ich erkläre, dass ich die vorliegende Arbeit selbständig und nur unter Verwendung der angegebenen Literatur und Hilfsmittel angefertigt habe.

Corinna Grosse

Acknowledgement

First of all I would like to thank Prof. Dr. S. F. Fischer for giving me the opportunity to work on this exciting field of research under her supervision and whose support and insightful comments were invaluable during the course of my study. I am grateful to Prof. Dr. D. C. Johnson from the University of Oregon, for letting me take part in the exciting research field of ferecrystals, for providing many samples and for many informative, motivating discussions. I also want to thank Dr. Matti B. Alemayehu, Zachary Jones and Dr. Ryan Atkins for synthesizing the samples and for numerous discussions. Furthermore, I want to thank Prof. Dr. W. Neumann for introducing me to the topic of this thesis and for helpful discussions. I would like to express my gratitude to Dr. A. Mogilatenko who provided a lot of help, comments and suggestions for the TEM investigations. Special thanks go to all members of the group Novel Materials who provided a lot of help and sincere encouragement. I also want to thank the members of the AG TEM at the Humboldt-Universität zu Berlin, especially Dr. H. Kirmse for discussion about the TEM investigations, Eva Oehlschlegel and Kristiane Elsner for their support with the TEM specimen preparation. I also want to thank Dr. M. Albrecht and Robert Schewski for further support with TEM specimen preparation. I would like to thank Dr. C. Janowitz for discussion and helpful comments. Finally, I would also like to express my gratitude to my family and Thomas Mattscherodt for their support and warm encouragements.